

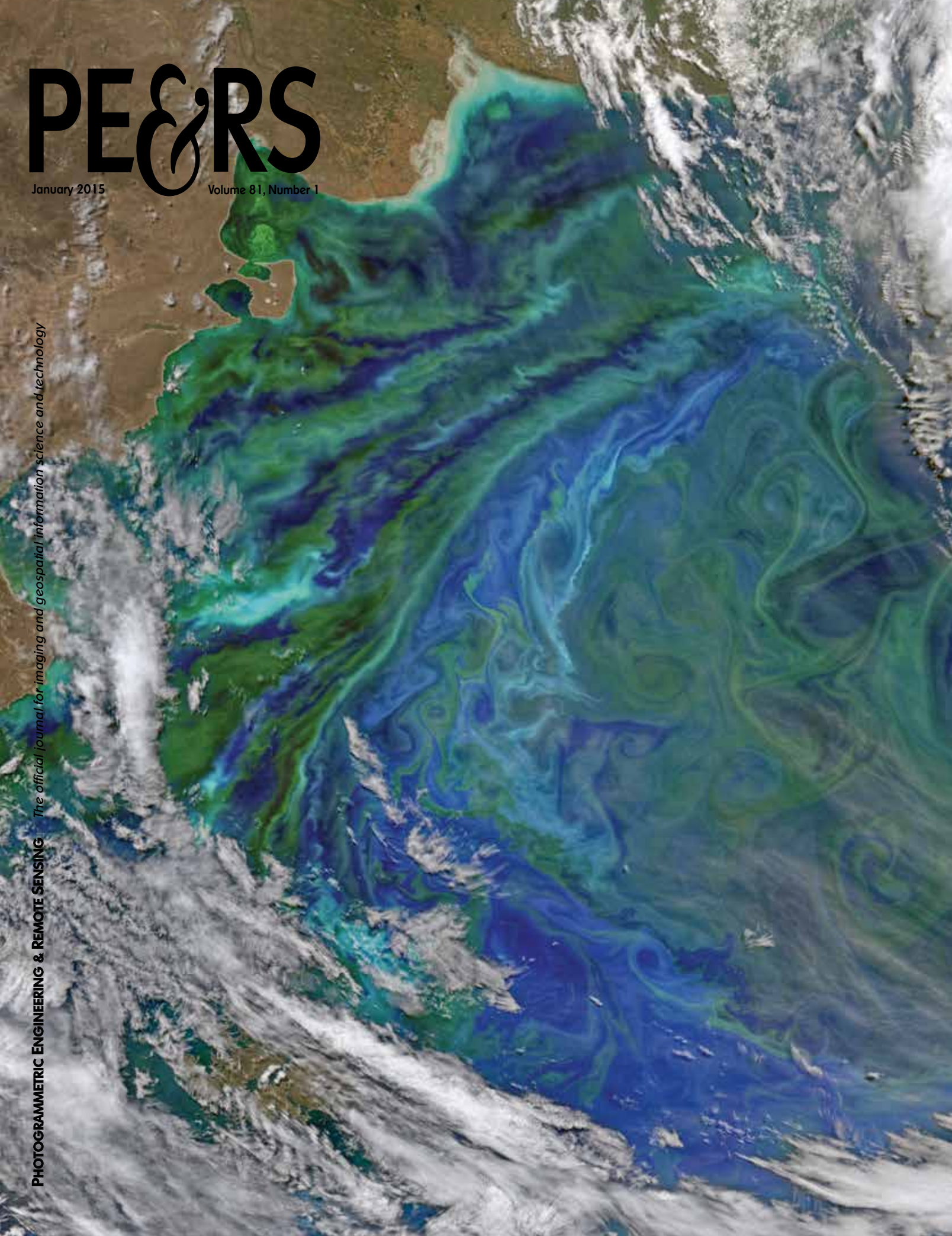
PE&RS

January 2015

Volume 81, Number 1

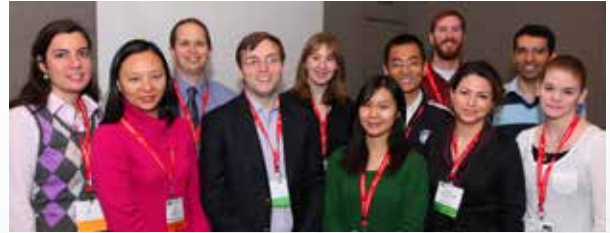
The official journal for imaging and geospatial information science and technology

PHOTOGRAMMETRIC ENGINEERING & REMOTE SENSING



The ASPRS Student Advisory Council (SAC)ensuring Student Member representation in ASPRS and more.

SAC is a group of students committed to serving all of the student members of ASPRS. Our goal is to ensure that ASPRS is a Society that both benefits from student involvement and creates opportunities for those students.



SAC is led by a Council of seven students who meet monthly to discuss issues pertaining to ASPRS Student Members. What do they do?

- **Organize special sessions** of interest to students at ASPRS Annual and fall conferences. <http://www.asprs.org/Annual-Conferences/Program/>
- **Create networking opportunities** during those conferences and bring together students looking for employment after graduation with potential employers in the industry.
- Inaugurate new programs within ASPRS.
- Design activities such as the **GeoLeague Competition** where students compete in teams using geospatial technology applications to solve a problem. <http://www.asprs.org/Students/GeoLeague-Challenge-2014.html>.



Promote student involvement in humanitarian projects such as crowdsourcing the manual interpretation of imagery in Somalia to identify shelters that are being used as homes by refugees. <http://irevolution.net/tag/tomnod/>.

All ASPRS Student Members are encouraged to become involved with SAC. Check out the SAC Social Networking sites and keep up with ongoing news.



Student Newsletter: <http://asprsignature.blogspot.com/>

Facebook page: <https://www.facebook.com/pages/ASPRS-Student-Advisory-Council/117943608233122>

LinkedIn Group: http://www.linkedin.com/groups?home=&gid=2487675&trk=anet_ug_hm

Email: asprs.chairsac@gmail.com

Save the Date!

ASPRS 2015 Annual Conference

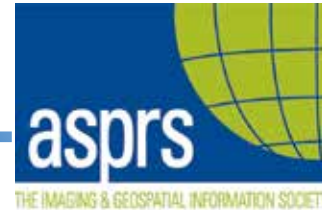
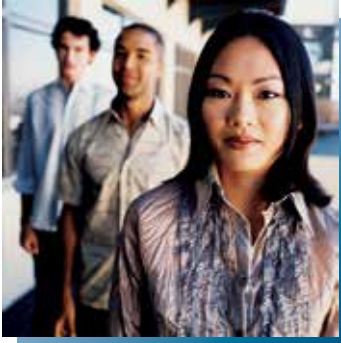
Tampa Bay Marriott Waterside Hotel

Tampa, Florida

May 4-8, 2015

asprs  **THE
IMAGING & GEOSPATIAL
INFORMATION SOCIETY**

Maximize Your ✓ Recognition ✓ Achievement ✓ Advancement



JOIN ASPRS TODAY! Benefits of ASPRS Membership

The benefits of membership in the American Society for Photogrammetry and Remote Sensing far exceed the initial investment.

Member benefits and services include:

- Monthly issue of *Photogrammetric Engineering & Remote Sensing (PE&RS)*
- Discounts on all ASPRS publications
- Job Fair Access
- Discounts on registration fees for ASPRS Annual Meetings and Specialty Conferences
- Discounts on ASPRS Workshops
- Receipt of Region Newsletter
- Region specialty conferences, workshops, technical tours and social events
- Opportunity to participate in ISPRS activities
- Invitations to Technical Committee and Division meetings
- Local, regional, national and international networking opportunities
- Eligibility for over \$18,000 in National and Region awards, scholarships and fellowships
- Opportunity to Access the ASPRS Membership Directory on the internet (search for other active individual members, sustaining members, and certified professionals)

VISIT [HTTP://WWW.ASPRS.ORG/JOIN-NOW.HTML](http://www.asprs.org/join-now.html) FOR MORE DETAILS!

COLUMNS

- Letter from the Executive Director 4
- Grids and Datums—*Republic of The Marshall Islands* 13
- Mapping Matters 15
- Book Review—*Elements of photogrammetry with Application in GIS, Fourth Edition* 19

ANNOUNCEMENTS

- ASPRS 2015 Annual Conference 1
- Signatures—SAC Blog 21
- January GeoByte—Relationship of and Transformations Between most Common Reference Frames Used in the U.S. 48
- Call for Papers 68

DEPARTMENTS

- Certification 18
- Region News 20
- ASPRS News 22
- Classifieds 22
- New Members 23
- Industry News 24
- Calendar 48
- Forthcoming Articles 48
- Who's Who in ASPRS 79
- Sustaining Members 80
- Instructions for Authors 82
- Membership Application 84

HIGHLIGHT ARTICLE

- 5 Geospatial Technologies Lead the Living to the Dead**
Nancy K. O'Hare, Brandon P. Adams, Marguerite Madden, and Thomas R. Jordan

PROFESSIONAL INSIGHT—AN INTERVIEW

- 11 UNM ASPRS Student Chapter**



PEER-REVIEWED ARTICLES

- 25 Correction of Distortions in YG-12 High-Resolution Panchromatic Images**
Yonghua Jiang, Guo Zhang, Deren Li, Xinming Tang, Wenchao Huang, and Litao Li
A method by which the positioning accuracy of YG-12 high-resolution panchromatic images using GCPs is significantly improved by eliminating inaccuracies caused by interior distortions and serious time-synchronization errors.
- 37 Optimal Land Cover Mapping and Change Analysis in Northeastern Oregon Using Landsat Imagery**
Michael Campbell, Russell G. Congalton, Joel Hartter, and Mark Ducey
compare a number of well-established techniques with some new methods using a two-county area in northeastern Oregon as a case study.
- 49 Reliable Spatial Relationship Constrained Feature Point Matching of Oblique Aerial Images**
Han Hu, Qing Zhu, Zhiqiang Du, Yeting Zhang, and Yulin Ding
A reliable feature point matching method for oblique aerial images using the spatial relationships of the point correspondences to remove outliers.
- 59 Sub-Pixel-Scale Land Cover Map Updating by Integrating Change Detection and Sub-Pixel Mapping**
Xiaodong Li, Yun Du, and Feng Ling
A land cover map updating method that involves the use of a current coarse-resolution remotely sensed image and a previous fine-resolution land cover map to update fine-resolution land cover maps.
- 69 Mapping Wetlands and Phragmites Using Publically Available Remotely Sensed Images**
Yichun Xie, Anbing Zhang, and William Welsh
Standard procedures for integrating NAIP (National Agriculture Imagery Program) and Landsat images with multiple processes of ground truthing, image classification and validation.



Late spring and summer weather brings blooms of color to the Atlantic Ocean off of South America. The Patagonian Shelf Break is a biologically rich patch of ocean where airborne dust from the land, iron-rich currents from the south, and upwelling currents

from the depths provide a bounty of nutrients for the grass of the sea—phytoplankton. In turn, those floating sunlight harvesters become food for some of the richest fisheries in the world.

The Visible Infrared Imaging Radiometer Suite (VIIRS) on Suomi NPP captured this false-color view of phytoplankton-rich waters off of Argentina on December 2, 2014. Scientists in NASA's Ocean Color Group used three wavelengths (671, 551, and 443 nanometers) of light to highlight different plankton communities in the water. Bands of color not only reveal the location of plankton, but also the dynamic eddies and currents that carry them.

The aquamarine stripes and swirls are likely coccolithophores, a type of phytoplankton with microscopic calcite shells that can give water a chalky color. The various shades of green are probably a mix of diatoms, dinoflagellates, and other species.

Blooms occur off of Patagonia because warmer, saltier waters from the subtropics meet the colder, fresher waters flowing up from the south. These currents collide along what oceanographers call a shelf-break front, a turbulent area of vertical and horizontal mixing on the edge of the continental shelf.

NASA images by Norman Kuring, NASA's Ocean Color Group. For more information, visit <http://earthobservatory.nasa.gov/IOTD/view.php?id=84870>



LETTER FROM THE EXECUTIVE DIRECTOR



Credit: http://www.nasa.gov/mission_pages/shuttle/flyout/multimedia/gallery/tribute_endeavour.html

REFITTING ASPRS

The Board of Directors has been laying the foundation to streamline the governance of ASPRS. Meanwhile, the staff have been working on four top priorities: 1) improving conferences; 2) fixing the business model and distribution of the journal; 3) modernizing the member database; and 4) getting better control of our many websites. On the conference front, perhaps you have already heard good things about UAS Mapping 2014 last October or the Pecora/ISPRS meeting in November. For the journal, we changed institutional pricing to be more in line with the market, and soon you will be able to access an improved and complete electronic version online. Although the member database may not sound exciting, when the modernization is complete we will be able to communicate with members more effectively, and they with each other. We will also roll out major website changes, adding capabilities like those showcased in uas.asprs.org.

Happy New Year – Happy New ASPRS!

To begin the New Year I invite you to take a journey with me. Some may say that ASPRS and its members have been on a journey for the past 80 years, but that lately the sailing has been rough, the ship has taken on water, and we've made little progress. Well, that's about to change. ASPRS is setting off on a new journey. We are charting a new course. Let's see if I can convince you to come on board.

Over the past nine months ASPRS has been hard at work refitting our ship and retraining our crew. The Board has begun repairs to the unwieldy governance structure, while Headquarters has begun making repairs in operations. For specifics, please see the sidebar. When these repairs are complete in the spring of 2014, our ship will be ready for sea once again. In anticipation, ASPRS seeks students, scientists, engineers, and business people to join the complement of women and men who choose to make this ship their professional home – who will call this ship “my ship”.

What's in it for you, the world's imaging and geospatial experts? Great rewards, including mem-

continued on page 20

PHOTOGRAMMETRIC ENGINEERING & REMOTE SENSING



JOURNAL STAFF

Publisher Dr. Michael Hauck

Editor Russell G. Congalton

Technical Editor Michael S. Renslow

Assistant Editor Jie Shan

Assistant Director — Publications Rae Kelley

Electronic Publications Manager/Graphic Artist Matthew Austin

Photogrammetric Engineering & Remote Sensing is the official journal of the American Society for Photogrammetry and Remote Sensing. It is devoted to the exchange of ideas and information about the applications of photogrammetry, remote sensing, and geographic information systems. The technical activities of the Society are conducted through the following Technical Divisions: Geographic Information Systems, Photogrammetric Applications, Lidar, Primary Data Acquisition, Professional Practice, and Remote Sensing Applications. Additional information on the functioning of the Technical Divisions and the Society can be found in the Yearbook issue of *PE&RS*.

Correspondence relating to all business and editorial matters pertaining to this and other Society publications should be directed to the American Society for Photogrammetry and Remote Sensing, 5410 Grosvenor Lane, Suite 210, Bethesda, Maryland 20814-2144, including inquiries, memberships, subscriptions, changes in address, manuscripts for publication, advertising, back issues, and publications. The telephone number of the Society Headquarters is 301-493-0290; the fax number is 301-493-0208; web address is www.asprs.org.

PE&RS. *PE&RS* (ISSN0099-1112) is published monthly by the American Society for Photogrammetry and Remote Sensing, 5410 Grosvenor Lane, Suite 210, Bethesda, Maryland 20814-2144. Periodicals postage paid at Bethesda, Maryland and at additional mailing offices.

SUBSCRIPTION. For the 2014 subscription year, ASPRS is offering two options to our *PE&RS* subscribers -- an e-Subscription and the print edition. E-subscribers can plus-up their subscriptions with printed copies for a small additional charge. Print subscriptions are on a calendar-year basis that runs from January through December. Electronic subscriptions run for twelve months on an anniversary basis. We recommend that customers who choose both e-Subscription and print (e-Subscription + Print) renew on a calendar-year basis. The new electronic subscription includes access to ten years' of digital back issues of *PE&RS* for online subscribers through the same portal at no additional charge. Please see the [Frequently Asked Questions](#) about our journal subscriptions.

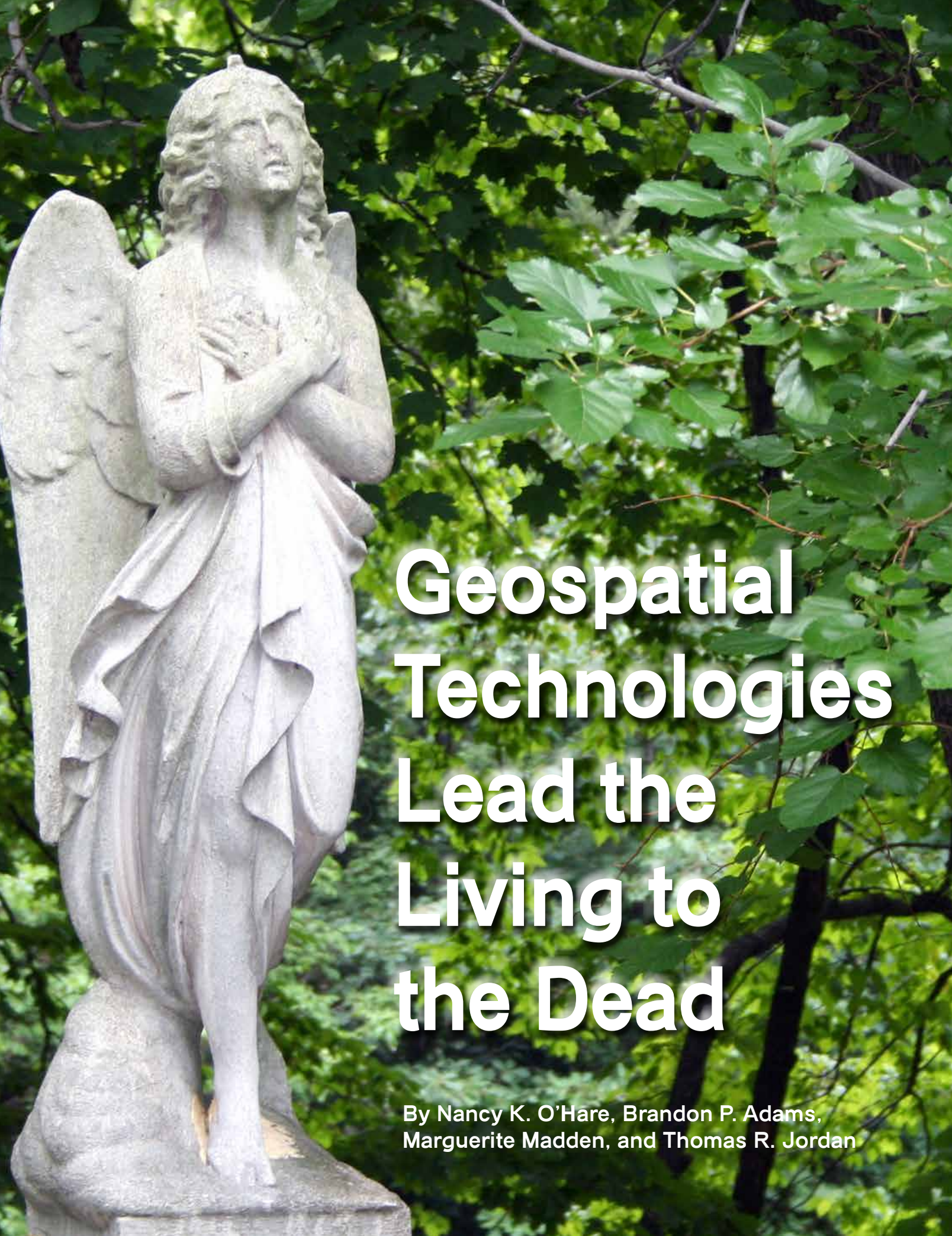
The rate of the e-Subscription (digital) Site License Only for USA and Foreign: \$899.00; e-Subscription (digital) Site License Only for Canada*: \$944.00; **Special Offers:** e-Subscription (digital) Plus Print for the USA: \$1,160.00; e-Subscription (digital) Plus Print Canada*: \$1,224.00; e-Subscription (digital) Plus Print Outside of the USA: \$1,175.00; Printed-Subscription Only for USA: \$959.00; Printed-Subscription Only for Canada*: \$1,013.00; Printed-Subscription Only for Other Foreign: \$974.00. *Note: e-Subscription/Printed-Subscription Only/e-Subscription Plus Print for Canada include 5% of the total amount for Canada's Goods and Services Tax (GST #135123065).

POSTMASTER. Send address changes to *PE&RS*, ASPRS Headquarters, 5410 Grosvenor Lane, Suite 210, Bethesda, Maryland 20814-2144. CDN CPM #40020812

MEMBERSHIP. Membership is open to any person actively engaged in the practice of photogrammetry, photointerpretation, remote sensing and geographic information systems; or who by means of education or profession is interested in the application or development of these arts and sciences. Membership is for one year, with renewal based on the anniversary date of the month joined. Membership Dues include a 12-month subscription to *PE&RS*. Subscription is part of membership benefits and cannot be deducted from annual dues. Beginning with the January 2014 issue of *PE&RS*, all members outside of the USA will receive access to the full digital edition of the journal rather than the printed copy. Dues for ASPRS Members outside of the U.S. will now be the same as for members residing in the U.S. Annual dues for Regular members (Active Member) is \$150; for Student members it is \$50 for USA and Canada; \$60 for Other Foreign (E-Journal – No hard copy for all Students); for Associate Members it is \$100 (member must be under the age of 35, see description on application in the back of this Journal). A tax of 5% for Canada's Goods and Service Tax (GST #135123065) is applied to all members residing in Canada.

COPYRIGHT 2015. Copyright by the American Society for Photogrammetry and Remote Sensing. Reproduction of this issue or any part thereof (except short quotations for use in preparing technical and scientific papers) may be made only after obtaining the specific approval of the Managing Editor. The Society is not responsible for any statements made or opinions expressed in technical papers, advertisements, or other portions of this publication. Printed in the United States of America.

PERMISSION TO PHOTOCOPY. The appearance of the code at the bottom of the first page of an article in this journal indicates the copyright owner's consent that copies of the article may be made for personal or internal use or for the personal or internal use of specific clients. This consent is given on the condition, however, that the copier pay the stated per copy fee of \$3.00 through the Copyright Clearance Center, Inc., 222 Rosewood Drive, Danvers, Massachusetts 01923, for copying beyond that permitted by Sections 107 or 108 of the U.S. Copyright Law. This consent does not extend to other kinds of copying, such as copying for general distribution, for advertising or promotional purposes, for creating new collective works, or for resale.



Geospatial Technologies Lead the Living to the Dead

By Nancy K. O'Hare, Brandon P. Adams,
Marguerite Madden, and Thomas R. Jordan

INTRODUCTION

Increasingly, cultural institutions are turning to geospatial technologies to manage resources, enhance visitor experience, and provide “virtual tourism”, among other uses (Majó *et al.*, 2004; Brown, 2006; Scott, 2006). For many local cultural or historical sites, such a turn has been difficult because these types of institutions often lack the funding and/or technical knowledge to leverage geospatial technologies. As part of our commitment to community service, members of the ASPRS Student Chapter at the University of Georgia (UGA) volunteered assistance to a local group, the Friends of Oconee Hill Cemetery (OHC).

The Friends of OHC was established in 1999 to encourage community attention and involvement in the restoration and preservation of OHC. Seeking funding to assure that the gravesites of all veterans receive regular maintenance, the Friends needed to determine how many veterans’ gravesites required care and where these gravesites were located. Such needs were the result of several factors. First, regular care of lots was originally the responsibility of the lot owner. Since 1915, lot care by the cemetery Sexton (caretaker) could be purchased separately. It was only since 1946 that perpetual lot care by the cemetery Sexton has been included in the lot purchase. The Sexton does provide nominal care for all lots each winter, yet lacks the resources to do so on a regular basis during the long summer growing season. Second, each cemetery lot accommodates several internments. Maps of the lots exist, but not internments within a lot. Lastly, original records prior to 1896 were lost in a fire and could only be partially reconstructed through other sources including direct knowledge, tombstone inscriptions, and newspaper obituaries (Marshall, 1971; Marshall, 2009).

“We soon realized that other geospatial technologies could be used to assist in preserving the cemetery, easily locate specific gravesites by name, and help the public navigate to and appreciate the many areas of historical significance within the cemetery.”

The ASPRS Student Chapter at UGA was initially approached by the Friends of OHC to map veterans’ gravesites. We soon realized that other geospatial technologies could be used to assist in preserving the cemetery, easily locate specific gravesites by name, and help the public navigate to and appreciate the many areas of historical significance within the cemetery. This local collaboration also provided students with an opportunity for community outreach and an introduction to several open-source geospatial software tools.

OCCONEE HILL CEMETERY BACKGROUND

Established in 1856, OHC is one of the oldest public cemeteries in Athens, Georgia, USA (Figure 1). The Old section of the cemetery follows the “rural” (also referred to as garden or Victorian) cemetery design first introduced in the USA in 1831 with the founding of Mount Auburn Cemetery in Massachusetts (French, 1974). As the various names suggest, this type of cemetery idealized park-like design with magnificent trees, impressive monuments, decorative ironwork, and statuary (Figure 2). In 1900, the cemetery expanded. The design of the New section reflected changing aesthetics and the realities of maintaining garden type cemeteries. Monuments in the New section are more uniform and large trees less common. Together, both the Old and New sections of OHC reveal the changing nature of societal attitudes to burials.

Regardless of their dissimilar designs, both the Old and New sections of OHC are meaningful in terms of local and national history. OHC serves as the final resting place for Athenians from all walks of life, ranging from wealthy business owners to paupers. Some non-Athenians are also buried at OHC, including a group of Travelers (aka, Roaders or American gypsies). Nationally well-known or historically significant persons interred at OHC include Wilson Lumpkin, state and federal politician and supervisor of the forced march of Cherokee Indians on the Trail of Tears, prominent generals in the Confederate States Army including T.R.R. Cobb, Dr. Crawford Long who first adopted anesthesia for surgery, aviation pioneer Ben Epps, portrait miniature artist Lucy May Stanton, Dean Rusk who served as the US Secretary of State from 1961 to 1969, and musician Ricky Wilson of the iconic band the B52s.

Because OHC is both an historic and an active cemetery, it has the distinction of being the final resting place of veterans from every war or conflict in which the USA has participated. Veterans involved in the country’s early conflicts died before the cemetery’s founding in 1856; their remains are now interred at OHC after being moved from their initial burial locations. Until the mid-1800s, burials were commonly made on family land, land associated with churches, or in other public burial grounds, but none of these guaranteed that gravesites would remain undisturbed (Sloane, 1995). As public cemeteries opened, which promised gravesites would be undisturbed, existing burials on family/private land were frequently moved. The regular maintenance of the gravesites was the responsibility of the living family members; only in the mid twentieth century did the responsibility of regular maintenance, shift to the cemetery. However, in an historic cemetery, such as OHC, many lots are not in perpetual care, including those of veterans.

USING GEOSPATIAL TECHNOLOGIES

The following sections are organized by geospatial technology and include within each section both the methods and results.

PAPER RECORDS TO GIS

All existing cemetery maps and burial records were on paper. We used both sets of information to create a GIS database.

We first created a polygon feature layer of the individual lots in the Old section of the cemetery from the 8 ½" x 11" map in Marshall (2009), which was the only hard copy of this map available to us. This map was a composite of traditional land survey maps produced in 1894, 1906, and 1909. The maps lacked references to a geographic coordinate system, and to any features outside of the cemetery boundaries that could be used to place the map within a geographic coordinate system. This is simply a reflection of the era that produced the maps rather than any sort of inherent deficiencies in relative spatial locations. Placing the maps within a geographic coordinate system requires relating the local coordinates of at least four points on the map to the locations of the same points in a known geographic coordinate system. These points should be well-distributed, since rectification accuracy decreases outside of the spatial bounds of the ground control points (Welch and Jordan, 1996; McGlone, 2013). The known coordinates can come from ground collected GPS points or from newer orthorectified imagery of adequate spatial resolution and positional accuracy. We first attempted rectification using freely distributed 2009 National Agriculture Imagery Program (NAIP) true-color, growing season (leaf-on) imagery with 1-m spatial resolution. However, the spatial distribution of coincident identifiable features between the paper map and the NAIP imagery was limiting. The map of lots lacked accurate geographic references outside of the lot boundaries. In the NAIP imagery, the extensive tree canopy obscured many ground features. We then used a Trimble Geo6000 Xh GPS to collect ground control points within OHC, with a post-processed accuracy of ± 1 to 2 m. The resultant root mean square error (RMSE) after georeferencing was ± 3.6 m and this is the error associated with the spatial location accuracy of our GIS feature layer.

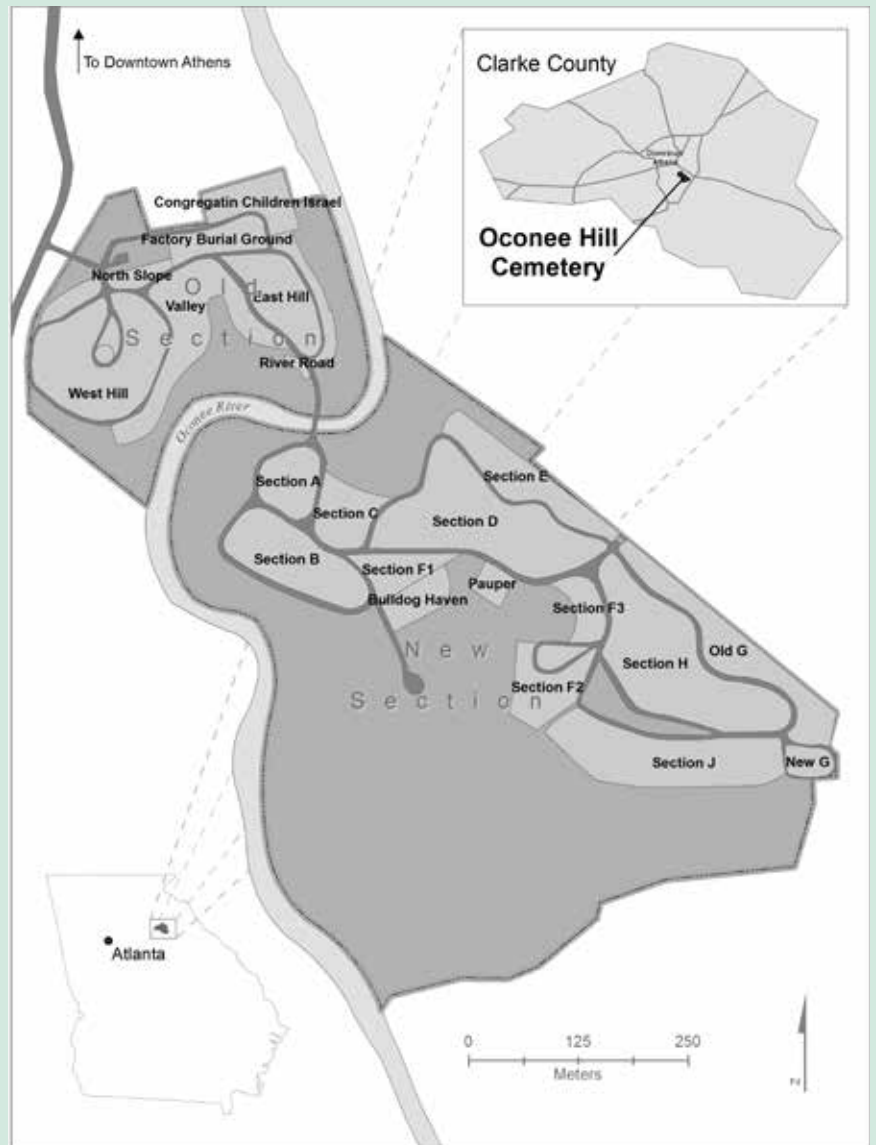


Figure 1. Location of Oconee Hill Cemetery in Athens, Georgia, USA.

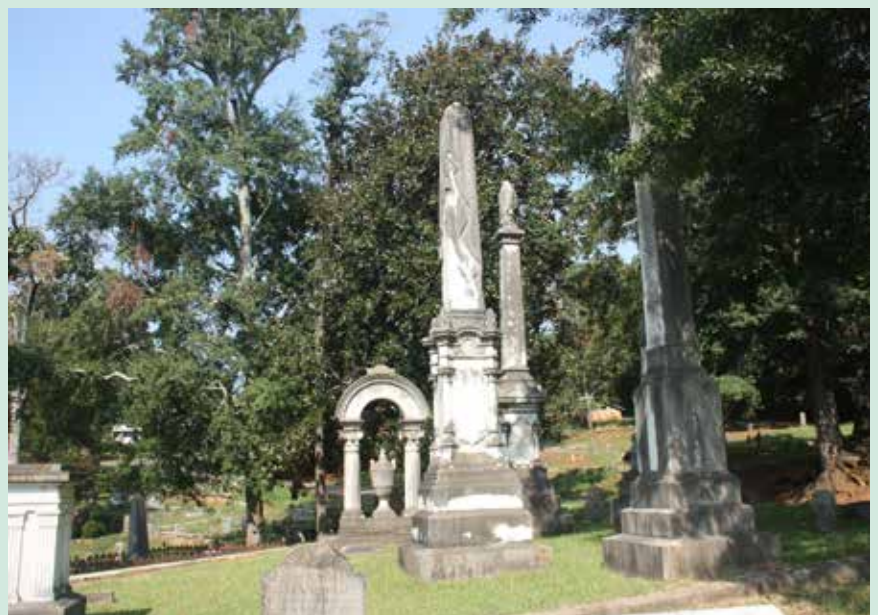


Figure 2. Example of the monuments in the Old section of Oconee Hill Cemetery.

After rectification of the scanned cemetery map, boundaries of OHC lots were manually digitized. Automated vectorization was not suitable since the original maps had background lettering and numbering. Polygon features were attributed with lot number, family/owner's name, and level of care (perpetual or none). We then created an associated data table, joined through the lot number, for each veteran's burial, using Marshall (2009). This table included date of birth, date of death, military branch, military rank, conflict(s) served in, and whether the person was killed or disabled during military service. Marshall (2009) provided not only the tombstone inscription, but also supplementary information from the official Record of Internments for the cemetery, newspaper obituaries, and Charlotte Marshall's extensive genealogical knowledge.

Of the 516 lots in the Old section of OHC, veterans' gravesites occurred in 199 lots. The 199 lots contained gravesites of 316 veterans. These veterans served in the American Revolutionary War (2 veterans), War of 1812 (4), Mexican War (4), various conflicts related to Native American removal from the expanding USA territory (5), American Civil War (207), Spanish-American War (6), Philippines War (1), WW I (30), WW II (23) and Vietnam (2)¹, plus veterans that served during times of peace (30). Of these 316 veterans, the gravesites of 93 veterans were interred in 76 lots that lacked perpetual care. Using this information, the Friends of OHC were able to secure a \$25,000 donation to assure perpetual care for all veterans' graves in the Old section of OHC.

GeoPDF AND QR CODES FOR MAP DISTRIBUTION

The perpetual care of lots by the cemetery Sexton does not include the costs for preserving the stone monuments which are suffering from 150+ years of weathering, soil erosion, vandalism, and damage from tree limbs falling from mature trees. One act of vandalism scarred more than 60 statues in one night (Banner-Herald, November 22, 1963). The Friends of OHC need a way to relate to visitors, promote local awareness to generate community support and respect of the historic nature of the cemetery, and to stimulate financial support.

Geographic data can be exported to portable document format (pdf) to create a GeoPDF which can be viewed using a free map application for mobile devices, such as Avenza reader (Wulrich, 2006; Pardue, 2008). If the mobile device is GPS enabled, the GeoPDF displays the user's real time location on the map thereby providing an intuitive way to navigate. GeoPDFs could be used by OHC to guide a family to an ancestor's gravesite or for self-guided tours highlighting, for example, historical figures or Victorian-era gravestone symbolism or veterans' gravesites.

1 The New portion of the cemetery contains gravesites of veterans from Korea, both Iraq Wars, and the Afghanistan War. Our surveys in the New portion of the cemetery have not been completed. Therefore, this article focused on the completed surveys in the Old portion of OHC.

GeoPDFs for viewing only can be easily created through standard GIS software. For example, in ArcGIS, the map is simply exported to the GeoPDF format. Interactive GeoPDFs also can be created, but this currently requires TerraGo Tech's proprietary stand-alone software or their plug-in for ArcGIS. An interactive GeoPDF allows the user to select layers to display and view supplemental information, such as photographs, videos, or hyperlinks. While a network connection to the server hosting the GeoPDF file is required for map distribution to the mobile device, once the GeoPDF is loaded, internet connectivity is not required.

For any GeoPDF to be useful for self-guided tours, real-time location accuracy is needed. We created a GeoPDF of an existing tour, designed by the Friends of OHC and currently distributed on paper, for Veteran's Day. Typical cemetery lots are 6 m x 6 m. The base GIS layer created by rectifying a paper map had an RMSE of ± 3.6 m after rectification. Additionally, there would be real-time GPS receiver error. The self-guided GeoPDF tour was tested in the field on an Apple iPad 4 using the free Avenza GeoPDF map viewer. Self-navigation by referencing the location of the iPad relative to the OHC GeoPDF placed the user in or on the edge of the desired cemetery lot 18 out of 19 times. Average error of the center of cemetery lot locations in real-time was ± 4.3 m ($n=19$; range of 1.3 to 14.5 m). This level of accuracy is believed to be suitable for the general public to navigate to specific OHC lots to locate an ancestor's gravesite or for the general public on self-guided thematic tours of the cemetery.

A way to distribute the GeoPDF tour of OHC also was necessary. This was accomplished by creating a quick response (QR) code to direct users to a web server for GeoPDF download (Figure 3). Both the software to generate and read QR codes



Figure 3. Quick response (QR) code that links to a GeoPDF tour of veterans' gravesites in the Old section of Oconee Hill Cemetery. To access, scan the QR code with a smart phone or tablet, open the link in a browser, then choose to open the map in a map app, such as Avenza PDF Maps (free). Once the map is opened in Avenza, it is available to the user even when an internet connection is not available. The user's GPS location will be displayed as distance to the OHC map. The user's GPS location will display as dot (typically blue) when physically within the OHC map extent.

is freely available. Users with mobile devices equipped with a camera can scan the QR code on handouts provided at the cemetery or on their website which automatically directs the user to a server at the UGA Geography-CGR website to view and download the GeoPDF featuring veterans' gravesites. Users who are not physically within the map extent can view the map, but will not see their location on the map.



Figure 4. Digital photograph of monument (left) and three dimensional model (right) created from 33 images using free online version of AutoDesk 123D catch (www.123dapp.com/catch).

3D MODELS OF STATUES

The cemetery contains marble and granite statues and tombstones (collectively referred to as monuments) dating from the 1850s. All monuments are subject to weathering, and some have been vandalized or damaged by falling tree limbs or erosion. One act of vandalism scarred more than 70 monuments in one night (Banner-Herald, November 22, 1963). There is no photographic inventory of the monuments in OHC. If an inventory is done in the future, the value of the photographic record could be amplified by taking overlapping images so they could later be converted to three dimensional (3D) models using Structure from Motion (SfM).

Structure from Motion (SfM) algorithms create 3D models from a series of overlapping two dimensional (2D) images (Szeliski and Kang, 1994). While initially used for computer vision, SfM has been widely adapted for a variety of applications, including cultural and historic preservation (Westoby *et al.*, 2012). While images input to SfM software have typically been acquired from handheld cameras, 3D models recently have been created from images acquired from unmanned aerial vehicles (Mancini *et al.*, 2013; Mathews and Jensen, 2013; Zarco-Tejada *et al.*, 2014). Although SfM can be used for multiple purposes (Stefanik *et al.*, 2011; Westoby, Brasington, Glasser, Hambrey and Reynolds, 2012; Mathews and Jensen, 2013), our use was for the creation of 3D models of individual statues. More rigorous application would be capturing actual measurements and textural variation. We only evaluated the ability to capture measurements from a single statue.

We used AutoDesk 123D Catch (www.123dapp.com/catch) online SfM software, since one of our objectives was to use freely available software to introduce a local non-profit

comprised of volunteers as well as UGA students to developing geospatial technologies. A high-resolution model was created from a series of 33 photographs (Figure 4). The software allows creation of a single scale measurement between two 3D points. We defined the scale of the model using a single measurement of the width of the letter “M” within the name, “Norma” on the model (90 cm). We measured 12 other features on the 3D model that were relatively distinct and compared these to the actual measurements from the statue (Table 1). All of the features lacked significant tonal differences, and many of the edges were either rounded, rough-hewn, or chipped, complicating placement of the marker at the same point from different viewpoints. The 3D model and actual measurements had an average difference of 3.3%. An animation of the final model can be viewed at <http://maestro.crms.uga.edu/QRdocs/norma.avi>.

Table 1. Comparison of 3D model measurements to actual measurements, in cm.

Feature	3D model	Actual	Difference	% Difference
Width “N”	61.8	60	1.8	3.0%
Width “O”	59.8	60	0.2	0.3%
Width “R”	63.5	60	3.5	5.8%
Width “A”	88.5	90	1.5	2.5%
Height “N”	104.9	104	0.9	0.9%
Height “O”	108.4	104	4.4	4.2%
Height “R”	107.2	104	3.2	3.0%
Height “M”	107.4	104	3.4	3.3%
Height of scroll	542.0	545	3.0	0.5%
Width of base	1664.4	1570	94.4	6.0%
Height 1 st step	121.7	130	8.3	6.3%
Height 2 nd step	125.2	130	4.8	4.0%

SUMMARY

This project connected the living to the dead in ways that enriched visitor experience and preservation of an historic cemetery. The enumeration and documentation of the physical locations of veteran's gravesites in the Old section of OHC secured a \$25,000 donation to guarantee their regular care and maintenance. UGA undergraduate and graduate students were introduced to a local cemetery with historic connections, statuary art, and how to apply geospatial technologies. One group of UGA students used SfM to create 3D models of OHC monuments that are accessible online (<https://www.youtube.com/watch?v=G4PMA5Y1ZDA>).

Proprietary software would undoubtedly enhance the visual quality of our final projects, but open software may be preferred for initial access to geospatial technologies. For example, educational institutions and non-profits organizations are more likely to first explore new geo-spatial technologies with freely distributed, open-source geospatial methods, software and image/map data before committing financial resources to purchase and learn proprietary software.

In our opinion, many local groups are in need of assistance with basic geospatial skills. Technical skills required in this project (i.e., rectification, digitizing, developing attribute tables, simple queries, taking photographs) would be considered novice-level skills for professional GIS or remote sensing specialists. Sometimes, however, that is all that is needed to benefit the communities in which we live.

ACKNOWLEDGEMENTS

The Friends of Oconee Hill Cemetery approached us with the seed of this project; we are especially grateful to Helen Mills, Helen Constatino and Jane Begnaud. Brian Adler, Sexton of Oconee Hill Cemetery, kindly provided access to paper maps and shared his knowledge of the Cemetery. Larry Nackerud and Lauren Ricciardelli, School of Social Work at the University of Georgia, took over other aspects of the project not included here with enthusiasm and a grand ability to provide "volunteers". UGA seminar class GEOG8550 in spring 2014 generated the 3D models displayed on the YouTube channel; this class was taught by Dr. Marguerite Madden and Dr. Deepak Mishra. Dr. Andrea Presotto provided thoughtful comments from a different perspective.

LITERATURE CITED

Banner-Herald, November 22, 1963. Athens, GA
Brown, D., 2006. Ko to ringa ki nga rakau a te Pakeha: Virtual Taonga, Maori, and Museums. *New Zealand Sociology*, 21(1):27-48.
French, S., 1974. The Cemetery as Cultural Institution: The Establishment of Mount Auburn and the 'Rural Cemetery' Movement. *American Quarterly*, 26(1):37-59.

Majó, J., J. Martínez and P.P. Vázquez, 2004. Virtual Museums: New added-value for Museums Web Sites. *Information & Communication Technologies in Tourism 2004: Proceedings of the International Conference in Cairo, Egypt, 2004*:195-204.
Mancini, F., M. Dubbini, M. Gattelli, F. Stecchi, S. Fabbri and G. Gabbianelli, 2013. Using Unmanned Aerial Vehicles (UAV) for High-Resolution Reconstruction of Topography: The Structure from Motion Approach on Coastal Environments. *Remote Sensing*, 5(12):6880-6898.
Marshall, C.T., 1971. *Oconee Hill Cemetery; tombstone inscriptions for that part of cemetery west of Oconee River and index to record of interments*. Athens Historical Society, Athens, GA, 149 p.
Marshall, C.T., 2009. *Oconee Hill Cemetery of Athens, Georgia*. Athens Historical Society, Athens, GA, 620 p.
Mathews, A.J. and J.L.R. Jensen, 2013. Visualizing and Quantifying Vineyard Canopy LAI Using an Unmanned Aerial Vehicle (UAV) Collected High Density Structure from Motion Point Cloud. *Remote Sensing*, 5(6):2164-2183.
McGlone, J.C., 2013. *Manual of Photogrammetry*. ASPRS, Bethesda, MD, 1318 p.
Pardue, J., 2008. *The GeoPDF File; a new solution for the digital publication, distribution, and collaboration of geospatial data*. U. S. Geological Survey, Reston, VA, 30 p.
Scott, P., 2006. Virtual journeys: the museum with no frontiers. *Canvas: Art and Culture from the Middle East and Arab World*, 2(4):60-65.
Sloane, D.C., 1995. *The Last Great Necessity: Cemeteries In American History, Creating The North American Landscape*. The John Hopkins University Press,
Stefanik, K.V., J.C. Gassaway, K. Kochersberger and A.L. Abbott, 2011. UAV-Based Stereo Vision for Rapid Aerial Terrain Mapping. *GIScience & Remote Sensing*, 48(1):24-49.
Szeliski, R. and S.B. Kang, 1994. Recovering 3D Shape and Motion from Image Streams Using Nonlinear Least Squares. *Journal of Visual Communication and Image Representation*, 5(1):10.
Welch, R. and T.R. Jordan. 1996. Using scanned aerial photographs, *Raster Imagery in Geographic Information Systems*, (S. Morain and S. Lopez Baros, editors). OnWord Press, Santa Fe, NM, pp. 55-69.
Westoby, M.J., J. Brasington, N.F. Glasser, M.J. Hambrey and J.M. Reynolds, 2012. 'Structure-from-Motion' photogrammetry: A low-cost, effective tool for geoscience applications. *Geomorphology*, 179:300-314.
Wulrich, D., 2006. Data sharing with GeoPDFs. *Geospatial Solutions*, 16(1):34-35.
Zarco-Tejada, P.J., R. Diaz-Varela, V. Angileri and P. Loudjani, 2014. Tree height quantification using very high resolution imagery acquired from an unmanned aerial vehicle (UAV) and automatic 3D photo-reconstruction methods. *European Journal of Agronomy*, 55:89-99.

Cover photo courtesy of Kenn W. Kiser, morgueFile.com.

UNM ASPRS STUDENT CHAPTER

INTERVIEW

Introducing ASPRS' newest student chapter at the University of New Mexico.

Christopher D. Lippitt, Faculty Advisor, UNM ASPRS Student Chapter, Vice President, Rio Grande Chapter; and Su Zhang, Chapter President, UNM ASPRS Student Chapter discuss the importance of student chapters to the industry.



UNM ASPRS Student Chapter members after receiving their charter.

Why did you decide to develop a student chapter at UNM?

Chris — We started as a venue to facilitate cooperation and self-determination amongst our GIScience students. Workshops, trainings, visits to facilities, hosting speakers, all of the activities of the student chapter allow a greater number of students to be exposed to greater number of opportunities and to determine the course of their own education, network, and career. We've already hosted a workshop focused on the use of R for spatial analysis and data handling thanks to Steve Sesnie and Sarah Lehnen of the US Fish and Wildlife Service here in Albuquerque.

We've got plans to establish a Volunteer Hazard Mapping Corp (VHMC) through the chapter, modeled after the VHMC at San Diego State University. I for one can't wait to see what they do with the chapter next.

How is having a student chapter beneficial to the students?

Chris — In one word: exposure - to opportunities, to industry, to professional networks, to the culture of their intended industry, to scholarships. The chapter has the potential to allow a group of students to strategically augment their skillsets and professional network beyond those available in their formal program of study.

Su — From the standpoint of a student, the chapter works as a nexus for us to know other professionals, other faculty members, and other students. In a traditional academic environment, the only way for a student to know others who have the same interest through faculty members or classmates. Like Chris said, the student chapter will provide massive exposure benefits to any students who are interested in geospatial technologies.

How was the process of setting up the student chapter with ASPRS?

Su — It was a wonderful experience setting up the student chapter with ASPRS. The officers from the ASPRS Rocky

Mountain Region helped us a lot with the whole process. They walked us through each step of the process and even helped us navigate the bumps that popped up along the way. They were always ready to answer questions we had and they took care of any issues right away. We want to specially thank Harold Cline, Michaela Buenemann, Jeff Young, and Sokhan Hing for their enormous help.

What are the goals of the chapter?

Su — The chapter has identified a number of goals, including: (1) advancing scientific knowledge in the disciplines of photogrammetry and remote sensing; (2) working with governmental and private organizations in promoting programs related to photogrammetry and remote sensing to the general public; (3) expediting the exchange of knowledge and ideas among the members of ASPRS and with those of other national and international organizations with similar or related interests; (4) serving the members as a central source of information related to photogrammetry and remote sensing.



A UNM ASPRS organized workshop focused on the use of R for spatial analysis and data handling. Steve Sesnie and Sarah Lehnen of the US Fish and Wildlife Service instructed the day long workshop.



UNM ASPRS student chapter members with Rio Grande Chapter board members at the Rio Grande Chapter Fall meeting.

How can ASPRS better assist their student chapters?

Chris — I like the idea of making funds available to support hosting local/regional events such as speakers or workshops - anything to facilitate interaction between the student chapters and the regional membership.

Su — I support the idea of allocating more “resources” to support the growth the student chapters. For example, an officer could be designated to interact with student chapters to listen to the special needs of a specific chapter. In addition, ASPRS could help student chapters interact with the industry by exposing members to more opportunities. It would also great if we could get free state-of-art technology training routinely to prepare the students to be ready for various challenges.

Will the student chapter plan any activities to expose local elementary and high school students to the industry?

Su — We are planning to do a series of events on the next GIS Day to expose local elementary and high school students to the industry. We are also planning to organize a field trip to Blue Skies Aerial Survey firm to provide a unique geospatial exposure to local students. Students will be able to experience the procedures used when acquiring aerial photography and the post-processing that leads to the final products. We hope such activities will arouse interests in local elementary and high school students for learning geospatial knowledge.

What do you feel should be the student chapters role in the Society?

Chris — I believe student chapters can act as the “boots on the ground” in between meetings. What I mean by that is they can organize events that are open to the regional membership, which serves both the chapter’s members and the regions. More practically, student chapter members are literally the future of the society, and obviously warrant the larger societies’ support. Supporting them in their role as regional facilitators of events serves everyone’s interests.

What is the future of ASPRS in your opinion?

Chris — ASPRS plays a critical role in the remote sensing and the GIS community; its established track record at the intersection of industry, academia, and government,

independent from any particular corporate entity, and explicit relationship with the international society make it unique and, I believe, well positioned to foster and represent the larger geospatial community.

Su — The 21st Century is a century of “Digital Earth”. Significant progress towards Digital Earth has been achieved over the last couple of decades. Geospatial technologies are the fundamental elements of Digital Earth and I think ASPRS will play a significant role in promoting Photogrammetry, Remote Sensing, and GIS knowledge to the general public to prepare them to be ready for the Digital Earth Century. In addition, ASPRS plays a critical role in collaborating with other international geospatial groups across the world representing the U.S. geospatial community.



GeoBytes!

ASPRS GIS DIVISION — FREE ONLINE SEMINARS

The ASPRS GIS Division,
in cooperation with
CaGIS and GLIS, is
sponsoring free online
live seminars throughout
the year.

*Attention those seeking ASPRS
Certification: ASPRS Online
Seminars are a great way to gain
Professional Development Hours!*

[http://www.asprs.org/
GISD-Division/Online-
Seminars.html](http://www.asprs.org/GISD-Division/Online-Seminars.html)



& GRIDS & DATUMS

BY Clifford J. Mugnier, CP, CMS

REPUBLIC OF

THE MARSHALL ISLANDS

“Little is clearly understood about the prehistory of the Marshall Islands. Researchers agree on little more than that successive waves of migratory people from Southeast Asia spread across the Western Pacific about 3,000 years ago and that some of them landed on and remained on these islands. The Spanish explorer *de Saavedra* landed there in 1529. They were named for English explorer John Marshall, who visited them in 1799. The Marshall Islands were claimed by Spain in 1874. Germany established a protectorate in 1885 and set up trading stations on the islands of Jaluit and Ebon to carry out the flourishing copra (dried coconut meat) trade. Marshallese *iroij* (high chiefs) continued to rule under indirect colonial German administration. At the beginning of World War I, Japan assumed control of the Marshall Islands. Their headquarters remained at the German center of administration, Jaluit. U.S. Marines and Army troops took control from the Japanese in early 1944, following intense fighting on Kwajalein and Enewetak atolls. In 1947, the United States, as the occupying power, entered into an agreement with the UN Security Council to administer Micronesia, including the Marshall Islands, as the Trust Territory of the Pacific Islands. On May 1, 1979, in recognition of the evolving political status of the Marshall Islands, the United States recognized the constitution of the Marshall Islands and the establishment of the Government of the Republic of the Marshall Islands. The constitution incorporates both American and British constitutional concepts” (*Background Notes, U.S. Dept. of State, 2014*).

“U.S. nuclear testing took place between 1946 and 1958 on the islands of Bikini and Eniwetok. The people of Bikini were removed to another island, and a total of 23 U.S. atomic and hydrogen bomb tests were conducted. Despite cleanup attempts, the islands remain uninhabited today because of nuclear contamination. The U.S. paid the islands \$183.7



million in damages in 1983, and in 1999, the U.S. approved a one-time \$3.8-million payment to the relocated people of Bikini atoll. Kwajalein atoll is the site of an American military base and has been used for missile defense testing since the 1960s” (*InfoPlease, 2014*).

The Marshall Islands terrain is low coral limestone and sand islands. The lowest point is the Pacific Ocean (0 m), the highest point is an unnamed location on Likiep (10 m). About the same size as Washington, D.C., the coastline is 370.4 km long. (*World Factbook, 2014*)

Dr. Helmut Schmid was one of the original German V-2 Rocket Scientists from Peenemünde that were brought to the U.S. at the end of WWII. While most of the Germans were taken to White Sands Missile Proving Grounds, Dr. Schmid was moved to Aberdeen Proving Grounds in Maryland. His protégé was Dr. Duane C. Brown, the Father of American Computational Analytical Photogrammetry. While at Aberdeen, Dr. Schmid designed the WILD Heerbrugg BC-4 ballistic camera for tracking the flights of guided missiles at night. (*I personally own one that I converted for terrestrial photogrammetry. Every Spring semester I have it taken out for my students to see how the “old timers” used to do things. Personally, I haven’t been*

able to pick the thing up for the last 30 years. – Ed.) Some of the BC-4 camera systems were transferred to the U.S. Coast & Geodetic Survey for the BC-4 Photogrammetric Geodesy program of the 1960s and early 1970s and were directed by Dr. Schmid. (*I once was introduced to Dr. Schmid. He was not impressed with a U.S. Army Captain; I got a grunt for an acknowledgement. – Ed.*) The remainder of the BC-4 camera systems were transferred to the Kwajalein atoll for missile defense testing, their original purpose.

Thanks to Mr. Ed Carlson of NOAA, “There are at least 2 existing Marshall Island horizontal datums; the islands of Kwajalein, Eniwetok, and Roi-Namur defined by the U.S. Air Force in 1959 referenced to the International ellipsoid ($a = 6,378,388$ m, $1/f = 297$ – Ed.), and densified by the U.S. Coast & Geodetic Survey (USC&GS), now NGS, during 1960-63, and the island of Majuro defined by the U.S. Geological Survey (USGS) referenced to the Clarke 1866 ellipsoid ($a = 6,378,206.4$ m, $b = 6,356,583.8$ m – Ed.). Differences in positions (latitude and longitude) between the these datums and a geocentric reference system defined by GPS can vary in excess of over 320 meters across the country.”

Thanks to Mr. John W. Hager, “Ailinginae (1952,) at 6 Astro, $\Phi_0 = 11^\circ 06' 48.5''$ N, $\Lambda_0 = 166^\circ 28' 43.4''$ E, $\alpha_0 = 279^\circ 18' 43.0''$ to 7 from south, International, $H_0 = 2.1$ m. Ailinglapalap (1951), at 2 Astro, $\Phi_0 = 7^\circ 17' 22.3''$ N, $\Lambda_0 = 168^\circ 44' 39.1''$ E, International, $H_0 = 7$ ft. Ailuk (1951,) at 1 Astro, $\Phi_0 = 10^\circ 12' 50.3''$ N, $\Lambda_0 = 169^\circ 58' 46.8''$ E, $\alpha_0 = 230^\circ 03' 19.9''$ to 2 from south, International. Aon Island, code APB, $\Phi_0 = 11^\circ 13' 04.79''$ E, $\Lambda_0 = 169^\circ 45' 53.04''$ E. Arno (1951), at 2 Astro, $\Phi_0 = 7^\circ 03' 01.3''$ N, $\Lambda_0 = 171^\circ 33' 28.1''$ E, $\alpha_0 = 178^\circ 56' 24.4''$ to 2a from south, International, $H_0 = 2.3$ m. Arumenii Island, code ARB, $\Phi_0 = 12^\circ 14' 53.5''$ N, $\Lambda_0 = 170^\circ 07' 44.4''$ E. Aur (1951), at 1a, Astro Point, $\Phi_0 = 8^\circ 18' 54.9''$ N, $\Lambda_0 = 171^\circ 09' 10.8''$ E, $\alpha_0 = 327^\circ 24' 21.8''$ to 26a from south, International, $H_0 = 1.5$ m. Bikar (1952), at Astro Point, $\Phi_0 = 12^\circ 14' 25.11''$ N, $\Lambda_0 = 170^\circ 07' 53.93''$ E, $\alpha_0 = 321^\circ 56' 28.7''$ to 8 from south, International, $H_0 = 5.8$ ft. Bikini (1946), code BIK, at BIK, $\Phi_0 = 11^\circ 37' 54.5''$ N, $\Lambda_0 = 165^\circ 31' 17.5''$ E, $\alpha_0 = 118^\circ 45' 55.5''$ to MON from south, Clarke 1866. Scaled from Japanese Chart 458 (1:50,000, 1926), which was copied as H.O. Chart 6032 (1944) by U.S.S. Sumner and Bowditch. Stellar α_0 by Sumner. Used by Holmes & Narver, Inc. May also be defined as AIR (Beacon “H”), $\Phi_0 = 11^\circ 30' 24.906''$ N, $\Lambda_0 = 165^\circ 24' 55.168''$ E, $\alpha_0 = 268^\circ 00' 01.4''$ to ENYU from south. Also called USN 1946 and BIK (assumed). Bokku Island, code BOK, $\Phi_0 = 9^\circ 30' 49''$ N, $\Lambda_0 = 170^\circ 00' 04''$ E. Bonto, code BON, $\Phi_0 = 8^\circ 32' 48''$ N, $\Lambda_0 = 171^\circ 06' 53''$ E. Dalap 1968 Astro, at Dalap 1968, $\Phi_0 = 7^\circ 05' 14.0''$ N, $\Lambda_0 = 171^\circ 22' 34.5''$ E, Clarke 1866. Department of the Interior, Geological Survey coordinate list. Dodo Island Observation Spot, code DOA, $\Phi_0 = 7^\circ 07' 38''$ N, $\Lambda_0 = 171^\circ 41' 06''$ E. Ebon (1951), at Astro Point, $\Phi_0 = 4^\circ 35' 08.9''$ N, $\Lambda_0 = 168^\circ 41' 14.7''$ E, $\alpha_0 = 223^\circ 10' 46.8''$ to 1 from south, International. Eniirikku 1919, code ENG, $\Phi_0 = 11^\circ 29' 49''$ N, $\Lambda_0 = 165^\circ 20' 22''$ E. Trig List, Washington, D.C., Feb. 1970. Enijun Island, code ENJ, $\Phi_0 = 8^\circ 36' 05''$ N, $\Lambda_0 = 171^\circ 02' 44''$ E. Eniwetok Astro 1944, code ENI,

at Eniwetok Astro Pier, $\Phi_0 = 11^\circ 33' 23.480''$ N, $\Lambda_0 = 162^\circ 21' 10.250''$ E, $\alpha_0 = 58^\circ 44' 57.70$ to North Base from south, Clarke 1866, U.S.S. Bowditch. Also Privilege at $\Phi_0 = 11^\circ 21' 51.439$ N, $\Lambda_0 = 162^\circ 21' 14.735''$ E, or ... $51.383''$ N and ... $14.736''$ E, or Eniwetok of Holmes & Narver ... $51.466''$ N and ... $14.736''$ E. Eniwetok-Wake 1960, code ENW, at Wake (8) , $\Phi_0 = 19^\circ 16' 19.606''$ N, $\Lambda_0 = 166^\circ 39' 21.798''$ E, Hough. Readjustment of USAF 1959 Datum (*q.v.*). Essentially the mean values based on the absolute positions on Wake and Eniwetok. Enuebing (1919), code ETS, at Eniibing, $\Phi_0 = 7^\circ 17' 25.50''$ N, $\Lambda_0 = 168^\circ 45' 11.90$ E. From a tabulation of geographic positions by J.H.O. Enyvertok (Eniwetok) Island, code ENH, at Observation spot, $\Phi_0 = 11^\circ 17' 43''$ N, $\Lambda_0 = 167^\circ 28' 27''$ E. Erappu Channel, code ERA, $\Phi_0 = 10^\circ 19' 34.9''$ N, $\Lambda_0 = 169^\circ 54' 23.5''$ E. Jaluit Astro, code ASK, as 61a, $\Phi_0 = 5^\circ 55' 19.5''$ N, $\Lambda_0 = 169^\circ 38' 37.2''$ E, $\alpha_0 = 18^\circ 30' 07.0''$ to 59 from south, International, $H_0 = 2.2$ m. Jemo (1951), code ASD, at A (Astro), $\Phi_0 = 10^\circ 04' 47.5''$ N, $\Lambda_0 = 169^\circ 31' 18.6''$ E, International, $H_0 = 9.0$ ft. Kili, code KKM, at Kili Island W. Coast Observation Spot (1923), $\Phi_0 = 5^\circ 38' 47''$, $\Lambda_0 = 169^\circ 07' 00''$ E. Kwajalein Astro 1952, code ASJ, at Station 42, Ennylabegan I., $\Phi_0 = 8^\circ 47' 19.2'' \pm 0.1''$ N, $\Lambda_0 = 167^\circ 37' 26.8'' \pm 0.2''$ E, $\alpha_0 = 304^\circ 33' 39.0'' \pm 0.5''$ to 43 from north, International, height = 2.39 ft. Observed by 71st Engineer Survey Liaison Detachment with 60° astrolabe. Kwajalein Astro U.S. Navy 1944, code KWA, at Astro, $\Phi_0 = 8^\circ 44' 06.33''$ N, $\Lambda_0 = 167^\circ 44' 28.63''$ E. Prismatic astrolabe used with chronograph checked by radio time signals. Approximately 300 stars computed. Observed by LT. E. V. Mohl, U.S.N.R., U.S.H.O., March 1944. Lae (1952), at 2. Astro Point, $\Phi_0 = 8^\circ 55' 31.6''$ N, $\Lambda_0 = 166^\circ 15' 58.6''$ E, $\alpha_0 = 64^\circ 07' 56.1''$ to 1 from south, International, $H_0 = 5.7$ ft. Leuen Anchorage Observation Spot, code LET, $\Phi_0 = 7^\circ 45' 32''$ N, $\Lambda_0 = 168^\circ 13' 23''$ E. Likiep, code LIK (?), at South Pass Reef. $\Phi_0 = 9^\circ 50' 22''$ N, $\Lambda_0 = 169^\circ 13' 23''$ E. Likiep, code LIK (?), at 1 Astro Point, $\Phi_0 = 9^\circ 50' 24.1''$ N, $\Lambda_0 = 169^\circ 18' 51.3''$ E, $\alpha_0 = 126^\circ 00' 14.9''$ to 2 from south, International, $H_0 = 5.0$ ft. Lotj Island, code LAD, at Observation Spot, $\Phi_0 = 8^\circ 55' 18''$ N., $\Lambda_0 = 166^\circ 12' 58''$ E. Majuro Astro, 1944, code MAJ, at Majuro Astro, 1944, $\Phi_0 = 7^\circ 04' 25.73''$ N, $\Lambda_0 = 171^\circ 19' 18.08''$ E. U.S.S. Bowditch, prismatic astrolabe used with chronograph checked by radio time signals. Approximately 300 stars computed. Majuro 1951, code ATR, at Astronomic Station No. 2, $\Phi_0 = 7^\circ 05' 02.2''$ N, $\Lambda_0 = 171^\circ 22' 25.2''$ E, $\alpha_0 = 83^\circ 53' 22.9''$ to α mark (1) from south, International, $H_0 = 9.3$ ft. Maleolap (1952), at 1. Astropoint, $\Phi_0 = 8^\circ 54' 15.5''$ N, $\Lambda_0 = 170^\circ 50' 41.1''$ E, $\alpha_0 = 40^\circ 04' 27.4''$ to 2 from south, International, $H_0 = 7.9$ ft. Mejit (1919), code MEC, at Astro Station B1, $\Phi_0 = 10^\circ 16' 54''$ N, $\Lambda_0 = 170^\circ 52' 36''$ E. Mellu Island, code MEB, $\Phi_0 = 11^\circ 21' 38''$ N, $\Lambda_0 = 166^\circ 59' 13''$ E. Mili (1951), at 17a Astro Point, $\Phi_0 = 6^\circ 01' 45.9''$ N, $\Lambda_0 = 171^\circ 56' 50.6''$ E, $\alpha_0 = 134^\circ 23' 10.7''$ to 13 from south, International, $H_0 = 2.2$ m. Namorik (1951), code ATQ, at 1a Astro Point, $\Phi_0 = 5^\circ 36' 34.0''$ N, $\Lambda_0 = 168^\circ 06' 08.3$ E, $\alpha_0 = 348^\circ 14' 35.1''$ to 2 from south, International, $H_0 = 0.6$ m. Namu (1951), at 1. Astro, $\Phi_0 = 7^\circ 45' 47.6''$ N, $\Lambda_0 = 168^\circ 13' 14.2''$ E, $\alpha_0 = 303^\circ 01' 41.7''$ to 2 from south, International, $H_0 = 4.5$ ft. Pokaakku, code POK, $\Phi_0 = 14^\circ 34' 03''$ N, $\Lambda_0 = 168^\circ 57'$

continued on page 18



MAPPING MATTERS

YOUR QUESTIONS ANSWERED

The layman's perspective on technical theory and practical applications of mapping and GIS

BY Qassim A. Abdullah, Ph.D., PLS, CP**

QUESTION:

I was among the attendees of your session on the new ASPRS Map Accuracy Standards during the last ASPRS fall conference held in Denver in November 2014. Could you please elaborate more on the new standards, its similarity with the previous standards and how to use it?

Anonymous

Dr. Abdullah: The topic of understanding the new standards, referred to as the “ASPRS Positional Accuracy Standards for Digital Geospatial Data”, is very important for all users of the new standards during this transition period. Therefore, I will dedicate more than one article to introduce the new standards, highlight its similarity with the legacy standards of the ASPRS 1990 and the National Map Accuracy Standards (NMAS), and provide examples on how to relate the new standards to the legacy standards. The new standards were approved by the ASPRS board during their meeting in Denver on November 17, 2014 and became the official new ASPRS map accuracy standards replacing the old standards of 1990.

As stated in the standards, the new standards are published to meet the dire needs of new era for the geospatial community. Such an era is characterized by rapid advancement in the field of geospatial data collection and data production. Among the main reasons that led to the development of the new standards are the following:

1. Legacy map accuracy standards, the ASPRS 1990 standards and the NMAS of 1947, are outdated. (over 30 years since the ASPRS1990 standards were published)
2. Many of the data acquisition and mapping technologies that legacy standards were based on are no longer used in today's mapping process.
3. More recent advances in mapping technologies and methods enabled us to produce better quality and higher accuracy geospatial products and maps.
4. Legacy map accuracy standards were designed to deal with plotted or drawn maps as the only medium to represent geospatial data. Today's digital mapping workflow requires different accuracy measures that are more suitable for the digital products.
5. Within the past two decades (during the transition period from hardcopy to softcopy mapping environments), most

measures for relating image Ground Sampling Distance (GSD), map scale, and contours interval to the final product accuracy were based on film scanning practices which were established prior to the introduction of the first digital camera. Such practices and measures are no longer suitable for the products from digital sensors.

6. New mapping processes and methodologies have become much more sophisticated with advances in technology and advances in our knowledge of mapping processes and mathematical modeling. Such sophistication resulted in more accurate mapping products.
7. Mapping accuracy can no longer be associated with the camera geometry and flying altitude alone (focal length, x_p , y_p , B/H ratio, etc.). Accuracy of new mapping products is influenced by many other factors such as:
 - the quality of camera calibration parameters;
 - quality and size of a Charged Coupled Device (CCD) used in the digital camera CCD array;
 - quality of parallax determination or photo measurements;
 - quality of the GPS signal;
 - quality and density of ground controls;
 - quality of the aerial triangulation solution;
 - capability of the processing software to handle GPS drift and shift;
 - capability of the processing software to handle camera self-calibration,
 - quality of the digital terrain model used for the production of orthoimagery.

These factors can vary widely from project to project, depending on the sensor used and specific methodology. For these reasons, existing accuracy measures based on map scale, film scale, GSD, c-factor and scanning resolution no longer apply to current geospatial mapping practices.

8. Elevation products from modern active sensors such as LiDAR and IFSAR were not considered by the legacy mapping standards as it did not exist then. Therefore, new accuracy standards are needed to address elevation products derived from these technologies.

More information on the motivation behind publishing the new standards can be found in annex A of the new standards document (<http://www.asprs.org/PAD-Division/Map-Accuracy-Standards-Working-Group.html>)

The new standards bring new and improved approaches in dealing with current mapping products. It also provides a wealth of information and measures for the users to utilize that were never introduced by the legacy standards. Among such improvements are the following:

1. Providing unlimited number of horizontal and vertical accuracy classes that can accommodate products from any of the current or future mapping technologies.
2. Dealing with LiDAR and other modern technologies.
3. Utilizing positional accuracy thresholds for digital orthoimagery and digital elevation data that are independent of published GSD, map scale or contour interval.
4. Providing aerial triangulation accuracy measure.
5. Providing ground controls accuracy measure.
6. Providing orthoimagery seam lines accuracy measure.
7. Providing lidar relative swath-to-swath accuracy measure for LiDAR and IFSAR data.
8. Providing recommended minimum Nominal Pulse Density (NPD) for LiDAR data.
9. Providing horizontal accuracy measure for elevation data,
10. Providing definitions and guidelines for the delineation of low confidence areas for elevation data.
11. Providing guidelines on the required number and spatial distribution of QA/QC check points based on project area.
12. Providing methodology for reporting products accuracy.
13. Providing definitions of statistical terms that are related to accuracy computations and provide practical examples on its use.
14. Providing tutorial sections with practical examples on relating the new standards to the legacy standards.

In the following sections I will try to introduce the structure of the accuracy classes and the newly introduced sections of the new standards.

HORIZONTAL ACCURACY STANDARDS FOR GEOSPATIAL DATA

The new standards defines horizontal accuracy classes in terms of the value of errors presented in data represented by the Root Mean Square (RMSE). Such accuracy class definition do not limit the classes to a certain ranking or certain number of classes as the legacy standards did. This approach offers many advantages and flexibility for the users of the standards as it assigns an accuracy class for any product from any current or future technologies. Table 1 provides the horizontal accuracy classes for geospatial data.

Table 1 Horizontal Accuracy Standard for Geospatial Data

Horizontal Accuracy Class	Absolute Accuracy			Relative Accuracy Measures
	RMSE _x and RMSE _y (cm)	RMSE _r (cm)	Horizontal Accuracy at 95% Confidence Level (cm)	Orthoimagery Mosaic Seamline Mismatch (cm)
X-cm	≤X	≤1.41*X	≤2.45*X	≤ 2*X

Based on Table 1, data users, when they request products such as digital orthoimagery or digital planimetric data, can specify that the data must be produced to meet ASPRS Accuracy Standards for the RMSE_x and RMSE_y Horizontal Accuracy Class he or she is interested in. If 10 cm accuracy is desired, then the statement can be written as “the data set should be produced to meet ASPRS Positional Accuracy Standards for Digital Geospatial Data (2014) for 10.0 (cm) RMSE_x and RMSE_y Horizontal Accuracy Class”. The standards, Table 2, lists 24 common accuracy classes for orthoimagery and planimetric maps.

Table 2 Common Horizontal Accuracy Classes according to the new standards

Horizontal Accuracy Class RMSE _x and RMSE _y (cm)	RMSE _r (cm)	Orthoimage Mosaic Seamline Maximum Mismatch (cm)	Horizontal Accuracy at the 95% Confidence Level (cm)
0.63	0.9	1.3	1.5
1.25	1.8	2.5	3.1
2.50	3.5	5.0	6.1
5.00	7.1	10.0	12.2
7.50	10.6	15.0	18.4
10.00	14.1	20.0	24.5
12.50	17.7	25.0	30.6
15.00	21.2	30.0	36.7
17.50	24.7	35.0	42.8
20.00	28.3	40.0	49.0
22.50	31.8	45.0	55.1
25.00	35.4	50.0	61.2
27.50	38.9	55.0	67.3
30.00	42.4	60.0	73.4
45.00	63.6	90.0	110.1
60.00	84.9	120.0	146.9
75.00	106.1	150.0	183.6
100.00	141.4	200.0	244.8
150.00	212.1	300.0	367.2
200.00	282.8	400.0	489.5
250.00	353.6	500.0	611.9
300.00	424.3	600.0	734.3
500.00	707.1	1000.0	1223.9
1000.00	1414.2	2000.0	2447.7

“the new standards are published to meet the dire needs of new era for the geospatial community.”

Table 3 Digital Orthoimagery Accuracy Examples for Current Large and Medium Format Metric Cameras

Common Orthoimagery Pixel Sizes	Recommended Horizontal Accuracy Class RMSE _x and RMSE _y (cm)	Orthoimage RMSE _x and RMSE _y in terms of pixels	Recommended use
1.25 cm	≤1.3	≤1-pixel	Highest accuracy work
	2.5	2-pixels	Standard Mapping and GIS work
	≥3.8	≥3-pixels	Visualization and less accurate work
2.5 cm	≤2.5	≤1-pixel	Highest accuracy work
	5.0	2-pixels	Standard Mapping and GIS work
	≥7.5	≥3-pixels	Visualization and less accurate work
5 cm	≤5.0	≤1-pixel	Highest accuracy work
	10.0	2-pixels	Standard Mapping and GIS work
	≥15.0	≥3-pixels	Visualization and less accurate work
7.5 cm	≤7.5	≤1-pixel	Highest accuracy work
	15.0	2-pixels	Standard Mapping and GIS work
	≥22.5	≥3-pixels	Visualization and less accurate work
15 cm	≤15.0	≤1-pixel	Highest accuracy work
	30.0	2-pixels	Standard Mapping and GIS work
	≥45.0	≥3-pixels	Visualization and less accurate work
30 cm	≤30.0	≤1-pixel	Highest accuracy work
	60.0	2-pixels	Standard Mapping and GIS work
	≥90.0	≥3-pixels	Visualization and less accurate work
60 cm	≤60.0	≤1-pixel	Highest accuracy work
	120.0	2-pixels	Standard Mapping and GIS work
	≥180.0	≥3-pixels	Visualization and less accurate work
1 meter	≤100.0	≤1-pixel	Highest accuracy work
	200.0	2-pixels	Standard Mapping and GIS work
	≥300.0	≥3-pixels	Visualization and less accurate work
2 meter	≤200.0	≤1-pixel	Highest accuracy work
	400.0	2-pixels	Standard Mapping and GIS work
	≥600.0	≥3-pixels	Visualization and less accurate work
5 meter	≤500.0	≤1-pixel	Highest accuracy work
	1,000.0	2-pixels	Standard Mapping and GIS work
	≥1,500.0	≥3-pixels	Visualization and less accurate work

“Many of the data acquisition and mapping technologies that legacy standards were based on are no longer used in today’s mapping process.”

The standards also provide users with guidelines for associating orthoimagery pixel sizes and associated RMSE_x and RMSE_y accuracy, Table 3. As stated in the new standards, the associating pixel size and products accuracy are largely based on experience with current sensor technologies and primarily apply to large and medium format metric cameras. The table is only provided as a guideline for users during the transition period to the new standards. These associations may change in the future as mapping technologies continue to advance and evolve.

The new standards also provide the following examples to guide the user to relate the new standards to the legacy standards. Such examples are important for the users to prevent confusion and to assure a smooth transition to the new standards.

Example 1: Converting the horizontal accuracy of a map or orthoimagery from the new 2014 standards to the legacy ASPRS map standards of 1990

Given: a map or orthoimagery with an accuracy of RMSE_x = RMSE_y = 15 cm according to the new 2014 standards, compute the equivalent accuracy and map scale according to the legacy ASPRS map standards of 1990, for the given map or orthoimagery.

Solution:

- 1) Because both standards utilize the same RMSE measure, then the accuracy of the map according to the legacy ASPRS map standards of 1990 is RMSE_x = RMSE_y = 15 cm
- 2) To find the equivalent map scale according to the legacy ASPRS map standards of 1990, follow the following steps:
 - a. Multiply the RMSE_x and RMSE_y value in centimeters by 40 to compute the map scale factor (MSF) for a Class 1 map, therefore:

$$MSF = 15 \text{ (cm)} \times 40 = 600$$
 The map scale according to the legacy ASPRS map standards of 1990 is equal to:
 - i. Scale = 1:MSF or 1:600 Class 1;
 - ii. The accuracy value of RMSE_x = RMSE_y = 15 cm is also equivalent to Class 2 accuracy for a map with a scale of 1:300.

(TO BE CONTINUED)

The contents of this column reflect the views of the author, who is responsible for the facts and accuracy of the data presented herein. The contents do not necessarily reflect the official views or policies of the American Society for Photogrammetry and Remote Sensing and/or Woolpert, Inc.

STAND OUT FROM THE REST EARN ASPRS CERTIFICATION

ASPRS congratulates these recently
Certified and Re-certified individuals:

CERTIFIED PHOTOGRAMMETRIST

Erick Gonzales, Certification #1576

Effective December 3, 2014, expires December 3, 2019

CERTIFIED MAPPING SCIENTIST, GIS/LIS

Erik Strandhagen, Certification#GS277

Effective December 3, 2014, expires December 3, 2019

CERTIFIED MAPPING SCIENTIST, REMOTE SENSING

Sara Kasperek, Certification #RS223

Effective December 9, 2014, expires December 9, 2019

ASPRS Certification validates your professional
practice and experience. It differentiates you from
others in the profession.

For more information on the ASPRS Certification
program: contact certification@asprs.org
visit <http://www.asprs.org/membership/certification>



asprs  **THE
IMAGING & GEOSPATIAL
INFORMATION SOCIETY**

Grids & Datums

continued from page 14

24" E. Rikuraru, code RIK, $\Phi_0 = 10^\circ 01' 28.34''$ N, $\Lambda_0 = 169^\circ 00' 47.77''$ E. Rongelap, at Observation Spot, $\Phi_0 = 11^\circ 08' 55''$ N, $\Lambda_0 = 166^\circ 53' 35''$ E. Rongelap (1952), code ROP, at 25. Astro, $\Phi_0 = 11^\circ 09' 02.5''$ N, $\Lambda_0 = 166^\circ 52' 03.2''$ E, $\alpha_0 = 75^\circ 03' 50.1''$ to 24 from south, International, $H_0 = 2.5$ m. Rongelap 1959, $\Phi_0 = 11^\circ 26' 43.62''$ N, $\Lambda_0 = 167^\circ 03' 27.56''$ E. Rongerik (1952), at 1a. Astro station, $\Phi_0 = 11^\circ 22' 27.8''$ N, $\Lambda_0 = 167^\circ 30' 59.0''$ E, $\alpha_0 = 174^\circ 00' 56.2''$ to 2a from south, International, $H_0 = 1.9$ m. Rube Point, code RUA, at Observation Spot, $\Phi_0 = 4^\circ 35' 13''$ N, $\Lambda_0 = 168^\circ 13' 23''$ E. Takowa Island, code TAA, at Observation Spot, $\Phi_0 = 6^\circ 13' 36''$ N, $\Lambda_0 = 171^\circ 48' 14''$ E. UK requested change from Takowaka. Taongi Astro 1952, code TAO, at 2. Astro, $\Phi_0 = 14^\circ 37' 43.5''$ N, $\Lambda_0 = 169^\circ 01' 04.0''$ E, $\alpha_0 = 20^\circ 00' 23.5''$ to 1 from south, International, $H_0 = 5.6$ ft. Taroa Island Trig Station, $\Phi_0 = 8^\circ 42' 44''$ N, $\Lambda_0 = 171^\circ 13' 48''$ E. Ujelang (1952), at 3. Astro, $\Phi_0 = 9^\circ 46' 07.1''$ N, $\Lambda_0 = 160^\circ 59' 10.2''$ E, International, elevation = 5.2 ft. Ujelang, at Observation Spot, $\Phi_0 = 9^\circ 46' 29''$ N, $\Lambda_0 = 160^\circ 57' 43''$ E. USAF 1959, at WAKE (8), $\Phi_0 = 19^\circ 16' 19.637''$ N, $\Lambda_0 = 166^\circ 39' 21.745''$ E, $\alpha_0 = 273^\circ 29' 34.503''$ Bikini (4) to Rolap (2), Hough. Preliminary determination of position of Initial Point. Utirik (1951), at 2. Astro, $\Phi_0 = 11^\circ 13' 08.5''$ N, $\Lambda_0 = 169^\circ 50' 42.5''$ E, $\alpha_0 = 73^\circ 04' 55.0''$ to 1. from south, International, $H_0 = 5.9$ ft. Wotho (1952), at 3. Astro, $\Phi_0 = 10^\circ 10' 24.3''$ N, $\Lambda_0 = 166^\circ 00' 03.3''$ E, $\alpha_0 = 306^\circ 04' 31.2''$ to 1 from south, International, $H_0 = 9.7$ ft. Wotje Atoll 1952, code WOJ, at 2 Astro Point, $\Phi_0 = 9^\circ 27' 58.6''$ N, $\Lambda_0 = 170^\circ 14' 09.7''$ E, $\alpha_0 = 320^\circ 12' 34.7''$ to 42 azimuth mark from south, International, $H_0 = 6.4$ ft. Wotje, at Observation Spot, $\Phi_0 = 9^\circ 27' 31''$ N, $\Lambda_0 = 170^\circ 14' 32''$ E. I never was aware of any classified datums in the area. There could have been but it would have been on a need-to-know basis. There could well be duplicates in this list. JWH"

Majuro Atoll has a local grid system based on the Azimuthal Equidistant projection with origin at station Dalap where: latitude of origin, $\phi_0 = 7^\circ 05' 14.0''$ N, central meridian, $\lambda_0 = 171^\circ 22' 34.5''$ E, scale factor at origin, $m_0 = 1.0$ (by definition), False Easting = 85 km, and False Northing = 40 km. Reference ellipsoid is the Clarke 1866. (Herbert W. Stoughton, Ph.D., P.E., P.L.S., C.P., FASPRS, 1 April 2008)

According to TR 8350.2, **From** Wake-Eniwetok 1960 Datum **To** WGS84, $\Delta X = +102$ m, ± 3 m, $\Delta Y = +52$ m, ± 3 m, $\Delta Z = -38$ m, ± 3 m; and **From** Wake Island Astro 1952 **To** WGS84, $\Delta X = +276$ m, ± 25 m, $\Delta Y = -57$ m, ± 25 m, $\Delta Z = +149$ m, ± 25 m.

The contents of this column reflect the views of the author, who is responsible for the facts and accuracy of the data presented herein. The contents do not necessarily reflect the official views or policies of the American Society for Photogrammetry and Remote Sensing and/or the Louisiana State University Center for GeoInformatics (C'G).

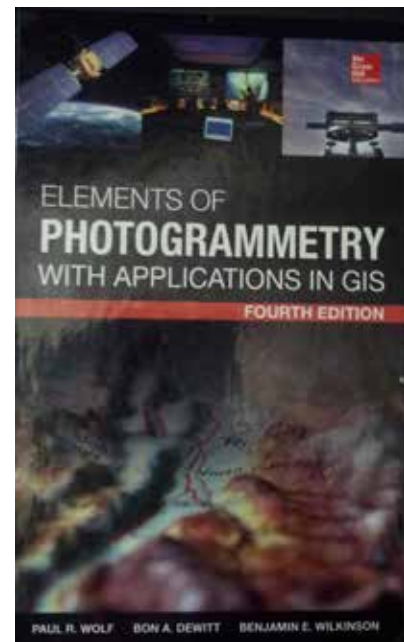
This book addresses fundamental and foundational theories and principles of photogrammetry and its advancements. The target audience varies with students and users of imagery for measurement purposes. The book is organized into basic concepts including; coordinate systems, stereoscopic techniques, laser scanning, GIS applications using photogrammetry, and advanced topics of photogrammetry.

The book is divided into sections and chapters as follows:

- ❖ Foundational principles of photogrammetry
 - ◆ Principles of photography and imaging
 - ◆ Cameras and other imaging devices
 - ◆ Image measurements and refinements
 - ◆ Object space coordinate systems
- ❖ Angle of tilt and types of photographs
 - ◆ Vertical photographs
 - ◆ Stereoscopic viewing
 - ◆ Stereoscopic parallax
 - ◆ Stereoscopic plotting instruments
 - ◆ Titled and oblique photographs
- ❖ Terrestrial and close-range photogrammetry
- ❖ New technological advancement
 - ◆ Laser scanning systems
- ❖ Mapping and GIS
 - ◆ Elementary methods of planimetric mapping for GIS
 - ◆ Introduction to analytical photogrammetry
 - ◆ Topographic mapping and spatial data collection
 - ◆ Fundamental principles of digital image processing
 - ◆ Photogrammetric applications in GIS
- ❖ Control surveys in photogrammetry
 - ◆ Control for aerial photogrammetry
 - ◆ Aerotriangulation
 - ◆ Project planning

This text has been very well written with precise information. The fourth edition has been thoroughly revised from its previous edition. This edition has a new chapter called Laser Scanning Systems, emphasizing its timely technological advancement. This is a significant change in the realm of photogrammetry. The problems in the examples provide and clarify the computational procedures. The various images, maps and figures illustrate the information provided. The language utilized is very simple for even novice practitioners attempting to learn photogrammetry. The references are comprehensive for each chapter and well updated. The organization of the book is well structured and easy to follow.

In my opinion, the Elements of photogrammetry with Application in GIS have accomplished its goal defining photogrammetric foundational principles while also addressing the advanced concepts of photogrammetry. This text is much



Elements of photogrammetry with Application in GIS, Fourth Edition

Paul Wolf, Bon Dewitt, Benjamin Wilkinson

McGraw-Hill Professional. 2013 and 688 pp., diagrams, maps, photos, images, index. Hardcover. ISBN-13: 9780071761116. \$150.00

Reviewed by: Sowmya Selvarajan, PhD, Assistant Professor, Geomatics, Utah Valley University, Orem, UT.

more comprehensive in photogrammetric principles than other similar books that I have evaluated. The authors, well established experts in the field of photogrammetry, provide a text that is well suited for any audience interested in photogrammetry. The book is well written in terms of layout, binding, typography, notes, figures, diagrams, maps, imagery, appendices and index. Imagery technical specifications and example problems were accurate per this reviewer's spot check.

ASPRS HAS A NEW REGION!

During the Board of Directors meeting for all of ASPRS, the Southwest US Region was dissolved and their territory was re-assigned to the Northern California Region. The next piece of business was the renaming of the newly expanded Region to the Pacific Southwest Region.

For those of you unfamiliar with the geographic coverage of both the old Northern California and Southwest US Regions, our new Region includes the entire states of California, Nevada, Arizona and Hawaii.

The next piece of business will be the adoption of new by-laws and the election of a new slate of officers to govern the new Region. That will be followed up with an election early in 2015.

The officers of both the old Northern California and Southwest US Regions would like to extend a big THANK YOU to all who have involved in the leadership in the last few years and those involved in overseeing the formation of the new Pacific Southwest Region.

Letter for the Executive Director

continued from page 4

bership in an organization that values quality workmanship, adherence to principles of managed precision and accuracy, dedication to detail, and the deeply seated notion of giving to others what the profession has given to us.

Take a look around. There is no other professional organization that offers this to people with our skills and capabilities. Doesn't it just make sense for you to be a member of that kind of organization?

You may be thinking, "Is there really a need for me to be part of this group?" Indeed there is; the need for this organization may be greater than it ever has been before. The growing commercialization of geospatial information over the last decade has created a deep societal dependence upon the work of our members. Our contributions may be unknown and unappreciated by most citizens and policy makers, but they are necessary to the functioning of modern society.

As a member of ASPRS you will have a much greater opportunity to inform people about what we do. Society needs us, our expertise, our standards, our publications, our support for education, and our professional engagement. Our members understand and expertly address the big issues of our time – from agriculture to defense, from climate change to transportation planning, and from water resources to energy management, to name just a few.

Even as the work of our members has become increasingly important, the challenges faced by members have also increased. Members face cheap labor outsourcing from abroad, broken government contracting models, gaps in our educational system, the ever-constant pressure to lower costs, and the urgent need to innovate business models. Globalization and commoditization challenge traditional services and products, while, ironically, the new technologies we create to stay competitive also disrupt our existing businesses. We face these and other challenges in common, so we are stronger if we identify them and address them together.

Getting our ship ready to sail on its most important voyage

in many years is taking some time, of which we have precious little. The tides and currents around us are flowing at a rapid pace. Our ship's design is outdated. Nonetheless, our members know how to fit a ship for sailing, and they are busy making the necessary changes. (See sidebar.) Even the officers have rolled up their shirt sleeves and are doing carpentry, sheeting sails, and hauling supplies on board. We are almost ready. Within a few months, our plan is to set sail from Tampa, the site of our annual meeting.

Where shall we sail? Should we simply allow the wind and tide carry us where they will? Of course not! Should we chart a course for a known land and prove that we can reach a shore that others have found before us? Perhaps. Or, will we instead boldly point the helm into uncharted waters in search of something entirely new, unknown, and possibly tremendously rewarding?

Consider the example of HMS Endeavour, which set sail in 1768 on a mission to explore Terra Australis Incognita ("unknown southern land"). After she nearly sank on the Great Barrier Reef, Lieutenant James Cook beached her for repairs. Cook wrote, "...it was happy for us that a place of refuge was at hand, for we soon found that the ship would not work..." Endeavour proceeded to sail around the Cape of Good Hope and complete her journey home. The spirit of HMS Endeavour lives on today. Over 200 years later her namesake also circled the earth – but this time from space – OV-105 Space Shuttle Endeavour.

Those who sail with ASPRS on our new endeavor will be in for an adventure in all senses of the word – anticipation, challenge, excitement, exhilaration, education, and perhaps even fame and fortune. We promise not only an adventure, but also the chance to accomplish something that is bigger than any one of us can achieve on our own.

New frontiers await us in the next 80 years, I am certain of it. This ship is sea-worthy, but it needs a good complement of passengers and crew. Please, board the ship with me and let us sail together toward a bright future.

Dr. Michael Hauck, ASPRS Executive Director

WELCOME TO THE NEW YEAR, STUDENT MEMBERS!

The Student Advisory Council (SAC) along with executive members of ASPRS have begun to make incredible changes to the organization to benefit student members. We are thrilled to be implementing new policies and programs to improve how students experience membership—now is the time and 2015 is the year to engage with ASPRS!

In the months to come, the SAC will be extending support to ASPRS Student Chapters on campuses throughout the US and Canada. Please be on the lookout for Student Advisory Councilors who will be contacting your Student Chapter, or contact us if you are interested in establishing a Chapter on your campus! If you are planning any university-sponsored ASPRS events; we would love to feature your chapter on our online blog *Signatures: The ASPRS Student Newsletter* at www.asprssignature.blogspot.com and in our online social media pages.

Your student membership will be the passport to a host of new incentives and opportunities. We want to ensure that you receive the best value from your membership and are an active student member in the Society. Most importantly, we want you to be *interactive* with your fellow ASPRS members nationally, in your region, and on your campus. To get the most of your ASPRS Student Membership, we encourage you to:

- ◇ **Attend national conferences—it is easiest thing to do!** ASPRS conferences function to introduce and connect students to the geospatial community. When we attend conferences, we are able to:
 - Meet the leaders who are innovating geospatial technology and may have written our textbooks!
 - Find potential employers at the Student-Employer Meet & Greet and throughout the conference
 - Present our research and receive feedback from industry and research professionals
 - Have fun with other students who share our interests and will be collaborators for years to come!
- ◇ **Enroll in the Geospatial Intern Program (GIP)!** The Geospatial Intern Program puts you on the path to professional certification as a scientist or a technician. Since 2014, GIP applicants no longer require on-the-job experience, the requirement can be delayed up to 5 years

after receiving the GIP for full certification. Geospatial Interns can be certified as Photogrammetrists, Remote Sensing or GIS/LIS Mapping Scientists, or as Lidar Scientists (*NEW for 2015!*)

- ◇ **Submit articles here in *Photogrammetric Engineering and Remote Sensing (PE&RS)*!** This is an amazing opportunity for any student! PE&RS is a widely read, peer-reviewed technical journal in the geospatial sciences, featuring important breakthroughs and best practices. In fact, the Impact Factor of the journal is steadily rising, meaning that the article that you submit will be read and cited!
- ◇ **Participate in the GeoLeague Competition!** GeoLeague is a competition between ASPRS student chapters who participate as teams to solve a problem with geospatial tools! The teams are provided a study site and relevant geographic data from which they must conduct research and geospatial analysis to solve an existing problem. This year, the competition is based on preserving trails and campsites for the Boy Scouts. Please assemble your campus team and register for GeoLeague by January 26!

By taking these steps, you will not only take the best advantage of ASPRS student-focused events and programs, you will gain desirable skills and experiences to enhance your career! We hope that you start by coming to the next national conference in Tampa, Florida, the **Imaging and Geospatial Technology Forum (IGTF)** taking place May 4-8, 2015. We also invite you to respond to the Call for Papers this month with your abstracts to be included in the conference program!

Best wishes for the New Year,
The Student Advisory Council

ASPRS STUDENT ADVISORY COUNCIL

MINGSHU WANG
COUNCIL CHAIR
AMANDA ARAGON
DEPUTY COUNCIL CHAIR

BENJAMIN VANDER JAGT
EDUCATION COUNCILOR
JAMES BIALAS
DEP EDUCATION COUNCILOR

JESSICA FAYNE
COMMUNICATIONS COUNCILOR
NIAZ MORSHED
DEP COMMUNICATIONS COUNCILOR

BRITTANY KL MABRY
NETWORKING COUNCILOR
MOUSTAFA ARASTOUNIA
DEP NETWORKING COUNCILOR

JOURNAL STAFF

Publisher

Dr. Michael Hauck, mhauck@asprs.org

Editor

Russell G. Congalton,
russ.congalton@unh.edu

Technical Editor

Michael S. Renslow,
renslow76@comcast.net

Assistant Editor

Jie Shan, jshan@ecn.purdue.edu

Assistant Director — Publications

Rae Kelley, rkelly@asprs.org

Electronic Publications Manager/ Graphic Artist

Matthew Austin, maustin@asprs.org

Manuscript Coordinator

Jeanie Congalton,
jcongalton@asprs.org

Circulation Manager

Priscilla Weeks, pweeks@asprs.org

Advertising Sales Representative

Mohanna Sales Representatives
Brooke King, brooke@mohanna.com
Kelli Nilsson, kelli@mohanna.com

Contributing Editors

Grids & Datums Column

Clifford J. Mugnier, cjmce@lsu.edu

Book Reviews

John Iames,
iames.john@epamail.epa.gov

Mapping Matters Column

Qassim Abdullah,
Mapping_Matters@asprs.org

Behind the Scenes

Jim Peters, jpeters@asprs.org

Website

webmaster@asprs.org

JACIE JOINS ASPRS AGAIN!

This May, for the second year, the American Society for Photo Grammetry and Remote Sensing (ASPRS) and the Joint Agency for Commercial Imagery Evaluation (JACIE) will be co-located!

The Joint Agency Commercial/Civil Imagery Evaluation (JACIE) effort formed to leverage Federal agencies' resources for the characterization of commercial remote sensing data and to share those results across the Federal Government and beyond. Consisting of representatives from the U.S. Geological Survey (USGS), the National Aeronautics and Space Administration (NASA), the National Oceanic and Atmospheric Administration (NOAA), and the U.S. Department of Agriculture (USDA), the JACIE team performs product analysis of commercial and other remote sensing data and information products, providing earth scientists and other users with awareness and independent verification of commercial imagery data quality.

Ever increasing numbers of available commercial sources for remotely sensed data offers users more choices than historically possible. The ability to use data from these new sources hinges on understanding their characteristics, capabilities, and quality of data they produce.

The JACIE team provides independent characterizations of delivered image and image-derived end products. Each team member brings their resources and strengths to this task, providing Federal users in-depth assessments of commercial imagery quality. The JACIE team efforts have been instrumental in several improvements to commercial image quality and have enhanced working relationships between government and the commercial remote sensing industry.

JACIE works to provide insights into the capabilities of upcoming and recently launched remote sensing systems. This year's 14th Annual JACIE Workshop will feature presentations from vendors and users describing new systems and reporting on their data quality and capabilities.



CLASSIFIEDS

EMPLOYMENT

The Department of Geomatics at the University of Alaska Anchorage invites applicants for a full-time tenure-track Assistant/Associate Professor position.

The primary duty of this position is full-time teaching for the ABET accredited BS in Geomatics. Courses may include surveying, GPS, GIS, geodesy, map rojections, photogrammetry, LiDAR, remote sensing, boundary law, adjustments, hydrographic surveying, land development design, and CAD. The position may include a research component depending on the background of the successful applicant.

To apply go to www.uakjobs.com , Posting Number 0069856.

ASPRS MEMBERSHIP

ASPRS would like to welcome the following new members!

At Large

Lizy Abraham
Amr Al-Hamad
Muwaffaq Alqurashi
Naif Muidh Alsubaie
Rizwan Ahmed Ansari
Chi Chen
Zhen Dong
Anna Fryskowska, Ph.D.
Marça Rosa Varela Gonzblez
Bianca Hoersch
Martin Kada
Maria Gabriela Lenzano
Zeyu Li
Yuenan Li
Julien Li-Chee-Ming
Dorota Iwaszczuk
Werner Mayr
Somayeh Mollae
Marcus V T Monteiro
Navid Mostofi
Arnadi D. Murtiyoso
Agata Orych
Andrej Peisker
Saied Pirasteh
Kurtis Poettcker
Ralf Reulke
Shiqian Wang
Berthold Winck
Bisheng Yang
Yunsheng Zhang, Ph.D.
Zhu Ying

Florida

Richard A. Botta
Aleks Bridwell
Carla Castillo
Fils Dieu-Conserve
Nicole Gamboa
James Henn
Paul Keays
Danielle Kittredge
Kate Kraynak
Kaylee LaManna
Lynda Mamasse
Alyssa Murakami

Mark Rochelo
Paige Rogolino
Augustus O. Slaven
Brian Smith
Molly Elizabeth Smith
Leonardo V. Trejo
Natasha Vidal
Darren Zap

Columbia River

Evan Applegate
Lori Baer
Christopher Barnes
Nicole Brunner
Michael Budde
Michael Choate
Jon B. Christopherson
Catherine Costello
Angie Diefenbach
Sean Dinsmore
Joshua Emmons
Eugene Fosnight, Ph.D.
Todd Hawbaker
Dennis L. Helder, Ph.D.
Nathan Herzog
Tera Hinkley
Collin G. Homer
Stephen M. Howard
Douglas Jatton
Linda Jonescheit
Suzette Kimball
Robert Klinger
James M. Lacasse
Jennifer Lacey
Rynn Lamb
Colin Leslie
Holly Miller
Ron Morfitt
Jim Nelson
Kurtis Nelson
Birgit Peterson
Richard Poss
Gabriel Rousseau
Sarah Ryker
Aparajithan Sampath
Kristi Sayler

Larisa Serbina
James Storey
George Xian
Hankui Zhang

Heartland

Evan Menke
Robert C. Anderson
Craig Edward Hoover
David Meyer
Matthew Trani
Tim D. Washechek

Mid-South

Rachel Snavely
Laila Almutairi
Elivelton Fonseca, Ph.D.
Pan Gao
Maryellen Sault

Northern California

Matthew Bromley

New England

Sean Cunningham
Faith Justus
Qian Lei
Jason R. Parent
Chen Shi
Rebecca Trueman

Potomac

Julia Barsi
Chad Bates
Kelly A. Canham
Kenneth Carey
Mark Carroll
Christopher J. Crawford
Wayne Friedman
Todd T. GORITY
Del Jenstrom
Jonathan Knapp
Walter Kropp
Lisa M. Laforest
Robert LeRoy
Jeffrey Masek
Travis Nauman

Timothy M. Niemietz
Anthony O. Rabbani
Rishu Saxena
Amber Soja
Melvin L. Tucker
Eric Vermote

Rocky Mountain

Matthew R. Bobo
Brian Buechler
Megan Kathleen Caldwell
Joseph Clark
Christopher Cole
Thomas Fogarty, Jr.
Jason Frels
Wendy Goetz
Kelly E Grooms
Brian Hadley
Lee F. Johnson
Emily Kachergis
Mark Kautz
Darcee Killpack
Sarah Lamagna
Jung-kuan Liu, Ph.D.
Brian Lottman
Susan Lowrance
Bob B. Machus
Neffra Matthews
Randy A. McKinley
Di Ana Mendiola
Tommy Noble
Steve C. Raber
Mark Roberts
Austin O. Stevens
Michael H. Story
Jerry Tagestad
Tammira Taylor
Jennifer Turner-Valle
Chelsie Worth

Southwest US

Sarah Shivers

West Great Lakes

Zoltan Koppanyi
Susan Wirth

FOR MORE INFORMATION ON ASPRS MEMBERSHIP, VISIT

[HTTP://WWW.ASPRS.ORG/JOIN-NOW/](http://www.asprs.org/join-now/)

Your path to success in the geospatial community

Thank You!

Erik Brewster | Bon Dewitt | B. Haack
Jonathan Li | Sudhagar Nagarajan | Xiaojun Yang
FOR SPONSORING SOME OF OUR NEW MEMBERS!

PRODUCTS

Optech is pleased to announce the latest addition to its innovative line of airborne laser terrain mappers (ALTM), the Optech Titan, launching a new era in remote sensing. For the first time ever, multispectral active imaging of the environment can occur day or night, enabling new vertical applications and information extraction capabilities for lidar.

In the past, single or dual-wavelength sensors were developed for specific market verticals and application requirements. Titan breaks away from this convention by combining three beams with separate wavelengths, increasing the information content that can be derived from the target surface and allowing surveying professionals to address many more applications using a single sensor solution. Whether the goal is high-precision, high-density topographic surveying, land cover classification, vegetation mapping, or shallow water bathymetry, the Optech Titan can accommodate them all.

Titan incorporates three independent laser beams at different wavelengths, with a combined ground sampling rate approaching 1 MHz. The sensor includes full gyro-stabilization compatibility for predictable point distribution and a fully-programmable scanner for significant point density increases at narrower FOVs. Passive imagery support is available via fully-embedded high-resolution metric mapping cameras, including multispectral, thermal, NIR and RGB. For applications that demand it, Titan also includes full-waveform recording capability for each independent lidar wavelength.

Workflow is a critical component of any successful remote sensing solution. Standard software deliverables with Titan include Optech FMS, a fully-featured flight management system that enables integrated mission planning for both lidar and camera, aircraft navigation, and real-time monitoring of

the 3D active point clouds from each data channel alongside passive image thumbnails for in-air collection confidence. Also included is Optech's Lidar Mapping Suite (LMS), an industry benchmark for production lidar processing and accuracy quantification across the entire project extent. Unique to Titan is an LMS software extension that provides enhanced map product deliverables for bathymetric and land cover classifications by leveraging Titan's multispectral capability.

For further information, please contact your Regional Sales Manager or www.optech.com.

GeoCue Group Inc. is pleased to announce the release of GeoCue 2014.1. This release includes many new features, performance improvements and stability enhancements. A number of features are aimed specifically at supporting LAS 1.4 data while easing usability and installation of GeoCue's client and server components.

Highlights of the new release include:

- Dramatically Simplified Installation and Client Start-Up
- Improved Performance of Distributed Workflows
- Email Alerts on Dispatched Jobs
- New Window Arrangement Feature
- New Coordinate Reference Systems and Vertical Datum
- Comprehensive support for LAS 1.4. (LIDAR 1 CuePac)
- Additional Options for DirectDrive of MicroStation/Terrasolid
- Improved Look Up Table (LUT) Support (DMC PPS CuePac)
- Enhanced FramePro Data Import and Streamlined Workflow (RCD30 CuePac)

In addition to the major new features highlighted above, we have also addressed many areas of the software to improve both performance and stability.

Everyone who has GeoCue on current maintenance will receive the release on DVD. We will send out an email blast when the new release has been posted to the download server.

For more information, visit www.GeoCue.com.



Save the DATE!



ASPRS 2015 Annual Conference
Tampa Bay Marriott Waterside Hotel
Tampa, Florida May 4–8, 2015

Correction of Distortions in YG-12 High-Resolution Panchromatic Images

Yonghua Jiang, Guo Zhang, Deren Li, Xinming Tang, Wenchao Huang, and Litao Li

Abstract

Design deficiencies and hardware limitations cause a number of issues with the images acquired by Chinese satellites launched before 2012, such as YG-12. The geometric quality of the images recorded by YG-12 cannot match its high resolution because of serious time-synchronization errors and interior distortions. To improve the geometric quality of YG-12 images, this paper proposes a method of interior calibration for the YG-12 panchromatic sensor. In addition, an innovative method is proposed to eliminate time-synchronization errors using parallel observations of the panchromatic sensor onboard YG-12. The experimental results indicate the interior parameters of the panchromatic sensor are determined with an accuracy of better than 0.32 pixels, and seamless mosaic images can be obtained after the elimination of distortions. Furthermore, the positioning accuracy with relatively few ground control points is shown to be better than 1.5 pixels.

Introduction

The high-resolution YaoGan-Weixing 12 (YG-12) satellite was launched by China in November, 2011, and is located in a 500 km circular orbit. It is intended for scientific experiments, land surveys, crop yield assessments, and disaster monitoring (Barbosa, 2011). YG-12 can acquire panchromatic images with a resolution of 1 m using a pushbroom camera, whose focal plane is briefly illustrated in Figure 1. Detailed camera information is provided in Table 1.

The positioning accuracy of YG-12 using ground control points (GCPs) is known to be very poor due to large distortions, and this seriously restricts the satellite's applications. As an example, Figure 2 shows the positioning errors after using sufficient GCPs to compensate for systematic orbit and attitude errors, with the image line (representing scanning time) on the horizontal axis and residual errors on the vertical axis. Obviously, the residual errors vary randomly with scanning time, so increasing the number of GCPs will not improve the geometric accuracy. The reasons for such large distortions in YG-12 panchromatic images are as follows: (a) The time system is not unified onboard YG-12. Therefore, time-synchronization errors exist because of delays between the time of orbit data, attitude data, and scanning time. The magnitude of the error was found to be several ms (for comparison, the average integral time of the panchromatic sensor is about 0.13

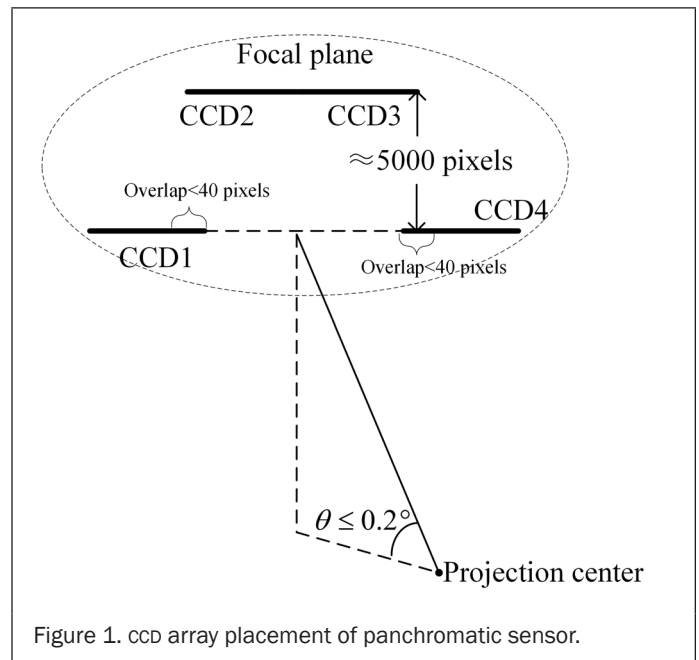


Figure 1. CCD array placement of panchromatic sensor.

TABLE 1. DETAILED PAYLOAD INFORMATION FOR YG-12

Payload Information	
Spectral range	0.5 – 0.8 μm
Ground sample distance	1 m
Focal length	5 m
CCD array information	3072 pixels \times 4 CCDs \times 0.00001 m
Field of view (FOV)	1.4°
Agility	32°

ms); (b) The panchromatic sensor of YG-12 was designed as a large-distortion optical system, meaning that high-order distortions exist in panchromatic images without precise interior calibration; and (c) there may be some large random errors in the measurements of orbit and attitude data.

While scanning in orbit, YG-12 uses a single-frequency GPS system to measure the satellite position and velocity relative to the WGS84 coordinate system with accuracies of 10 m and

Yonghua Jiang, Guo Zhang, Deren Li, Wenchao Huang, and Litao Li are with the State Key Laboratory of Information Engineering in Surveying, Mapping and Remote Sensing (LIESMARS), Wuhan University, 129 Luoyu Road, Wuhan, 430079, P.R. China (guozhang@whu.edu.cn).

Xinming Tang is with the Satellite Surveying and Mapping Application Center (SASMAC), National Administration of Surveying, Mapping and Geoinformation, 28 Lianhuachi West Road, Haidian District, Beijing, 100830, P.R. China.

Photogrammetric Engineering & Remote Sensing
Vol. 81, No. 1, January 2015, pp. 25–36.
0099-1112/15/811–25

© 2014 American Society for Photogrammetry
and Remote Sensing
doi: 10.14358/PERS.81.1.25

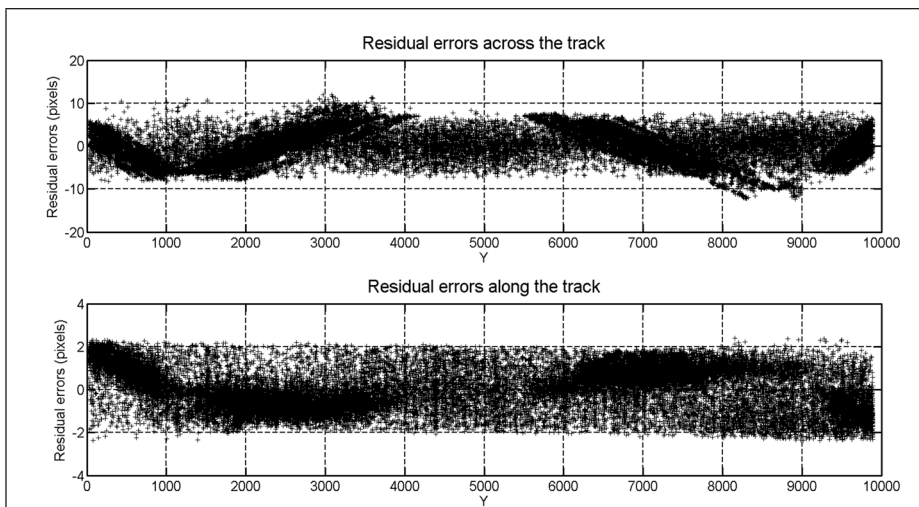


Figure 2. Variation of residual errors (vertical axis) with scanning time (horizontal axis).



Figure 3. The lack of overlap between adjacent CCD arrays.

0.15 m/s, and the satellite attitude is determined by onboard star-trackers and gyroscopes with an accuracy of better than 5". The sampling frequencies are about 1 Hz and 4 Hz for the orbit and attitude data. The orbit and attitude data for a certain scanning time are calculated by the Lagrange interpolation method and linear interpolation method, respectively. During the design phase of YG-12, the random errors of these measurements were made as small as possible. In addition, these measurements mainly behave systematically during a very short period, such as the period of one image (<2.5 s), so item (c) can be neglected. Therefore, in this paper, we focus on methods to resolve (a) and (b). Regarding (b), many researchers have studied methods of distortion elimination by improving interior calibration, and good results have been achieved for the SPOT5, Ikonos, ALOS, and Ziyuan-3 satellites, among others (Bouillon *et al.*, 2003; Breton *et al.*, 2002; Gachet, 2004; Leprince *et al.*, 2008; Grodecki and Dial, 2002; Tadono *et al.*, 2006; Tadono *et al.*, 2009; Yonghua *et al.*, 2013; Guo *et al.*, 2013; Mulawa, 2004; Radhadevi and Solanki, 2008). Different from previous studies, determining the precise interior parameters of YG-12's panchromatic sensor is difficult because of the time-synchronization errors. As for the elimination of time-synchronization errors, related studies have been carried out for the sensors onboard the international space station (Dou *et al.*, 2013). However, they aimed at the frame camera that instantaneously scans an entire image.

Time-synchronization errors of frame camera can equal to systematic orbit errors and attitude errors, which are totally different with the errors of CCD push-broom sensors. Moreover, few studies have been carried out on the elimination of time-synchronization errors for the CCD push-broom sensors.

The influence of time-synchronization errors on positioning is analyzed in detail, based on which we determine the precise interior parameters of the panchromatic sensor by shortening the calibration period. Further, an innovative method is proposed that eliminates time-synchronization errors using parallel observations of the panchromatic sensor. The overlaps between adjacent CCD arrays are sensitive to the imaging side-angle and terrain (De Lussy *et al.*, 2005). As an example, the ellipse in Figure 3 shows the lack of overlap between adjacent CCD images caused by large imaging side-angles. A virtual imaging method that is independent of the overlap is introduced to generate mosaic images. We conduct a series of experiments by collecting several YG-12 panchromatic images and corresponding control data to verify the feasibility and validity of the proposed method. The results indicate that the interior parameters of the panchromatic sensor are determined with an accuracy of better than 0.32 pixels, and seamless mosaic images can be obtained after eliminating distortions. Furthermore, the positioning accuracy using a few GCPs is shown to be better than 1.5 pixels, and equivalent to the accuracy of the GCPs.

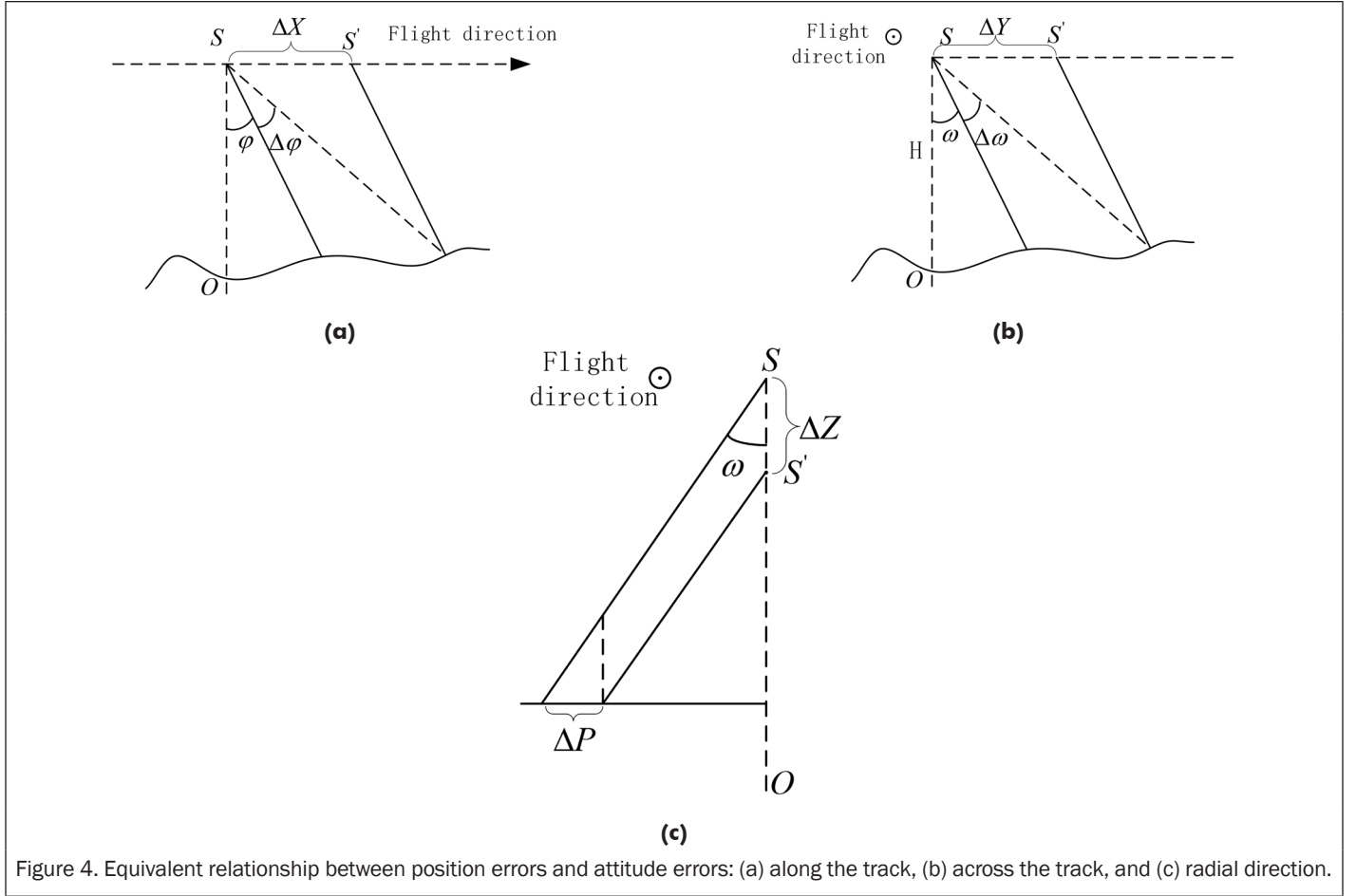


Figure 4. Equivalent relationship between position errors and attitude errors: (a) along the track, (b) across the track, and (c) radial direction.

Methodology

Characteristics of the Time-Synchronization Errors

The rigorous geometric model of the panchromatic sensor can be established as Equation 1 based on the geometric parameters of the panchromatic sensor and the measurements of orbit data and attitude data (Poli, 2012; Xinming *et al.*, 2012):

$$\begin{bmatrix} X \\ Y \\ Z \end{bmatrix} = \begin{bmatrix} X_S \\ Y_S \\ Z_S \end{bmatrix} + m R_{body2wgs84} R_{camera2body} \begin{bmatrix} x - \Delta x \\ y - \Delta y \\ f \end{bmatrix} \quad (1)$$

where (X, Y, Z) is the object position vector in the WGS84 coordinate system; (X_S, Y_S, Z_S) is the position vector of the satellite with respect to the WGS84 coordinate system; $R_{camera2body}$ denotes the rotation matrix to convert the satellite body coordinate system to the WGS84 coordinate system; $R_{body2wgs84}$ denotes the rotation matrix to convert the camera coordinate system to the satellite body coordinate system; (x, y, f) is the position vector in the camera coordinate system; $(\Delta x, \Delta y)$ is the distortion of pixel (x, y) ; and m denotes the scaling factor.

Suppose the time-synchronization error among orbit data, attitude data, and scanning time is Δt . When processing the image line scanned at time t , Equation 1 can be used to derive:

$$\begin{bmatrix} X \\ Y \\ Z \end{bmatrix}_t = \begin{bmatrix} X_S \\ Y_S \\ Z_S \end{bmatrix}_{t+\Delta t} + m (R_{body2wgs84})_{t+\Delta t} R_{camera2body} \begin{bmatrix} x - \Delta x \\ y - \Delta y \\ f \end{bmatrix}_t \quad (2)$$

from Equation 2, the position and attitude data of the satellite measured at time $t + \Delta t$ are used to process the image line at time t . Therefore, the time-synchronization errors essentially affect the positioning, and these can be regarded as position errors and attitude errors that vary with scanning time. These variational position errors and attitude errors can be expressed as:

$$\Delta p = v \Delta t, \Delta a = a \Delta t \quad (3)$$

where Δp denotes the variational position error, v is the satellite's velocity at time t , Δa denotes the variational attitude error, and a is the satellite's angular velocity.

Furthermore, the time-synchronization errors can be simplified based on the equivalent relationship between orbit positioning error and attitude error under the condition of a small field of view, as illustrated in Figure 4. In this Figure, S denotes the correct position of the satellite, S' denotes the wrong position, and SO points from the satellite to the earth's center of mass. In Figure 4a, the position error along the track ΔX is equivalent to a pitch angle error $\Delta \phi$, because an almost identical value of pitch angle ϕ is the response to all detectors in the CCD arrays. However, the situation in Figure 4b is more complex, as different roll angles ω correspond to different detectors. The positioning error caused by a roll angle error $\Delta \omega$ can be calculated as:

$$\Delta Y = H \tan(\omega) - H \tan(\omega + \Delta \omega) \quad (4)$$

and taking the partial derivative of ΔY with respect to ω :

$$d(\Delta Y) = H[\tan^2(\omega) - \tan^2(\omega + \Delta \omega)] d\omega \quad (5)$$

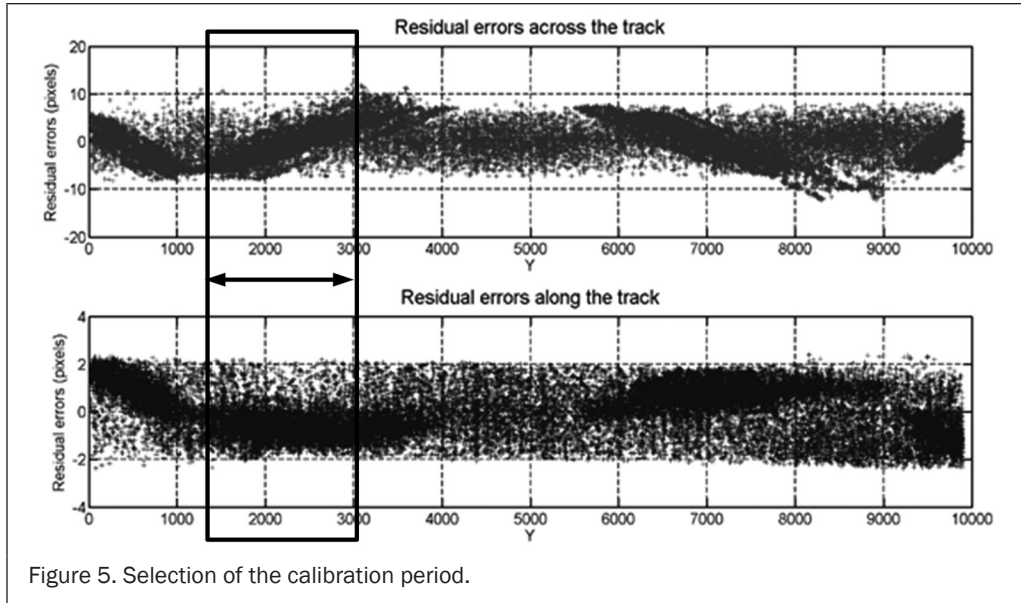


Figure 5. Selection of the calibration period.

According to the design of the YG-12 panchromatic sensor (Table 1), let $d\omega \leq 1.4^\circ$ (the field of view of the panchromatic sensor), $\omega \leq 32^\circ$ (the largest side angle of YG-12), $\Delta\omega \leq 5''$, and $H \approx 500 \text{ km}$. This implies that $d(\Delta Y)$ is less than 0.51 m under the worst conditions, so a roll angle error can generally be considered as a constant positioning error for all detectors, and this is approximately equivalent to the position error across the track ΔY .

In Figure 4c, the positioning error ΔP caused by the radial position error ΔZ can be very small, as shown in Equation 6, while scanning downward. According to the inference on Figure 4b, ΔZ can also be regarded as a constant positioning error, even when scanning with a large side angle, owing to the small field of view, based on which this is equivalent to a corresponding angle error:

$$\Delta P = \Delta Z \tan(\omega) \leq 10 \cdot \tan(1.4/2) = 0.12 \text{ m} \quad (6)$$

For this reason, time-synchronization errors can be regarded as variational attitude errors, since position errors are equivalent to corresponding attitude errors.

Interior Calibration of YG-12 Panchromatic Sensor

The time-synchronization errors can be counted as systematic errors over very short time periods, because the satellite can maintain a steady velocity and angular velocity during such short time-frames. As shown in the example of Figure 5, the positioning errors in the black box caused by time-synchronization errors can be eliminated by several GCPs. This means interior calibration is no longer affected by time-synchronization errors. Therefore, we can shorten the calibration period by selecting an appropriate image area for the acquisition of GCPs for calibration, because time-synchronization errors can be eliminated in this area. This will ensure the precision of the calibration.

To eliminate systematic installation errors of onboard equipment (camera, star sensor, etc.) and attitude errors during the calibration period, a matrix is introduced into Equation 2 (Radhadevi *et al.*, 2011):

$$\begin{bmatrix} X \\ Y \\ Z \end{bmatrix}_t = \begin{bmatrix} X_S \\ Y_S \\ Z_S \end{bmatrix}_{t+\Delta t} + m(R_{body2wgs84})_{t+\Delta t} R_U R_{camera2body} \begin{bmatrix} x - \Delta x \\ y - \Delta y \\ f \end{bmatrix}_t \quad (7)$$

where R_U denotes the matrix to be resolved. As the positioning errors in the black box in Figure 5 shows a linear change with time, R_U can be defined as:

$$R_U = \begin{bmatrix} \cos(\varphi + v_\varphi t) & 0 & \sin(\varphi + v_\varphi t) \\ 0 & 1 & 0 \\ -\sin(\varphi + v_\varphi t) & 0 & \cos(\varphi + v_\varphi t) \end{bmatrix} \begin{bmatrix} 1 & 0 & 0 \\ 0 & \cos(\omega + v_\omega t) & -\sin(\omega + v_\omega t) \\ 0 & \sin(\omega + v_\omega t) & \cos(\omega + v_\omega t) \end{bmatrix} \begin{bmatrix} \cos \kappa & -\sin \kappa & 0 \\ \sin \kappa & \cos \kappa & 0 \\ 0 & 0 & 1 \end{bmatrix} \quad (8)$$

Then, φ , ω , κ , v_φ , and v_ω can be calculated with several GCPs after linearizing Equation 7.

The panchromatic sensor of YG-12 consists of multiple linear CCD arrays. Each may have different interior errors due to the different arrangement in the focal plane. Therefore, we adopt the following look-angle model for interior calibration to avoid establishing different distortion models for each CCD array (Leprince *et al.*, 2008):

$$\begin{aligned} \frac{x - \Delta x}{f} &= \tan \psi_x \\ \frac{y - \Delta y}{f} &= \tan \psi_y \end{aligned} \quad (9)$$

From Equation 7, we can derive:

$$\begin{bmatrix} X \\ Y \\ Z \end{bmatrix}_t = \begin{bmatrix} X_S \\ Y_S \\ Z_S \end{bmatrix}_{t+\Delta t} + m(R_{body2wgs84})_{t+\Delta t} R_U R_{camera2body} \begin{bmatrix} \tan \psi_x \\ \tan \psi_y \\ 1 \end{bmatrix}_t \quad (10)$$

Hence, the look-angles (ψ_x , ψ_y) can be calibrated for a certain detector using only one GCP in the corresponding row. When more than one GCP is obtained, the look-angles can be determined based on the least-squares method. However, there must be some error in parts of the obtained look-angles if no restrictions are adopted to restrain the effects caused by inaccurate GCPs. Therefore, a suitable smoothing fit is required to eliminate these errors. For a linear CCD array look-angle with a principal point offset (Δx_0 , Δy_0), focus-length bias Δf , zooming scale error s_y , CCD chip rotation error θ , radial distortion (k_1 , k_2), and decentering distortion (p_1 , p_2) (Brown, 1971; Fryer and Brown, 1986):

$$\begin{cases} \tan(\psi_x) = \frac{x - (\Delta x_0 + (k_1 r^2 + k_2 r^4)x + p_1(r^2 + 2x^2) + 2p_2 xy + y \sin \theta)}{-(f - \Delta f)} \\ \tan(\psi_y) = \frac{y - (\Delta y_0 + (k_1 r^2 + k_2 r^4)y + 2p_1 xy + p_2(r^2 + 2y^2) + s_y y)}{-(f - \Delta f)} \end{cases} \quad (11)$$

where $r = \sqrt{x^2 + y^2}$.

For a linear CCD array, x is constant, so Equation 7 can be approximated as (Yonghua et al., 2013):

$$\begin{cases} \tan(\psi_x) = a_0 + a_1 s + a_2 s^2 + \dots + a_i s^i \\ \tan(\psi_y) = b_0 + b_1 s + b_2 s^2 + \dots + b_i s^i \end{cases}, \quad (12)$$

where s denotes the image row. The variables $a_0, a_1, \dots, b_0, b_1, \dots, b_i$ are obtained using the direct calibrated look-angles on the basis of polynomial regression analysis for each CCD array.

Elimination of the Time-Synchronization Errors Based on Parallel Observations

As shown in Figure 6, the adjacent CCD arrays scan the same ground object within a very short period of time τ , which is determined by the shift between the adjacent CCD arrays of the panchromatic sensor ($\tau \approx 5000 \times 0.00013 = 0.65s$, where 0.00013 is the average integral time).

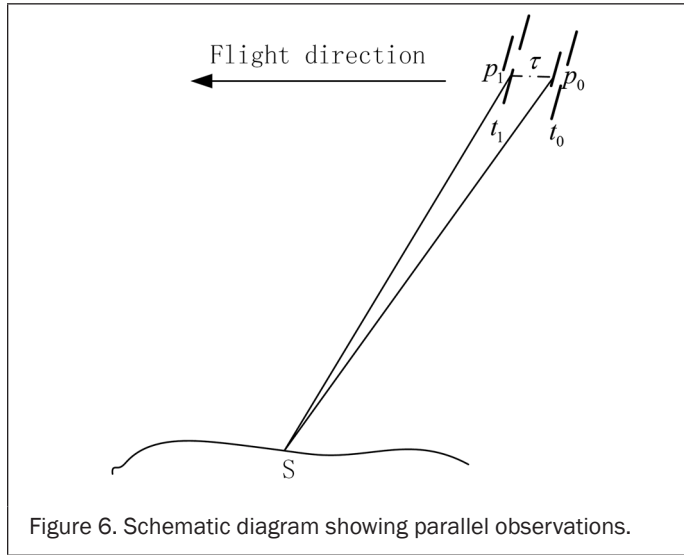


Figure 6. Schematic diagram showing parallel observations.

If there are no errors in the imaging geometry during the period τ , the conjugate points p_0 and p_1 should be positioned on the same ground object S , as shown in Figure 6. This can be expressed as:

$$\begin{cases} \begin{bmatrix} X \\ Y \\ Z \end{bmatrix} = \begin{bmatrix} X_S \\ Y_S \\ Z_S \end{bmatrix}_{t_0} + m_{t_0} R_{body2wgs84}^{t_0} R_{cam2body} \begin{bmatrix} \tan \psi_x \\ \tan \psi_y \\ 1 \end{bmatrix}_{t_0} \\ \begin{bmatrix} X \\ Y \\ Z \end{bmatrix} = \begin{bmatrix} X_S \\ Y_S \\ Z_S \end{bmatrix}_{t_1} + m_{t_1} R_{body2wgs84}^{t_1} R_{cam2body} \begin{bmatrix} \tan \psi_x \\ \tan \psi_y \\ 1 \end{bmatrix}_{t_1} \end{cases} \quad (13)$$

After precisely determining the interior parameters of the panchromatic sensor, the unknown height of S and the time-synchronization errors invalidate Equation 13. The influence of height error on Equation 13 is illustrated in Figure 7 where panel 7a shows the stereoscopy error across the track, and panel 7b shows the stereoscopy error along the track. In Figure 7, Δh is the height error of the ground object S , α_0 and α_1 are the side angles of the conjugate points in adjacent CCD arrays, while θ_0 and θ_1 are the angles of pitch; ΔX and ΔY denote the stereoscopy errors across and along the track, respectively. For the panchromatic sensor of YG-12, the overlap between adjacent CCD arrays is less than 40 pixels and the focal length is about 5 m. In the extreme case, the sensor is assumed to scan with a maximum side-angle of 32° . Considering the maximum difference between α_0 and α_1 in Figure 1, we let α_0 be the side angle of the left-most pixel in the CCD2 array, and α_1 be that of the conjugate pixel in CCD1:

$$\alpha_0 \approx 32^\circ + \tan^{-1}(0.00001 \times 3072/5) = 32.352^\circ$$

$$\alpha_1 \approx 32^\circ + \tan^{-1}(0.00001 \times 3072 + 40) = 32.356^\circ$$

The maximum stereoscopy error across the track (ΔX) can be calculated as:

$$\Delta X = \Delta h (\tan(32.356^\circ) - \tan(32.352^\circ)) = 0.000098 \Delta h \quad (14)$$

Similarly, we let $\theta_1 \leq 0.20^\circ$ and $\theta_0 \approx 0.20^\circ + \tan^{-1}(5000 \times 0.00001/5) = 0.77^\circ$ according to Figure 1, and calculate the stereoscopy error along the track (ΔY) as:

$$\Delta Y = \Delta h (\tan(0.77^\circ) - \tan(0.20^\circ)) = 0.01 \Delta h \quad (15)$$

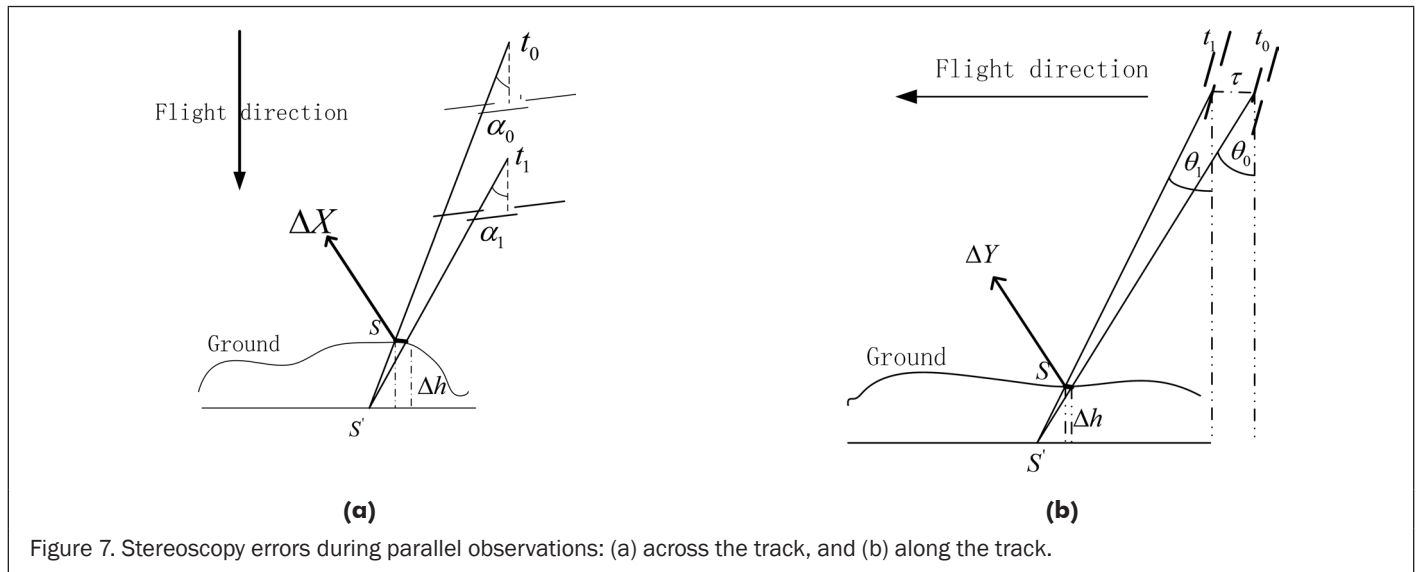


Figure 7. Stereoscopy errors during parallel observations: (a) across the track, and (b) along the track.

The direct positioning accuracy of YG-12 without GCPs can be <90 m. When a 90 m shuttle radar topography mission (90 m SRTM) digital elevation model (DEM) is used for correction, the height error of ground objects is less than 30 m (Consortium for Spatial Information, 2012), and the stereoscopy errors are both less than 0.3 m according to Equations 14 and 15, so the influence on Equation 13 caused by height error can be neglected. Therefore, Equation 13 is only affected by the time-synchronization errors. To regard the time-synchronization error as a variational attitude error, it can be eliminated by introducing an attitude offset matrix into Equation 13 (Yonghua *et al.*, 2014), giving:

$$\begin{cases} \begin{bmatrix} X \\ Y \\ Z \end{bmatrix} = \begin{bmatrix} X_S \\ Y_S \\ Z_S \end{bmatrix}_{t_0} + m_{t_0} R_{body2wgs84}^{t_0} R_{offset}^{t_0} R_{cam2body} \begin{bmatrix} \tan \psi_x \\ \tan \psi_y \\ 1 \end{bmatrix}_{t_0} \\ \begin{bmatrix} X \\ Y \\ Z \end{bmatrix} = \begin{bmatrix} X_S \\ Y_S \\ Z_S \end{bmatrix}_{t_1} + m_{t_1} R_{body2wgs84}^{t_1} R_{offset}^{t_1} R_{cam2body} \begin{bmatrix} \tan \psi_x \\ \tan \psi_y \\ 1 \end{bmatrix}_{t_1} \end{cases} \quad (16)$$

where R_{offset}^t denotes the attitude offset matrix at time t , which can be defined as:

$$R_{offset}^t = R_{\varphi} R_{\omega} R_{\kappa} = \begin{bmatrix} \cos \varphi_t & 0 & -\sin \varphi_t \\ 0 & 1 & 0 \\ \sin \varphi_t & 0 & \cos \varphi_t \end{bmatrix} \begin{bmatrix} 1 & 0 & 0 \\ 0 & \cos \omega_t & -\sin \omega_t \\ 0 & \sin \omega_t & \cos \omega_t \end{bmatrix} \begin{bmatrix} \cos \kappa_t & -\sin \kappa_t & 0 \\ \sin \kappa_t & \cos \kappa_t & 0 \\ 0 & 0 & 1 \end{bmatrix}$$

where φ_t , ω_t and κ_t denote the variables which are indeed resolved.

There are two main problems if we solve R_{offset}^t directly using Equation 16 when the ground object location (X, Y, Z) is unknown: (a) too many calculations are required, because six unknowns ($\varphi_t, \omega_t, \kappa_t, X, Y, Z$) must be found for each conjugate point; (b) the accuracy of (X, Y, Z) obtained by the forward intersection is severely affected by the extraction accuracy of the conjugate points when there is only a very low base-height ratio between adjacent CCD arrays, which may reduce the correction accuracy of time-synchronization errors. To overcome these problems, the location (X, Y, Z) of a ground object can be calculated at time t_0 with an identity offset matrix and a 90 m SRTM, and the attitude offset matrix at time t_1 can then be computed. If the attitude offset matrix is solved for each conjugate point in this manner, there will be errors in parts of the attitude offset matrixes due to unavoidable mismatched points. Thus, techniques to reduce the detrimental effects of mismatched points should be applied. Given that the errors may remain regular over a very short period, we can divide all of the conjugate points into different groups. We then need only solve an attitude offset matrix for one group to suppress the mismatched points, because the majority points in a group will be correctly matched. If we suppose that n conjugate points $((x_{ccd_j}, y_{ccd_j}, x_{ccd_{j+1}}, y_{ccd_{j+1}}), j \leq n)$ have been obtained from adjacent CCD arrays CCD_i and CCD_{i+1} , the division process proceeds as follows (Yonghua *et al.*, 2014).

1. First, calculate the location $(X, Y, Z)_j$ that corresponds to $(x_{ccd_{j+1}}, y_{ccd_{j+1}})$ with a 90 m SRTM, and calculate the image coordinates $(x'_{ccd_j}, y'_{ccd_j})_j$ in CCD_i that correspond to $(X, Y, Z)_j$.
2. Calculate the conjugate positioning errors for all points as follows: $(\Delta x, \Delta y)_j = (x'_{ccd_j} - x_{ccd_j}, y'_{ccd_j} - y_{ccd_j})_j, j \leq n$, (17)
3. Set a threshold r such that if two conjugate points satisfy $\sqrt{(\Delta x_{j+1}^2 + \Delta y_{j+1}^2) - (\Delta x_j^2 + \Delta y_j^2)} \leq r$, they should be placed in the same group. Otherwise, generate a new group.
4. Eliminate the group for which the number of points is very small (e.g., <5). We then solve the attitude offset matrixes for each group.

Virtual Imaging Method to Generate Mosaic Image Products

Finally, after determining the interior parameters and eliminating time-synchronization errors, a virtual imaging method is adopted to generate the mosaic image products of the panchromatic sensor. The virtual imaging method proceeds as follows (Hongbo *et al.*, 2013):

1. A geometric model of the virtual CCD is established on the basis of the interior orientation defined by its position in the focal plane (shown in Figure 8). The object coordinates (X, Y, Z) of any pixel (x', y') in the virtual CCD are then obtained using the model and the corresponding height from 90 mSRTM.
2. The image coordinates (x, y) in the original image corresponding to (X, Y, Z) in Step 1 are calculated using the geometric model for the original image.
3. The gray value of a pixel (x, y) in the original image, obtained by resampling with a raised cosine function (Cho *et al.*, 2005), is assigned to pixel (x', y') in the virtual CCD.
4. The mosaic image is generated by repeating Steps 1, 2, and 3 for all pixels.
5. The rational polynomial coefficients (RPCs) are then generated based on the geometric model of the virtual CCD obtained in Step 1.

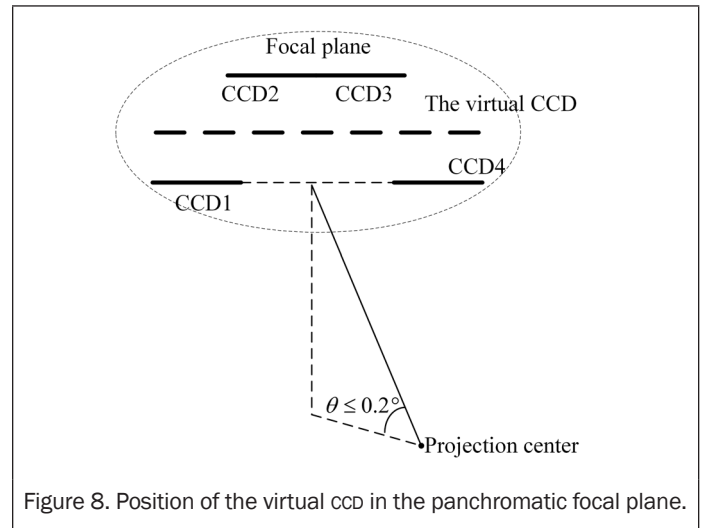


Figure 8. Position of the virtual CCD in the panchromatic focal plane.

Results and Analysis

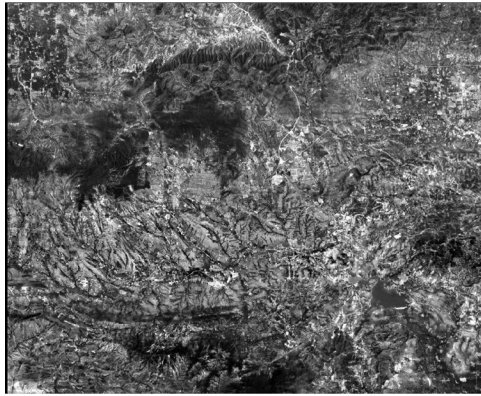
Study Area and Data Sources

To validate the feasibility of the proposed method, we collected 1:2000 scale digital orthophoto maps (DOMs) and DEMs as shown in Figure 9 and the corresponding panchromatic images of YG-12. The Tianjin data contain flat regions and a height range of 12 m. The Henan region covers a 50 km x 50 km area with a small mountainous region in the southwest, and has a height range of about 600 m. Information on the YG-12 images is listed in Table 2.

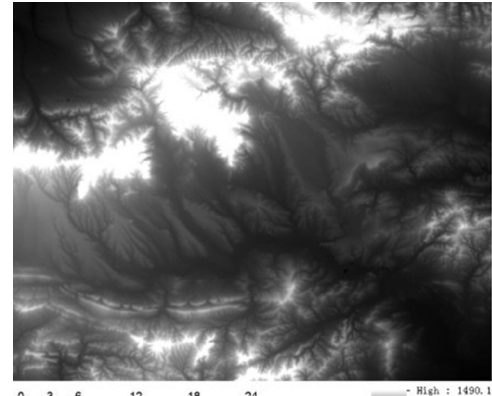
TABLE 2. DETAILS OF THE YG-12 EXPERIMENT DATA

Area	Imaging time	Side-angle (°)	Max /Ave (m)
2012-3-27-Henan	2012-3-27	-3.05	641.78/400.34
2012-4-17-Tianjin	2012-4-17	17.89	9.74/1.24
2012-5-8-Tianjin	2012-5-8	8.13	10.82/29.81
2012-10-18-Henan	2012-10-18	-19.51	541.76/664.88
2012-11-16-Henan	2012-11-16	0.16	513.68/709.93

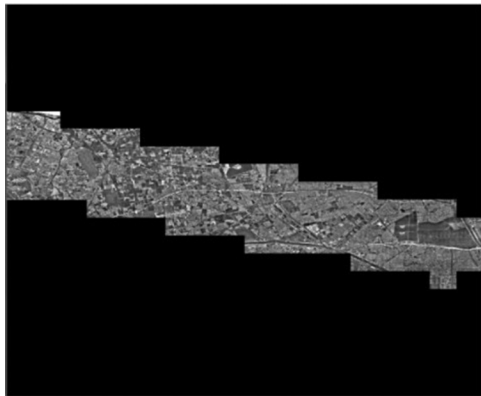
* Max denotes maximum altitude difference and Ave denotes average altitude.



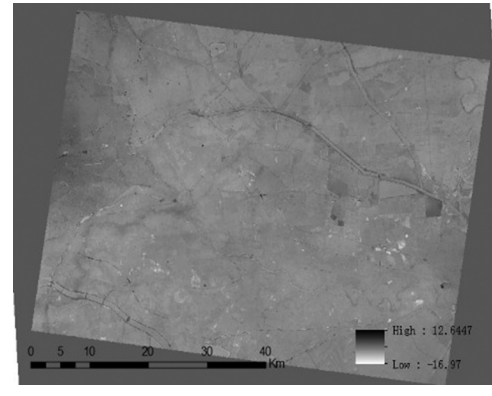
(a)



(b)



(c)



(d)

Figure 9. Control data for validation: (a) DOM and (b) DEM of Henan area, and (c) DOM and (d) DEM of Tianjin area.

First, the interior parameters of the panchromatic sensor were determined using the 27 March 2012 Henan image. Using these, the proposed method of eliminating time-synchronization errors was applied to the other images. Finally, the mosaic image products were generated, and their accuracy was estimated to verify the feasibility and validity of the proposed method.

Correction of Distortions for the Panchromatic Sensor

According to the characteristics of the positioning errors in 2012-3-27-Henan, the appropriate image area was determined from lines 12 000 to 14 000. GCPs were obtained for every third row from the 1:2000 scale DOM using a high-accuracy matching method with a theoretical accuracy of better than 0.02 pixels (Leprince *et al.*, 2008). Finally 9,982 evenly distributed GCPs were acquired. The distribution of the GCPs is shown in Figure 10.

The interior calibration accuracy is given in Table 3, where the maximum along- and across-track residual errors are both less than 1.5 pixels, and the overall accuracy is better than 0.32 pixels. This indicates two points: (a) the systematic errors can be totally eliminated with the proposed calibration model, and (b) the influence on interior calibration of the time-synchronization errors can be restrained by shortening the calibration period. The residual errors after calibration are shown in Figure 11 where the left panel denotes the variation rule of the residual errors along the CCD direction, and the right panel denotes that with respect to scanning time. It can be seen that time-synchronization errors are completely eliminated since there is no trend in the variation with scanning time, unlike in Figure 2, which further verifies the equivalence between the time-synchronization errors and systematic attitude errors within the short calibration period.

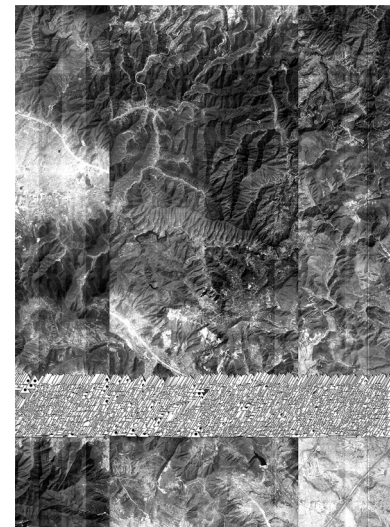


Figure 10. Distribution of GCPs in 2012-3-27-Henan (Δ : GCPs).

TABLE 3. INTERIOR CALIBRATION ACCURACY

Accuracy	Along the track (pixel)			Across the track (pixel)		
	MAX	MIN	RMS	MAX	MIN	RMS
2012-3-27-Henan	1.48	0.00	0.31	1.21	0.00	0.27

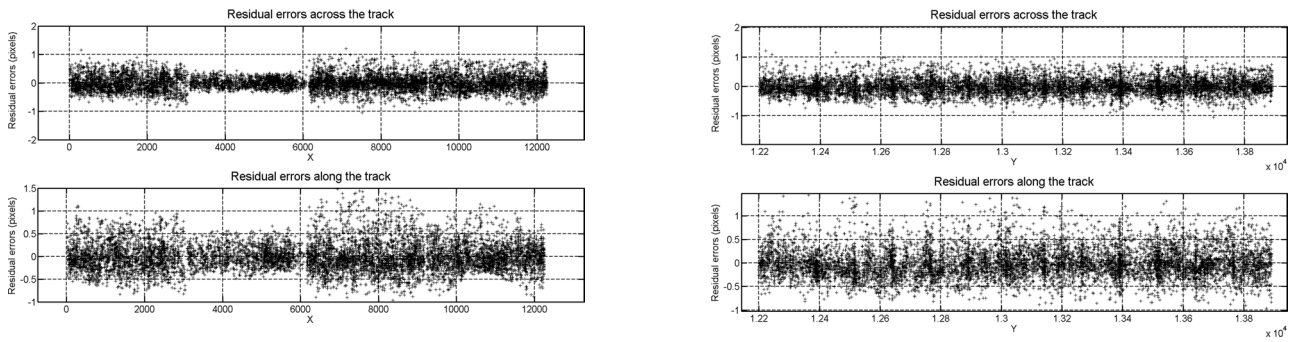


Figure 11. Residual errors after interior calibration.

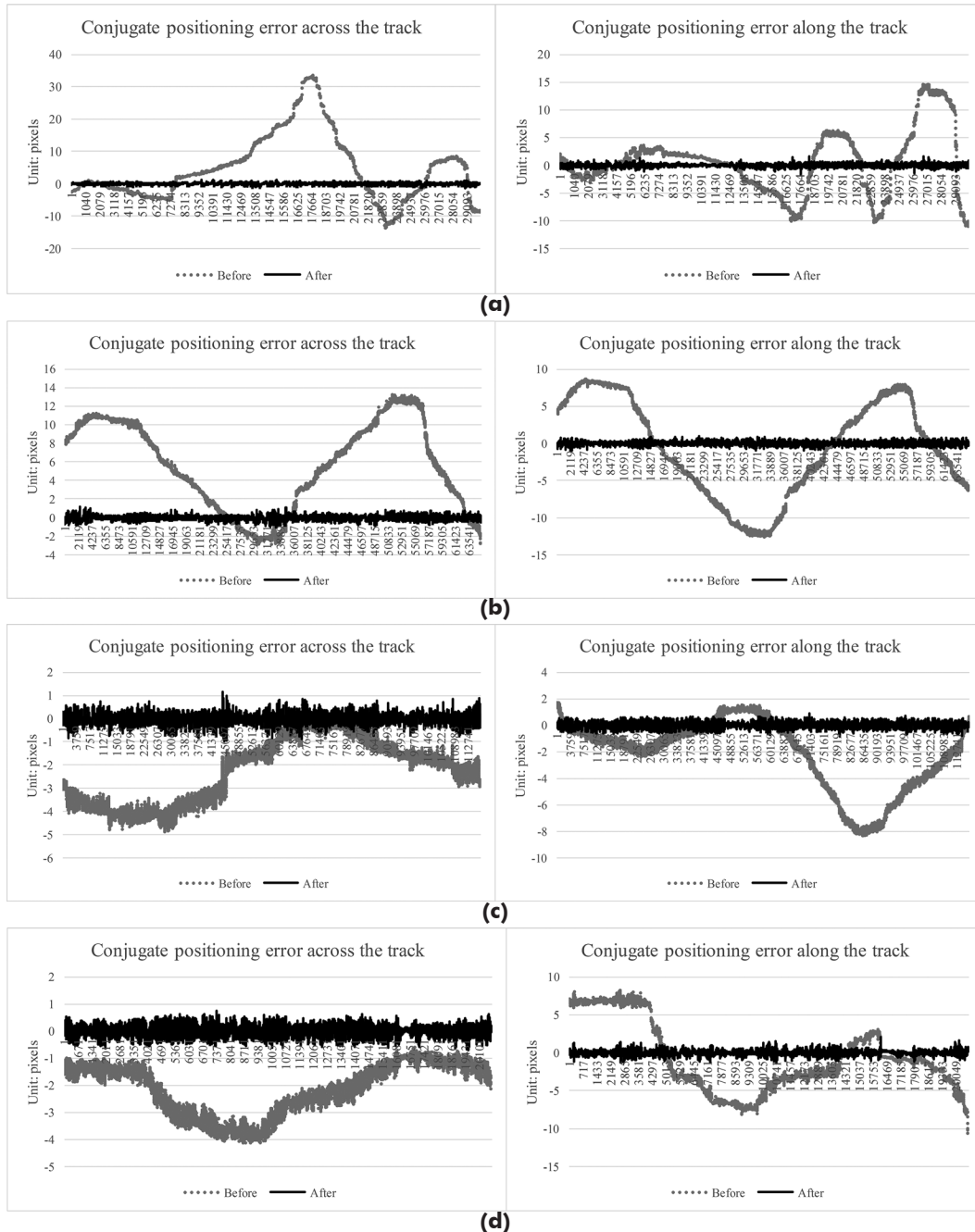


Figure 12. Comparison of the conjugate positioning errors: (a) 2012-4-17-Tianjin, (b) 2012-5-8-Tianjin, (c) 2012-10-18-Henan, and (d) 2012-11-16-Henan;

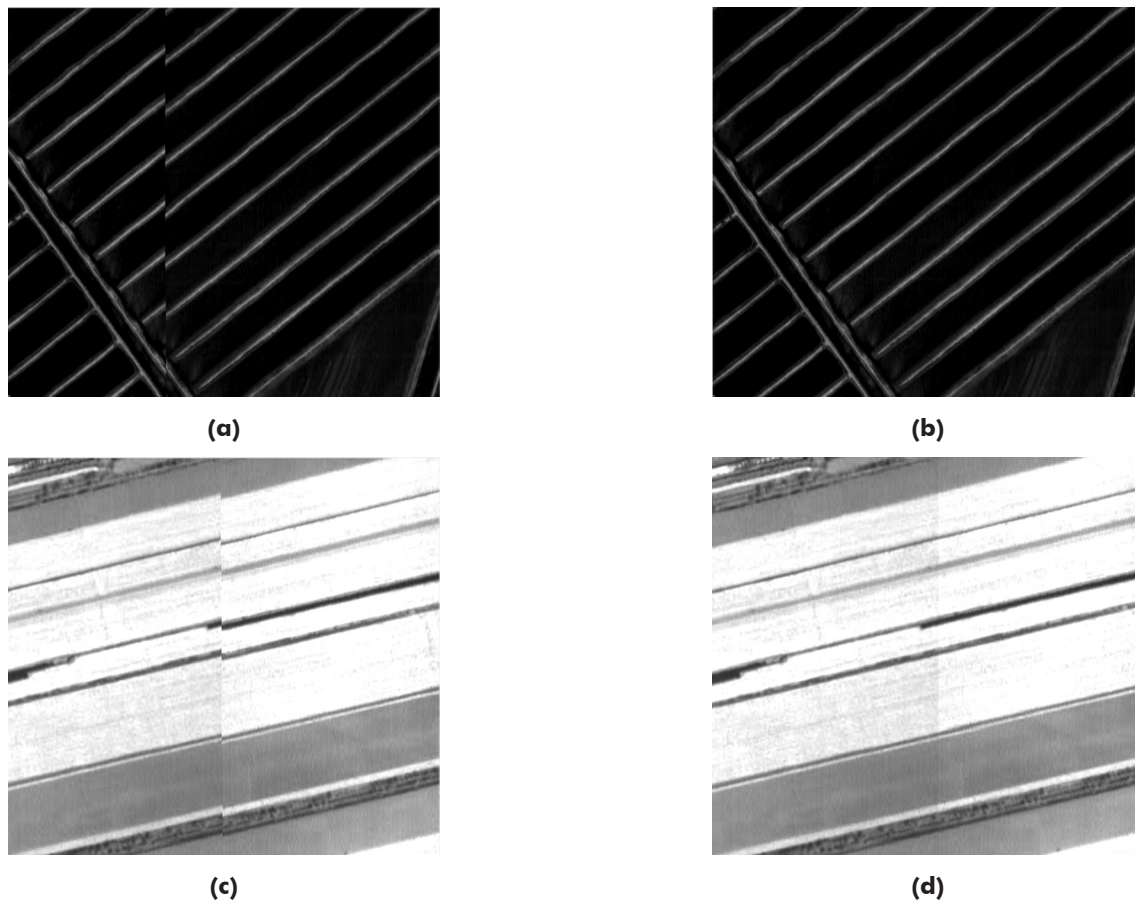


Figure 13. Comparison of the mosaic effects: (a) Before, (b) After, (c) Before, and (d) After.

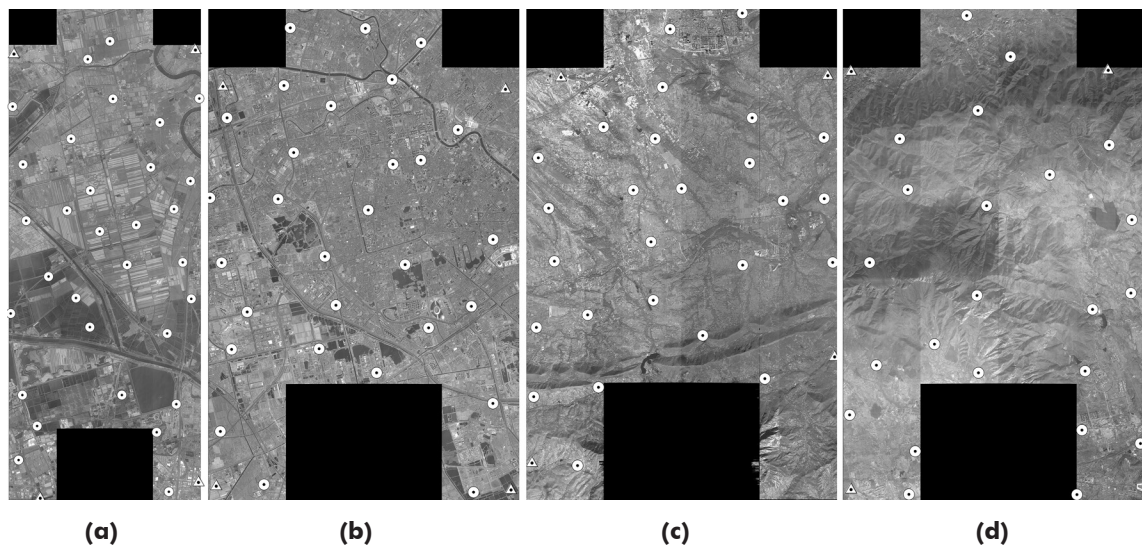
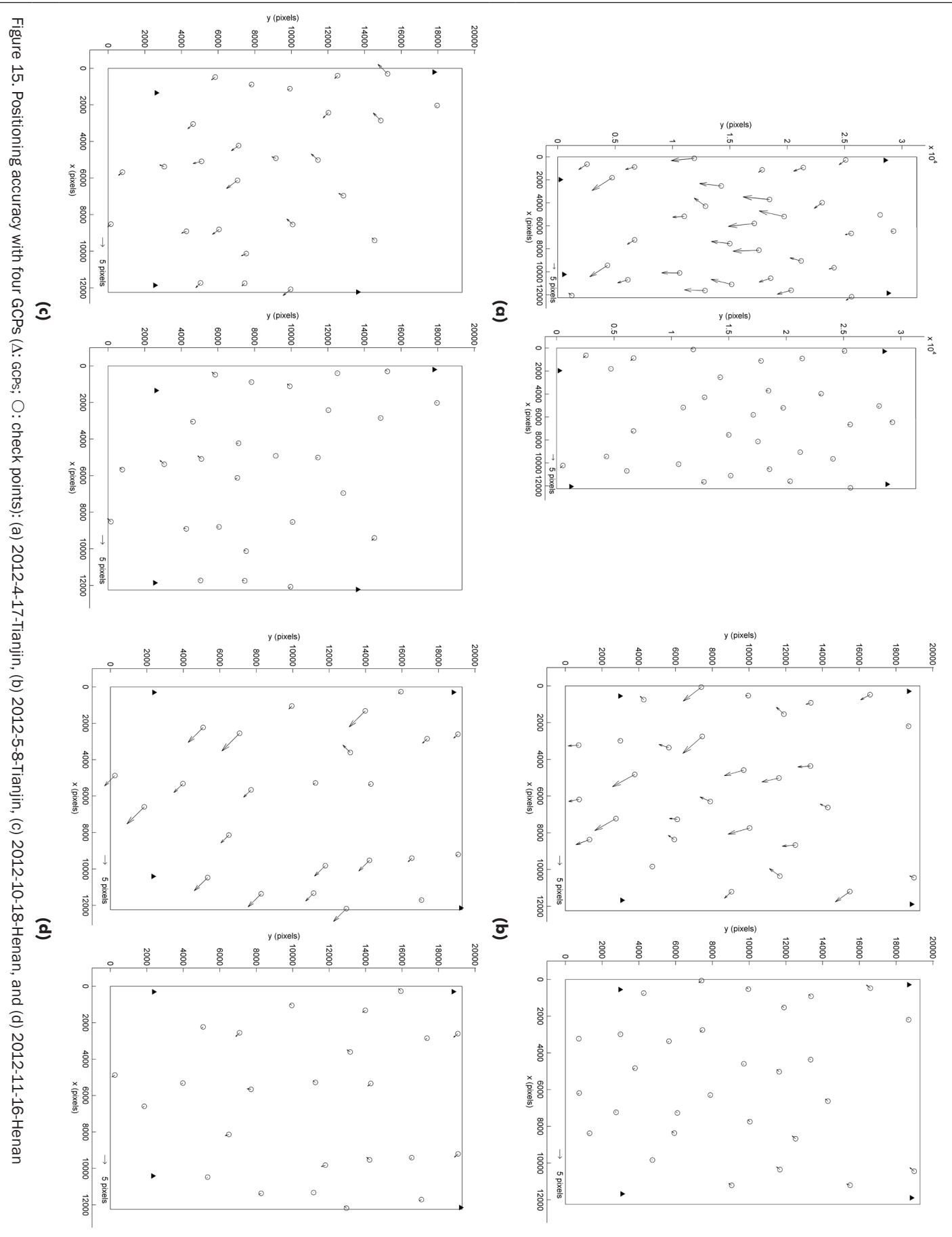


Figure 14. Distribution of GCPs (Δ : GCPs; \circ : check points): (a) 2012-4-17-Tianjin, (b) 2012-5-8-Tianjin, (c) 2012-10-18-Henan, and (d); 2012-11-16-Henan

A total of 30,420, 66,493, 117,860, and 21,174 conjugate points were obtained by the matching method (Yonghua *et al.*, 2014) for 2012-4-17-Tianjin, 2012-5-8-Tianjin, 2012-10-18-Henan, and 2012-11-16-Henan, respectively. These conjugate points and the calibrated interior parameters from 2012-3-27-Henan were applied to eliminate the time-synchronization errors in the other images. Because only

variational attitude errors invalidate Equation 13, we calculated the conjugate positioning errors based on Equation 17 to estimate the elimination accuracy of the time-synchronization errors. The conjugate positioning errors before and after eliminating time-synchronization errors are compared in Table 4.

From Table 4, we can see that the conjugate positioning errors after eliminating the time-synchronization errors are less



than 0.3 pixels both along and across the track, which proves the time-synchronization errors were well compensated by the attitude offset matrixes. On the other hand, the appearance of the time-synchronization errors shown in Figure 12 accords with the characteristic mentioned above, that random variation occurs in the steady state during very short periods. This is so complex and random that we cannot establish a rigorous model for it.

Evaluation Based on the Mosaic Image Products

The mosaic image products of all images were generated after eliminating distortions. A comparison of the mosaic effect before and after these distortions were removed is shown in Figure 13.

The mosaic effect of the mosaic images mainly depends on the accuracy of the geometric model. In Figure 13, only very poor mosaic effects were achieved using the original geometric model that suffers from time-synchronization errors. However, seamless mosaic effects were achieved with the accurate geometric model after eliminating all distortions. Further, 35, 33, 30, and 28 GCPs were manually extracted from the 1:2000 scale DOMs and DEMs over Henan and Tianjin to validate the positioning accuracy with a few GCPs (shown in Figure 14). The accuracy of the image coordinates of all GCPs is better than 1.5 pixels. The affine model based on RPC was taken as the exterior orientation model (Fraser and Hanley, 2003; Hanley *et al.*, 2002):

$$x + a_0 + a_1x + a_2y = \text{RPC}_x(\text{lat}, \text{lon}, h)$$

$$y + b_0 + b_1x + b_2y = \text{RPC}_y(\text{lat}, \text{lon}, h).$$

From Table 5, we can see that the positioning accuracy using a few GCPs improves considerably after the elimination of distortions. The accuracy with four GCPs is better than 1.5 pixels, and is equivalent to the accuracy of the GCPs. Because the DOMs and DEMs over Henan and Tianjin were taken in 2010 and 2007, respectively, the obvious variation in ground features reduces the accuracy of the manually extracted GCPs. With more accurate GCPs, the numbers in Table 5 would approach the accuracy levels in Table 3. However, because of the limited number of GCPs and their distribution, the accuracies given in Table 5 do not reflect the actual distortions in the mosaic image products, and hence Table 5 differs from Table 4.

The residual errors with four GCPs are shown in Figure 15, where the left panels denote the accuracies before elimination, and the right panels are the accuracies after elimination. It can be seen that no systematic errors exist after exterior orientation with four GCPs in the right panels, which proves that the internal accuracy of the panchromatic sensor onboard YG-12 was improved significantly by the proposed method.

Conclusions

This paper has presented a method for the correction of large distortions in the panchromatic images of YG-12 caused by time-synchronization errors and interior distortions. The influence of time synchronization errors on positioning was analyzed in detail, and their effects were removed by shortening the calibration period, allowing interior parameters to be precisely calibrated. In addition, we proposed an innovative technique to eliminate time-synchronization errors using parallel observations from the panchromatic sensor onboard YG-12. The experimental results indicate that the interior parameters of the panchromatic sensor can be determined with an accuracy of better than 0.32 pixels, and seamless mosaic images were obtained after eliminating the time-synchronization errors. Furthermore, the positioning accuracy with a few GCPs was shown to be better than 1.5 pixels, and equivalent to the accuracy of the GCPs. However, further study is required

TABLE 4. COMPARISON OF CONJUGATE POSITIONING ERRORS

Area	Before solving attitude error Unit: pixels		After solving attitude error Unit: pixels	
	RMS(x)	RMS(y)	RMS(x)	RMS(y)
2012-4-17-Tianjin	11.33	5.67	0.25	0.24
2012-5-8-Tianjin	7.31	6.61	0.20	0.22
2012-10-18-Henan	2.61	3.46	0.17	0.20
2012-11-16-Henan	2.34	4.67	0.18	0.28

TABLE 5. POSITIONING ACCURACY USING DIFFERENT NUMBERS OF GCPs

Area	Leve1-l image	Number of GCPs	Accuracy (RMSE: pixels)		
			Line	Sample	Plane
2012-4-17-Tianjin	Original	4	4.11	12.29	12.95
		ALL	3.51	9.67	10.29
	Corrected	4	0.92	1.11	1.45
		ALL	0.74	0.81	1.10
2012-5-8-Tianjin	Original	4	3.61	5.71	6.75
		All	3.16	3.82	4.96
	Corrected	4	0.93	0.74	1.19
		ALL	0.64	0.51	0.81
2012-10-18-Henan	Original	4	2.47	1.91	3.12
		All	2.03	1.39	2.46
	Corrected	4	0.89	0.79	1.19
		All	0.69	0.65	0.95
2012-11-16-Henan	Original	4	5.39	0.78	5.44
		All	3.13	0.71	3.21
	Corrected	4	1.10	1.00	1.48
		All	0.98	0.76	1.25

* Original: before eliminating distortions, Corrected: after eliminating distortions.

to determine whether the proposed method can be applied in practice to ensure the geometric quality of YG-12 panchromatic images, which depends on a tradeoff between the computational cost and the number of matching points acquired.

Acknowledgments

This work was supported by Public Science Research Programme of Surveying, Mapping and Geoinformation (201412007), National Technology Support Project (2012BAH28B04) and National Natural Science Foundation of China (Grant No. 41201361). The authors also thank the anonymous reviews for their constructive comments and suggestions.

References

- Barbosa, R.C. 2011. Long March 4B launches YaoGanWeixing-12 for China. URL: <http://www.nasaspaceflight.com/2011/11/long-march-4b-launches-yaogan-weixing-12/> (last date accessed: 17 November 2014).
- Bouillon, A., E. Breton, F. De Lussy, and R. Gachet, 2003. SPOT5 geometric image quality, *Proceedings of 2003 IEEE International Geoscience and Remote Sensing Symposium*, Toulouse, France. I(2003):303-305.
- Breton, E., A. Bouillon, R. Gachet, and F. De Lussy, 2002. Pre-flight and in-flight geometric calibration of SPOT5 HRG and HRS Images, *International Archives of Photogrammetry, Remote Sensing and Spatial Information Sciences*, 34(Part 1).

- Brown, D.C., 1971. Close-range camera calibration, *Photogrammetric Engineering*, 37(8):855-866.
- Cho, B.L., Y.K. Kong, and Y.S. Kim, 2005. Interpolation using optimum Nyquist filter for SAR interferometry, *Journal of Electromagnetic Waves and Applications*, 19(1):129-135.
- Consortium for Spatial Information, 2012. URL: <http://www.cgiar-csi.org/data/srtm-90m-digital-elevation-database-v4-1> (last date accessed: 17 November 2014).
- Fraser, C.S., and H.B. Hanley, 2003. Bias compensation in rational functions for Ikonos satellite imagery, *Photogrammetric Engineering & Remote Sensing*, 69(1):53-57. Fryer, J.G., and D.C. Brown, 1986. Lens distortion for close-range photogrammetry, *Photogrammetric Engineering & Remote Sensing*, 52(1):51-58.
- Gachet, R., 2004. Spot5 in-flight commissioning: inner orientation of HRG and HRS instruments, *International Archives of Photogrammetry, Remote Sensing and Spatial Information Sciences*, 35(Part B1):535-539.
- Grodecki, J., and G. Dial, 2002. IKONOS geometric accuracy validation, *Proceedings of ISPRS Commission I Mid-Term Symposium*, 10-15 November, Denver, Colorado, unpaginated CD-ROM..
- Guo, Z., J. Yonghua, L. Deren, H. Wenchao, P. Hongbo, T. Xinming, and Z. Xiaoyong, 2013. In-orbit geometric calibration and validation of ZY-3 linear array sensors, *The Photogrammetric Record*, 29(145):68-88.
- Hanley, H.B., T. Yamakawa, and C.S. Fraser, 2002. Sensor orientation for high-resolution satellite imagery, *International Archives of Photogrammetry and Remote Sensing*, 34(1):69-75.
- Hongbo, P., Z. Guo, T. Xinming, L. Deren, and Z. Xiaoyong, 2013. Basic products of the ZY-3 satellite and accuracy evaluation, *Photogrammetric Engineering & Remote Sensing*, 79(11):1131-1145.
- Leprince, S., P. Musé, and J. Avouac, 2008. In-flight CCD distortion calibration for pushbroom satellites based on subpixel correlation, *IEEE Transactions on Geoscience and Remote Sensing*, 46(9):2675-2683.
- De Lussy, F., P. Kubik, D. Greslou, V. Pascal, P. Gigord, and J.P. Cantou, 2005. Pleiades HR-image system products and quality, Pleiades-HR image system products and geometric accuracy, *Proceedings of the ISPRS Hannover Workshop*.
- Mulawa, D., 2004. On-orbit geometric calibration of the OrbView-3 high resolution imaging satellite, *International Archives of the Photogrammetry, Remote Sensing and Spatial Information Sciences*, 35(B1):1-6.
- Poli, D., 2012. Review of developments in geometric modelling for high resolution satellite pushbroom sensors, *The Photogrammetric Record*, 27(137):58-73.
- Radhadevi, P.V., and S.S. Solanki, 2008. In-flight geometric calibration of different cameras of IRS-P6 using a physical sensor model, *The Photogrammetric Record*, 23(121):69-89.
- Dou, C., X. Zhang, H. Kim, J. Ranganathan, D. Olsen, D., and H. Guo, 2013. Geolocation algorithm for earth observation sensors onboard international space station, *Photogrammetric Engineering & Remote Sensing*, 79(6):625-637.
- Tadono, T., M. Shimada, H. Murakami, T. Hashimoto, J. Takaku, A. Mukaida, and S. Kawamoto, 2006. Initial results of calibration and validation for PRISM and AVNIR-2, *Asian Journal of Geoinformatics*, 6(4):11-20.
- Tadono, T., M. Shimada, H. Murakami, and J. Takaku, 2009. Calibration of PRISM and AVNIR-2 onboard ALOS "Daichi", *IEEE Transactions on Geoscience and Remote Sensing*, 47(12):4042-4050.
- Xinming, T., Z. Guo, Z. Xiaoyong, P. Hongbo, J. Yonghua, Z. Ping, and W. Xia, 2012. Triple linear-array imaging geometry model of ZiYuan-3 surveying satellite and its validation, *Acta Geodaetica et Cartographica Sinica*, 41(2):191-198.
- Yonghua, J., Z. Guo, T. Xinming, H. Wenchao, and P. Hongbo, 2013. Geometric calibration and accuracy assessment of ZiYuan-3 multispectral images, *IEEE Transactions on Geoscience and Remote Sensing*, 52(7):4161-4172.
- Yonghua, J., Z. Guo, L. Deren, T. Xinming, and H. Wenchao, 2014. Detection and correction of relative attitude errors for ZY1-02C, *IEEE Transactions on Geoscience and Remote Sensing*, 52(12):7674-7683.

(Received 09 December 2013; accepted 21 July 2014; final version 23 July 2014)

Optimal Land Cover Mapping and Change Analysis in Northeastern Oregon Using Landsat Imagery

Michael Campbell, Russell G. Congalton, Joel Hartter, and Mark Ducey

Abstract

The necessity for the development of repeatable, efficient, and accurate monitoring of land cover change is paramount to successful management of our planet's natural resources. This study evaluated a number of remote sensing methods for classifying land cover and land cover change throughout a two-county area in northeastern Oregon (1986 to 2011). In the past three decades, this region has seen significant changes in forest management that have affected land use and land cover. This study employed an accuracy assessment-based empirical approach to test the optimality of a number of advanced digital image processing techniques that have recently emerged in the field of remote sensing. The accuracies are assessed using traditional error matrices, calculated using reference data obtained in the field. We found that, for single-time land cover classification, Bayes pixel-based classification using samples created with scale and shape segmentation parameters of 8 and 0.3, respectively, resulted in the highest overall accuracy. For land cover change detection, using Landsat-5 TM band 7 with a change threshold of 1.75 standard deviations resulted in the highest accuracy for forest harvesting and regeneration mapping.

Introduction

Remote sensing technologies are unparalleled in their ability to monitor and analyze Earth's natural resources rapidly, cost-effectively, and with ever-increasing levels of precision and accuracy (Jensen, 2005). Although a number of high spatial resolution imagery platforms have emerged in recent years (e.g., Ikonos, QuickBird), the Landsat program has greatly benefited the remote sensing community by providing consistently high quality, medium spatial resolution imagery since 1972 (Green, 2006). Landsat-5 Thematic Mapper (TM) has proven particularly valuable, having contributed almost 30 years worth of essentially uninterrupted data (well beyond its expected life span of three years) at a bi-monthly temporal resolution (Chander and Markham, 2003). With Landsat data now freely available, the potential for remote sensing studies of all kinds has exploded as indicated by a 60-fold increase in data downloads since January, 2009 (NASA).

Central to the study of natural resource management is the ability to monitor changes in the landscape over time. The remote sensing community is constantly seeking newer and better ways to accomplish this very goal. Programs like the

National Land Cover Database (NLCD) are extremely valuable in providing a baseline of data which can be utilized in studies spanning an array of disciplines (Homer *et al.*, 2004). Additionally, the NLCD provides a generalized framework by which similar land cover assessments can be accomplished, including a tried-and-true methodology for land cover change analysis (Xian *et al.*, 2009). Similarly, the National Oceanic and Atmospheric Administration's (NOAA) Coastal Change Analysis Program (C-CAP) has informed this study and others by suggesting a number of standardized techniques by which land cover change can be monitored (Dobson *et al.*, 1995).

Traditionally, land cover mapping and analysis was performed on a pixel basis, i.e., a purely spectral approach wherein reflectance values for each pixel (and derivative information) of an image are the sole basis for classifying the imagery into a map. Within the last decade, object-based image analysis (OBIA, also called GEOBIA) has gained momentum in the remote sensing community (Blaschke, 2010). OBIA is based on segmenting images (i.e., grouping of pixels) into meaningful areas of spatial and spectral homogeneity called "objects" (Jensen, 2005). There is a great degree of user flexibility in generating these objects, guided by the manipulation of three parameters: scale, shape, and compactness to produce the optimal segmentation (e.g., Moller *et al.*, 2007). While the results tend to be case-specific, there appears to be general agreement that images can be over-segmented (objects are too small) and under-segmented (objects are too large) (Kim *et al.*, 2008; Holt *et al.*, 2009; Liu and Xia, 2010; MacLean and Congalton, 2011).

While the majority of OBIA studies tend to focus on feature extraction from high-resolution image data (e.g., Moran, 2010; Alganci *et al.*, 2013), a few have explored its applications on medium-resolution data sources such as Landsat (e.g., Geneletti and Gorte, 2003; Gamanya, 2009). An increasing number of studies are inquiring into the feasibility of using OBIA techniques to analyze land cover change (e.g., Im *et al.*, 2008; Chen *et al.*, 2012), but we have found few studies that link object-based land cover change and Landsat-5 TM data; Robertson and King (2011) is a notable exception.

While the remote sensing community has consistently pushed the limits of technical and computational capacity, seeking to develop new and improved methodologies, there is a critical need for the implementation of broad-scale monitoring operations that employ relatively simple, repeatable, and comprehensible processes. The focus of this study is precisely that: to establish an analytical and processing workflow for

Michael Campbell, Russell G. Congalton, and Mark Ducey are with the Department of Natural Resources & the Environment, 56 College Road, 114 James Hall, University of New Hampshire, Durham, NH 03824 (russ.congalton@unh.edu).

Joel Hartter is with the Department of Geography, University of New Hampshire, Durham, NH 03824, and currently at the Environmental Studies Program, University of Colorado Boulder, Boulder, CO 80309.

Photogrammetric Engineering & Remote Sensing
Vol. 81, No. 1, January 2015, pp. 37–47.
0099-1112/15/811–37

© 2014 American Society for Photogrammetry
and Remote Sensing
doi: 10.14358/PERS.81.1.37

a land cover change assessment upon which future studies can be based. In so doing we compare a number of well-established techniques with some new methods using a two-county area in northeastern Oregon as a case study.

The objectives of this study are to (a) evaluate pixel-based versus object-based image analysis for a generalized land cover change assessment of medium resolution data (i.e., Landsat Thematic Mapper) at the landscape level, (b) explore a variety of change analysis techniques including a modified principal component analysis to provide the best change maps of the area, and (c) use the optimal/best change analysis method to conduct an assessment of forest harvesting and regeneration from 1986 to 2011.

Study Area

Union and Baker Counties in northeastern Oregon, USA are large counties (13,267km²) with a combined population of 41,882, as of the 2010 Census (Figure 1). The region is characterized by a highly varied topography ranging from very mountainous terrain to expansive valley bottoms. Elevations range from 512 m at the lowest point to 2,915 m in the Wallowa Mountains. This region is relatively dry, receiving less than 50 cm average annual precipitation on the valley floors. Large water bodies are relatively few and far between, with only a few notably-sized lakes and rivers being present throughout the two-county area. As a result, forested environments are found only in the higher elevations, where temperatures remain consistently cool enough and the evapotranspirative balance enables tree growth. Despite this relative aridity, cropland is plentiful on the valley bottoms (hay, alfalfa), benefitting from heavy irrigation and fertile Mount Mazama ash soils. In between these two extremes, there is a dominance of two land cover types: grassland and shrub/scrub. The former tends to fill the elevation transition zone between cropland and forest and is often found in drier patches and south-facing slopes within the forested areas. The latter dominates the middle elevations of the southern portion of the study area, forming vast expanses of rolling hills dominated by sagebrush with little to no undergrowth. Almost 40 percent (5,111 km²) of the land in Union and Baker counties is public land, managed by the USDA Forest Service, 522 km² of which falls within the Eagle Cap Wilderness area. For the purposes of this study, elevations above 2,000 m and designated wilderness areas were removed from consideration because they are excluded from active forest management and wildfire suppression. It is believed that land cover changes that occur in these areas are simply the result of differential presence/absence of snow and/or other natural disturbance events (e.g., fire). Of interest to this study are only the anthropogenic effects on regional land cover.

Methods

Reference Data

Ground-based land cover reference data were collected between the months of June and August in 2011. Global Positioning System (GPS) data were captured using a Trimble YUMA unit and Esri ArcPad 10 software. Sample units were selected based on a few criteria: (a) the sample unit must be ≥ 90 m \times 90 m in size (3 \times 3 Landsat pixels) (as per the recommendation of Congalton and Green (2009)) (most units were significantly larger and then the collection was done at or near the center), (b) the entire area must be visually (and spectrally) homogeneous within the unit, (c) the areas must be heterogeneous between units (capturing maximum variability), and (d) the sampling units must be spatially distributed throughout the entire study area.

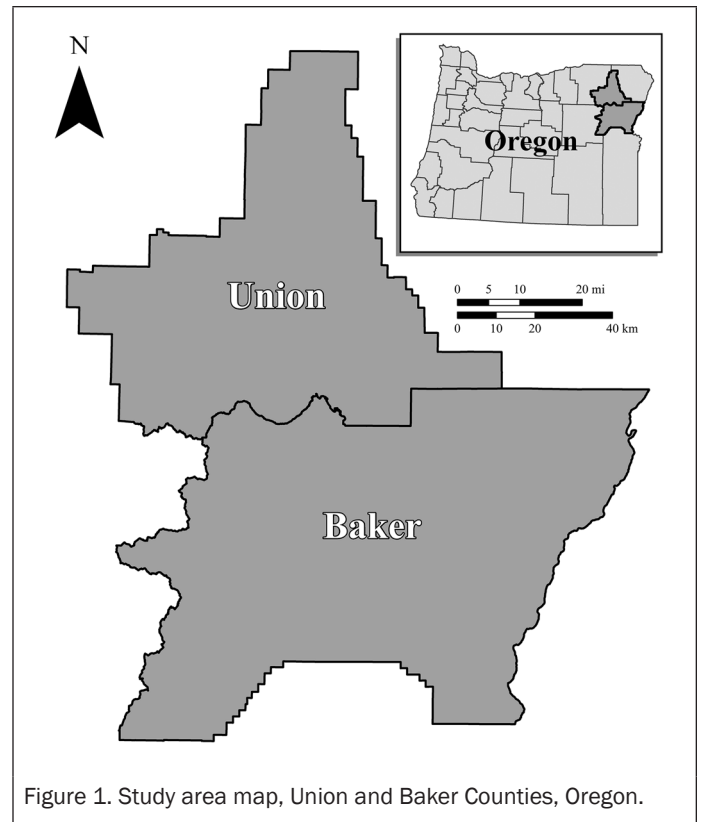


Figure 1. Study area map, Union and Baker Counties, Oregon.

A six-class land cover classification scheme was developed based on local knowledge, high resolution photo interpretation, and preliminary unsupervised classifications. These broad classes were designed to best capture the variability across this vast, heterogeneous landscape and to enable the analysis of generalized cover changes that occur in this region. Table 1 shows the land cover classes and their accompanying sample unit totals. The initial goal of collecting at least 100 sample units per class was realized for four out of the six classes. In order to avoid high sample spatial autocorrelation and to minimize spectral redundancy in land cover classes that were fairly sparsely distributed or were found in units of insufficient size, the goal of 100 sample units was not attained for the classes of water and developed. The reference samples were then randomly divided into two groups; data used to train the classification and data used to assess the thematic accuracy of the classification.

TABLE 1. LAND COVER REFERENCE DATA

LC Class	Total	Training	Accuracy
Cropland	100	50	50
Developed	80	40	40
Forest	100	50	50
Grassland	100	50	50
Shrub/scrub	100	50	50
Water	60	30	30

Image Data

Two Landsat-5 TM scenes were needed to encompass the vast majority of Union and Baker counties: Path 43, Row 28 (approximate scene center: 46°1'50.9"N, 117°46'19.2"W) and Path 43, Row 29 (44°36'43.9"N, 118°17'9.6"W). A temporal series of late spring to early fall images (May through October) with <5 percent cloud cover were obtained at a five-year interval

between the years of 1986 and 2011. In order to capture the seasonality of the highly moisture- and temperature-dependent land cover classes in this region, two images were used for each year of interest. An “early summer,” or growing season image and a “late summer,” or senescence image were used in the classification process (Table 2). As the late summer images ultimately played a more significant role in the classification process, every effort was made to utilize near-anniversary images at or around the end of August into early September. The exception to this rule was the year of 1986, during which the cloud-free, senescence image availability was limited to October. The time frames of the early summer images were more variable, given the typically higher cloud cover present during the growing season.

TABLE 2. LANDSAT-5 TM IMAGE DATES

Year	Early Summer	Late Summer
2011	07/09	08/26
2006	06/25	08/28
2001	05/10	08/30
1996	06/13	09/01
1991	07/02	09/04
1986	07/20	10/08

Image Preprocessing

For each image date, six of the seven spectral bands (Bands 1 to 5 and 7) were stacked together and adjacent path-rows were mosaicked together. In order to enhance image comparability between dates and reduce the effects of differential topographic illumination, topographic normalization was performed on these mosaicked images. The C-Correction algorithm (Meyer *et al.*, 1993) was selected as the normalization algorithm of choice, given its demonstrated effectiveness (Riaño *et al.*, 2003). The first step in the C-Correction process is to determine the magnitude of illumination across the entire study area, as defined by:

$$Illumination = \cos \gamma_i = \cos \theta_z \cos \alpha_s + \sin \theta_z \sin \alpha_s \cos(\delta_a - \delta_o) \quad (1)$$

where γ_i is the solar incidence angle relative to the sloped ground surface, θ_z is the solar zenith angle, α_s is the slope of the ground surface, δ_a is the solar azimuth angle, and δ_o is the aspect of the ground slope. In order to create an illumination surface, slope and aspect layers were derived from a USGS 30-m Digital Elevation Model (DEM). The solar zenith angle and azimuths for each image date were obtained from their respective Landsat header files. In order to assess the effect of illumination on the Landsat DN values, a random sample of 10,000 points was used to extract the spectral and illumination values at each point. A linear regression was run to determine the relative effect of illumination on the “brightness” of the pixel in each spectral band. The purpose of C-Correction (and other non-Lambertian normalization techniques) is to normalize the data such that the presumed positive relationship between illumination and DN value would be reduced to a null effect (Meyer *et al.*, 1993). In order to do so, the C-Correction algorithm was used:

$$DN_{\lambda i, h} = DN_{\lambda i} \left(\frac{\cos \theta_z + c_\lambda}{\cos \gamma_i + c_\lambda} \right) \quad (2)$$

where $DN_{\lambda i, h}$ is the DN value of a pixel (i) in a given spectral band (λ) on a horizontal surface (h) (with no influence of solar illumination), $DN_{\lambda i}$ is the value of that pixel on a sloped surface (subject to illumination influence), and c_λ is a

band-specific parameter defined by slope (m_λ) and y-intercept (b_λ) of the linear regression line between illumination and DN values, such that:

$$c_\lambda = \frac{b_\lambda}{m_\lambda} \quad (3)$$

To further enhance image comparability and eliminate the effects of atmospheric interference on image data, atmospheric correction was performed on all images. The COST corrected surface was calculated as follows (Chavez, 1988):

$$\rho = \frac{\left[\pi d^2 \left(L_{min} + \frac{DN_i (L_{max} - L_{min})}{DN_{max}} \right) - \left(L_{min} + \frac{DN_{min} (L_{max} - L_{min})}{DN_{max}} \right) - \left(\frac{0.01 d^2 \cos^2 \theta_z}{\pi E_{sun}} \right) \right]}{E_{sun} \cos^2 \theta_z} \quad (4)$$

where d is the sun-earth distance, L_{min} and L_{max} are spectral radiance calibration factors, DN_i is the DN value at a given pixel i , DN_{max} is the maximum possible DN value (255 for 8-bit data), DN_{min} is the band-specific minimum DN value found through an exploration of the layer histogram (smallest value with ≥ 1000 pixels), and E_{sun} is the solar spectral irradiance. L_{min} , L_{max} , E_{sun} , and d can all be found in Chander & Markham (2003).

In order to improve the accuracy of resultant classifications, a number of commonly used derivative image layers were generated from the topographically and atmospherically corrected images, including the Normalized Difference Vegetation Index (NDVI) and the Tasseled Cap transformation features (Brightness, Greenness, and Wetness).

The ten resulting bands (six raw, four derivatives) were then stacked together into a single image. For each year of interest, the early and late summer ten-band images were then stacked together to form a 20-band image. Finally, given the important link between land cover and topography in this region, slope, aspect, and elevation layers were stacked with the 20-band image to create a 23-band spectral and topographic image.

Image Segmentation and Classification

All subsequent image processing and classification took place using Trimble eCognition® Developer 8.7. An analysis was performed to determine the optimal segmentation parameters needed to attain the highest land cover classification accuracy. Of interest in the segmentation process were two parameters: (a) scale, and (b) shape. Using the multi-resolution segmentation algorithm, a series of image segmentations were performed on the 2011 23-band image. Assigning equal weights to all 23 spectral, derivative, and topographic bands, the image was segmented at every combination of the following parameter settings:

- Scale 2-20, intervals of 2
- Shape 0.0-0.5, intervals of 0.1.

There were a number of considerations that went into the determination of these test ranges. In terms of scale, a visual exploration of images segmented at a variety of scales facilitated the determination of 20 as a suitable high-end extreme. Beyond a scale of 20, the segments became exceedingly large and quickly began to lose their within-segment land cover homogeneity (i.e., at a scale of 30, a single polygon could contain Forest, Shrub/Scrub and Grassland). In terms of shape/color, it was believed that spatial qualities of a segment (shape) should never have a stronger influence on determining the size and shape of the segments than the 23 “spectral” bands (color). Accordingly, the high end of shape influence was determined to be 0.5 or 50 percent of the segmentation weight.

Each of the resulting segmentations was examined closely for the input parameters’ effects on segment size, and other spatial and spectral characteristics. Of interest to this study was not only the general effect of scale parameter on segment size, but also the relative variation in segment size that

resulted at each scale level. Accordingly, an analysis was performed to explore the relationship between segment size relative standard deviations (RSD) and the scale parameter. Because the segment sizes at large scale parameters will have significantly larger standard deviations, the normalized or relative standard deviation was deemed an appropriate representation of *within scale* segment size variation. RSD was calculated as such:

$$RSD = \frac{s_{ij}}{\mu_{ij}} \quad (5)$$

where s_{ij} is the sample standard deviation of segment size (in pixels) at a given scale parameter i and shape parameter j , and μ_{ij} is the mean size at those same parameters. The mean RSDs by scale parameter were then calculated.

Each of the image segmentations then underwent a separate land cover classification. Land cover classifications were performed in both a pixel- and object-based environment, using a non-parametric classification algorithm (Classification and Regression Tree (CART)) and a parametric classification algorithm (Bayes - Maximum Likelihood). These two approaches were selected because both are commonly used in land cover mapping. The Bayes-Maximum Likelihood classification technique is by far the most used traditional pixel-based method while CART has gained wide use in the last five years. Taking into account all of the segmentation and classification permutations, 240 classifications of the 2011 imagery were performed (10 scale \times 6 shape \times 2 environments \times 2 algorithms = 240 classifications in total). An important distinction between what was being tested in the pixel- and object-based environments must be made here. For both pixel- and object-based classifications, image segments were intersected with training data sample unit centroids (as created through field reconnaissance and photo interpretation) to determine the segment training units. This approach is not unlike using a region-growing algorithm or visually defining a training area boundary to maintain homogeneity in the training data selection. In both cases, the classification algorithm was trained with the resultant image segment sample data. In the object-based environment, this trained model was then applied to the remaining, unclassified image segments. In the pixel-based environment, however, the trained model was then applied to the remaining, unclassified pixels on the image, effectively ignoring the boundaries of the remaining segments. So, in essence, the impact of the segment characteristics has a twofold impact on the resultant classification accuracy (training samples *and* segment classification) in the object-based environment. In the pixel environment, however, the impact is singular, merely affecting the nature of the training data. Additionally, in the object-based environment, a host of segment features can be used to both train the model and classify the imagery, whereas pixels rely purely on the training data's per-band mean values and variances. The input features for object-based analysis were computed in eCognition as follows:

- Mean layer value of each of 23 bands by object
- Standard deviation for each band by object
- Skewness
- Brightness
- Maximum pixel value
- Minimum pixel value
- Mean of object inner border
- Mean of object outer border
- Contrast to neighboring pixels
- Mean difference to neighboring objects
- Hue, saturation, intensity transformations (early & late image dates, original image bands only)
- Gray Level Co-occurrence Matrix (GLCM) homogeneity
- Area
- Border length
- Compactness
- Roundness
- Rectangular fit
- Shape index

Accuracy Assessment

Error matrices (Congalton *et al.*, 1983) were constructed to determine which combination of segmentation parameters, analytical environment and classification algorithm attained the highest accuracies. Overall accuracies, class-specific user's and producer's accuracies, and Kappa were all calculated for each of the 240 classifications (Congalton and Green, 2009). An area-based error matrix (MacLean and Congalton, 2012) was used for the 120 object-based classifications. For each combination of CART versus Bayes and object versus pixel, a mean overall accuracy was computed across each scale and shape parameter. The combination of segmentation parameters, classification type, and classification algorithm that produced the highest overall accuracy for the 2011 land cover classification was selected for use in all subsequent classifications (2006, 2001, 1996, 1991, and 1986) following the change detection process described below. Lastly, each land cover map was filtered to a minimum mapping unit of 4,500 m² to remove mostly spurious single pixels remaining in the map.

Change Detection

In order to assess changes in the land cover, an image difference was performed. For each five-year interval of interest a ten-band difference image was created based on a simple pixel-by-pixel subtraction between sequential image dates (i.e., image differencing). Following a methodology introduced by Gong (1993), a principal components analysis (PCA) was performed on the ten-band difference image to create a single principal component (PC1) that would account for most of the variability (change) found in all ten bands. All ten change bands and PC1 were then used individually as the bases for change-based image segmentations to create 11 separate sets of "potential change segments" for comparison. Using two standard deviations from the mean as the base threshold for delineating change areas within each land cover class, segments were classified into change and non-change areas.

The 11 different change area delineations were the evaluated for correctness. Using a 15,000 ha heavily-logged area in northern Union County as a reference area, change polygons were manually digitized for the 2006 to 2011 interval at a scale of approximately 1:15 000. This scale was selected because it provided sufficient detail for the change analysis. These reference polygons were then compared to each of the 11 change classifications and an area-based 2 \times 2 change-no change error matrix was produced (Congalton and Green, 2009). With these error matrices, overall accuracies, user's accuracies (errors of omission) and producer's accuracies (errors of commission) were computed to determine which change image produced the best representation of "actual" change. Of interest to this study were change detection algorithms with high overall accuracies, and similar user's and producer's accuracies (in the interest of avoiding vast over- or under-estimation of change). The highest accuracy/best change detection band was then selected for further analysis.

Given the relatively high overall omission errors using the two-standard deviation threshold across all bands, an analysis of optimal threshold selection was performed using the most accurate single-band change detection method. Assuming that higher thresholds would only result in greater omission errors, four smaller standard deviation-based thresholds were tested for change detection accuracy: 1 SD, 1.25 SD, 1.5 SD and 1.75 SD. Using the same change detection accuracy methods described above, the highest accuracy threshold was chosen for use in the change detection and subsequent classification process.

Change Classification

With the optimal/best change detection methodology in place, a full change classification was performed using the C-CAP change classification protocol (Dobson *et al.*, 1995). According to this methodology, each image was classified separately backwards in time using training data from non-change

areas. For example, the 2011 classification was created using all of the original training data. However, given the land cover changes that occurred between 2006 and 2011, some of the training data collected in 2011 may no longer be valid because of new forest harvesting or younger trees growing into forests. As such, in order to classify the 2006 image, those data that fell within the change areas were removed and replaced via image interpretation. The new training dataset was then used to classify only those areas where change has occurred. This change area classification was then merged back with the non-change-area 2011 classification to form a wall-to-wall 2006 land cover classification. This process was repeated for each interval of interest.

Additionally, the same change detection accuracy assessments were performed on each interval, comparing the automatically-detected change areas to manually digitized areas of similarly high logging activity. Last, all of the land cover classifications were compared by five-year interval to determine the changes that have occurred in the landscape. Change matrices were created to assess the types of change occurring and their magnitudes. These changes were also assessed according to the land ownership type in which they fell, including public lands, private industrial lands, and private non-industrial lands. As the changes in the forested environment are of key importance to this study, the 6×6 land cover change matrices were reduced to simple 2×2 forest-non forest matrices to assess forest harvesting and regeneration trends, both across the entire landscape and across different ownership classes

Results and Discussion

The scale segmentation parameter has a substantial and direct effect on resultant image segment size. In order to obtain a quantitative estimate of this impact, an analysis was performed using the accuracy assessment sample data. For each segmentation performed at incremental levels of the scale parameter, the accuracy assessment sample data were used to obtain a mean value of segment size (in pixels). Figure 2 shows segment size displayed by scale parameter, with each point representing a different shape parameter input. A power function trend line was fitted to the model and a R^2 value was computed. There is a positive relationship between scale parameter and segment size at least up to a scale parameter of 20 for Landsat TM imagery. Beyond a certain scale parameter value, we anticipate that the distribution of resultant segment sizes will reach an asymptote. Where this leveling off occurs, however, will depend on image spatial extent and resolution, and no evidence of an asymptote is apparent over the range of the scale parameter used here.

A test was performed to explore the relationship between the scale parameter and segment size variability, as measured by the segment size RSD. The results of this test can be seen in Figure 3, where two notable trends emerge. The first is a peak RSD at the lowest scale parameter of 2 (RSD = 1.03). This suggests that at a scale of 2, high variability in segment size can be expected. This trend declines to a trough at scale of 8, where segment size was the most consistent. Following this low RSD, a slow steady rise in variability emerges as the segment size increases up to the scale parameter maximum of 20.

The manipulation of the shape parameter did not result in a predictable distribution of segment sizes. Instead, the tradeoff between shape and color parameters primarily affected the segments' spatial and spectral characteristics, as would be expected. For every combination of scale and shape parameter segmentations, a classification was performed using all four combinations of CART versus Bayes and pixel-based versus object-based classification. Henceforth, CART object-based

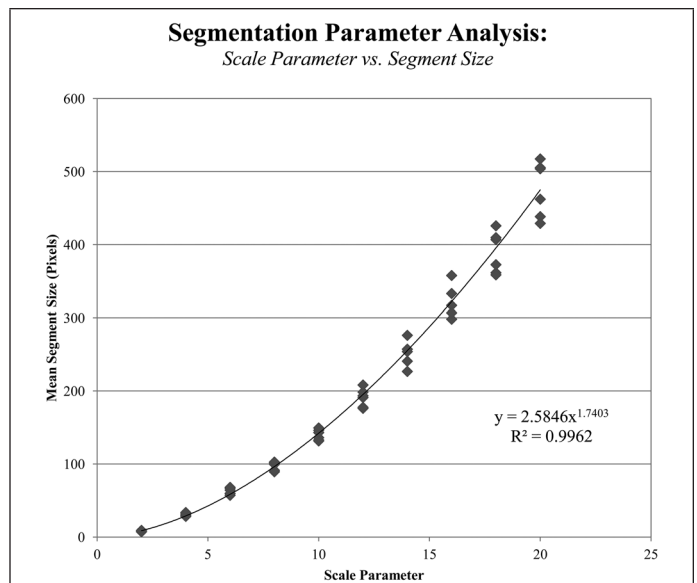


Figure 2. The effect of scale parameters on resultant segment size.

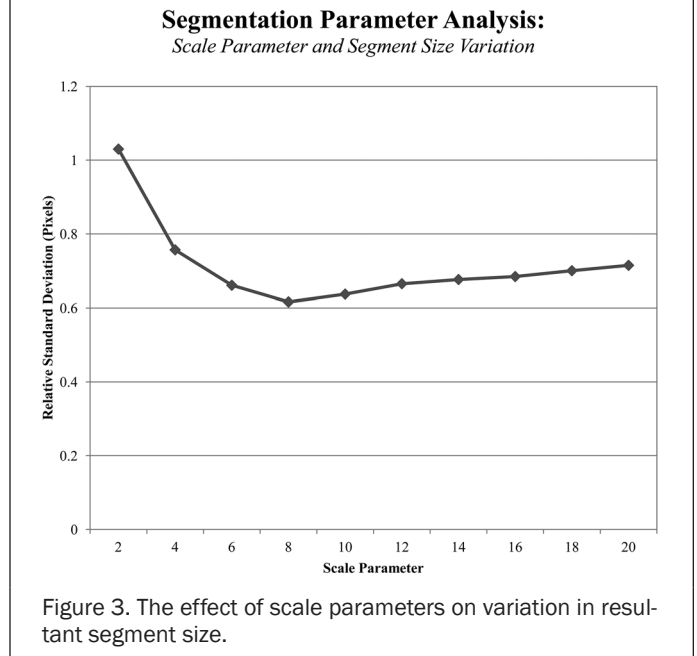


Figure 3. The effect of scale parameters on variation in resultant segment size.

= CO, CART pixel-based = CP, Bayes object-based = BO, and Bayes pixel-based = BP. As a result, 240 classifications in all were performed and their thematic accuracies were assessed using the traditional error matrix (Congalton *et al.*, 1983). The overall accuracies for CO, CP, BO and BP were averaged for each different scale parameter segmentation. The resulting mean accuracies can be seen in Figure 4. In every case, BP produced the highest classification accuracies, with a peak at a scale parameter of 8 and a mean overall accuracy of 90.68 percent. Interestingly, CP, also pixel-based, although consistently less accurate than BP, shares a similar trend, albeit less smooth, with a peak occurring at or around a scale of 8 and a trough at 18. The two object-based classifications, CO and BO similarly share a generalized trend in accuracy across the range of scale parameters. In both cases, there appears to be a fairly distinct positive relationship between the scale parameter and overall classification accuracy. The relationship is certainly stronger in BO than in

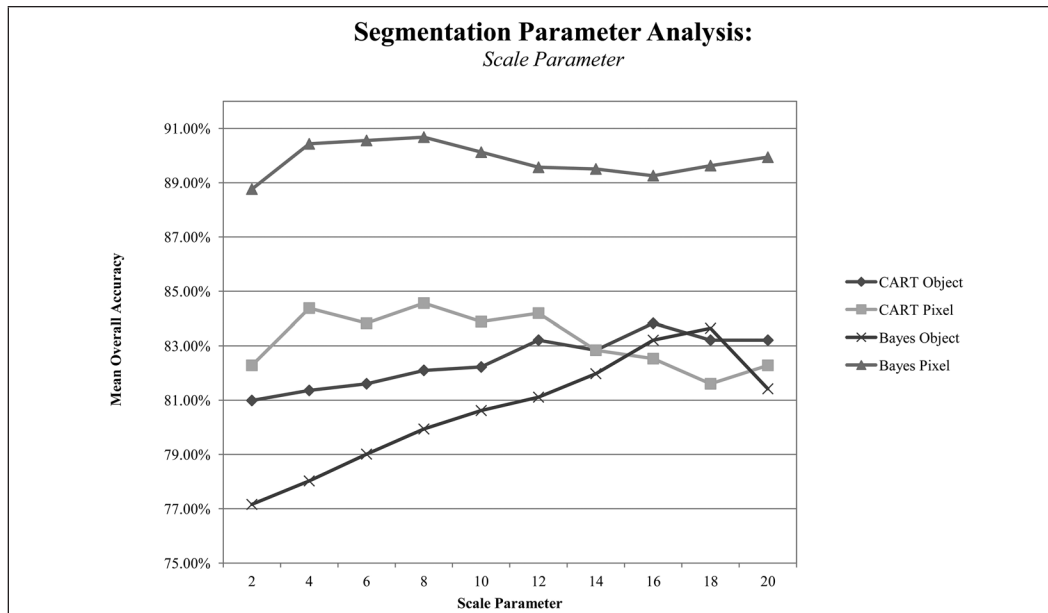


Figure 4. Average overall accuracies of CO, CP, BO, and BP across the range of scale parameters.

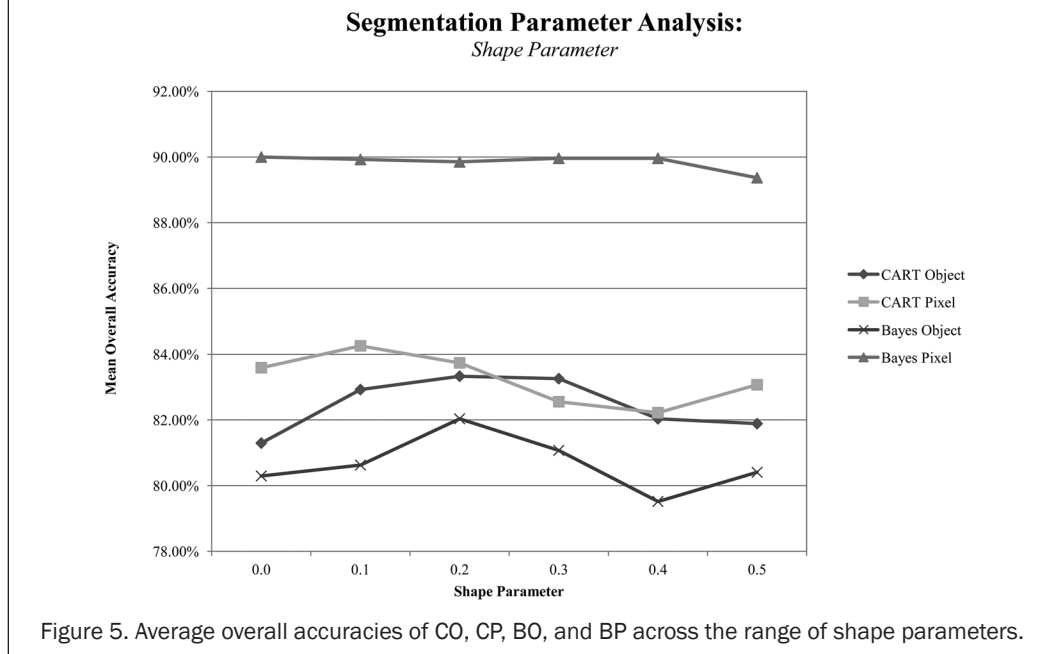


Figure 5. Average overall accuracies of CO, CP, BO, and BP across the range of shape parameters.

CO, but in BO there is a sharp decrease in accuracy at the very last scale parameter tested, 20. While BP greatly outperformed CP, CO almost exclusively outperformed BO, if only slightly.

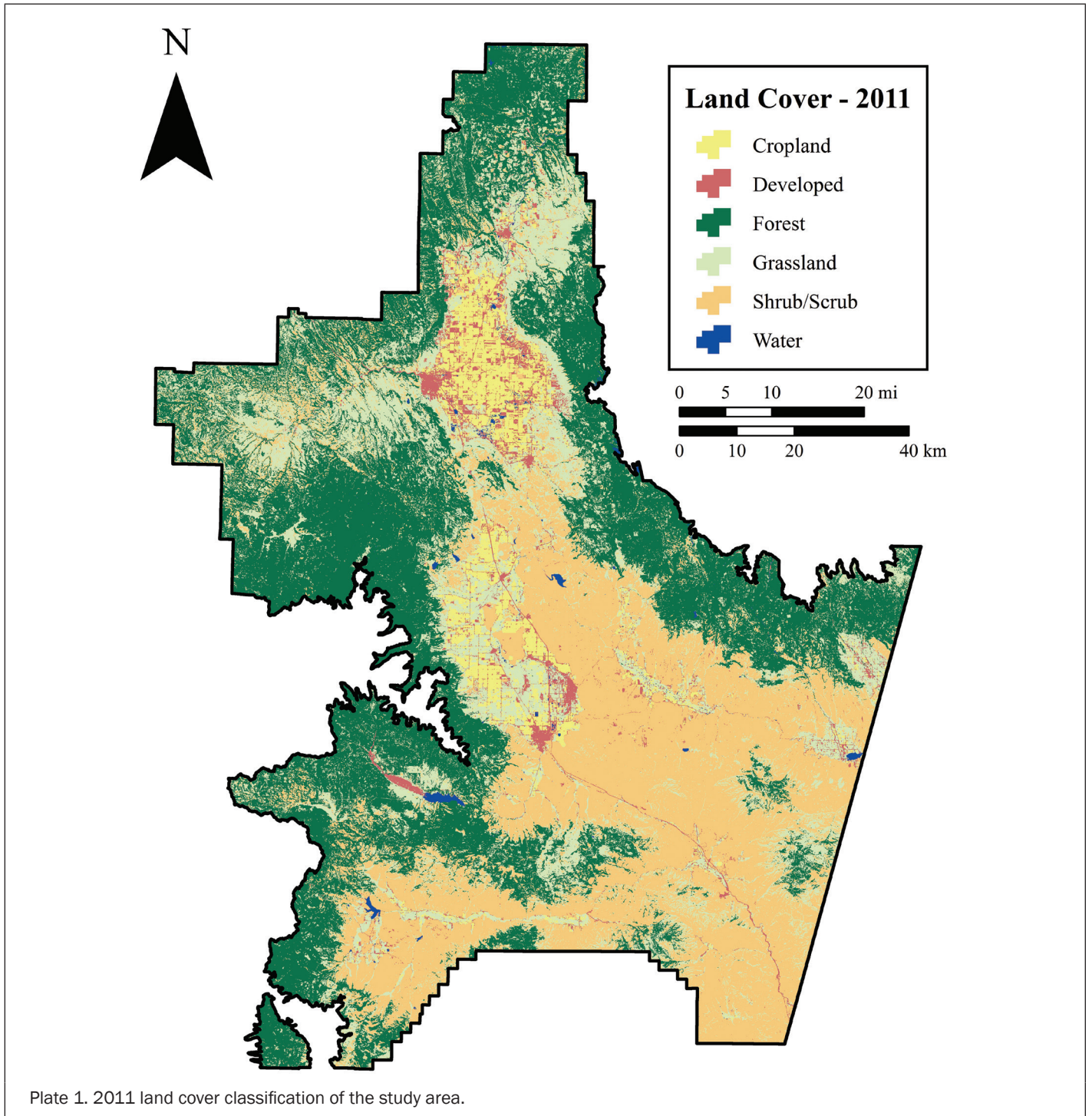
Similarly, the overall accuracies for CO, CP, BO, and BP were averaged for each of the different shape parameter segmentations. The resulting mean accuracies can be seen in Figure 5. It is important to note that Figures 4 and 5 should be considered together, rather than in isolation of one another, particularly when comparing *between classification method* accuracies, because these results tend to be similar across the entire ranges of scale and shape parameters, with the order of descending accuracy being roughly equivalent to BP (best), CP, CO, and BO (worst). That being said, these graphs do function as good indicators of *within classification method* accuracies. The trend lines of scale versus accuracy themselves are believed to be the most revealing. Accordingly, some important trends emerge in Figure 5 as well. The most accurate method,

BP, appears to function almost entirely independent of shape, with functionally equal accuracies across the board. However, the marginally highest mean accuracy was produced at a shape parameter of 0.3 (accuracy of 89.96 percent). Conversely, CP, CO, and BO all appear to have an accuracy peak in the 0.1 to 0.3 ranges and a trough in the 0.4 to 0.5 range, with a slight uptick in accuracy at shape 0.5.

Taking all of these accuracies into consideration, a selection of segmentation parameters (scale and shape), image analysis environment (pixel versus object) and classification algorithm (CART versus Bayes) was made. The optimal combination was found to be Bayes pixel-based classification with training samples segmented at a scale of 8 and a shape of 0.3 (overall accuracy of 91.48 percent, and Kappa = 0.897). The error matrix with class-specific user's and producer's accuracies can be seen in Table 3. The final 2011 land cover classification can be seen in Plate 1.

TABLE 3. ERROR MATRIX FOR HIGHEST ACCURACY LAND COVER CLASSIFICATION (SAMPLE UNIT TALLIES)

		Reference Data						Sum Units	User Accuracy
		Cropland	Developed	Forest	Grassland	Shrub/Scrub	Water		
Map Data	Cropland	43	1	0	1	0	0	45	95.56%
	Developed	4	37	0	2	0	0	43	86.05%
	Forest	0	0	49	0	1	0	50	98.00%
	Grassland	2	1	1	40	1	0	45	88.89%
	Shrub/Scrub	1	1	0	7	48	0	57	84.21%
	Water	0	0	0	0	0	30	30	100.00%
Sum Units		50	40	50	50	50	30	270	
Producer Accuracy		86.00%	92.50%	98.00%	80.00%	96.00%	100.00%		91.48%



To determine the optimal change detection technique, the first change interval of interest, 2006 to 2011 was used for analysis. Ten separate difference images and one principal components image were tested to see which produced the best change detection accuracy. The PCA was performed on the ten-band difference image to capture as much change across all of the input bands as possible into a single band (approximately 70 percent of the change variance is captured in PC1). Using the most accurate 2011 land cover classification, a within-class segmentation was performed for each of the 11 change bands of interest (ten difference bands and PC1). From the resultant segments, a distribution of class-specific change values emerged. For each band and class, the change distributions resembled a normal distribution and the class-specific differences visualized in the spread of change magnitudes. In order to determine change thresholds, the class-specific change means and standard deviations were calculated for each band.

Using two standard deviations from the mean as a base threshold for change, each band was then tested for its ability to accurately detect change. These class-specific band threshold values were applied to the binary classification of change versus non-change for the 2006 to 2011 interval. As a result, 11 different classifications were performed and assessed for accuracy using an error matrix approach. Band 7 (middle infrared) was determined to be the optimal band for use in the change analysis given the preferential emphasis placed on minimizing errors of omission and highest overall performance. Given that change omission and commission errors can be seen as a direct product of the change threshold used (i.e., a higher standard deviation-based change threshold will likely produce greater omission error and a lower threshold will produce increased errors of commission), band 7 was then further evaluated for a range of standard deviation change thresholds (1 SD to 2 SD, intervals of 0.25 SD). The results show that the best change analysis occurred at 1.75 SD, and this threshold was selected for all further use (Table 4).

TABLE 4. CHANGE DETECTION ERROR MATRIX FOR BAND 7, THRESHOLD 1.75 SD (AREA IN HECTARES)

		Reference		Sum Area	User
		Change	No Change		
Map	Change	1,356.38	415.69	1,772.07	76.54%
	No Change	389.74	14,726.92	15,116.67	97.42%
Sum Area		1,746.13	15,142.62	16,888.74	
Producer		77.68%	97.25%		95.23%

Band 7 was used to classify change and non-change areas for each five-year interval of interest iteratively backwards in time starting with 2006 to 2011 and ending with 1986 to 1991. Based on this change analysis, land cover classifications were performed only on the detected change areas for each year. These change area classifications were then merged with the corresponding year's classification to attain wall-to-wall classification. The resulting classifications were intersected to assess class-specific land cover classification changes. Areas were calculated in hectares to determine change magnitude.

These change maps were then simplified to forest and non-forest changes in order to further study forest harvesting and regrowth patterns. Four combinations resulted: forest to forest (non-change), forest to non-forest (change), non-forest to non-forest (non-change), and non-forest to forest (change). Forest to non-forest changes were assumed to be the result of harvesting and non-forest to forest changes were assumed to represent forest regeneration. These totals were then intersected with land ownership data to determine owner-specific

changes. The forest to non-forest totals and ownership breakdown can be seen in Figure 6. A few definitive trends emerge. In terms of overall forest harvesting, the first two time intervals (1986 to 1991 and 1991 to 1996) saw very similar total hectares removed at slightly below 8,500 ha each. Following these early highs, a precipitous drop occurred between 1996 and 2001, when only 2,126 ha were removed in total. The final two intervals saw consistently increasing totals with 5,477 ha removed between 2001 and 2006, and 9,227 ha removed in the most recent interval, reaching the highest total of any interval tested. In terms of ownership-specific patterns, some clear trends can be seen as well. A notable decrease in harvesting on public land occurred between 1986 and 2001 (1986 to 1991: 6,242 ha; 1991 to 1996: 3,434 ha; 1996 to 2001: 749 ha), followed by a less aggressive, steady increase between 2001 and 2011. Harvesting on private industrial land saw significant increases between the 1986 to 1991 interval (402 ha removed) and the 2006 to 2011 interval (3,975 ha removed). Private non-industrial land typically saw relatively low harvesting totals, with the one exception being between 1991 and 1996 where 3,603 ha were removed.

These results however, should be viewed with the understanding of differential total forest land ownership. For example, in 2011, there were 418,144 ha of forested land throughout the entire study area, 312,284 ha (74.68 percent) is owned by public entities (most of which is USFS), followed by private, non-industrial land owners (77,732 ha, 18.59 percent), and last, private industrial (28,127 ha, 6.73 percent). Accordingly, these removal totals were divided into total forested land ownership to compute the "normalized" or percent by ownership removal. The resulting removal percentages can be seen in Figure 7.

The forest and non-forest change classification process not only yields change areas that suggest forest removal, but additionally forest areas that are regenerated (non-forest to forest). From the forest management perspective, this variable is in many ways as valuable, if not more so, than the harvesting totals. Accordingly, forest regeneration totals were calculated across the entire study area and, again, broken down by land ownership class. The results of these analyses can be seen in Figure 8. The total forest regeneration across all ownership classes does not take on any major trend in the positive or negative direction, with the exception of a steep decline in the 1991 to 1996 interval, which makes sense, given the heavy harvesting that occurred in that year. The ownership-specific trends, however, are of interest. For instance, again with the exception of 1991 to 1996, regeneration on public land has steadily declined. Conversely, both kinds of private land have seen somewhat steady growth in forest regeneration from the 1991 to 1996 interval to 2006 to 2011.

Conclusions

This study had a wide-ranging set of objectives, in terms of both remote sensing methods and real world applications; the study utilized a largely exploratory approach to determining the optimal conditions for conducting efficient land cover classification and change detection. In incremental fashion, each procedure in the process was carefully vetted for optimal accuracy. Only when conditions were met to attain an acceptably high analytical accuracy was forward progress made. While the specific results of any remote sensing study are only immediately applicable to that study, certain broader trends can emerge upon which future analyses can be based. The incremental approach used here can function not only as a framework for future investigation, but because the methods were explored using such a wide range of input parameters, a number of the specific results can help inform future research as well.

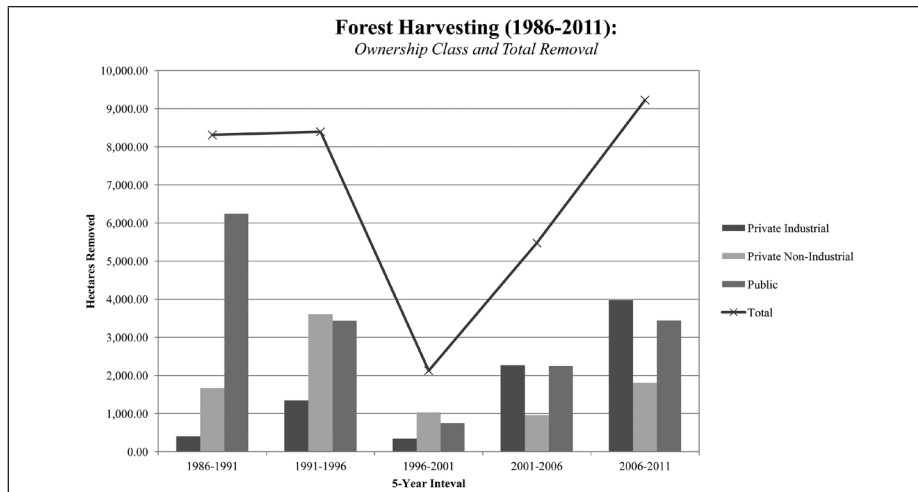


Figure 6. Total harvesting by five-year interval broken down by land ownership class.

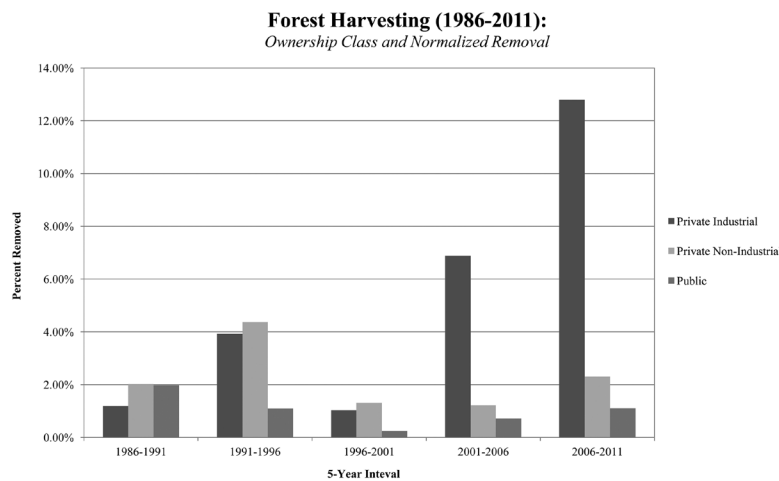


Figure 7. Percentage of total forested land removed by ownership by five-year interval.

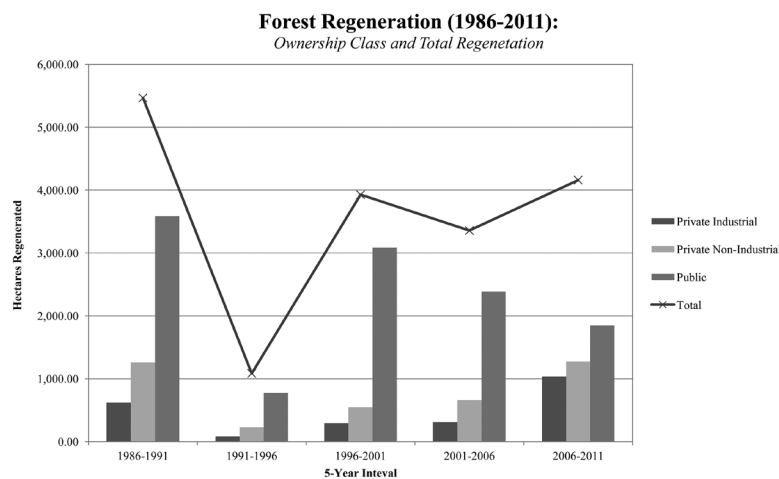


Figure 8. Total regeneration by five-year interval broken down by land ownership class.

Of particular interest in this study is the analysis of pixel-based versus object-based image classification. While OBIA has become often used for high spatial resolution imagery, few studies have documented the utility of using OBIA on medium resolution image datasets such as Landsat-5 TM. This absence is not without justification; Landsat's 30 m pixels are, in many ways, image objects in their own right and have

historically been very successful in land cover analyses of all kinds. For a land cover study conducted over a relatively small area with a fairly detailed classification scheme, a 30 m pixel may sufficiently reduce the spectral noise contained within an image to produce accurate, functional ground units, despite their indiscriminate spatial placement. At the regional or landscape scale with more generalized classes

such as this study, however, perhaps the noise reduction caused by grouping of pixels over large areas (OBIA) would produce a more desirable result. This study was not intended to determine outright whether pixel-based analysis or object-based analysis is preferable. The results depended heavily on the classification algorithm used. Across the entire range of scale and shape parameters, Bayes pixel-based classification significantly outperformed Bayes object-based classification and had the highest overall accuracy. However, the relationship between CART pixel-based and object-based classifications was much more heavily influenced by the segmentation parameters used.

Finally, detailed, quantitative accuracy assessment formed the basis for not only the individual date land cover maps, but also the land cover change detection analysis and the detailed forest harvesting and regeneration conducted as part of this study. The primary application of interest in this study involved detecting and classifying changes in the forested environments of a two-county area in northeastern Oregon. The results highlight predominant trends in overall and ownership-specific changes in total forested area throughout this region over a 25-year time span at five-year intervals. Three main trends in forest harvesting practices emerge. In terms of overall change, we see that the greatest amount of forest removal occurred in the most recent interval, 2006 to 2011; in total, 9,227 ha of forest were removed. This total decreases to 1996 to 2001 where an estimated 2,127 ha of forest was removed. This total then climbs back up to a plateau for the intervals of 1986 to 1991 and 1991 to 1996 where 8,311 ha and 8,394 ha were removed, respectively. In addition to the overall forest harvesting trends, two ownership-specific trends emerge: (a) an increase in private industrial harvesting, and (b) an initial decrease in public land harvesting followed by a slower increase from 1986 to 2011. These trends are likely the result of a variety of factors. Speculation into the social, economic, and political mechanisms at work that have resulted in this shift from predominantly public land harvesting to primarily private industrial warrants an entire study in and of itself. However, one important geospatial factor that is immediately relevant is that all timberlands are not equally harvestable. The ability to harvest timber from a given location in a forest depends primarily on three factors: (a) accessibility, (b) topography, and (c) rules and regulations. Accessibility is simply the ability for a logger to reach a given area of timber, i.e., a factor that is controlled by the specific locations and densities of the forest road network. Closely related to accessibility is the quality of the terrain, or topography, of the timberlands. Some areas are simply too steep or otherwise impeded by natural, geologic features to harvest timber. And last, there are a variety of legislative and regulatory road blocks to a variety of logging operations, particularly relating to the preservation of wilderness and protection of endangered species. For instance, riparian environments are often protected against logging due to their importance in the preservation of certain fish species that could be harmed by increased runoff and/or other industrial pollutants thought to be caused by logging operations. Taking all of these factors together, a scenario can readily be imagined wherein private industrial timberlands, which tend to be on lower-lying elevations with less dramatic topography, having higher road densities and fewer regulatory impediments, are simply more harvestable than, for example, public lands. Accordingly, this study reveals ownership-specific trends that are related to the degree to which forested areas are harvestable.

Acknowledgments

Funding for this project, The Communities and Forests in Oregon, (CAFOR) is from the Disaster Resilience for Rural Communities Program, which is part of the National Institute of Food and Agriculture program of the US Department of Agriculture (Award No. 2010-67023-21705). We greatly appreciate collaboration with Mike Shaw at Oregon Department of Forestry, Nils Christoffersen and everyone at Wallowa Resources, Paul Oester and Bob Parker at Oregon State University College of Forestry Extension, and Ken Gebhardt and others at the USDA Forest Service and Wallowa - Whitman National Forest. Other project team members Dan Maynard, Larry Hamilton, and Forrest Stevens contributed significantly to the project. Finally, we acknowledge the efforts of the three anonymous reviewers and Assistant Editor Jie Shan for their helpful suggestions and comments that improved this paper.

References

- Alganci, U., E. Sertel, M. Ozdogan, and C. Ormeci, 2013. Parcel-level identification of crop types using different classification algorithms and multi-resolution imagery in southeastern Turkey, *Photogrammetric Engineering & Remote Sensing*, 79(11):1053–1065.
- Blaschke, T., 2010. Object based image analysis for remote sensing, *ISPRS Journal of Photogrammetry and Remote Sensing*, 65:2–16.
- Byrne, G.F., P.F. Crapper, and K.K. Mayo, 1980. Monitoring land-cover change by principal component analysis of multitemporal Landsat data, *Remote Sensing of Environment*, 10:175–184.
- Chander, G., and B. Markham, 2003. Revised Landsat-5 TM radiometric calibration procedures and post calibration dynamic ranges, *IEEE Transactions on Geoscience and Remote Sensing*, 41(11):2674–2677.
- Chavez, Jr., P.S., 1988. An improved dark-object subtraction technique for atmospheric scattering correction of multispectral data, *Remote Sensing of Environment*, 24:459–479.
- Chavez, Jr., P.S., 1996. Image-based atmospheric corrections - Revisited and improved, *Photogrammetric Engineering & Remote Sensing*, 69(2):1025–1036.
- Chen, G., G.J. Hay, L.M.T. Carvalho, and M.A. Wulder, 2012. Object-based change detection, *International Journal of Remote Sensing*, 33(14):4434–4457.
- Congalton, R., R. Oderwald, and R. Mead, 1983. Assessing Landsat classification accuracy using discrete multivariate analysis statistical techniques, *Photogrammetric Engineering & Remote Sensing*, 49(12):1671–1678.
- Congalton, R.G., and K. Green, 2009. *Assessing the Accuracy of Remotely Sensed Data: Principles and Practices*, Second edition, CRC Press, Boca Raton, Florida, 208 p.
- Dobson, J.E., E.A. Bright, R.L. Ferguson, D.W. Field, L.L. Wood, K.D. Haddad, H. Iredale, J.R. Jensen, V.V. Klemas, R.J. Orth, and J.P. Thomas, 1995. NOAA Coastal Change Analysis Program (CCAP): Guidance for regional implementation, *NOAA Technical Report NMFS 123*, US Dept. of Commerce, Seattle, Washington.
- Gamanya, R., P. De Maeyer, and M. De Dapper. 2009. Object-oriented change detection for the City of Harare, Zimbabwe, *Expert Systems with Applications*, 36:571–88.
- Geneletti, D., and B.G.H. Gorte, 2003. A method for object-oriented land cover classification combining Landsat TM data and aerial photographs, *International Journal of Remote Sensing*, 24(6):1273–1286.
- Gong, P., 1993. Change detection using principal component analysis and fuzzy set theory, *Canadian Journal of Remote Sensing*, 19:22–29.
- Green, K., 2006. Landsat in context: The land remote sensing business model, *Photogrammetric Engineering & Remote Sensing*, 72(10):1147–1153.
- Holt, A.C., E.Y.W. Seto, T. Rivard, and P. Gong, 2009. Object-based detection and classification of vehicles from high-resolution aerial photography, *Photogrammetric Engineering & Remote Sensing*, 75(7):871–880.

- Homer, C., C. Huang, L. Yang, B. Wylie, and M. Coan, 2004. Development of a 2001 National Land Cover Database for the United States, *Photogrammetric Engineering & Remote Sensing*, 70(7):829–840.
- Im, J., J.R. Jensen, and J.A. Tullis, 2008. Object-based change detection using correlation image analysis and image segmentation, *International Journal of Remote Sensing*, 29(2):399–423.
- Jensen, J.R., 2005. *Introductory Digital Image Processing: A Remote Sensing Perspective*, Third edition, Pearson Prentice Hall, Upper Saddle River, New Jersey, 526 p.
- Kim, M., M. Madden, and T. Warner, 2008. Estimation of optimal image object size for the segmentation of forest stands with multispectral IKONOS imagery, *Object-Based Image Analysis - Spatial Concepts for Knowledge-driven Remote Sensing Applications* (T. Blaschke, S. Land, and G.J. Hay, editors), Springer-Verlag, Berlin, pp.291–307.
- Lambin, E.F. and A.H. Strahler, 1994. Change-vector analysis in multitemporal space: A tool to detect and categorize land-cover change processes using high temporal-resolution satellite data, *Remote Sensing of Environment*, 48:231–244.
- Liu, D., and F. Xia. 2010. Assessing Object-Based Classification: Advantages and Limitations, *Remote Sensing Letters*, 1:187–94.
- MacLean, M.G., and R.G. Congalton, 2011. Investigating issues in map accuracy when using an object-based approach to map benthic habitats, *GIScience and Remote Sensing*, 48(4):457–477.
- MacLean, M.G., and R.G. Congalton, 2012. Map accuracy assessment issues when using an object-oriented approach, *Proceedings of the American Society for Photogrammetry and Remote Sensing 2012 Annual Conference*, unpaginated CD-ROM.
- Mahlny, A.S., and B.J. Turner, 2007. A comparison of four common atmospheric correction methods, *Photogrammetric Engineering & Remote Sensing*, 73(4):361–368.
- Meyer, P., K.I. Itten, T. Kellenberger, S. Sandmeier, and R. Sandmeier, 1993. Radiometric corrections of topographically induced effects on Landsat TM data in an alpine environment, *ISPRS Journal of Photogrammetry and Remote Sensing*, 48(4):17–28.
- Möller, M., L. Lymburner, and M. Volk, 2007. The comparison index: A tool for assessing the accuracy of image segmentation, *International Journal of Applied Earth Observation and Geoinformation*, 9:311–321.
- Moran, E.F., 2010. Land cover classification in a complex urban-rural landscape with QuickBird imagery, *Photogrammetric Engineering & Remote Sensing*, 76(10):1159–1168.
- Moran, M.S., R.D. Jackson, P.N. Slater, and P.M. Teillet, 1992. Evaluation of simplified procedures for retrieval of land surface reflectance factors from satellite sensor output, *Remote Sensing of Environment*, 41:169–184.
- National Aeronautics and Space Administration (NASA), “Landsat 7” - *The Landsat Program*, URL: <http://landsat.gsfc.nasa.gov/about/landsat7.html> (last date accessed: 18 November 2014).
- Radoux, J., P. Bogaert, D. Fasbender, and P. Defourny, 2010. Thematic accuracy assessment of geographic object-based image classification, *International Journal of Geographical Information Science*, 25(6):895–911.
- Riaño, D., E. Chuvieco, J. Salas, and I. Aguado, 2003. Assessment of different topographic corrections in Landsat-TM data for mapping vegetation types, *IEEE Transactions on Geoscience and Remote Sensing*, 41(5):1056–1061.
- Robertson, L.D., and D.J. King. 2011. Comparison of pixel- and object-based classification in land cover change mapping, *International Journal of Remote Sensing*, 32:1505–29.
- Xian, G., C. Homer, and J. Fry, 2009. Updating the 2001 National Land Cover Database land cover classification to 2006 using Landsat imagery change detection methods, *Remote Sensing of Environment*, 113:1133–1147.

(Received 07 March 2014; accepted 30 July 2014; final version 08 August 2014)

Reliable Spatial Relationship Constrained Feature Point Matching of Oblique Aerial Images

Han Hu, Qing Zhu, Zhiqiang Du, Yeting Zhang, Yulin Ding

Abstract

This paper proposes a reliable feature point matching method for oblique images using various spatial relationships and geometrical information for the problems resulted by the large view point changes, the image deformations, blurring, and other factors. Three spatial constraints are incorporated to filter possible outliers, including a cyclic angular ordering constraint, a local position constraint, and a neighborhood conserving constraint. Other ancillary geometric information, which includes the initial exterior orientation parameters that are obtained from the platform parameters and a rough DEM, are used to transform the oblique images geometrically and reduce the perspective deformations. Experiment results revealed that the proposed method is superior to the standard SIFT regarding both precision and correct matches using images obtained by the SWDC-5 system.

Introduction

Beginning in 2000, oblique aerial camera systems garnered attention from the photogrammetry community due to their ability to capture the facades of buildings and their ability to be briefly interpreted (Petrie, 2009). Many penta-view camera systems that feature four 45° oblique cameras and one nadir camera, including Pictometry (Gerke and Kerle, 2011), MIDAS (Madani, 2012), and SWDC-5 that are used in this paper, have collected numerous datasets. However, traditional photogrammetry techniques and software are designed primarily for nadir images and are difficult to adapt for oblique aerial images. New challenges have been posed to photogrammetry practitioners to integrate all of the images to extract more compact and accurate information, especially for oblique views (Jacobsen, 2009; Nyaruhuma *et al.*, 2012; Fritsch and Rothermel, 2013).

Exterior orientation (EO) parameters for the images are necessary prior to 3D reconstruction (Gerke, 2009), texture mapping (Wang *et al.*, 2008), position measurement (Xiong *et*

al., 2014), and other mapping applications. Because all of the cameras are installed on a rigid platform and held stationary after manufacturing, the bore-sight angles and translations (called platform parameters) between the nadir view and the four oblique views are fixed in the ideal condition (Wiedemann and Moré, 2012) and are calibrated using retro-reflect coded targets in the calibration field (Fraser, 1997). In theory, only the EO parameters for the nadir images need to be estimated in the bundle adjustment. However, due to reinstallations, limitations in mechanical manufacturing, and possible asynchronous exposures among different cameras, the platform parameters are not stable and can only be considered as fixed in a single flight (Jacobsen, 2009). In this situation, a combined bundle adjustment with both the nadir and oblique images in the same block are necessary, which requires sufficient tie points to sew the block together.

It turns out that feature matching between nadir images and oblique images is astonishingly difficult because of the obvious difference in their appearances, which consists of occlusions, perspective deformations, light conditions, and blur that are caused by the wide baseline and large tilting angles (Yao and Cham, 2007; Yang *et al.*, 2012). Additionally, in production practice, an existing solution with traditional software is to process images for each camera separately and then manually select enough inter-camera tie points to assemble different blocks of images together. However, this solution is not only time consuming, but it is also prone to inter-camera inconsistencies due to the lack of accurate tie points.

To eliminate the drudgery of manual selection and to improve the quality of bundle adjustment, we propose to amend the standard feature matching process by injecting additional spatial relationships of feature points into the process to increase the reliability, rather than only using the appearance information of the images. Specifically, we propose a cyclic angular order constraint, a local position constraint and a neighborhood conserving constraint. Furthermore, the initial geometric information of the five cameras that is obtained from the global positioning system (GPS) and inertial measurement unit (IMU) onboard the aircraft, calibrated platform parameters, and a rough DEM are used to geometrically transform the images, in order to reduce the perspective deformations. In our previous work (Zhu *et al.*, 2007), a filter strategy using information content is proposed to improve the repeatability of the interest points and the reliability of the matches, which is also based on the appearance information. However, when the images are essentially dissimilar in appearance,

Han Hu, Zhiqiang Du, and Yeting Zhang are with the State Key Laboratory of Information Engineering in Surveying Mapping and Remote Sensing, Wuhan University, P.O. Box C310, 129 Luoyu Road, Wuhan, Hubei, 430079, P.R. China (huan@whu.edu.cn).

Qing Zhu is with the National-local Joint Engineering Laboratory of Spatial Information Technology for High-speed Railway Running Safety, Southwest Jiaotong University, P.R. China; and the State Key Laboratory of Information Engineering in Surveying Mapping and Remote Sensing, Wuhan University, P.R. China.

Yulin Ding is with the State Key Laboratory of Information Engineering in Surveying Mapping and Remote Sensing, Wuhan University, P.R. China, and the Institute of Space and Earth Information Science, The Chinese University of Hong Kong, Shatin, N.T., Hong Kong.

Photogrammetric Engineering & Remote Sensing
Vol. 81, No. 1, January 2015, pp. 49–58.
0099-1112/15/811–49

© 2014 American Society for Photogrammetry
and Remote Sensing
doi: 10.14358/PERS.81.1.49

the spatial relationships are more important cues that are responsible for reliable feature correspondence. Furthermore, the spatial relationship constraint has been confirmed to be a powerful method for wide baseline-dense matching in our previous work.

In the next section, feature matching methods based on appearance and spatial relationships are briefly introduced. Then, we present two core innovative steps of the proposed methods followed by information for the configurations of the oblique camera system and the datasets obtained. The performance of the proposed methods is subsequently evaluated leading to concluding remarks.

Related Works

In an early investigation of image matching, three fundamental properties of the correct correspondences were set up (Ullman, 1979): *Similarity*: the correspondences must be similar in appearance among the matching images. *Proximity*: the correspondences must have tenable spatial relationships. For example, in the situation of repeated patterns, images of textureless, spatial relationships provide clues for establishing correspondences or removing outliers among identical features. *Exclusion*: the final feature matches should be established one-on-one and can simply be enforced by cross check, which is a two-step procedure of forward and backward matching.

In the photogrammetry and computer vision communities, feature matching methods have been prosperous; most of these methods resorted to appearance information alone to identify correspondences. To the best of our knowledge, the earliest feature matching method dates to the Moravec (1981) corner detector and normalized cross correlation (NCC). Since then, the robust pyramid matching strategy (Wang, 1990) has been the software standard, which uses intersecting points to detect corners (Moravec, 1981; Förstner and Gülch, 1987; Harris and Stephens, 1988) and NCC to match the features from coarse to fine. In applications where accuracy is important, the least square matching (LSM) strategy is also mandatory for locating the matches in a sub-pixel position (Gruen, 1985). The sophisticated paradigm that uses pyramid matching and LSM is widely adopted in both aerial and close range applications. Liang and Heipke (1996) integrate an automatic relative orientation method with a modified Moravec detector and a coarse-to-fine matching strategy into their method. Several hundreds of well distributed correspondences are found, and the results indicate that internal accuracies reached less than 0.3 pixels, even in scanned digital images. Lerma *et al.* (2013) compare different matching strategies for close range applications, in which artificial retro-reflect targets are not used. They confirm that NCC and LSM result in better accuracies for images with near parallel bore-sight directions.

The methods that match features with NCC can be considered to use the appearance information in a fixed square window around the corners. Consequently, NCC is essentially sensitive to scale and rotation changes (Lowe, 2004). Lindeberg (1993) proposes to detect blob-like features that are stable in the scale space, and the same author also provides a practical solution to build the scale space that is the Laplacian of Gaussian (Lindeberg, 1998), which has triggered the development of numerous invariant features. Based on the scale space theory, Lowe (2004) presents the milestone work of scale invariant feature transform (SIFT), which detects features in the scale space using the difference of Gaussian and describes the image blob with the histograms of gradients. Mikolajczyk and Schmid (2005) compare various features against different situations and claim that SIFT presents the best performances, except for the case of large affine deformations.

Some approaches attempt to restrict the features to be affine-invariant (Matas *et al.*, 2004; Mikolajczyk and Schmid, 2004); however, these approaches can cause either decreases in the amount of detected features or performance losses in the cases of small affine deformations (Lowe, 2004). Attempts to surpass the performance of SIFT have focused on descriptor dimensions (Ke and Sukthankar, 2004), speed (Bay *et al.*, 2008) and affinity (Morel and Yu, 2009).

The methods described above use appearance information either in a square window or in a salient blob. The extracted feature descriptors are matched using NCC and Euclidean distances, respectively. When the appearances of the images are fundamentally dissimilar, their performances will predominantly decrease and cause a huge amount of false correspondences. Spatial relation constraints are herein adopted to guide the matching process and remove outliers. Zhang (1988) invented a feature matching method called a “bridging mode” which is still widely used in the VirtuoZo software. The bridging mode assumes that a single feature point is not capable of describing a feature; thus, three points that form an image segment are adopted: two protruding points with a minimal intensity gradient and one point with a maximal gradient. The matching window is formed by the relation in the image segment. Zhang *et al.* (1991) extend the bridging mode to support search in two directions to enrich the matching information and use dynamic programming to increase the global consistency. Although the matching window is adapted by the spatial relationships, the matching criterion is still determined by the NCC; therefore, the issues of the NCC still exist for this method.

Unlike the low-level feature descriptors, which have similarity measurements that can be simply defined by Euclidean distances, the high-level spatial relations are complex to quantify. Existing methods that combine blob-like feature descriptors and spatial relations are usually formulated as a graph matching problem (Caetano *et al.*, 2009). Li *et al.* (2005) use a Bayesian formulation, which is modeled by a Markov random field (MRF). The likelihood term enforces the similarities of the feature appearance/descriptors, and the *a priori* term encodes the cyclic order constraint of the Delaunay triangulations. The model is casted to the corresponding factor graph and solved with the max-product algorithm. Torresani *et al.* (2008) formulate the feature matching problem as a unified energy minimization task that encodes additional information, including feature appearance, geometric compatibility, spatial coherence, and is solved using dual decomposition. The authors noticed that their method was equivalent to the graph matching problem that embodies pairwise constraints in edges and similarity measurements in the vertices of graphs. Liu *et al.* (2012) propose a similar method and consider the optimization problem as finding two matched graphs with minimum non-rigid transformation errors. However, these graph matching approaches, which combine appearance and structure information in a unified framework, are NP-hard because all of the combinations of the binary labels that denote true/false matches must be exhausted to find the global solution (Li *et al.*, 2005; Caetano *et al.*, 2009). The space complexity of the algorithm is generally $O(n^4)$ (Caetano *et al.*, 2009; Torki and Elgammal, 2010), and the time complexity is $O(n^3)$ (Liu *et al.*, 2012), where n is the number of features; this approach is often not appropriate for aerial images. Even 800 correspondences will take almost 1,200 seconds to solve the problem (Liu *et al.*, 2012), compared to nearly real time with the standard RANSAC approach. In our practical experience, the number of correspondences of a single stereo pair result in a magnitude of 10^3 to 10^4 .

Methodology

Algorithm Principle

As shown in Figure 1. We add two steps, which are detailed in the following Section, into the standard feature matching procedure. First, we use geometric transformation to relieve the perspective deformation between the oblique image and nadir images. Second, three spatial relation constraints are adopted to remove the remaining outlier by the random sample consensus (RANSAC) approach using epipolar information. Because epipolar constraint is only imposed on a line, there are still possibilities for unfiltered false correspondences when the image format is large. In this situation, additional constraints to filter off remaining outliers are necessary.

Preprocessing

Before detection and matching of the feature points, we exploit the initial EO parameters to geometrically transform the images in order to relieve the perspective deformations as shown in Figure 1. Assuming the terrain is exactly a plane, a one-to-one correspondence can be established between the nadir and the oblique images. After defining a plane $\pi \rightarrow z - h_{flight} = 0$ to roughly approximate the terrain in the coordinate system of vertical camera, a homography matrix H is estimated between the image plane of the vertical and oblique images. The homography matrix H is calculated in Equation 1 (Hartley and Zisserman, 2004) after giving calibrated camera matrix K_V and K_O for the vertical and oblique cameras, respectively:

$$H = K_O(R + \mathbf{t}\mathbf{n}_d^T)K_V^{-1} \quad (1)$$

where $\mathbf{n}_d = \mathbf{n}/d$, \mathbf{n} is the normal vector of plane π in the coordinate system of the nadir image, d is the distance between its center and π , and $[R, \mathbf{t}]$ is the relative rotation and translation between the nadir and oblique images. Using the homography matrix H , the image coordinate of the oblique camera \mathbf{m}_O can be mapped to the vertical view by $\mathbf{m}_V = H\mathbf{m}_O$. Using a specific resampling method, such as bilinear interpolation or bicubic interpolation, the pixels of the oblique image can be remapped to match the vertical view. Therefore, the perspective deformation in the oblique image is relieved.

To compensate for the differences of approximately 180° in the yaw angle between strips, a special method that treats all three rotation angles of the nadir images as zeros is adopted. Therefore, similar geometric transformations also apply to all of the nadir images. To enclose all of the transformed pixels, the rectified images must be enlarged and shifted according to the transformed boundaries. In this way, we can assume that the scale, rotation, and other perspective deformations have been eliminated.

The features are then detected, described and matched on the rectified images as shown in Figure 1; however, the point coordinates are reverse transformed to the original image coordinates because the geometric transformation defined by the homography matrix is invertible. Then, the follow-up outlier removal steps are performed because some constraints are only justifiable in the original image, such as the epipolar constraint. Because no invariant ability should be imposed on the features, we chose to use the FAST corner detector (Rosten *et al.*, 2010) as suggested by Jazayeri and Fraser (2010) and a BRIEF descriptor (Calonder *et al.*, 2012) for efficiency consideration. The binary descriptors are then matched in hamming distance using approximate nearest neighbor search techniques (Muja and Lowe, 2012), then reverse transformed to the original image coordinates. We also adopt the RANSAC approach to initially remove outliers; however, dozens of false correspondences out of the 10^4 matches still exist, even if the RANSAC threshold is set to 1 pixel, which will sometimes prevent the bundle adjustment from converging.

Spatial Relationship Constrained Outlier Removal

In this study we impose three more constraints on the initial correspondences based on spatial relations and classify them as inliers or outliers after quantifying the constraints, including the cyclic angular order constraint, local position consistency constraint, and neighborhood conserving constraint. The first constraint assume that any non-rigid transform of the correspondences will not change the cyclic angular order between them; the second assumes that the positions of the correspondences in a local neighborhood should not abruptly change; and the last constraint that the

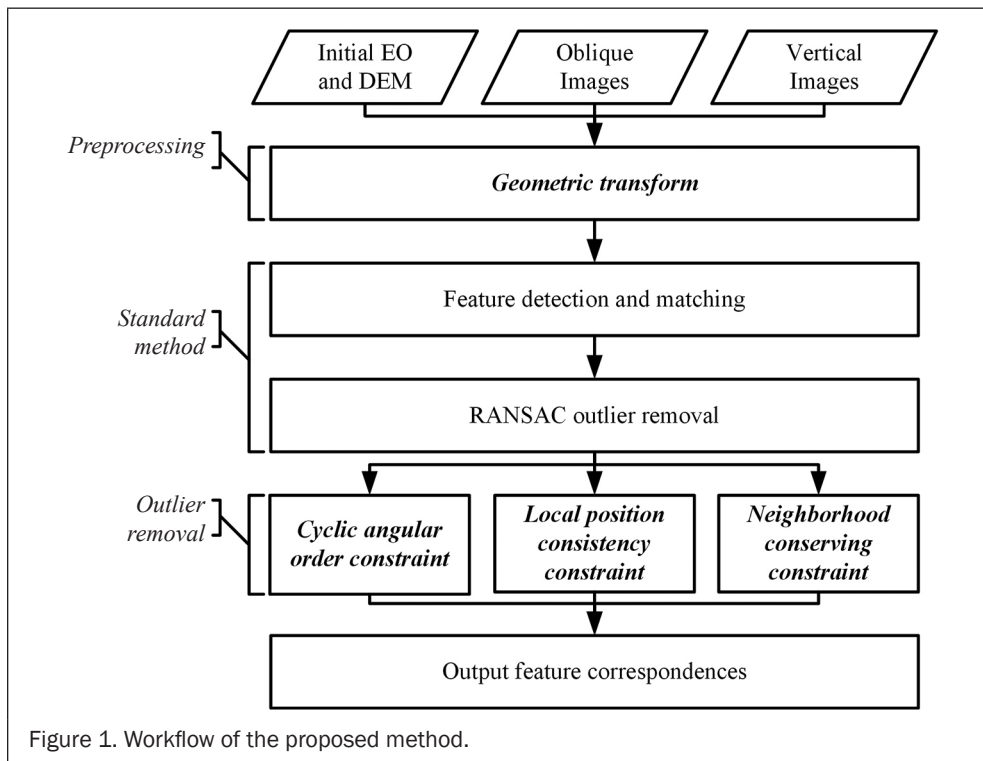


Figure 1. Workflow of the proposed method.

neighborhood relationship should be conserved in correspondences. It should be noted that all the three constraints are not processed sequentially, but in parallel with the refined correspondences after RANSAC outlier removal as shown in Figure 1. After executed in parallel, we removed the union set of the outliers detected in each constraint.

Cyclic Angular Order Constraint

In this study, the angular order of a feature point i in the reference image is denoted as S_i , where i is the point number, and that in the matching image is denoted as S'_i . S is formatted as the sequence of point numbers of the K nearest neighbors (denoted as $N(i)$; $k = 6$ is adopted in this study), which is ordered clockwise. For example, as shown in Figure 2a the angular order for point No. 96 is $S_{96} = \{103, 98, 94, 95, 97, 104\}$ and that in the matching image (Figure 2b) is $S'_{96} = \{97, 104, 103, 98, 95, 94\}$. Similarly, for the false correspondence point No. 94, the angular orders are $S_{94} = \{97, 104, 103, 95, 96, 98\}$ and $S'_{94} = \{104, 103, 97, 96, 95, 98\}$.

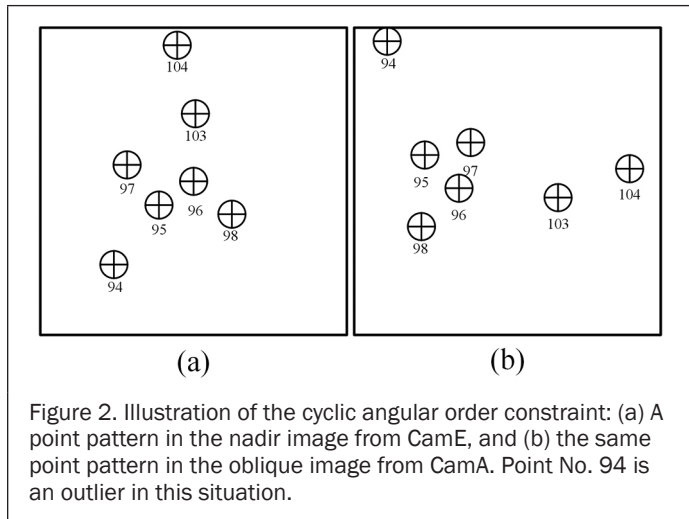


Figure 2. Illustration of the cyclic angular order constraint: (a) A point pattern in the nadir image from CamE, and (b) the same point pattern in the oblique image from CamA. Point No. 94 is an outlier in this situation.

We can consider the sequences of S and S' as two strings, and their differences can be measured by the edit distance. The edit distance quantifies the dissimilarity by counting the minimum number of operations to transform one string to another; the operations include insertion, deletion, and substitution of a single character. To compensate for the rotation effects, the cyclic edit distance (denoted as $CED(S, S')$) is adopted (Klein, 1998; Liu *et al.*, 2012). For example, as discussed above, $CED(S_{96}, S'_{96}) = 2$ because it involves one deletion and one assertion of No. 94; similarly, $CED(S_{94}, S'_{94}) = 4$.

Under the assumption that a non-rigid transformation will not change the cyclic angular order of a point around its neighbors, we have also found that the cyclic angular order constraint is sometimes indeterminate. Thus, we relax the constraint to the following statement:

Cyclic Angular Order Constraint - For each correspondence i , if $CED(S_i, S'_i) \geq 4$, then label correspondence i an outlier.

The constraint is established based on the following reasons: (a) When no outlier exists, the CED will be zero under the assumption that a non-rigid transformation will not change the cyclic angular order; (b) For a correct correspondence, if only one outlier exists among its KNN and the outlier changes the angular order, then $CED(S_i, S'_i)$ will always be two after careful investigations; and (c) For a false correspondence, if the outlier changes the angular order, then $CED(S_i, S'_i)$ will always be larger than four. Although the constraint will

sometimes cause a false alarm (i.e., label the correct correspondence an outlier) and neglect outliers, these cases are rare or can be remedied by other constraints. For example, there are two special cases: (a) more than two outliers exist around a correct correspondence, and (b) the outlier does not change the angular order. The first case is rather rare because the correspondences have already been filtered by RANSAC, and we only chose small neighbors. The latter case may be remedied by other steps, which is the reason that we use multiple spatial constraints.

Local Position Consistency Constraint

Using the initial correspondences, we can estimate a perspective transform function $T(\cdot)$ to approximately align the reference and matching image such that a point $\mathbf{p}(x, y)$ in the reference image can be mapped to the point $\mathbf{p}'(x', y')$ in the matching image as $\mathbf{p}' \approx T(\mathbf{p})$. For example, Sun *et al.* (2014) use a 2D translation to simulate a global transformation, and the affine transformation is adopted by Han *et al.* (2012). In this paper, the affine model is calculated as:

$$T(\mathbf{p}) = A\mathbf{p} + \mathbf{b} \quad (2)$$

where A is a 2×2 matrix and \mathbf{b} is a 2×1 translation vector. However, the non-rigid deformation caused by variations in elevation and perspective transform cannot be simplified by the affine model. Absolute discrepancies exist between the points in the matching image and $T(\mathbf{p})$ as denoted by the following 2×1 residual vector of $r(\mathbf{p})$:

$$r(\mathbf{p}) = \mathbf{p}' - T(\mathbf{p}). \quad (3)$$

The local position consistency constraint is based on the assumption that after the affine transformation, the residuals should be consistent across a local area. More explicitly, for a point \mathbf{p}_i and its KNN $\{\mathbf{p}_k \mid k \in N(i)\}$, we calculate the average residuals of the neighbors $\mu_r = \sum_k r(\mathbf{p}_k) / K$, and the mean and standard deviation of their lengths as $\mu_{\|r\|} = \sum_k \|r(\mathbf{p}_k)\| / K$ and $\sigma_{\|r\|} = \sqrt{\sum_k (\|r(\mathbf{p}_k)\| - \mu_{\|r\|})^2 / K}$, respectively. It should be noted that, in most cases, $\|\mu_r\| \neq \mu_{\|r\|}$. The local position consistency constraint imposes the following statement on the residual length and direction:

Local Position Consistency Constraint: The residual for a point \mathbf{p}_i in the reference image should satisfy the following constraint, otherwise label it as an outlier.

$$\begin{cases} r(\mathbf{p}_i) \bullet \mu_r > 0 \\ \|r(\mathbf{p}_i)\| \in [\mu_{\|r\|} - 3\sigma_{\|r\|}, \mu_{\|r\|} + 3\sigma_{\|r\|}] \end{cases} \quad (4)$$

where the first restricts the residual to be approximately in the same direction of its neighbors and the second impose constrain on the size of the residuals.

Neighborhood Conserving Constraint

The neighborhood conserving constraint is based on the assumption that the neighbors of a point in the reference image are also the neighbors in the matching image. Therefore, we compute both the KNN of \mathbf{p}_i and \mathbf{p}'_i as $N(i)$ and $N'(i)$, respectively. Ideally, the two ID sets should coincide with each other. The similarity of two sequence vectors of the points can simply be measured by their intersection, which is denoted as $I(\mathbf{p}_i, \mathbf{p}'_i)$. Similar to the second constraint, the statistical average μ_I and standard deviation σ_I are obtained, and the third constraint is formally stated as follows:

Neighborhood Conserving Constraint: The intersection number for the KNN of the two points in a correspondence, $I(\mathbf{p}_i, \mathbf{p}'_i)$, should satisfy the following:

$$I(\mathbf{p}_i, \mathbf{p}'_i) > \mu_i - 3\sigma_i. \quad (5)$$

Algorithm Complexities

As described above, previous matching algorithms that adopted spatial constraints often resort to the graph matching method, thus resulted in prohibitively expensive time and space complexities at the magnitude of $O(n^3)$, where n is the number of correspondences or even higher (Torki and Elgammal, 2010), which was unable to extend to aerial images applications. It can be noted that for all the three constraints, KNN search for all the correspondences are adopted and its time complexity is $O(n \log n)$ in average. For the first constraint, we need to calculate the cyclic edit distance for each points at the time complexity of approximate $O(Kn)$, where K is the selected number of nearest neighbors. For the second constraint, we need to calculate the statistical information of each cliques at the complexity of $O(Kn)$. And for the last one, only global statistical information is needed with time complexity of $O(n)$. Considering that K is a relative small number, the total time complexity is only at $O(n \log n)$ level. Furthermore, it is obviously that the space complexity is $O(n)$. So the low algorithm complexities have guaranteed the extendibility of our method.

Experimental Evaluations

Configurations and Dataset

In this study, the oblique imagery system, SWDC-5, adopts the “Maltese Cross” configuration (Petrie, 2009). This type of configuration consists of five cameras: a single camera (*CamE*)

pointing at nadir and four oblique cameras (*CamA*, *CamB*, *CamC*, and *CamD*). One pair of oblique cameras (*CamA* and *CamC*) point in opposite directions across the strips, whereas the other pair of cameras (*CamB* and *CamD*) view the same strip. Using a cross configuration system, the intuitive merits of having oblique views from four different directions are clearly emphasized by the ability to capture all of the possible facades of the buildings as shown in Figure 3.

The entire dataset consists of 27 strips that are collected during several flights by LEADOR SPATIAL over Jinyang, which is new development in the mountainous city of Guiyang. In fact, the flight conditions over the area were not good due to air movement and cloudy skies. The complete block contains 1,711 images for each camera at a strip overlap of 60 percent and side overlap of 50 percent, from which only some continuous strips of the fifth flight were chosen here. The average elevation of the coverage area is approximately 1,300 m, and the expected relative flight height is 600 m. The principal distances of the camera are approximately 50 mm for the nadir images and 80 mm for the oblique images. With this configuration, the ground sample distance (GSD) is approximately 0.08 m. In this study, the image distortion and principle point are pre-rectified to zero and to the image center, respectively. Additionally, a bundle adjustment of all of the nadir images was previously conducted using the integrated sensor orientation (Ip *et al.*, 2007). The initial EO information was obtained from the GPS/IMU devices and several manually selected ground control points to eliminate the datum shift. The mean square error of unit weight σ_0 is 0.3 pixels, and we treat triangulated 3D points from nadir images as control points in the experiments because no ground control points were available. Furthermore, the theoretical positioning error of the nadir images are at centimeters level. The platform parameters are calibrated in a calibration field as shown in Table 1. The initial EO parameters for *CamA* to *CamD* are estimated

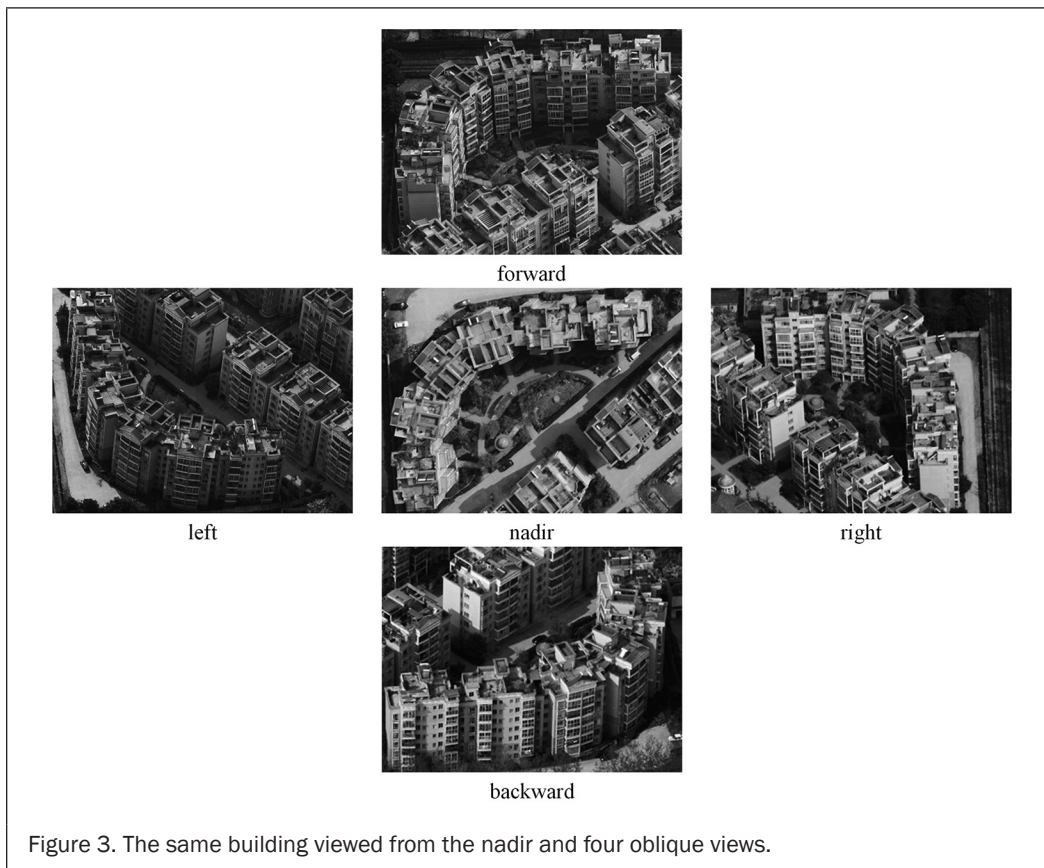


Figure 3. The same building viewed from the nadir and four oblique views.

with the platform parameters and the adjusted EO for *CamE*. Due to reinstallation and other miscellaneous reasons, the initial EO parameters may cause meters-level 3D positioning errors. However, the initial accuracies for the oblique EO parameters are enough, because they only contribute to the geometrical transformations.

TABLE 1. PLATFORM PARAMETERS OF THE CAMERA SYSTEM; THE EULERIAN ANGLES ARE IN THE ORDER OF $\omega \rightarrow \varphi \rightarrow \kappa$. CAMERA IS POINTING AT NADIR AND CAMERA TO CAMD ARE THE FOUR OBLIQUE CAMERAS

	Translation P_{OE}			Rotation R_{OE}		
	$X(m)$	$Y(m)$	$Z(m)$	$\varphi(^{\circ})$	$\omega(^{\circ})$	$\kappa(^{\circ})$
<i>CamA-CamE</i>	0.109	0.003	0.04	-0.744	44.824	90.704
<i>CamB-CamE</i>	0.019	0.13	0.056	-44.550	-0.171	180.187
<i>CamC-CamE</i>	-0.111	-0.014	0.037	0.705	-44.911	-89.346
<i>CamD-CamE</i>	-0.002	-0.138	0.046	45.459	0.412	0.248

To qualitatively and quantitatively evaluate the performance of the proposed methods, two types of experiments are conducted on two small subsets of images from the fifth flight, which include a dense built-up area and a rural area with vegetation and bare soil, as shown in Figure 4. First, we visually and statistically compare the match results with the standard SIFT methods using the two datasets. Next, we apply bundle adjustment to a block of 150 images and evaluate the quality of the bundle adjustment to quantify the performance of the correspondences.

Performance Evaluation of the Matching Results

In Plate 1, the match results of the proposed method and the standard SIFT method are displayed. For both methods, the ratio match (Lowe, 2004) is adopted, which detects the two nearest neighbors and only reserves those correspondences that exhibit a distance ratio between the two neighbors of less than 0.75. Furthermore, the cross check described previously is also adopted to ensure the one-on-one matching property. The successive RANSAC approach using a fundamental matrix follows the ratio match with a threshold of 1 pixel. To present a better understanding of the matching results, the key points and the images of the oblique views are geometrically transformed without a shift such that the correspondences are approximately parallel to each other. Otherwise, the correspondences will intersect and distort the meaning of the visual comparisons. The results of the proposed method are shown in Plate 1a and 1c. For the others, the matching results are obtained with the SIFT on the original images. The first column in each row provides the intuitional distributions of the correspondences, and the second column provides the matching results. The number of correspondences and the distribution are superior to those using SIFT, especially in the built-up areas where SIFT encountered enormous outliers after the RANSAC approach and most matches are centralized at few areas (Plate 1b). Furthermore, even in seriously occluded areas, such as the built-up areas in Plate 1a, we are also able to detect enough well-distributed tie points on building roofs when the shape of the roofs are relatively regular and simple.

To present a more comprehensive understanding of the performance of the proposed method, the matching results

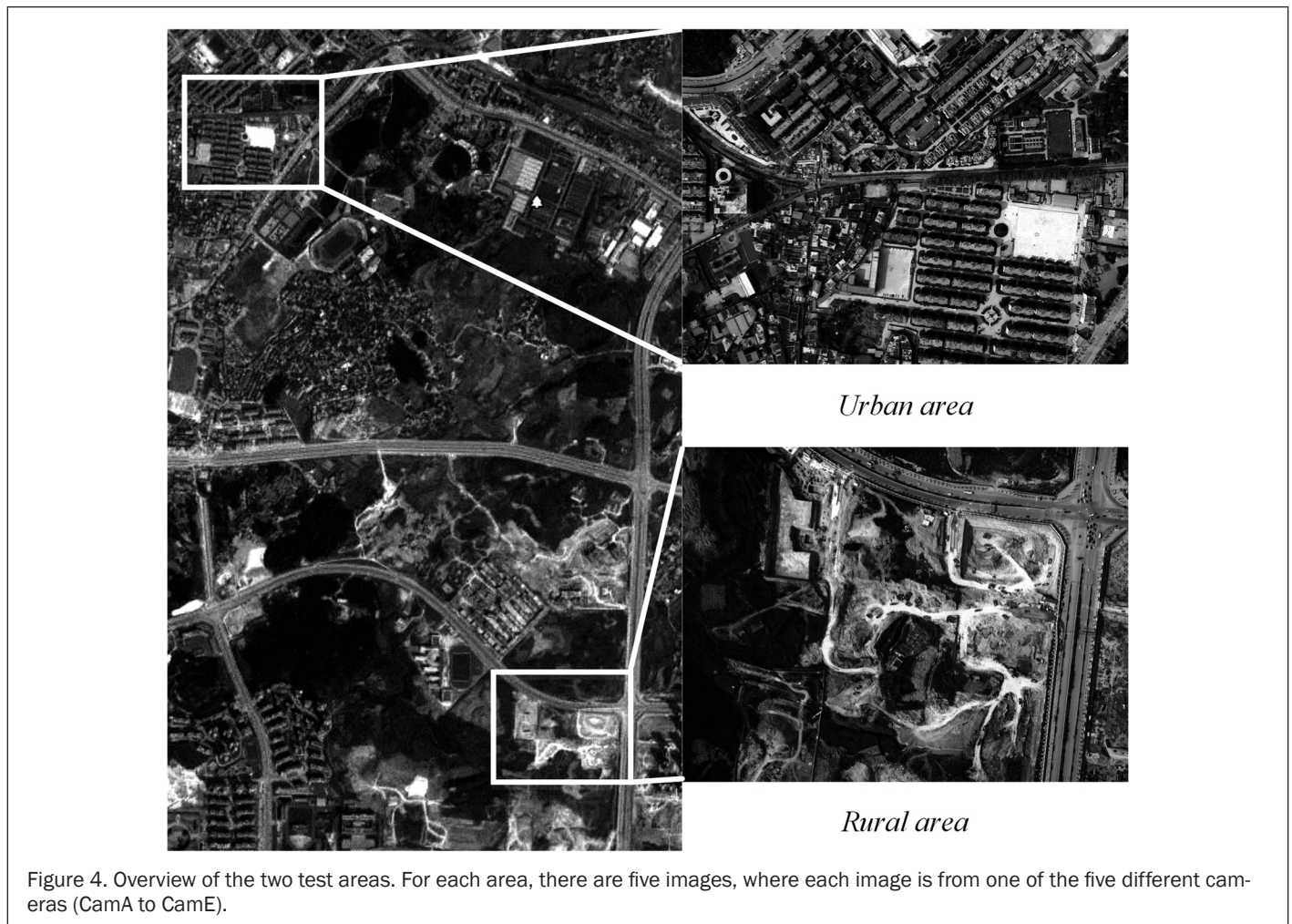


Figure 4. Overview of the two test areas. For each area, there are five images, where each image is from one of the five different cameras (CamA to CamE).

for the two areas are listed in Table 2. The number of final matches, the outliers detected by the spatial relationships constraint and the false alarms are presented. The false alarms are obtained by manual inspecting the detected outliers; specifically, they are the number of correct correspondences that are labeled as outliers. The false alarms rate is very low, partly because of the sparseness of the remaining outliers after previous outlier handling steps, such as cross check, ratio match and RANSAC. Another characteristic observed is that the performances for the images of the urban areas are slightly inferior to those of the rural areas. This is because occlusions are more severe in the previous scenario.

Turning into compare with other methods or software, we also use SIFT, VisualSFM (Wu, 2011) and Photoscan to test matching results with the same images. In the experiments, the SiftGPU (Wu, 2007) is adopted for the SIFT implementation, which is also used in VisualSFM for feature detection. It can be noted that whereas the performance of SIFT decreases dramatically in the urban areas, the proposed method performs considerably well; the geometric transformation relieves the perspective deformation, especially for regions that are parallel to the horizontal ground (i.e., the building roof and planar ground). In fact, in the urban area, more

correspondences are detected on the building roofs than on the ground, which are more inclined to be occluded and textureless. Furthermore, in the case of matching between images of different oblique cameras, SIFT will totally fail after RANSAC outlier removal and VisualSFM also will not perform well, as shown in the last two rows of Table 2a and 2b. The translational tilting angles (Morel and Yu, 2009) between the images are approximately 90°, which makes it almost impossible for the partially affine invariant SIFT descriptor to establish correct correspondences. However, the proposed method is also capable of handling these cases. Although Photoscan is able to obtain enough tie points, its performance is still inferior to the proposed method and after careful examinations, we discover that Photoscan will produce enormous false matches. In fact, when images is significantly different, large amount of outliers are expected if not handled appropriately.

Furthermore, one of the major considerations on the performance for practical applications is the runtime speed. As described above, some previous works on feature points matching with spatial relationship constraints are impracticable in applications of aerial images due to prohibitively high space and time complexities (Liu *et al.*, 2012). In order to provide some perspectives into the algorithm details, we

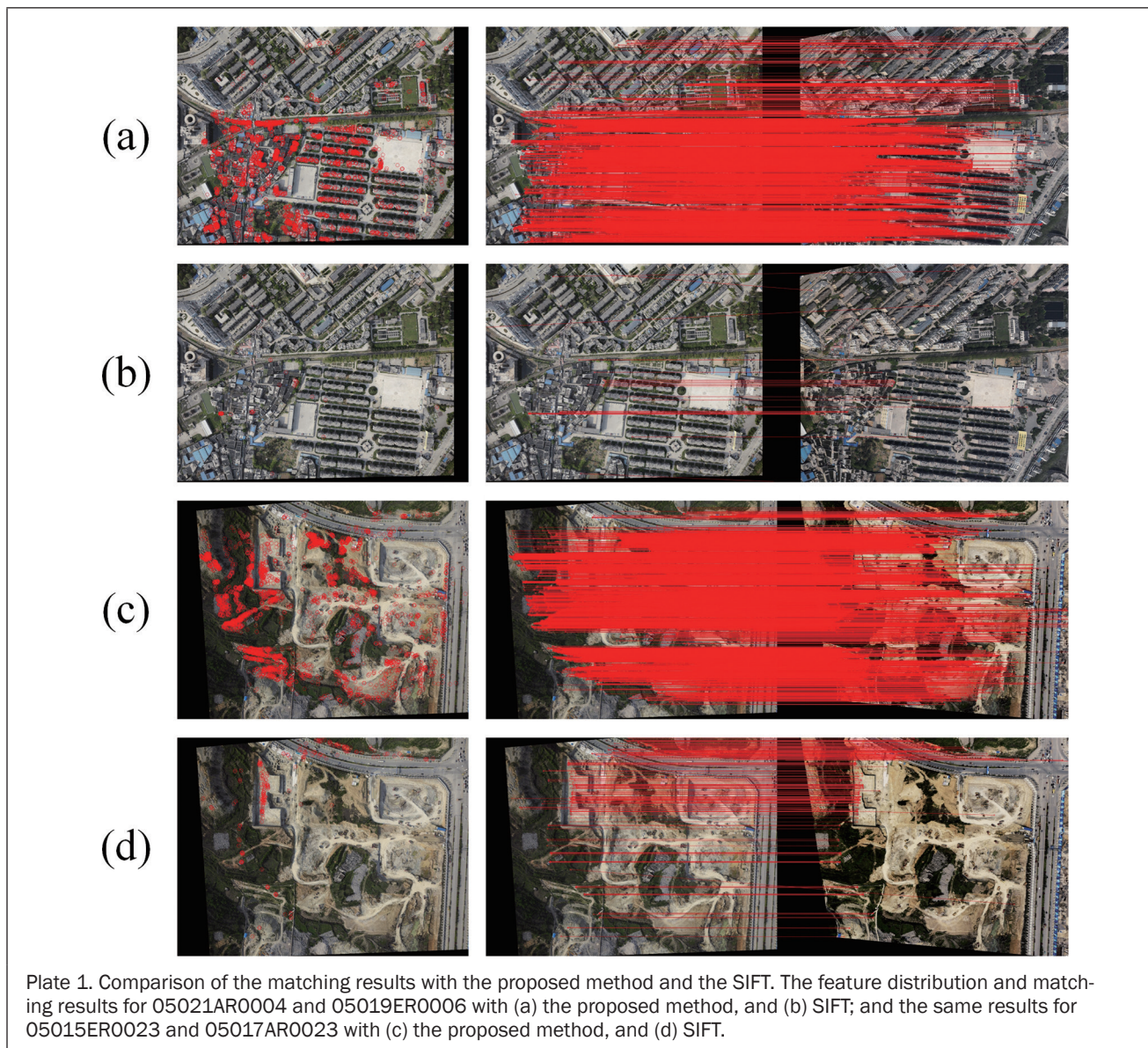


TABLE 2. MATCHING RESULTS FOR THE TWO TEST AREAS; THE 'E' DENOTES THE NADIR IMAGES AND A TO D DENOTE OBLIQUE IMAGES

a) Tests in the rural area, which features vegetation, bare earth and roads.

Pair	Proposed Method			SIFT	VisualSFM	Photoscan
	#Matches	#Outliers	#False Alarm	#Matches	#Matches	#Matches
E-A	3595	31	0	215	413	1369
E-B	9017	32	0	1730	182	2913
E-C	6498	32	0	2277	248	2145
E-D	7026	23	0	2315	294	2434
A-C	1253	21	0	N/A	N/A	78
B-D	1181	6	0	N/A	N/A	612

b) Tests in the built-up area, which features dense and tall buildings.

Pair	Proposed Method			SIFT	VisualSFM	Photoscan
	#Matches	#Outliers	#False Alarm	#Matches	#Matches	#Matches
E-A	3398	31	0	36	61	940
E-B	3943	41	0	138	62	934
E-C	4461	56	1	43	36	1730
E-D	4688	41	0	49	34	1096
A-C	726	17	0	N/A	N/A	286
B-D	2596	36	0	N/A	N/A	231

TABLE 3. PERFORMANCE RESULTS FOR THE RUNTIME SPEED OF THE PROPOSED METHOD

Pair	Feature detection (ms)	KNN search (ms)	RANSAC filter (ms)	Spatial filter (ms)	Miscellaneous (ms)	Total (ms)
E-A	8847	8290	9	26	102	17274
E-B	10607	10329	618	26	99	21679
E-C	10034	9038	30	28	107	19237
E-D	10814	9587	380	32	13	20826

TABLE 4. ADJUSTED RESULTS OF THE PLATFORM PARAMETERS FOR THE OBLIQUE IMAGES; THE BOLD VALUES DENOTE THE INTERNAL ACCURACIES OF THE PLATFORM PARAMETERS

	Translation P_{OE}			Rotation R_{OE}		
	$X(m)$	$Y(m)$	$Z(m)$	$\varphi(^{\circ})$	$\omega(^{\circ})$	$\kappa(^{\circ})$
CamA-CamE	0.107	0.003	0.038	-0.770	44.820	90.720
	3.20E-03	3.29E-03	3.26E-03	3.07E-04	2.30E-04	4.31E-04
CamB-CamE	0.018	0.118	0.051	-44.583	-0.155	180.223
	2.93E-03	2.27E-03	2.87E-03	1.83E-04	1.78E-04	2.12E-04
CamC-CamE	-0.094	-0.012	0.024	0.751	-44.974	-89.306
	2.81E-03	3.14E-03	2.96E-03	2.91E-04	2.19E-04	2.90E-04
CamD-CamE	-0.001	-0.116	0.039	45.519	0.374	0.295
	2.98E-03	2.43E-03	2.98E-03	1.79E-04	1.73E-04	2.50E-04

demonstrate the runtime speed with respect to different modules of the method. As summarized in Table 3, although we have carefully chosen the feature detection method and diligently optimized the KNN search, which is specially tuned for speed, the bottleneck still lies in feature detection and KNN search for the match candidates. The first two steps operate on all the feature points, whose amount is at the level of 10^5 , however the RANSAC filter and spatial filter proposed in this paper operate on the matching candidates succeeded to previous steps. This helps to explain the performance. Due to the low time complexities of the spatial filter as described above, the runtime of the three constraints are nearly negligible when compared to the hotspots in the procedures.

Performance Evaluation of Bundle Adjustment

To further evaluate the accuracies of the matching results, we select 150 images from seven strips (30 images for each camera) and conduct a bundle adjustment on the block of images using tie points that are generated and filtered by the

proposed method. In the bundle adjustment, the EO parameters for the nadir images (*CamE*) are held fixed because these images have already been oriented with ground control points. Because all of the strips are from the same flight, we considered that the platform parameters at all of the exposure positions are the same and unknown in the adjustment (Jacobsen, 2009). Among all of the images, we created 3,390 pair-wise images matches because of the dense overlap ratio for the oblique camera system. After connecting all of the matches, we select hundreds of points that are evenly distributed within each image. In the selection, we prefer the points that connect more images, and the maximum tied points even linked 31 images. Overall, there are 8,339 object points that formulate 47,522 image tie points for the bundle adjustment.

The mean square error of the unit weight is $\sigma_0 = 0.46$ pixels after the bundle adjustment, and the adjusted platform parameters together with their internal accuracies are listed in Table 4. The internal accuracies for the adjusted platform parameters are quite good because of the well-distributed block

TABLE 5. EVALUATION RESULTS WITH THE GROUND CONTROL POINTS: (A) THE PROJECTION ERROR OF THE OBLIQUE IMAGES, AND (B) THE 3D POSITION ERRORS TRIANGULATED BY POINTS ON THE OBLIQUE IMAGES

(a) Projection errors of the ground control points				
	<i>RMSE x (pixels)</i>	<i>RMSE y (pixels)</i>	<i>RMSE xy (pixels)</i>	<i>Max. RMSE (pixels)</i>
Before adjustment	7.45	11.50	13.70	25.78
After adjustment	0.60	0.81	1.00	4.18
(b) 3D position errors of the ground control points				
	<i>RMSE XY (m)</i>	<i>RMSE Z (m)</i>	<i>RMSE (m)</i>	<i>Max. RMSE (m)</i>
Before adjustment	0.603	0.942	1.114	3.504
	8.04×10^{-4}	1.26×10^{-3}	1.49×10^{-3}	4.6×10^{-3}
After adjustment	0.072	0.100	0.123	0.479
	9.6×10^{-4}	1.33×10^{-4}	1.64×10^{-4}	6.38×10^{-4}

network with multiple tie points among all of the images. The platform parameters changed only slightly compared to those before the adjustment as shown in Table 1.

To evaluate the consistencies in the block, we select another 3,000 sets of tie points from the remaining correspondences after removing the points used for the bundle adjustment. Each set must connect at least two nadir images and two oblique images. Thus, we treat the 3D points triangulated by the nadir images as ground control points. The projection errors and the 3D position errors of the oblique images are listed in Table 5, including the root mean square errors (RMSE) of the image coordinates and object space. The projection errors decreased nearly an order of magnitude, even with the small changes in the platform parameters. The position errors are reduced to approximately 1.5 GSD. When taking the flight height into, the relative accuracies (RMSE divided by relative flight height) are shown as the bolded rows in Table 5b, which is sufficient for subsequent processing considering the precision of the triangulated control points and the small baseline-height ratio of the medium format oblique images (Colomina and Molina, 2014).

Conclusions

We determined that translational shifts and rotational skewing exists in the platform parameters for the SWDC-5, even if the parameters are expected to be fixed after offline calibration, which will cause tens of pixels misalignments on the oblique images and more than one-meter positioning errors. Due to occlusions and perspective deformations, tie point matching for the images of oblique camera systems are extraordinarily difficult. To surmount this problem, we exploited the initial geometric information to rectify the images and reduce the perspective deformations. Furthermore, spatial relationship constraints are incorporated into the feature matching procedures and serve as important clues to remove outliers, which still exist after using the common approach to handling outliers because of the consequences of the essential image dissimilarities in appearances. Experimental evaluations and comparisons reveal that the proposed method outperforms the standard SIFT in both the numbers and distributions of the correspondences. After a bundle adjustment with the connected points that are generated by the proposed method, the translation and skewing of the platform parameters are remedied. Furthermore, the internal inconsistencies of the block are reduced to a satisfactory level. An obvious trend in processing oblique images is to exploit the measurement potentials (Haala, 2013), and our future works will focus on developing efficient and suitable method for the dense image matching of oblique images.

Acknowledgments

This study was supported by the National Basic Research Program of China (973 Program, No. 2010CB731801) and the National High Technology Research and Development Program of China (863 Program, No. 2012AA121305).

References

- Bay, H., A. Ess, T. Tuytelaars, and L. Van Gool, 2008. Speeded-up robust features (SURF), *Computer Vision and Image Understanding*, 110(3):346–359.
- Caetano, T.S., J.J. McAuley, L. Cheng, Q.V. Le, and A.J. Smola, 2009. Learning graph matching, *IEEE Transactions on Pattern Analysis and Machine Intelligence*, 31(6):1048–1058.
- Calonder, M., V. Lepetit, M. Ozuysal, T. Trzcinski, C. Strecha, and P. Fua, 2012. BRIEF: Computing a local binary descriptor very fast, *IEEE Transactions on Pattern Analysis and Machine Intelligence*, 34(7):1281–1298.
- Colomina, I., and P. Molina, 2014. Unmanned aerial systems for photogrammetry and remote sensing: A review, *ISPRS Journal of Photogrammetry and Remote Sensing*, 92:79–97.
- Förstner, W., and E. Gülch, 1987. A fast operator for detection and precise location of distinct points, corners and centres of circular features, *ISPRS Intercommission Conference on Fast Processing of Photogrammetric Data*, 02-04 June, Interlaken, Switzerland, pp. 281–305.
- Fraser, C.S., 1997. Innovations in automation for vision metrology systems, *The Photogrammetric Record*, 15(90):901–911.
- Fritsch, D., and M. Rothermel, 2013. Oblique image data processing - Potential, experience and recommendation, *Proceedings of Photogrammetric Week 2013*, 09-13 September, Stuttgart, Germany, pp. 73–88.
- Gerke, M., 2009. Dense matching in high resolution oblique airborne images, *International Archives of the Photogrammetry, Remote Sensing and Spatial Information Sciences*, 38(3/W4):77–82.
- Gerke, M., and N. Kerle, 2011. Automatic structural seismic damage assessment with airborne oblique Pictometry imagery, *Photogrammetric Engineering & Remote Sensing*, 77(9):885–898.
- Gruen, A., 1985. Adaptive least squares correlation: A powerful image matching technique, *South African Journal of Photogrammetry, Remote Sensing and Cartography*, 14(3):175–187.
- Haala, N., 2013. The landscape of dense image matching algorithms, *Proceedings of Photogrammetric Week 2013*, 09-13 September, Stuttgart, Germany, pp. 271–284.
- Han, Y.K., Y.G. Byun, J.W. Choi, D.Y. Han, and Y. Kim, 2012. Automatic registration of high-resolution images using local properties of features, *Photogrammetric Engineering and Remote Sensing*, 78(3):211–221.
- Harris, C., and M. Stephens, 1988. A combined corner and edge detector, *Proceedings of the Alvey Vision Conference*, 31 August-02 September, Manchester, UK, pp. 147–152.
- Hartley, R., and A. Zisserman, 2004. *Multiple View Geometry in Computer Vision*, Cambridge University Press, Cambridge, UK, 672 p.

- Ip, A., N. El-Sheimy, and M. Mostafa, 2007. Performance analysis of integrated sensor orientation, *Photogrammetric Engineering & Remote Sensing*, 73(1):1–9.
- Jacobsen, K., 2009. Geometry of vertical and oblique image combinations, *Remote Sensing for a Changing Europe: Proceedings of the 28th Symposium of the European Association of Remote Sensing Laboratories, Istanbul, Turkey*, 02-05 June 2008, pp. 16.
- Jazayeri, I., and C.S. Fraser, 2010. Interest operators for feature-based matching in close range photogrammetry, *The Photogrammetric Record*, 25(129):24–41.
- Ke, Y., and R. Sukthankar, 2004. PCA-SIFT: A more distinctive representation for local image descriptors, *IEEE Computer Society Conference on Computer Vision and Pattern Recognition (CVPR2004)*, 27 June-02 July, Washington, D.C., pp. 506–513.
- Klein, P.N., 1998. Computing the edit-distance between unrooted ordered trees, *Proceedings of the 6th Annual European Symposium on Algorithms (ESA98)*, 24-26 August, Venice, Italy, pp. 91–102.
- Lerma, J.L., S. Navarro, M. Cabrelles, A.E. Seguí, and D. Hernández, 2013. Automatic orientation and 3D modelling from markerless rock art imagery, *ISPRS Journal of Photogrammetry and Remote Sensing*, 76:64–75.
- Li, Y., Y. Tsin, Y. Genc, and T. Kanade, T., 2005. Object detection using 2D spatial ordering constraints, *IEEE Computer Society Conference on Computer Vision and Pattern Recognition (CVPR 2005)*, 20-26 June, San Diego, California, pp. 711–718.
- Liang, T., and C. Heipke, 1996. Automatic relative orientation of aerial images, *Photogrammetric Engineering & Remote Sensing*, 62(1):47–55.
- Lindeberg, T., 1993. Detecting salient blob-like image structures and their scales with a scale-space primal sketch: A method for focus-of-attention, *International Journal of Computer Vision*, 11(3):283–318.
- Lindeberg, T., 1998. Feature detection with automatic scale selection, *International Journal of Computer Vision*, 30(2):79–116.
- Liu, Z., J. An, and Y. Jing, 2012. A simple and robust feature point matching algorithm based on restricted spatial order constraints for aerial image registration, *IEEE Transactions on Geoscience and Remote Sensing*, 50(2):514–527.
- Lowe, D.G., 2004. Distinctive image features from scale-invariant keypoints, *International Journal of Computer Vision*, 60(2):91–110.
- Madani, M., 2012. Accuracy potential and applications of MIDAS aerial oblique camera system, *International Archives of the Photogrammetry, Remote Sensing and Spatial Information Sciences*, 39(PART B1):127–132.
- Matas, J., O. Chum, M. Urban, and T. Pajdla, 2004. Robust wide-base-line stereo from maximally stable extremal regions, *Image and Vision Computing*, 22(10):761–767.
- Mikolajczyk, K., and C. Schmid, 2004. Scale and affine invariant interest point detectors, *International Journal of Computer Vision*, 60(1):63–86.
- Mikolajczyk, K., and C. Schmid, 2005. A performance evaluation of local descriptors, *IEEE Transactions on Pattern Analysis and Machine Intelligence*, 27(10):1615–1630.
- Moravec, H.P., 1981. Rover visual obstacle avoidance, *Proceedings of the 7th International Joint Conference on Artificial Intelligence (IJCAI 1981)*, 24-28 August, Vancouver, Canada, pp. 785–790.
- Morel, J., and G. Yu, 2009. ASIFT: A new framework for fully affine invariant image comparison, *SIAM Journal on Imaging Sciences*, 2(2):438–469.
- Muja, M., and D.G. Lowe, 2012. Fast matching of binary features, *Proceedings of the Ninth Conference on Computer and Robot Vision (CRV2012)*, 27-30 May, Toronto, Canada, pp. 404–410.
- Nyaruhuma, A.P., M. Gerke, G. Vosselman, and E.G. Mtaló, 2012. Verification of 2D building outlines using oblique airborne images, *ISPRS Journal of Photogrammetry and Remote Sensing*, 71:62–75.
- Petrie, G., 2009. Systematic oblique aerial photography using multiple digital cameras, *Photogrammetric Engineering & Remote Sensing*, 75(2):102–107.
- Rosten, E., R. Porter, and T. Drummond, 2010. Faster and better: A machine learning approach to corner detection, *IEEE Transactions on Pattern Analysis and Machine Intelligence*, 32(1):105–119.
- Sun, Y., L. Zhao, S. Huang, L. Yan, and G. Dissanayake, 2014. L2-SIFT: SIFT feature extraction and matching for large images in large-scale aerial photogrammetry, *ISPRS Journal of Photogrammetry and Remote Sensing*, 91:1–16.
- Torki, M., and A. Elgammal, 2010. One-shot multi-set non-rigid feature-spatial matching, *Proceedings of the IEEE Conference on Computer Vision and Pattern Recognition (CVPR 2010)*, 13-18 June, San Francisco, California, pp. 3058–3065.
- Torresani, L., V. Kolmogorov, and C. Rother, 2008. Feature correspondence via graph matching: Models and global optimization, *Proceedings of the European Conference on Computer Vision (ECCV 2008)*, 12-18 October, Marseille, France, pp. 596–609.
- Ullman, S., 1979. *The Interpretation of Visual Motion*, The MIT Press, Cambridge, Massachusetts, 229 p.
- Wang, M., H. Bai, and F. Hu, 2008. Automatic texture acquisition for 3D model using oblique aerial images, *International Conference on Intelligent Networks and Intelligent Systems (ICINIS'08)*, 01-03 November, Wuhan, China, pp. 495–498.
- Wang, Z., 1990. *Principle of Photogrammetry: With Remote Sensing*, Press of Wuhan Technical University of Surveying and Mapping, Wuhan, 455 p.
- Wiedemann, A., and J. Moré, 2012. Orientation strategies for aerial oblique images, *International Archives of the Photogrammetry, Remote Sensing and Spatial Information Sciences*, 39(Part B1):185–189.
- Wu, C., 2007. SiftGPU: A GPU implementation of Scale Invariant Feature Transform (SIFT), URL: <http://cs.unc.edu/~ccwu/siftgpu> (last date accessed: 18 November 2014).
- Wu, C., 2011. VisualSFM: A Visual Structure from Motion System, URL: <http://ccwu.me/vsfm> (last date accessed: 18 November 2014).
- Xiong, X., Y. Zhang, J. Zhu, and M. Zheng, 2014. Camera pose determination and 3-D measurement from monocular oblique images with horizontal right angle constraints, *IEEE Geoscience and Remote Sensing Letters*, 11(11):1976–1980.
- Yang, H., S. Zhang, and Y. Wang, 2012. Robust and precise registration of oblique images based on scale-invariant feature transformation algorithm, *IEEE Geoscience and Remote Sensing Letters*, 9(4):783–787.
- Yao, J., and W. Cham, 2007. Robust multi-view feature matching from multiple unordered views, *Pattern Recognition*, 40(11):3081–3099.
- Zhang, Z., 1988. A new approach of epipolar-line image matching - Bridging Mode, *Journal of Wuhan Technical University of Surveying and Mapping*, 13(4):19–27.
- Zhang, Z., J. Zhang, and X. Wu, 1991. Developing of bridging mode and global image matching, *Journal of Wuhan Technical University of Surveying and Mapping*, 16(3):1–11.
- Zhu, Q., B. Wu, and N. Wan, 2007. A filtering strategy for interest point detecting to improve repeatability and information content, *Photogrammetric Engineering & Remote Sensing*, 73(5):547–553.

(Received 18 April 2014; accepted 04 August 2014; final version 24 August 2014)

Sub-pixel-scale Land Cover Map Updating by Integrating Change Detection and Sub-Pixel Mapping

Xiaodong Li, Yun Du, and Feng Ling

Abstract

Coarse-resolution remotely sensed images are high in temporal repetition rates, but their low spatial resolution limits their application in updating land cover maps. Our proposed land cover updating method involves the use of coarse-resolution images to update fine-resolution land cover maps. The method comprises change detection and sub-pixel mapping methods. The current coarse-resolution image is unmixed, and the previous fine-resolution map is spatially degraded to produce current and previous class fraction images. A change detection method is applied to these fraction images to create a fine-resolution binary change/non-change map. Finally, a sub-pixel mapping method is applied to update the fine-resolution pixel labels that are changed in the change/non-change map. The proposed method is compared with a pixel-based classification method and two sub-pixel mapping methods. The proposed method maintains most of the spatial patterns of land cover classes that are unchanged in the previous and current images, whereas other methods cannot.

Introduction

Remotely sensed images can provide reliable land cover information at different scales and are the primary data utilized in the production and updating of land cover maps. At the global scale, coarse-resolution images, such as those obtained with a moderate-resolution imaging spectroradiometer (MODIS), have been applied to build land cover products, such as the MODIS land cover product (Friedl *et al.*, 2002). Coarse-resolution images are high in temporal repetition rates, which allow the timely updating of land cover maps and the creation of long-term land cover products. However, the spatial resolution of coarse-resolution images is low. Coarse-resolution land cover products fail to satisfy regional-scale land cover resource and landscape analyses. At the regional scale, fine-resolution remotely sensed images are the primary data utilized to generate land cover maps. For instance, Landsat images at a spatial resolution of 30 m are utilized to produce and update the National Land Cover Database (NLCD) of the United States (Homer *et al.*, 2007). However, owing to the tradeoff between spatial and temporal resolution, fine-resolution images have their limitations because they are often acquired at a relatively low temporal resolution. The land cover products from fine-resolution images are derived only from remotely sensed data acquired during one or several years, and these products represent the land cover characteristics of a specific period. Therefore, they lack not only long-term but also timely land cover change information.

Using a current coarse-resolution image and a previous fine-resolution map to timely update fine-resolution land

cover products at the regional scale is meaningful and challenging. This task necessitates the use of multi-resolution images, which provide mutually supplementary land cover information at different scales. A popular approach that combines fine-resolution and coarse-resolution images is the use of coarse-resolution images that cover the entire area as the primary data source, as well as fine-resolution images that cover a part of the area as training samples. Braswell *et al.* (2003) combined coarse-resolution and fine-resolution images to extract land cover fraction images at the sub-pixel scale using soft classification, which predicts land cover class fractional information within each coarse-resolution pixel. The fine-resolution images were utilized to train endmember signatures, and the coarse-resolution images were utilized for spectral unmixing. Lu *et al.* (2011) integrated MODIS and Landsat images to map a fractional forest cover in the Brazilian Amazon. MODIS images were unmixed to forest fraction images, whereas Landsat images were utilized to calibrate the forest fraction images. However, the aforementioned methods can only detect land cover fraction within each coarse-resolution pixel and cannot produce fine-resolution land cover maps.

Sub-pixel mapping (SPM) or super-resolution mapping is a technique that transforms a coarse-resolution image or a spectral unmixing result into a fine-scale hard classification map by dividing pixels into sub-pixels and assigning different classes to these sub-pixels (Foody, 2006; Atkinson, 2009). SPM provides more information than spectral unmixing during the downscaling of coarse-resolution images because SPM can specify the location of each class within the coarse pixels. Generally, SPM adopts mono-temporal coarse-resolution remotely sensed images as input. In fact, SPM is an ill-posed inverse problem of transforming a coarse-resolution fraction image to a fine-resolution land cover map, and SPM accuracy is influenced by the uncertainty in determining fine-resolution pixel labels (Nguyen *et al.*, 2006; Ling *et al.*, 2010). The combination of a current coarse-resolution image and a previous fine-resolution land cover map is useful in reducing SPM uncertainty. Ling *et al.* (2011) developed a sub-pixel scale land cover change mapping method by using a current coarse-resolution remotely sensed image and a previous fine-resolution land cover map. This method was directly used on land cover fraction images obtained by spectral unmixing applied to remotely sensed images; fraction image errors reduced the accuracy of the result.

The integration of a previous fine-resolution land cover map into land cover classification and map updating accuracy

Photogrammetric Engineering & Remote Sensing
Vol. 81, No. 1, January 2015, pp. 59–67.
0099-1112/15/811–59

© 2014 American Society for Photogrammetry
and Remote Sensing
doi: 10.14358/PERS.81.1.59

Institute of Geodesy and Geophysics, Chinese Academy of sciences, 340 XuDong Rd. Wuhan 430077, Hubei, China (lingf@whigg.ac.cn).

has been developed in recent years. Previous studies have shown that pixel-based classification methods that integrate previous land cover map information outperform methods that independently classify images. Xian *et al.* (2010) updated 2001 NLCD impervious surface products to 2006 through a change detection method with Landsat imagery. Chen *et al.* (2012) proposed an automatic approach to update land cover maps. With the application of a change detection method to the previous map and current image (Chen *et al.*, 2011), the aforementioned land cover map updating approaches are simplified to update only the labels of changed pixels in the current image. However, these methods require that current remotely sensed images have a spatial resolution as fine as that of the previous land cover map and that the advantage of coarse-resolution images with a high temporal resolution be ignored.

This study proposes a novel land cover map updating method that involves the use of a current coarse-resolution image and a previous fine-resolution land cover map to update fine-resolution land cover maps. The proposed method comprises a change detection method and an SPM method. The change detection method is utilized to detect which fine-resolution pixels are changed in each coarse-resolution image pixel, whereas SPM is used to label only the changed fine-resolution pixels instead of all the fine-resolution pixels in the image. The proposed method was validated on the basis of synthetic multi-spectral and Landsat images by comparison of the proposed method with a hard classification method and two SPM methods.

Methods

The proposed method comprises a change detection method and an SPM method. The change detection method is used to produce a fine-resolution binary change/non-change map. SPM is utilized to label only the changed fine-resolution pixels according to the binary change/non-change map.

Change Detection Method

Change detection techniques can be grouped into two categories. One category involves detecting binary change/non-change information, and the other category involves detecting the “from - to” change trajectory. In this study, fine-resolution pixel change/non-change information is detected on the basis of coarse- and fine-resolution images. Although several remote sensing techniques have been successfully used in change detection, most of them focus on the change “between” classes measured in a crisp way through which each pixel label is changed or unchanged in different images. When the spatial resolution of a remotely sensed pixel is coarse, the pixel is usually not pure and comprises different land cover classes. Therefore, crisp change detection methods are inappropriate for coarse-resolution image change detection. Rather, the significance arises in the way that land cover fractions within each pixel may change in different images. Spectral unmixing applied to coarse-resolution images can generate land cover fraction images that represent land-cover area proportions within each pixel at the sub-pixel scale. Fraction image-based change detection methods quantify the change in different classes within each pixel by comparing the fraction images acquired at different times, so these methods are suitable for the change detection of coarse-resolution remotely sensed images (Lu *et al.*, 2004a). In this study, the fraction image-based change detection method is applied to detect sub-pixel land cover change information by comparing a pair of current and previous fraction images.

Current fraction images are produced by applying spectral unmixing to the current coarse-resolution image. Previous studies have confirmed that linear spectral mixture analysis (LSMA) can extract land cover fractions that represent area

proportions of the endmembers within the pixel and can be applied in land cover fractional change detection (Roberts *et al.*, 1998; Ju *et al.*, 2003; Lu *et al.*, 2004b). In this study, LSMA is applied to current coarse-resolution images to generate current land cover fraction images.

The previous coarse-resolution fraction images are spatially degraded on the basis of the previous fine-resolution land cover map with the use of a mean filter (Foody *et al.*, 2002; Tatem *et al.*, 2003; Wang *et al.*, 2014). We assume C classes in the previous map. C fine-resolution binary category maps are first produced. In the k^{th} ($k = 1, \dots, C$) fine-resolution land cover category map, a value of 1 is assigned to the fine-resolution pixel if it belongs to class k ; otherwise, a value of 0 is assigned to it. The scale factor between the size of the coarse-resolution image pixel and the pixel in the fine-resolution map is defined as s , and each coarse-resolution pixel contains s^2 fine-resolution pixels (sub-pixels). Each of the C fine-resolution binary category maps is then spatially degraded with a mean filter that has an $s \times s$ fine-resolution pixel window to generate a previous coarse-resolution fraction image of that class.

After the current and previous coarse-resolution fraction images are produced, the change/non-change information of each class in every coarse-resolution pixel can be obtained. A fraction differencing image for each class is produced by application of a subtraction operation to the current and previous fraction images of that class. Assume that $F_{k,pre}$ and $F_{k,cur}$ are the previous and current fraction images of class k . ΔF_k is the fraction differencing image of class k and is calculated as follows:

$$\Delta F_k = F_{k,pre} - F_{k,cur} . \quad (1)$$

In implementing change/non-change detection on each fraction differencing image, establishing a threshold level to define the land cover change of that class in each coarse-resolution pixel is necessary. In this study, the threshold is determined through the use of training images (Lu *et al.*, 2004b). These training images include a pair of a previous fine-resolution map and a current coarse-resolution remotely sensed image of a training region. The previous training image is acquired temporally close to the previous data as the input of proposed model, and the current training image is acquired temporally close to the current data as the input of proposed model. The previous fine-resolution training map is spatially degraded into the previous training fraction images, and the current coarse-resolution training image is unmixed into the current training fraction images. The training fraction differencing images are obtained from the pair of previous and current training fraction images according to Equation 1. The selection of thresholds for each class is based on statistical analysis of unchanged land-cover sample plots within the training fraction differencing image of that class, in consideration of the fact that unchanged land covers have normally distributed histograms in fraction differencing values (the mean value is close to zero), whereas changed land covers do not. Assume that SD_k is the standard deviation of the values of pixels that cover the unchanged sample plots in the training fraction differencing image of class k . The land cover fraction change/non-change threshold value for class k , called T_k , equals to $3 \times SD_k$ (Lu *et al.*, 2004b).

The fine-resolution binary change/non-change map is created after the fraction change/non-change threshold for each class is determined with the use of the training data. The change or non-change of each fine-resolution pixel is determined as follows. We assume that b_i is the i^{th} coarse-resolution pixel in the current image, and $a_{i,j}$ is the j^{th} fine-resolution pixel in b_i . We also assume that the label of $a_{i,j}$ in the previous map is class k . First, we determine whether the fraction value of class k in b_i is changed by comparing the value of coarse-resolution i in the fraction differencing image

ΔF_k (called $\Delta F_{k,i}$) and the threshold value T_k . If $\Delta F_{k,i}$ falls in the range of $-T_k$ to T_k , the fraction value of class k in b_i is unchanged; otherwise, the fraction value of class k in b_i is changed. We make the simple assumption that if the fraction value of class k in b_i is unchanged, then all the fine-resolution pixels labeled as class k in b_i in the previous map are unchanged; therefore, the fine-resolution pixel $a_{i,j}$ is labeled as “unchanged” in the fine-resolution binary change/non-change map. Likewise, if the fraction value of class k in b_i is changed, all the fine-resolution pixels labeled as class k in b_i in the previous map are changed, and the fine-resolution pixel $a_{i,j}$ is labeled as “changed” in the fine-resolution binary change/non-change map.

Sub-pixel Mapping

SPM is an approach to predict fine-resolution pixel (or sub-pixel) labels within each coarse-resolution pixel. SPM is essentially a hard classification technique at a finer spatial resolution than that of the input coarse-resolution remotely sensed image. Several SPM methods have been proposed in recent years (Table 1). These methods include pixel-swapping algorithm (Atkinson, 2005; Foody and Doan, 2007; Makido *et al.*, 2007; Li *et al.*, 2011; Tong *et al.*, 2013; Xu and Huang, 2014), Hopfield neural networks (Tatem *et al.*, 2003; Ling *et al.*, 2010; Muad and Foody, 2012), spatial attraction model (Mertens *et al.*, 2006; Ge *et al.*, 2009; Shen *et al.*, 2009; Ling *et al.*, 2013), Markov random field (Kasetkasem *et al.*, 2005; Tolpekin and Stein, 2009; Ardila *et al.*, 2011; Li *et al.*, 2012; Wang and Wang, 2013), spatial-spectral managed model (Ling *et al.*, 2012; Li *et al.*, 2014), spatial regularization (Villa *et al.*, 2011), indicator kriging (Boucher and Kyriakidis, 2007; Wang *et al.*, 2014), interpolation model (Ling *et al.*, 2013), multiple-point simulating model (Ge, 2013), particle swarm optimization (Wang *et al.*, 2012), and supervised fuzzy c-means-based model (Li *et al.*, 2012).

Spatial-spectral managed SPM algorithm (SSMA) is a simple yet effective method that can be applied directly to remotely sensed images. SSMA is utilized in this study to label current fine-resolution pixels marked as changed pixels in the fine-resolution change/non-change map, rather than labeling all current fine-resolution pixel labels in the entire image as traditional SPM methods do. SSMA comprises three parts: a spatial term, a spectral term, and a balance parameter. The spatial term is the regularization term aiming to make the solution smooth. The spectral term is the data term to preserve information of the original coarse-resolution image. The balance parameter is utilized to balance the contribution of the spatial and spectral

terms.

We assume that the coarse-resolution image is \mathbf{y} , and \mathbf{y} contains B bands with each band containing n pixels. The output of SPM is a fine-resolution land cover map (\mathbf{c}). The goal function (E) of SSMA is characterized as:

$$E = \lambda \cdot E^{\text{spatial}} + E^{\text{spectral}} \quad (2)$$

where E^{spatial} is the spatial term, E^{spectral} is the spectral term, and λ is the balance parameter.

The SSMA spatial term aims to maximize the spatial correlation of neighboring fine-resolution pixels based on the assumption that spatially proximate observations of a given property are more similar than distant observations (Verhoeve and De Wulf, 2002; Makido and Shortridge, 2007; Atkinson, 2009). The spatial term for fine-resolution pixel j in coarse-resolution pixel i , $a_{i,j}$, is computed as:

$$E^{\text{spatial}}(c(a_{i,j})) = \sum_{l \in N(a_{i,j})} \frac{1}{d(a_{i,j}, a_l)} \cdot \delta(c(a_{i,j}), c(a_l)) \quad (3)$$

where $N(a_{i,j})$ is a symmetric neighborhood system that includes all fine-resolution pixels inside a square window whose center is $a_{i,j}$ ($a_{i,j}$ itself is not included in the window); $d(a_{i,j}, a_l)$ is the Euclidian distance between $a_{i,j}$ and a_l ($a_l \in N(a_{i,j})$); $c(a_{i,j})$ and $c(a_l)$ are the land cover class labels of fine-resolution pixels $a_{i,j}$ and a_l . $\delta(c(a_{i,j}), c(a_l))$ is defined as:

$$\delta(c(a_{i,j}), c(a_l)) = \begin{cases} -1 & c(a_l) = c(a_{i,j}) \\ 0 & c(a_l) \neq c(a_{i,j}) \end{cases} \quad (4)$$

The spectral term is utilized to preserve information of the original coarse-resolution image. Assume that \mathbf{y}_i is the observed pixel spectral value of pixel b_i in \mathbf{y} , $\boldsymbol{\mu}_i$ is the synthetic coarse-resolution pixel spectral vector of pixel b_i . Assume that the spectrum measured by a sensor is a linear combination of the spectra of all components within the pixel, $\boldsymbol{\mu}_i$ is calculated as:

$$\boldsymbol{\mu}_i = \sum_{k=1}^C \theta_{ki} \boldsymbol{\mu}_k \quad (5)$$

where θ_{ki} is the proportion of class k in pixel b_i ; θ_{ki} is calculated from label map \mathbf{c} which is the SSMA intermediate result in each iteration, by dividing the number of fine-resolution

TABLE 1. SUB-PIXEL MAPPING (SPM) METHOD NAMES AND IMPORTANT MATHEMATICAL VARIABLES DEFINITION

SPM and variables names	Definition
PSA	Pixel-swapping algorithm based SPM
SSMA	Spatial-spectral managed SPM
CD_SSMA	Land cover map updating method that incorporates change detection and SSMA
MDC	Minimum distance classifier
\mathbf{y}	Current coarse-resolution image
\mathbf{c}	Current fine-resolution land cover map outputted from SPM
ΔF_k	Fraction differencing image of class k
T_k	Land cover fraction change/non-change threshold value for class k in ΔF_k
b_i	The i -th coarse-resolution pixel in the current image
$a_{i,j}$	The j -th fine-resolution pixel in b_i .
$c(a_{i,j})$	The land cover class label of the fine-resolution pixel $a_{i,j}$
s	Scale factor between the size of the coarse-resolution image pixel and the pixel in the fine-resolution map
λ	Balance parameter in SSMA and CD_SSMA

pixels labeled as class k in pixel b_i by total fine-resolution pixel number, i.e., s^2 , in b_i ; and μ_k is the endmember spectral vector of class k . The SSMA spectral term for pixel b_i is expressed as

$$E^{\text{spectral}}(b_i) = (\mathbf{y}_i - \boldsymbol{\mu}_i)^T (\mathbf{y}_i - \boldsymbol{\mu}_i) \quad (6)$$

where T is the transposition operation. Therefore, the goal function (E) of SSMA is calculated as:

$$E = \lambda \cdot \sum_{i,j} E^{\text{spatial}}(c(a_{i,j})) + \sum_i E^{\text{spectral}}(b_i) \quad (7)$$

SSMA optimization is achieved by minimizing the goal function through simulated annealing (Geman and Geman, 1984).

Land Cover Map Updating by Integrating Change Detection and SPM

The proposed land cover map updating method that incorporates change detection and SSMA (CD_SSMA) is a modification of SSMA. Compared with SSMA, CD_SSMA adopts the fine-resolution binary change/non-change map and the previous fine-resolution map as base maps to update the fine-resolution pixel labels. CD_SSMA determines if the fine-resolution pixel is changed before labeling this fine-resolution pixel. If a fine-resolution pixel is detected as “changed” in the binary change/non-change map, this fine-resolution pixel is labeled according to the SSMA goal function; if a fine-resolution pixel is detected as “unchanged” in the binary change/non-change map, this fine-resolution pixel

is labeled according to the previous fine-resolution land cover map. The flowchart of CD_SSMA is shown in Figure 1.

Methods for Comparison

CD_SSMA was compared with a hard classification method and two SPM methods. Minimum distance classifier (MDC) was employed as the hard classification method to generate the pixel-based classification map. The pixel-swapping algorithm (PSA) (Atkinson, 2005) and SSMA were utilized as SPM methods for comparison. PSA is a widely used SPM method. In the PSA initialization step, the fine-resolution pixels of each class within each coarse-resolution pixel are randomly labeled according to the numbers calculated with the use of land cover fraction images, which are the output of a spectral unmixing model. In each iteration, two fine-resolution pixels with different land cover labels are randomly selected from each coarse-resolution pixel. If swapping these two fine-resolution pixels increases the land cover spatial dependence of the land cover map, these two fine-resolution pixels are swapped. PSA stops when a fixed number of iteration is reached. MDC, PSA, and SSMA adopt a coarse-resolution mono-temporal image as input.

Experimental Results

Experiment on Synthetic Multi-spectral Images

A synthetic multi-spectral image was used as the current coarse-resolution image to avoid spectral signature bias in deriving the endmember signatures. The previous and current

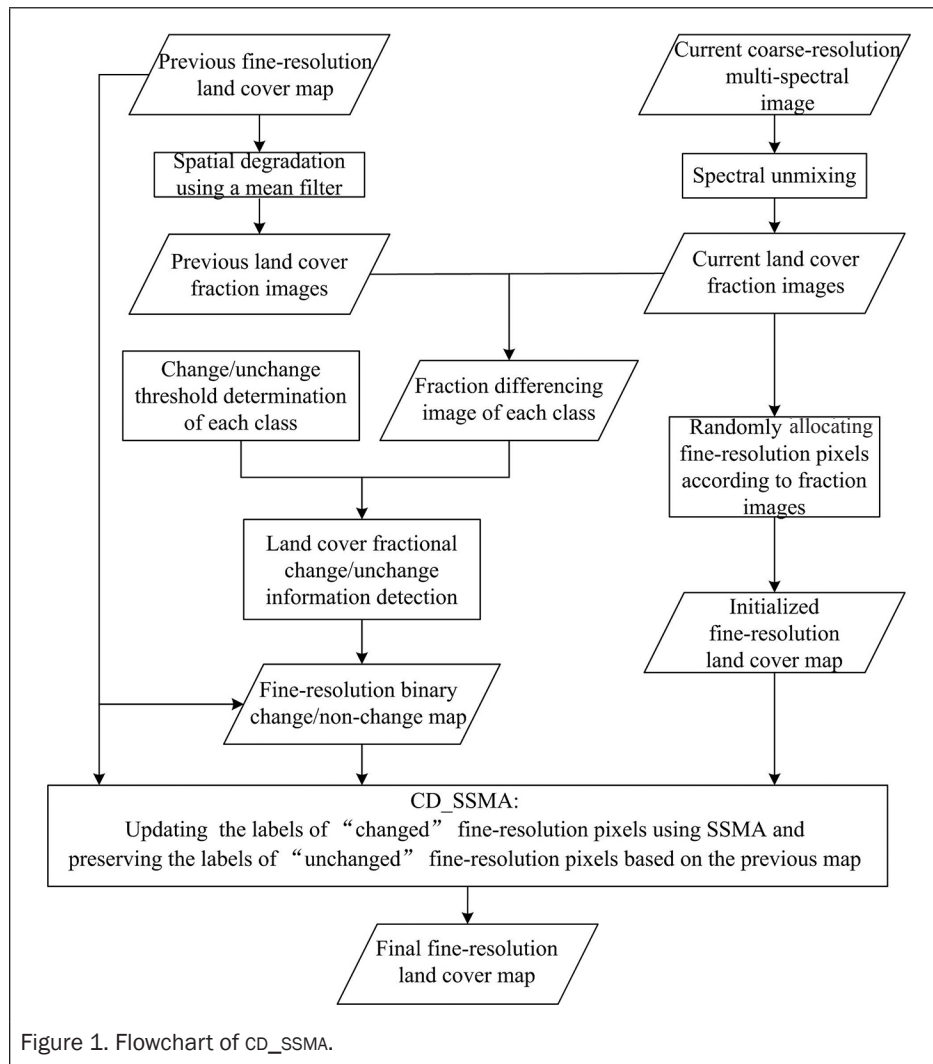


Figure 1. Flowchart of CD_SSMA.

fine-resolution land cover maps were obtained from NLCD 2001 and 2006, respectively. NLCD is a land cover classification scheme that has been applied consistently at a spatial resolution of 30 m across the United States. NLCD is based primarily on unsupervised classification of Landsat satellite data. NLCD 2001 and 2006 are strictly geo-registered to the Albers Equal Area projection grid (Homer *et al.*, 2004). In this study, the original 16 land cover classes in NLCD 2001 and 2006 were combined and reclassified into five classes, namely, Water-Wetlands, Developed-Barren, Forest, Shrubland-Herbaceous, and Planted/Cultivated.

Both the previous map obtained from NLCD2001 and the current map obtained from NLCD2006 contain 800×800 pixels of the same area located in Charlotte, North Carolina. The previous map is used as CD_SSMA input. The current map is used not only as the reference map for model validation, but also to produce the current coarse-resolution multi-spectral image. The number of bands was set to 4 to simulate the fine-resolution multi-spectral images. The five endmember signature DN values were set to $[380, 490, 300, 320]^T$, $[310, 335, 235, 260]^T$, $[250, 410, 180, 390]^T$, $[230, 360, 320, 345]^T$, and $[450, 220, 120, 170]^T$. The spectral response of each class was assumed to be normally distributed in each waveband. The covariance matrixes for all the classes were set to $600 \cdot \mathbf{M}$, where \mathbf{M} is a 4×4 matrix of 1. The coarse-resolution multi-spectral images were then generated by spatially degrading the fine-resolution multi-spectral image with a mean filter with scale factor $s = 5$ and $s = 10$ (Tolpekin and Stein, 2009).

The training images used to determine the land cover fraction change/non-change threshold values were also obtained from NLCD2001 and NLCD2006. The previous and current fine-resolution training maps contain $4,000 \times 4,000$ pixels near the study area. The current coarse-resolution multi-spectral image was produced on the basis of the current fine-resolution training map with the use of the same method as that used to produce the multi-spectral testing data as CD_SSMA input.

The parameters of the different SPM methods were set. Neighborhood window size, which is the length of the square side of the neighborhood, was set to 5 in PSA (Makido and Shortridge, 2007) and 7 in both SSMA and CD_SSMA (Ardila *et al.*, 2011). Balance parameter λ in SSMA and CD_SSMA was set empirically. If λ is small, the result maps are unsmoothed with isolated patches; if λ is large, the result maps are over-smoothed with rounded patches. In this study, $\lambda = 80$ was set at $s = 5$, and $\lambda = 5$ was set at $s = 10$.

The CD_SSMA training images are shown in Plate 1. A mean filter was used to spatially degrade the previous fine-resolution training map. LSMA was utilized to unmix the current coarse-resolution training image. Comparing the previous and current fraction images obtained from the training images and applying the supervised change detection method (Lu *et al.*, 2004b) to the images helped determine the land cover fraction change/non-change threshold values of the fractional change for each class (Table 2).

Plate 1 also shows the classification and SPM results, which differ significantly. The class boundaries in the MDC result are serrated and rough because the hard classification map is produced at the pixel scale and the mixed pixels are labeled as monotypes regardless of the spatial patterns of land cover classes within mixed pixels. In the PSA and SSMA results, the land cover patches are aggregated into rounded patches because SPM maximizes the spatial correlation of neighboring fine-resolution pixels. Many speckle artifacts in salt-and-pepper appearance can be seen in the PSA result. This is because the fine-resolution pixel number of a class, which is determined by class fractions of that class in the coarse-resolution pixel, is very few, and these fine-resolution pixels are characterized as speckle artifacts in the result map. In PSA,

TABLE 2. LAND COVER FRACTION CHANGE/NON-CHANGE THRESHOLD VALUES FOR DIFFERENT CLASSES FOR SYNTHETIC IMAGES

		$s=5$	$s=10$
Threshold value	Water-Wetlands	0.1043	0.0612
	Developed-Barren	0.1995	0.1301
	Forest	0.0432	0.0290
	Shrubland-Herbaceous	0.0835	0.0543
	Planted/Cultivated	0.0618	0.0473

TABLE 3. ACCURACIES OF THE DIFFERENT METHODS USING SYNTHETIC IMAGES

		Kappa	QD	AD	OA
$S = 5$	MDC	0.6753	0.0289	0.2050	0.7806
	PSA	0.7071	0.0080	0.2055	0.8008
	SSMA	0.7200	0.0390	0.1619	0.8110
	CD_SSMA	0.9172	0.0088	0.0513	0.9507
$S = 10$	MDC	0.5336	0.0535	0.2660	0.7004
	PSA	0.5188	0.0094	0.3442	0.6747
	SSMA	0.5527	0.0211	0.3016	0.6997
	CD_SSMA	0.7774	0.0103	0.1514	0.8575

swapping a pair of fine-resolution pixels within the coarse-resolution pixel does not change class fractions. By contrast, such speckle artifacts are mostly eliminated by SSMA in which the land cover fractions can be changed before and after SPM (Kasetkasem *et al.*, 2005; Tolpekin and Stein, 2009; Ling *et al.*, 2012; Li *et al.*, 2014). The CD_SSMA result matches the reference map better than the other results. The speckle artifacts are eliminated, and the spatial pattern of the linear-shaped Developed-Barren class, which is unchanged in the previous and current maps, is preserved in the zoomed area because CD_SSMA incorporates a change detection method and preserves the unchanged fine-resolution pixel labels. The scale factor plays an important role in the results. With the increase in the scale factor, the MDC map becomes coarse and the PSA and SSMA maps acquire more aggregated patches. By contrast, the CD_SSMA result does not change significantly.

A quantitative comparison was conducted with Kappa value, quantitative disagreement (QD), and allocation disagreement (AD) to assess the match between the reference land cover map and the resulting land cover map. QD is the difference between the reference and resulting maps caused by a less-than-optimal match in the proportions of categories. AD is the difference between the reference and resulting maps caused by a less-than-optimal match in the spatial allocation of categories given the proportions of the categories in the reference and resulting maps. Low values of QD and AD show a good match between the resulting and reference maps (Pontius and Millones, 2011). Overall accuracy (OA) calculated from the change/non-change matrix was utilized to quantify the match between the real change/non-change map and the resulting change/non-change map. The real change/non-change map is produced by a per-pixel comparison of the reference and previous maps, whereas the resulting change/non-change map is produced by a per-pixel comparison of the resulting and previous maps. The accuracies of the different methods are shown in Table 3. The Kappa and OA values for all the methods are higher at $s = 5$ than at $s = 10$, and the QD and AD values for all the methods are lower at $s = 5$ than at $s = 10$ except for the QD value for SSMA. This result shows that coarsening the current coarse-resolution remotely sensed image always reduces the accuracy of different methods in land cover map updates. The Kappa values of CD_SSMA are approximately 0.20 higher than

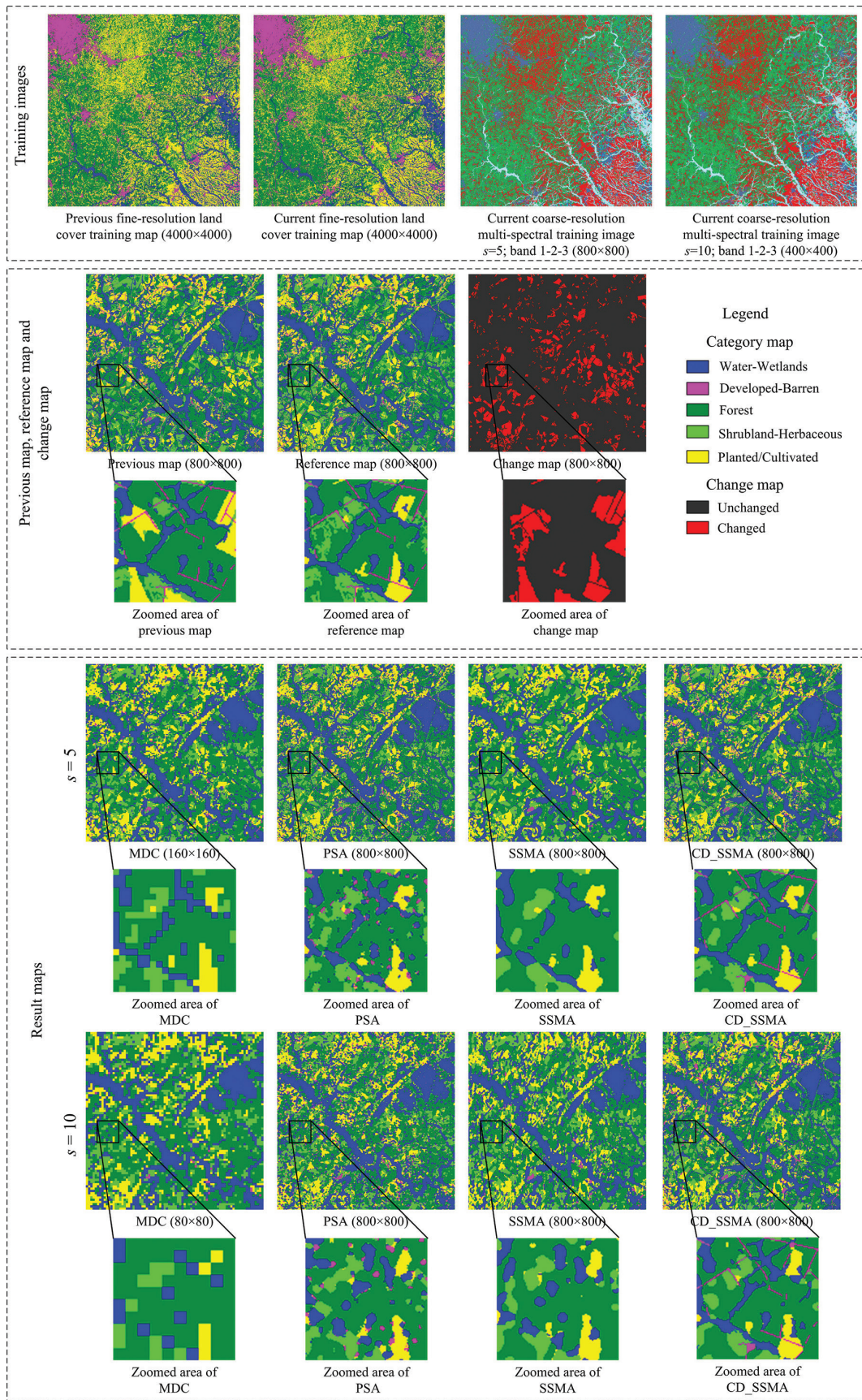


Plate 1. Training images, previous map, reference map, change map, and result maps of different methods using a synthetic multi-spectral image: (a) Training images, (b) Previous map, reference map, and change map, and (c) Results map.

those of the other methods, and the OA values of CD_SSMA are approximately 0.15 higher than those of the other methods at $s = 5$ and $s = 10$. The QD and AD values for MDC are high; this finding reveals the influence of the mixed pixel problem on pixel-based classification. The AD value for PSA is extremely high; this result shows that the uncertainty of the spatial locations of different land cover classes is the main factor that affects accuracy. The QD and AD values for CD_SSMA are lower than those of SSMA, MDC, and PSA at $s = 5$ and $s = 10$ (except for the QD value of PSA). Thus, CD_SSMA is effective to predict the locations of land cover classes at the sub-pixel scale.

Experiment on Landsat Images

CD_SSMA was validated on Landsat multi-spectral imageries in this experiment. The study area is located near Sorriso (12°33'21"S and 55°42'31"W) in Mato Grosso State, Brazil. This area is in the Brazilian Amazon Basin, which is mainly covered by tropical forests and has undergone a massive deforestation process in recent years. A Thematic Mapper (TM) image acquired on 11 July 1988 with a spatial resolution of 28.5 m was employed to produce the previous land cover map. A Landsat Enhanced Thematic Mapper+ (ETM+) image acquired on 18 July 2005 with a spatial resolution of 30 m was utilized to produce the reference land cover map. The TM

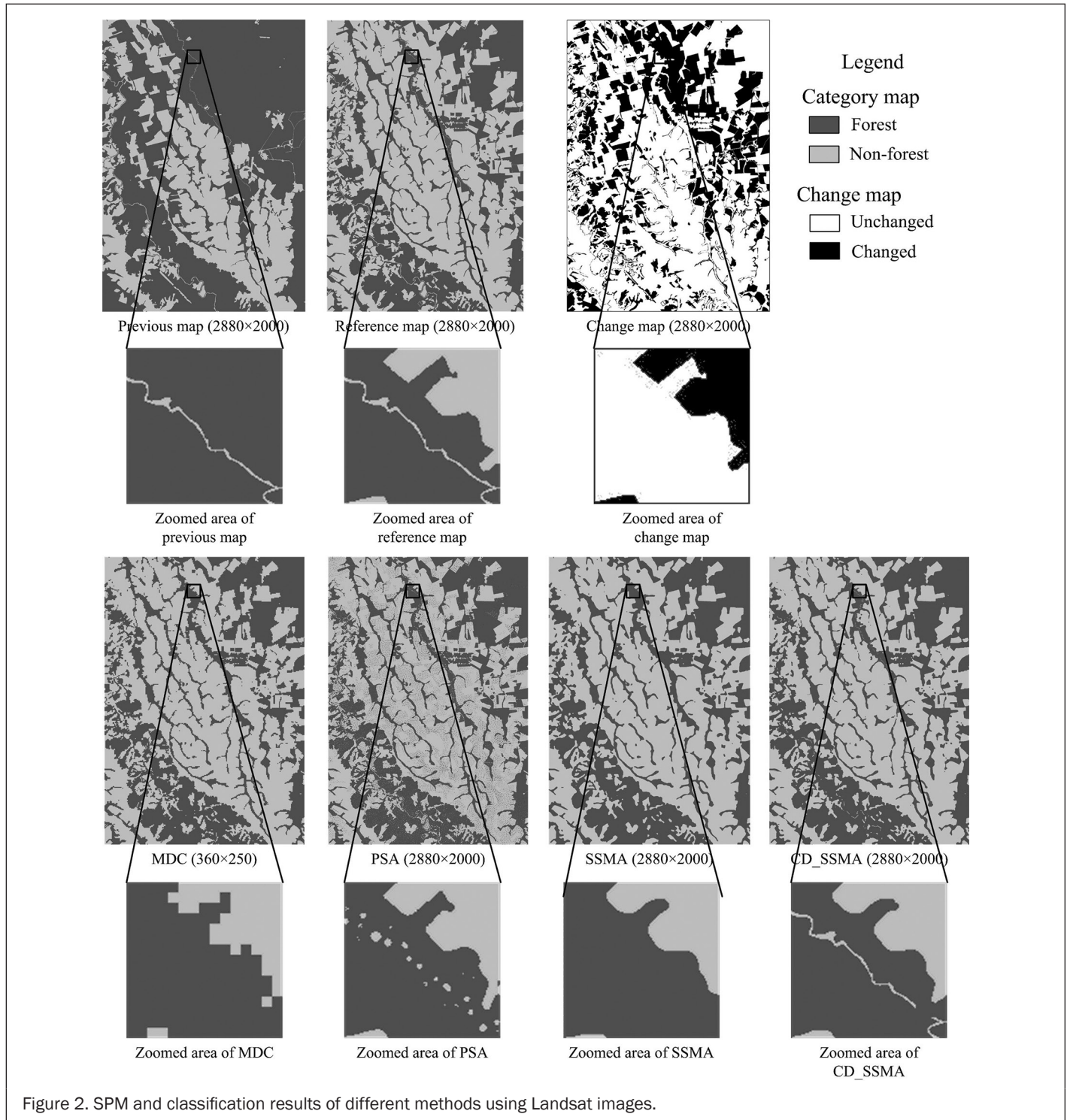


image was geo-registered to the ETM+ image and resampled at a spatial resolution of 30 m. The registration error between the TM and ETM+ images was less than 0.5 pixel. The TM and ETM+ images were subset with 2,880 × 2,000 pixels and then manually digitized to the previous and reference maps with forest and non-forest classes in the maps. In addition, the ETM+ image (red and near-infrared bands) was spatially degraded into the coarse-resolution image with a mean filter with the scale factor $s = 8$ to simulate the first two bands of MODIS image at a spatial resolution of 250 m.

The previous and current fine-resolution training images with 1,600 × 1,600 fine-resolution pixels were obtained from the same TM and ETM+ images located near the study area. The previous fine-resolution training image was manually digitized to the previous training land cover map, which was then spatially degraded into the previous fraction images with a mean filter at $s = 8$. The current fine-resolution training image was spatially degraded into the coarse-resolution multi-spectral images with a mean filter at $s = 8$, which was then unmixed into current fraction images with the use of LSMA. Comparison of the pair of previous and current training fraction images with the use of the supervised change detection method (Lu *et al.*, 2004b) shows that the land cover fraction change/non-change threshold values were 0.1585 for both forest and non-forest. The neighborhood window size values in PSA, SSMA, and CD_SSMA were set similar to those in the synthetic image experiment. $\lambda = 1$ was set in SSMA and CD_SSMA through numerous trials.

As can be seen in Figure 2, MDC generates aggregated and discontinuous patches. The small linear object in the zoomed area is eliminated because of the coarse resolution of the remotely sensed image. In the PSA result, the linear object is discontinuous. In the SSMA result, the linear object is eliminated because of the spatial smoothing effect. By contrast, the linear object is mostly preserved in the CD_SSMA result. Quantitative analysis shows that the Kappa and OA values of CD_SSMA are higher than those of other methods (Table 4). Although the QD value of CD_SSMA is approximately 0.003 higher than that of MDC and SSMA, the AD value of CD_SSMA is approximately 0.01 lower than that of the other methods.

TABLE 4. ACCURACIES OF THE DIFFERENT METHODS USING LANDSAT IMAGES

	Kappa	QD	AD	OA
MDC	0.8862	0.0147	0.0429	0.9524
PSA	0.8890	0.0203	0.0326	0.9471
SSMA	0.8993	0.0142	0.0336	0.9522
CD_SSMA	0.9116	0.0181	0.0239	0.9570

Conclusions

CD_SSMA, a sub-pixel scale land cover map updating method that integrates change detection and SPM, was developed in this study. CD_SSMA utilizes current coarse-resolution images with high temporal resolution and previous land cover maps with fine spatial resolution to update land cover maps with high temporal and fine spatial resolutions. Unlike other SPM methods that directly label all the fine-resolution pixels in the image, CD_SSMA employs a change detection method to produce a fine-resolution binary change/non-change map and only updates the fine-resolution pixels that are changed in the binary change/non-change map through the use of SSMA. The spatial patterns of the unchanged fine-resolution pixels in the previous map can be preserved in the CD_SSMA result.

The proposed method was tested on synthetic multi-spectral and Landsat images by comparing the proposed method with a hard classification method and two SPM methods,

namely, PSA and SSMA. The results show that the hard classification method generates land cover maps with serrated boundaries because of the coarse resolution of the remotely sensed image. PSA generates land cover maps with speckle artifacts, and SSMA generates land cover maps with over-smoothed boundaries. CD_SSMA generates land cover maps that are close to the reference map and preserves most of the spatial patterns of the unchanged classes. Quantitative analysis shows that the CD_SSMA results have higher Kappa values and lower allocation disagreement values in all experiments by comparison with the results of the other methods.

The accuracy of CD_SSMA is related to the number of constraints. First, CD_SSMA requires that the registration error between the previous fine-resolution land cover map and the current coarse-resolution image be strictly controlled because mis-registration will reduce the change detection accuracy. Furthermore, training images are necessary to obtain the threshold value for the identification of unchanged classes in every coarse-resolution pixel. Unsupervised threshold determination methods that can be applied without image training must be developed. Finally, the balance parameter in the SPM procedure of CD_SSMA was set by trials. A comprehensive study that involves the automatic estimation of the optimal balance parameter value is required in the future.

Acknowledgments

This work was supported in part by the Natural Science Foundation of China under Grant No. 41301398, in part by the National Basic Research Program (973 Program) of China under Grant No. 2013cb733205 and in part by Natural Science Foundation of Hubei Province for Distinguished Young Scholars under Grant No. 2013CFA031.

References

- Ardila, J.P., V.A. Tolpekin, W. Bijker, and A. Stein, 2011. Markov-random-field-based super-resolution mapping for identification of urban trees in VHR images, *ISPRS Journal of Photogrammetry and Remote Sensing*, 66(6):762–775.
- Atkinson, P.M., 2005. Sub-pixel target mapping from soft-classified, remotely sensed imagery, *Photogrammetric Engineering & Remote Sensing*, 71(7):839–846.
- Atkinson, P.M., 2009. Issues of uncertainty in super-resolution mapping and their implications for the design of an inter-comparison study, *International Journal of Remote Sensing*, 30(20):5293–5308.
- Boucher, A., and P.C. Kyriakidis, 2007. Integrating fine scale information in super-resolution land-cover mapping, *Photogrammetric Engineering & Remote Sensing*, 73(8):913–921.
- Braswell, B.H., S.C. Hagen, S.E. Frolking, and W.A. Salas, 2003. A multivariable approach for mapping sub-pixel land cover distributions using MISR and MODIS: Application in the Brazilian Amazon region, *Remote Sensing of Environment*, 87(2-3):243–256.
- Chen, J., X. Chen, and X. Cui, 2011. Change vector analysis in posterior probability space: A new method for land cover change detection, *IEEE Geoscience and Remote Sensing Letters*, 8(2):317–321.
- Chen, X., J. Chen, Y. Shi, and Y. Yamaguchi, 2012. An automated approach for updating land cover maps based on integrated change detection and classification methods, *ISPRS Journal of Photogrammetry and Remote Sensing*, 71:86–95.
- Congalton, R.G., 1991. A review of assessing the accuracy of classifications of remotely sensed data, *Remote Sensing of Environment*, 37(1):35–46.
- Foody, G.M., 2006. Sub-pixel methods in remote sensing, *Remote Sensing Image Analysis: Including the Spatial Domain*, pp. 37–49.
- Foody, G.M., and H.T.X. Doan, 2007. Variability in soft classification prediction and its implications for sub-pixel scale change detection and super resolution mapping, *Photogrammetric Engineering & Remote Sensing*, 73(8):923–933.
- Foody, G.M., P.M. Atkinson, and J. Wiley, 2002. *Uncertainty in Remote Sensing and GIS*, Wiley Online Library.

- Friedl, M.A., D.K. McIver, J.C. Hodges, X. Zhang, D. Muchoney, A.H. Strahler, C.E. Woodcock, S. Gopal, A. Schneider, and A. Cooper, 2002. Global land cover mapping from MODIS: Algorithms and early results, *Remote Sensing of Environment*, 83(1):287–302.
- Ge, Y., 2013. Sub-pixel land-cover mapping with improved fraction images upon multiple-point simulation, *International Journal of Applied Earth Observation and Geoinformation*, 22:115–126.
- Ge, Y., S. Li, and V.C. Lakhani, 2009. Development and testing of a sub-pixel mapping algorithm, *IEEE Transactions on Geoscience and Remote Sensing*, 47(7):2155–2164.
- Geman, S., and D. Geman, 1984. Stochastic relaxation, Gibbs distributions, and the Bayesian restoration of images, *IEEE Transactions on Pattern Analysis and Machine Intelligence*, 6(6):721–741.
- Homer, C., C. Huang, L. Yang, B. Wylie, and M. Coan, 2004. Development of a 2001 National Land-Cover Database for the United States, *Photogrammetric Engineering & Remote Sensing*, 70(7):829–840.
- Homer, C., J. Dewitz, J. Fry, M. Coan, N. Hossain, C. Larson, N. Herold, A. McKerrow, J.N. VanDriel, and J. Wickham, 2007. Completion of the 2001 National Land Cover Database for the conterminous United States, *Photogrammetric Engineering & Remote Sensing*, 73(4):337–341.
- Ju, J., E.D. Kolaczyk, and S. Gopal, 2003. Gaussian mixture discriminant analysis and sub-pixel land cover characterization in remote sensing, *Remote Sensing of Environment*, 84(4):550–560.
- Kasetkasem, T., M.K. Arora, and P.K. Varshney, 2005. Super-resolution land cover mapping using a Markov random field based approach, *Remote Sensing of Environment*, 96(3-4):302–314.
- Li, X., F. Ling, and Y. Du, 2012. Super-resolution mapping based on the supervised fuzzy c-means approach, *Remote Sensing Letters*, 3(6):501–510.
- Li, X., Y. Du, and F. Ling, 2012. Spatially adaptive smoothing parameter selection for Markov random field based sub-pixel mapping of remotely sensed images, *International Journal of Remote Sensing*, 33(24):7886–7901.
- Li, X., F. Ling, Y. Du, and Y. Zhang, 2014. Spatially adaptive super-resolution land cover mapping with multispectral and panchromatic images, *IEEE Transactions on Geoscience and Remote Sensing*, 52(5):2810–2823.
- Li, X., Y. Du, F. Ling, S. Wu, and Q. Feng, 2011. Using a sub-pixel mapping model to improve the accuracy of landscape pattern indices, *Ecological Indicators*, 11(5):1160–1170.
- Ling, F., W. Li, Y. Du, and X. Li, 2011. Land cover change mapping at the subpixel scale with different spatial-resolution remotely sensed imagery, *IEEE Geoscience and Remote Sensing Letters*, 8(1):182–186.
- Ling, F., Y. Du, F. Xiao, and X. Li, 2012. Subpixel land cover mapping by integrating spectral and spatial information of remotely sensed imagery, *IEEE Geoscience and Remote Sensing Letters*, 9(3):408–412.
- Ling, F., X. Li, Y. Du, and F. Xiao, 2013. Sub-pixel mapping of remotely sensed imagery with hybrid intra- and inter-pixel dependence, *International Journal of Remote Sensing*, 34(1):341–357.
- Ling, F., Y. Du, F. Xiao, H. Xue, and S. Wu, 2010. Super-resolution land-cover mapping using multiple sub-pixel shifted remotely sensed images, *International Journal of Remote Sensing*, 31(19):5023–5040.
- Ling, F., Y. Du, X. Li, W. Li, F. Xiao, and Y. Zhang, 2013. Interpolation-based super-resolution land cover mapping, *Remote Sensing Letters*, 4(7):629–638.
- Lu, D., M. Batistella, E. Moran, S. Hetrick, D. Alves, and E. Brondizio, 2011. Fractional forest cover mapping in the Brazilian Amazon with a combination of MODIS and TM images, *International Journal of Remote Sensing*, 32(22):7131–7149.
- Lu, D., P. Mausel, E. Brondizio, and E. Moran, 2004a. Change detection techniques, *International Journal of Remote Sensing*, 25(12):2365–2407.
- Lu, D., M. Batistella, and E. Moran, 2004b. Multitemporal spectral mixture analysis for Amazonian land-cover change detection, *Canadian Journal of Remote Sensing*, 30(1):87–100.
- Makido, Y., and A. Shortridge, 2007. Weighting function alternatives for a subpixel allocation model, *Photogrammetric Engineering & Remote Sensing*, 73(11):1233–1240.
- Makido, Y., A. Shortridge, and J.P. Messina, 2007. Assessing alternatives for modeling the spatial distribution of multiple land-cover classes at sub-pixel scales, *Photogrammetric Engineering & Remote Sensing*, 73(8):935–943.
- Mertens, K.C., B. De Baets, L.P.C. Verbeke, and R.R. De Wulf, 2006. A sub-pixel mapping algorithm based on sub-pixel/pixel spatial attraction models, *International Journal of Remote Sensing*, 27(15):3293–3310.
- Muad, A.M., and G.M. Foody, 2012. Super-resolution mapping of lakes from imagery with a coarse spatial and fine temporal resolution, *International Journal of Applied Earth Observation and Geoinformation*, 15:79–91.
- Nguyen, M.Q., P.M. Atkinson, and H.G. Lewis, 2006. Superresolution mapping using a hopfield neural network with fused images, *IEEE Transactions on Geoscience and Remote Sensing*, 44(3):736–749.
- Pontius, R.G., and M. Millones, 2011. Death to Kappa: Birth of quantity disagreement and allocation disagreement for accuracy assessment, *International Journal of Remote Sensing*, 32(15):4407–4429.
- Roberts, D.A., M. Gardner, R. Church, S. Ustin, G. Scheer, and R.O. Green, 1998. Mapping chaparral in the Santa Monica Mountains using multiple endmember spectral mixture models, *Remote Sensing of Environment*, 65(3):267–279.
- Shen, Z., J. Qi, and K. Wang, 2009. Modification of pixel-swapping algorithm with initialization from a sub-pixel/pixel spatial attraction model, *Photogrammetric Engineering & Remote Sensing*, 75(5):557–567.
- Tatem, A.J., H.G. Lewis, P.M. Atkinson, and M.S. Nixon, 2003. Increasing the spatial resolution of agricultural land cover maps using a Hopfield neural network, *International Journal of Geographical Information Science*, 17(7):647–672.
- Tolpekin, V.A., and A. Stein, 2009. Quantification of the effects of land-cover-class spectral separability on the accuracy of Markov-random-field-based superresolution mapping, *IEEE Transactions on Geoscience and Remote Sensing*, 47(9):3283–3297.
- Tong, X., X. Zhang, J. Shan, H. Xie, and M. Liu, 2013. Attraction-repulsion model-based subpixel mapping of multi-/hyperspectral imagery, *IEEE Transactions on Geoscience and Remote Sensing*, 51(5):2799–2814.
- Verhoeve, J., and R. De Wulf, 2002. Land cover mapping at sub-pixel scales using linear optimization techniques, *Remote Sensing of Environment*, 79(1):96–104.
- Villa, A., J. Chanussot, J.A. Benediktsson, and C. Jutten, 2011. Spectral unmixing for the classification of hyperspectral images at a finer spatial resolution, *IEEE Journal of Selected Topics in Signal Processing*, 5(3):521–533.
- Wang, L., and Q. Wang, 2013. Subpixel mapping using Markov random field with multiple spectral constraints from subpixel shifted remote sensing images, *IEEE Geoscience and Remote Sensing Letters*, 10(3):598–602.
- Wang, Q., W. Shi, and L. Wang, 2014. Indicator cokriging-based sub-pixel land cover mapping with shifted images, *IEEE Journal of Selected Topics in Applied Earth Observation and Remote Sensing*, 7(1):327–339.
- Wang, Q., L. Wang, and D. Liu, 2012. Particle swarm optimization-based sub-pixel mapping for remote-sensing imagery, *International Journal of Remote Sensing*, 33(20):6480–6496.
- Xian, G., and C. Homer, 2010. Updating the 2001 National Land Cover Database impervious surface products to 2006 using Landsat imagery change detection methods, *Remote Sensing of Environment*, 114(8):1676–1686.
- Xu, Y., and B. Huang, 2014. A spatio-temporal pixel-swapping algorithm for subpixel land cover mapping, *IEEE Geoscience and Remote Sensing Letters*, 11(2):474–478.

(Received 26 September 2013; accepted 11 August 2014; final version 26 August 2014)

Mapping Wetlands and *Phragmites* Using Publically Available Remotely Sensed Images

Yichun Xie, Anbing Zhang, and William Welsh

Abstract

Using publically available remotely sensed images to map wetlands and invasive plants is attractive to ecologists, environmental scientists, and managers. However, wetland and invasive plant mapping on the basis of no- or low-cost images has been challenged by the variability of mapping accuracy. In this paper, we are developing an innovative wetland and invasive plant mapping technique characterized with three integrations: the integration of image interpretation with feature extraction, the integration of high spatial-resolution images with high spectral-resolution images, and the integration of field reference data with interpreted and classified images. This technique advocates standard procedures for integrating NAIP (National Agriculture Imagery Program) and Landsat images with multiple processes of ground truthing, image classification, and validation. The case study conducted in the Detroit River International Wildlife Refuge concludes that the integration of NAIP and Landsat images provides sufficient spatial and spectral information for mapping coastal wetlands and *Phragmites*.

Introduction

Wetlands provide critical ecosystem services, such as support of biodiversity, improvement of water quality, flood abatement, and carbon sequestration (Mitsch and Gosselink, 2007). Despite their value, wetlands have often been filled, drained, or otherwise destroyed. Wetland losses in Michigan over the past two centuries are estimated at over 50 percent (Dahl, 1990; Reyer *et al.*, 2009). The wetlands that remain often face severe stressors, especially in urban landscapes. These stressors include altered hydrology, increased loads of nutrients and contaminants from within the watershed, fragmentation, and invasion of non-native species. The Great Lakes region has a long history of biological invasions, with over 40 percent of established exotic species being wetland plants (Mills *et al.*, 1993). At least 10 percent of invasive species in this region have caused well-documented environmental problems and substantial economic losses (Mills *et al.*, 1993). One such problematic invasive species currently spreading across the Great Lakes region is the common reed, *Phragmites australis*. Although native strains of this large (2 to 4 m) clonal reed are endemic to North America, an aggressive non-native genotype (Galatoswitsch *et al.*, 1999) has resulted in its recent expansion throughout the Great Lakes (Wilcox *et al.*, 2003) and other regions. Mapping of wetlands and *Phragmites* will provide

baseline data for monitoring *Phragmites* invasion and distribution and for assessing the effects of *Phragmites* invasion and *Phragmites* removal efforts on wetland ecosystem function.

Remote sensing technology has proven to be a practical and economical means to study land cover changes, for resource monitoring, and resource assessment, especially over large areas (Langley *et al.*, 2001; Nordberg and Evertson, 2003; Nielsen *et al.*, 2008). Recent advances in hyperspectral, microwave (radar) and multispectral remote sensing provide powerful and efficient techniques for monitoring plant activities at multiple spatial and temporal scales (Xie *et al.*, 2008). Hyperspectral data, also known as imaging spectroscopy, is generally composed of hundreds of spectral bands with narrow bandwidths (5 to 10 nm), and can accurately detect the absorption features of individual plant components (Varshney and Arora, 2004). Hence, hyperspectral remote sensing is widely applied to identify different species in plant communities. (Andrew and Ustin, 2008; Asner and Martin, 2008; Pengra *et al.*, 2007; Pignattia *et al.*, 2009; Lopez *et al.*, 2006; Ustin *et al.*, 2002; Zhang and Xie, 2014). Radar data have also been used to identify wetland plant communities (Corcoran *et al.*, 2011; Henderson and Lewis, 2008; Kasischke and Bourgeau-Chavez, 1997), including *Phragmites* in the Great Lakes Basin (Bourgeau-Chavez *et al.*, 2004). Radar's active sensors emit energy at a very low angle and create backscattered energy. The backscattered energy is sensitive to the dielectric constant and is primarily affected by the volume, physical structure, and amount of moisture in a material (Kozlov *et al.*, 2001; Kwoun and Lu 2009; Skolnick, 2008). However, in general, the accessibility to hyperspectral and radar data is limited and the associated costs of acquiring and processing are very high.

Multispectral images are the largest family among remotely sensed images. Many among them are free for public access. For instance, NAIP imagery is publically available multispectral data, acquired at a one-meter ground sample distance with four bands of data: RGB and Near-infrared. NAIP imagery has a high spatial resolution, but a coarse spectral resolution. Another publically free accessible image dataset is the Landsat imagery archive, which dates back to 1972. The Landsat images have been a major component of NASA's Earth observation program, with five primary sensors evolving over forty years: MSS (Multi-spectral Scanner), TM (Thematic Mapper), ETM+ (Enhanced Thematic Mapper Plus), OLI (Operational Land Imager), and TIRS (Thermal Infrared Sensor). Landsat-8 contains 11 bands and their spatial resolution is 30 m ground area, except the panchromatic band 8 (15 m) and the thermal infrared

Yichun Xie is with the Institute for Geospatial Research & Education, Eastern Michigan University, 125 King Hall, Ypsilanti, MI 48197 (yxie@emich.edu).

Anbing Zhang is with The School of Hydropower, Hebei University of Engineering, Handan 056021, China.

William Welsh is with the Department of Geography, Eastern Michigan University, 203 Strong Hall, Ypsilanti, MI 48197.

Photogrammetric Engineering & Remote Sensing
Vol. 81, No. 1, January 2015, pp. 69–78.
0099-1112/15/811-69

© 2014 American Society for Photogrammetry
and Remote Sensing
doi: 10.14358/PERS.81.1.69

bands 10 and 11 (100 m). Landsat imagery, through its 16 to 18 day fixed temporal resolution, has a great potential to provide intra-annual image time series. In other words, Landsat imagery has a medium spectral resolution and a high temporal resolution. However, its spatial resolution is often not sufficient for identifying plant species. Although Landsat imagery has long been used to detect wetland vegetation types (Lunetta and Balogh, 1999), high spatial resolution images have been preferred as image datasets for detecting invasive plants by some researchers (Everitt *et al.*, 2005; Walsh *et al.*, 2008).

Image vegetation classification over grassland and wetland from Landsat images is often a challenge (Baker *et al.*, 2006; Sohn and Qi, 2005). Over the land covers with mixed vegetation compositions, the same vegetation type may exhibit different spectral features while different vegetation types may show similar spectra. It is common that plant communities present mosaic-like patterns, which can make it difficult to extract vegetation information from images with acceptable accuracy (Cingolani *et al.*, 2004; Stuart *et al.*, 2006; Lan and Xie, 2013; Xie *et al.*, 2010). This challenge is mainly caused by image resolutions (spatial, spectral, and temporal) when the cost of image acquisition is a limiting factor. For public projects, such as mapping wetlands over a large area for the purpose of natural resource management or ecosystem restoration, the cost of image acquisition can be a critical obstacle. It would be an ideal situation if freely-accessible imagery sources could be used to produce wetland or *Phragmites* maps that are as good as (or close to) those produced with high-resolution commercial images. Therefore, we proposed to fuse the publically-available, no-cost NAIP and Landsat images to overcome the limitations of the spectral resolution of NAIP and the spatial resolution of Landsat imagery for mapping wetlands.

The second challenge is to get a sufficient number of high-quality reference points in order to obtain training signatures and to validate classification results. Lack of coincident ground information with which either to establish discrete land cover classes or to assess the accuracy of their identification has been demonstrated to be a serious limitation for effective use of remotely sensed imagery (Xie *et al.*, 2010). There are three approaches of collecting training samples, either through ground truthing to gather ground reference points (GRPs) or by image data extraction to obtain the surrogates of GRPs, or in combination (Zhang and Xie, 2014). It is usually an expensive and time-consuming task to collect a large number of high-quality field samples (Chi and Bruzzone, 2005). This issue is particularly critical when mapping coastal wetlands and invasive plant species. In these areas, harsh terrain, standing water, rotting plants and litters hinder observers' accessibility. Because of the confounded impact of inaccessibility and high cost, it is often impossible to get a sufficient number of training samples for supporting a proper training of a classification algorithm or validating it.

Another challenge is to determine which image classifier is most successful to extract or identify various plant communities. Numerous image classifiers have been developed to improve classification accuracy, generally divided into unsupervised and supervised approaches (Langley *et al.*, 2001). For supervised classification, a maximum likelihood (ML) classifier is usually regarded as a classic and mostly used for image classifications resting on the normal curve statistical distribution pattern (Higdon and Schafer, 2001; Sohn and Rebello, 2002; Xu *et al.*, 2005). However, ML has its limitation for classifying mixed land uses (or covers) since the assumption of ML that the data follow Gaussian distribution may not always be the case in heterogeneous areas.

A growing volume of literature on new approaches to classification for mapping wetlands or invasive plants has been seen in recent years. In general, these new classifiers fall into

three groups: (a) object-based classifications (OBC) (Benz *et al.*, 2004; Lu and Weng, 2007; Rampi *et al.*, 2014); (b) rule-based classifiers (RBC), which usually involve some type of learning process in image classification, such as fuzzy rules and functions, neural network algorithms, decision trees (Guo *et al.*, 2008; Lan and Xie, 2013; Malon *et al.*, 2008); and (c) the algorithms derived from support vector machine (SVM).

Artificial neural network (NET) and fuzzy logic classifiers are representatives of the RBC. Although the NET method is appropriate for most types of data irrespective of their statistical properties, the interpretability of the results as well as the probability of local minima restrains its application (Eerná and Chytrý, 2005). Fuzzy logic classification is a kind of probability-based classification rather than a hard classification (Triepeke *et al.*, 2008; Sha *et al.*, 2008). Moreover, there are a growing number of RBC classifiers. In fact, there is a new trend taking place within this category, in which several rules are integrated to form newly improved classifiers called hybrid or multiple classifiers (Baraldi, 2011; Maulik and Saha, 2010; Mitrakakis *et al.*, 2008; Stavrakoudis *et al.*, 2012). Due to a broad scope of RBC, the artificial neural network (NET) algorithm was adopted in this paper as a representative RBC.

Recently, the support vector machine (SVM) has been introduced as a new technique for solving a variety of learning, classification and prediction problems (Guo *et al.*, 2008; Malon *et al.*, 2008; Zhao *et al.*, 2008). SVM-based approaches have also been applied for the classification of remotely sensed data (Mittra *et al.*, 2004). Unlike the aforementioned classifiers, SVM is a state-of-the-art learning algorithm having a solid theoretical foundation in statistical learning theory (Vapnik, 1995; Vapnik, 1998). SVM fixes decision functions based on structural risk minimization (SRM) instead of minimization of the misclassification on the training set to avoid overfitting (Du and Sun, 2008). It solves a binary classification problem by searching for maximal margin hyperplanes in terms of a subset of the input data (also referred to as support vectors) between different classes (Wu *et al.*, 2008). Although both NET and SVM are regarded as learning machines and the capability of NET for image classification is well known, empirical testing showed that SVM performance in most cases is better than that of NET in terms of accuracy (Chen *et al.*, 2005). Another advantage of SVM over other classifiers is attributed to its lower sensitivity to the overall size of training samples. Given the fact that the cost of acquiring GRPs to train image classifiers is often a concern (Chi and Bruzzone, 2005), SVM is prominent since, theoretically, SVM can use a smaller size of training samples and is able to achieve higher accuracy than similar classifiers, e.g., NET (Nemmour and Chibani, 2006).

In this paper, efforts are made to develop an innovative and synthetic procedure to meet the aforementioned challenges by answering the questions: how best to use NAIP imagery to extract GRPs for training and validation; how best to take advantage of NAIP high spatial resolution when processing Landsat imagery; and how to obtain higher classification accuracy from Landsat imagery.

Methodology

Study Area and Data Description

The study area, Detroit River International Wildlife Refuge (DRIWR), is situated 41°43' to 42°16'N and 83°06' to 83°30'W (Figure 1). DRIWR occupies 48 miles of Lake Erie shoreline and contains thousands of acres of wetlands. DRIWR is well vegetated with *Phragmites australis* (giant reed cane), grass, shrubs, trees, cattail, marshland, cropland, and various other types. Many of these wetlands have been invaded by *Phragmites* in recent years. Previous studies and onsite survey showed that the invasion of *Phragmites* presents a severe threat to the

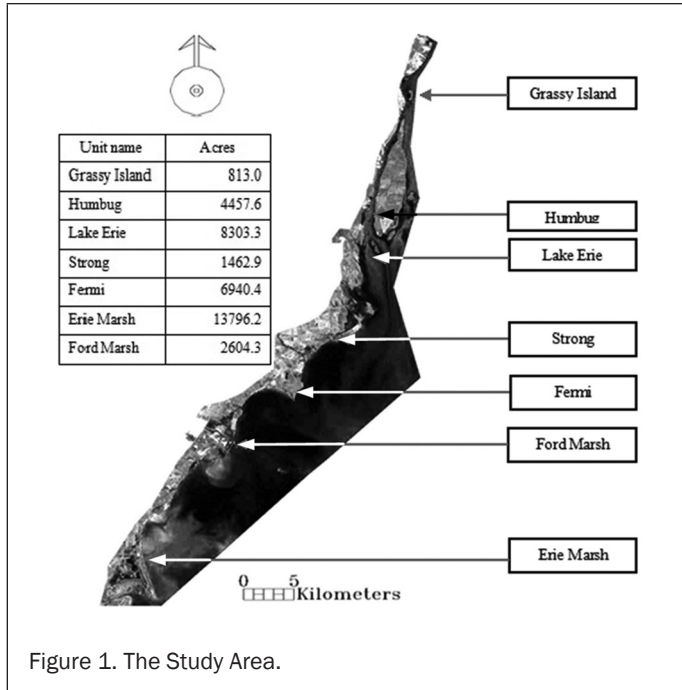


Figure 1. The Study Area.

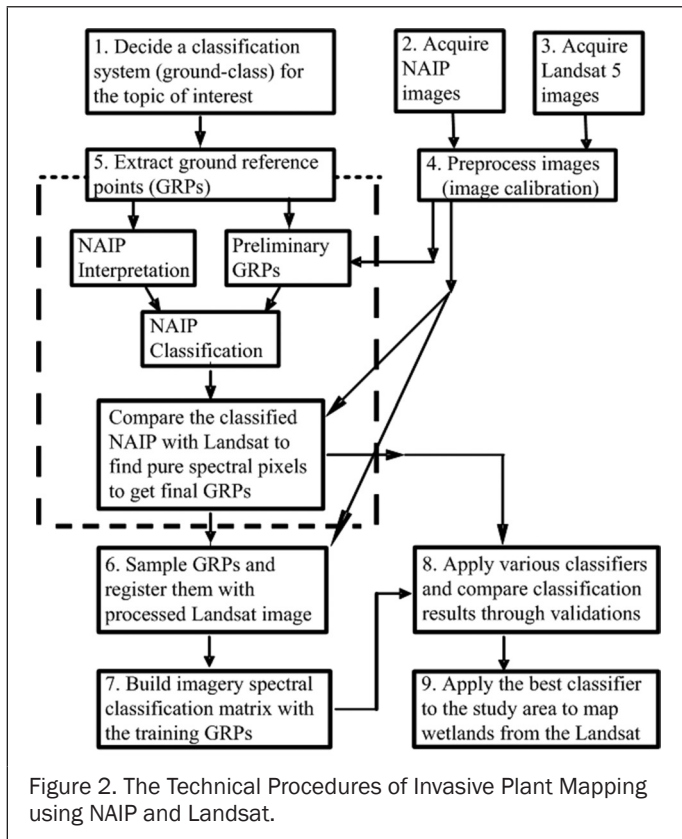


Figure 2. The Technical Procedures of Invasive Plant Mapping using NAIP and Landsat.

indigenous plants of the wetland ecosystem. Wetland mapping and the collection of the present and historical vegetation cover through remote sensed images could provide critical information to support the research of the *Phragmites* invasion.

Data used in this case study includes aerial NAIP images, Landsat-5 Thematic Mapper (TM) images, and field habitat survey data. Fifteen NAIP images over the study area were interpreted and processed to provide reference data for this case study. Moreover, 22 transects of field habitat surveys were

conducted in July 2010, which served as important ground reference data along with the interpreted NAIP images. A Landsat-5 TM scene acquired on 10 September 2010, covering the entire study area, was obtained and preprocessed. We searched Landsat-5 images from the later-spring leave-on season to the early-fall leave-on season. From the viewpoint of phenology, *Phragmites* was easily separable from other tall shrubs and plants in the early-fall season. Moreover, it was easier to find cloud-free Landsat images during the early-fall season. This Landsat image was then classified to extract vegetation information for mapping *Phragmites* and wetland plant communities.

One of the important purposes of this research is to design and experiment a standard technique, through which the publically available imagery sources, NAIP and Landsat, can be processed to extract vegetation data for wetland and invasive plant mapping with a reasonable accuracy level (at least above 80 percent). This procedure should be transparent and repeatable by other groups with a similar set of information and applicable in other regions. The procedure worked out through the Detroit River case study includes nine steps, grouped into three phases (Figure 2): Phase 1 (Steps 1 through 4): Data Preparation and Imagery Preprocessing; Phase 2 (Step 5): Ground Reference Data Extraction; and Phase 3 (Steps 6 through 9): Image Classification and Validation.

Data Preparation and Imagery Preprocessing

This case study was part of the DRIWR NOAA research project conducted by Eastern Michigan University. A component of this project included the field collection of vegetation and habitat data using the transect sampling approach. A total of 22 vegetation/soil transects were staked and plant sample data were collected at 22 sites over 13 DRIWR units, including: Humbug Marsh and Island (3), Strong (1), Gibraltar Bay (2), Gibraltar Marsh (2), Fix (1), Burke (1), Pte. Aux Peaux (1), Plum Creek (1), Our Lady of the Lake (1), Brancheau (2), Lake Erie Metropark (3), Ford Marsh (2), and Pte. Mouillee (2). The locations of transect stakes, plant community types and boundaries, soil samples, and field photos were georeferenced using GPS. Detailed transect field data collection forms were devised and implemented by the data collection team. All data were compiled into fully digital forms after the conclusion of the field season, and were quality checked. The field transect samples were an important source of GRPs for developing training signatures. However, due to the limitations of the spatial distribution and the quantity of the field transects, additional GRPs were needed in order to increase the number and the quality of classification training signatures as well as testing samples.

The Landsat-5 TM scene was located at Path 20/Row31 of the WRS2. NAIP images were warped to the Landsat image by using the first order polynomial rectification with the accuracy of the root mean squared error of less than half a pixel with the ground control points gathered at the field transects. The scene fitted well with the training, testing and other ancillary datasets. Since we had no *in-situ* atmospheric measurements, image-based atmospheric corrections were applied to remove haze effects. So, a strictly image-based atmospheric correction, as proposed by Chavez (1996), was followed to remove atmospheric haze impact. The atmospheric correction was done with the flash module in ENVI. The reflective bands (band 1, 2, 3, 4, 5, and 7) of Landsat-5 TM image were used for classification.

Ground Reference Data Extraction

A four-step process was designed to extract the ground reference data for classifying and validating the Landsat-5 image (Figure 2):

1. NAIP images at selected scenes (i.e., two of the DRIWR management units, Humbug and Strong) were interpreted with traditional aerial photo interpretation techniques;
2. a set of training and testing signatures were obtained from the interpreted NAIP images in conjunction with

TABLE 1. THE DISTRIBUTION OF TRAINING AND VALIDATION SAMPLES IN THE DRIWR STUDY AREA*

Class / Location	Grassy Island	Humbug	Lake Erie	Strong	Fermi	Erie Marsh	Gibraltar Marsh	Pointe Mouillee	Other locations	Total training samples
Phragmites	10	0	10	14	10	6	0	26	40	116
Cattails	0	0	6	3	5	0	0	11	9	34
Open water	0	0	0	0	0	0	0	18	76	94
Cropland	0	0	0	8	16	5	4	0	24	57
Aquatic plants	0	0	0	3	0	12	0	0	66	81
Urban land	0	0	4	2	13	5	0	0	11	35
Pond and lake	0	0	0	0	0	10	0	14	34	58
Forested wetlands	6	7	3	7	6	0	14	0	59	102
Shrub wetland	0	8	4	0	6	0	6	0	15	39

Class / Location	Grassy Island	Humbug	Lake Erie	Strong	Fermi	Erie Marsh	Ford Marsh	Other locations	Total validation samples
Phragmites	6	0	10	14	0	6	0	20	56
Cattails	0	0	0	3	0	0	0	18	21
Open water	5	0	0	0	0	0	0	29	34
Aquatic plants	0	3	0	0	0	3	0	21	27
Urban land	0	0	0	0	0	0	0	39	39
Forested wetlands	3	7	7	8	7	5	4	0	41
Shrub wetland	4	10	4	0	0	0	0	10	28

* The upper section is the distribution of training samples, while the lower section is for validation samples.

TABLE 2. THE ERROR MATRIX OF THE SVM CLASSIFIER FOR NAIP IMAGERY IN STRONG UNIT

Class	Produ. Acc. (Percent)	User Acc. (Percent)	Prod. Acc. (Pixels)	User Acc. (Pixels)
Phragmites	85.1	84.9	3930/4616	3930/4631
Cattails	91.2	91.7	1239/1359	1239/1351
Wet meadow	99.9	99.9	4788/4794	4788/4792
Shrubs	85.1	86.1	4544/5342	4544/5278
Open water	98.5	96.0	5055/5131	5055/5264
Pond and lake	95.5	98.3	4426/4635	4426/4502
Forested wetland	92.8	94.9	1059/1141	1059/1116

Overall Accuracy = (32329/34467) 93.8%
Kappa Coefficient = 0.93

TABLE 3. THE ERROR MATRIX OF THE SVM CLASSIFIER FOR NAIP IMAGERY IN HUMBUG UNIT

Class	Produ. Acc. (Percent)	User Acc. (Percent)	Prod. Acc. (Pixels)	User Acc. (Pixels)
Phragmites	99.6	85.5	679/682	679/794
Urban land	94.7	100.0	1220/1288	1220/1220
Cropland	98.5	80.8	399/405	399/494
Open water	100.0	100.0	4569/4569	4569/4569
Pond and lake	100.0	99.9	4120/4120	4120/4124
Forested wetland	95.5	99.9	2985/3125	2985/2988

Overall Accuracy = (13972/14189) 98.5%
Kappa Coefficient = 0.98

the field transect samples;

- the remaining NAIP images were classified by various classifiers and validated with the reference signatures and, then, the best classification outcome was chosen; and
- a final set of reference points was determined based on visual comparison of the classified NAIP images and the preprocessed Landsat image.

First, a classic aerial photo interpretation was conducted over two NAIP images covering the DRIWR management units, Humbug and Strong. Next, the interpreted NAIP maps were used as the primary source to extract a preliminary set of GRPs for classifying the NAIP images. The preliminary GRPs were extracted from a set of image area of interest (IAOI). The strategy of using small areas instead of single pixels is based on two considerations (Chen and Stow, 2002): (a) single pixels are hardly capturing spectral and spatial information for spatially heterogeneous classes; and (b) the IAOI method reduces

the amount of searching time for image analysts to find representative samples for spatially heterogeneous classes. An IAOI was determined by the following rules:

- An IAOI should be representative of a feature of interest.
- The shape of an IAOI should follow the shape of the feature of interest and is contained within the boundary of that feature.
- An IAOI usually contains at least ten pixels.
- An IAOI for each class signature should be comprised of pixels with similar tone/color, texture, and other relevant interpretative elements of the class.
- Multiple IAOI were chosen for each class feature to ensure representative training signatures were obtained.
- The whole set of IAOI should be distributed evenly over the study area.

Third, the set of IAOI was randomly divided into the

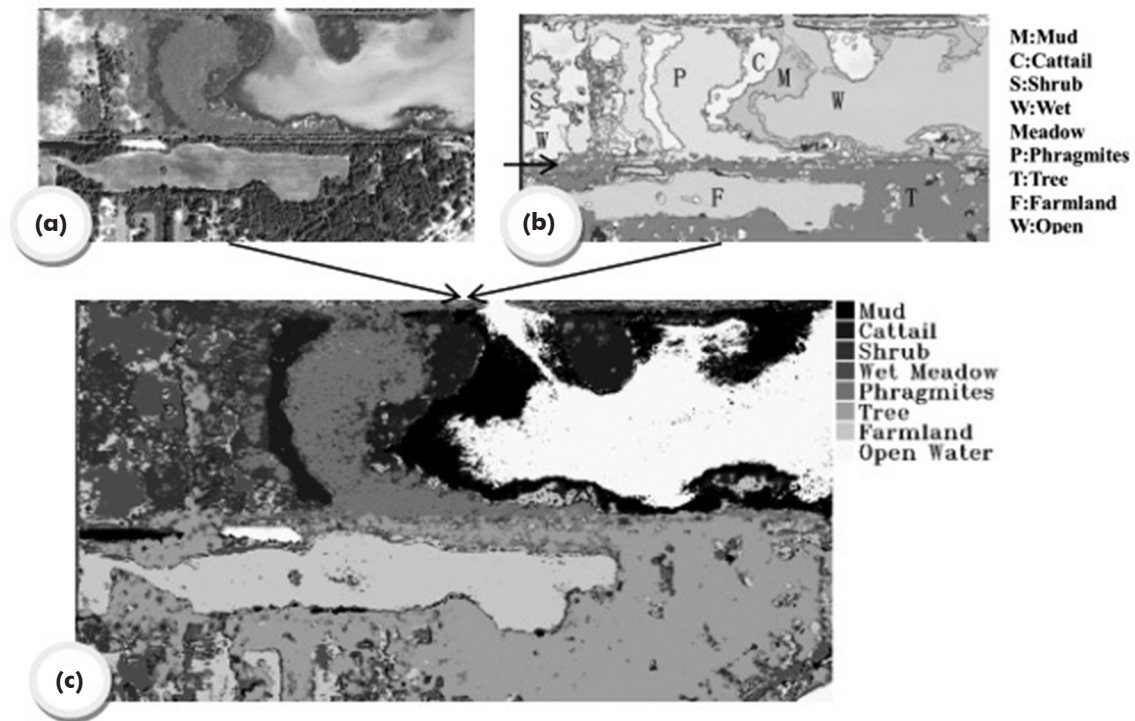


Figure 3. The original NAIP image in (a) Strong Unit, (b) its interpreted map, and (c) its SVM classified image.

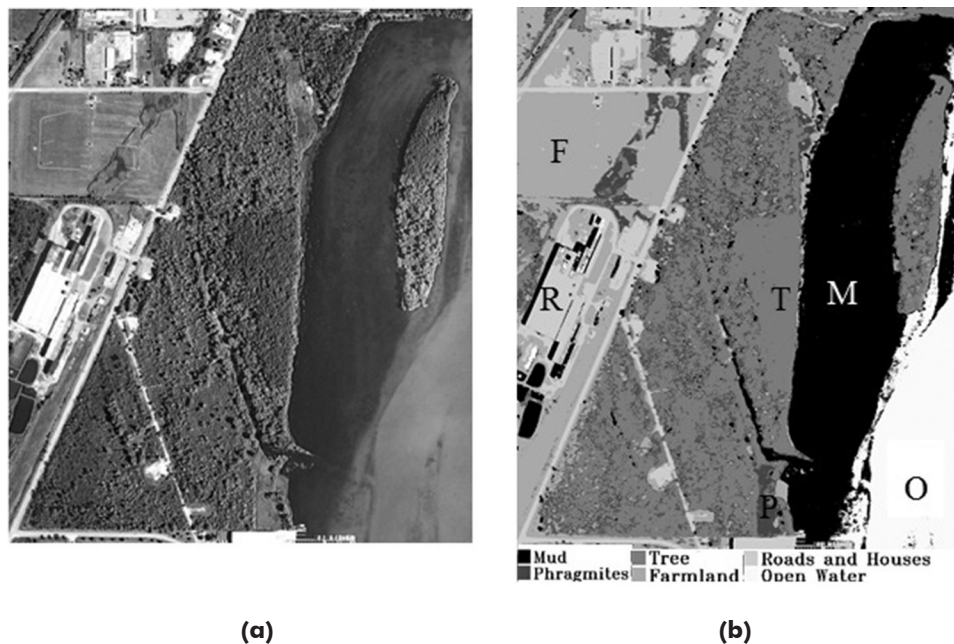


Figure 4. The original NAIP image in (a) Humbug Unit, and (b) its SVM classified image.

training and the testing subsets following the ratio 3:1. NAIP images were then classified by adopting a selected classifier (which will be described in a latter section) with the training subset. The classification results were validated by using the testing IAOI subset. Fourth, when the classification accuracy met the predetermined expectation (>80 percent), a comparison of the interpreted NAIP images with the preprocessed Landsat-5 image was conducted to select a new set of image area of interest. The same procedures used for selecting the

preliminary set of IAOI from the NAIP images were applied over the Landsat image to identify the new set of IAOI. Finally the centers of the new set of IAOI were picked as the final set of GRPs. As a result, 546 GRPs, which were originally derived from the NAIP imagery, were identified on the Landsat image.

With an additional 70 ground reference points chosen from the field transects, a total of 616 reference points covering eight different covers was obtained. These 616 reference samples were randomly divided into the training set and the

testing set at the ratio about 3:1. As the result, 418 samples were in the training set and 198 samples were in the testing set (Table 1). In the following sections, all image analyses were conducted based on the training samples, while the accuracy

assessment was carried out from the testing samples. One critical point that needs to be mentioned is the reference points derived from the NAIP imagery were selected with a comparative visual analysis of the differences between the NAIP imagery and the Landsat-5 imagery. Only pure (not mixed) pixels found on both NAIP and overlain Landsat-5 images were selected as reference points. Through the tests conducted in this case study, the selection of pure pixels as training sets dramatically improved the outcomes of image classification.

Image Classification and Validation

Image classification over grassland or shrubland, which is often the predominant land cover in coastal wetlands, involves much more complexities than over forested areas (Xie *et al.*, 2010). Based on the literature review of various classifiers and the characteristics of wetland and invasive plant mapping, SVM was chosen as the primary classifier, while neural NET and ML were adopted for the purpose of comparison and validation in this paper. Some specifics of adopting SVM were provided below.

SVM is built with a solid theoretical foundation in statistical learning theory (Vapnik, 1995; Vapnik, 1998; Su, 2009). SVM solves a binary classification problem by searching for maximal margin hyperplanes in terms of a subset of the input data (also referred to as support vectors) between different classes (Wu *et al.*, 2008). SVM is a supervised learning method used mainly for data classification and has been applied in various fields (Pal, 2008; Zhang and Xie, 2014). In SVM, the input data is viewed as two sets of cases (denoted as 1 or -1, indicating that any case can be classified as positive or negative) in an n -dimensional space. Building a SVM model involves finding a separating hyperplane in n -dimensional space to maximize the margin between the two sets of cases and thus derive a classification machine for new input cases. Theoretically, a reasonable separation is achieved by the maximum-margin hyperplane that has the largest distance to the neighboring data points of both classes, since the larger the margin, the lower the generalization error of the classifier. In most cases, the input data may not be linearly separated by a hyperplane. In building an effective SVM model, a key concern is to select an appropriate kernel. The SVM kernel tries to map the input vectors through SVM kernel into a very high-dimensional feature space in which data can be linearly separated.

A kernel function and its related kernel parameters are required to design an SVM. We chose the radial basis function (RBF) in this study and the parameters to be optimized include the penalty parameter C and the kernel function parameter, namely gamma (γ). The RBF kernel has better accuracy than the three other kernels (Linear, Polynomial, and Sigmoid) (Tan and Du, 2009; Du *et al.*, 2010). A grid algorithm, or cross-validation, was adopted to select appropriate values for γ and C (Hsu and Lin, 2002). Specifically, we systematically changed the values for γ and C from low to high. For each combination of γ and C , considering the possible side effect caused by the uneven sizes of positive cases and negative cases, we followed the method, as proposed by Huang and Du (2005), by setting the ratio of penalties for different classes (positive and negative) with the inverse ratio of the training class sizes of positive to negative. This weighted SVM could compensate for the undesirable effects caused by the uneven training class sizes among various habitat types.

Outcomes and Maps

NAIP Images

The maps produced using aerial photo interpretation over NAIP images were used as surrogates of the training and validation sets. The interpretations and classifications were carried out in two DRIWR management units, Humbug and Strong. The experiments were carried out with three

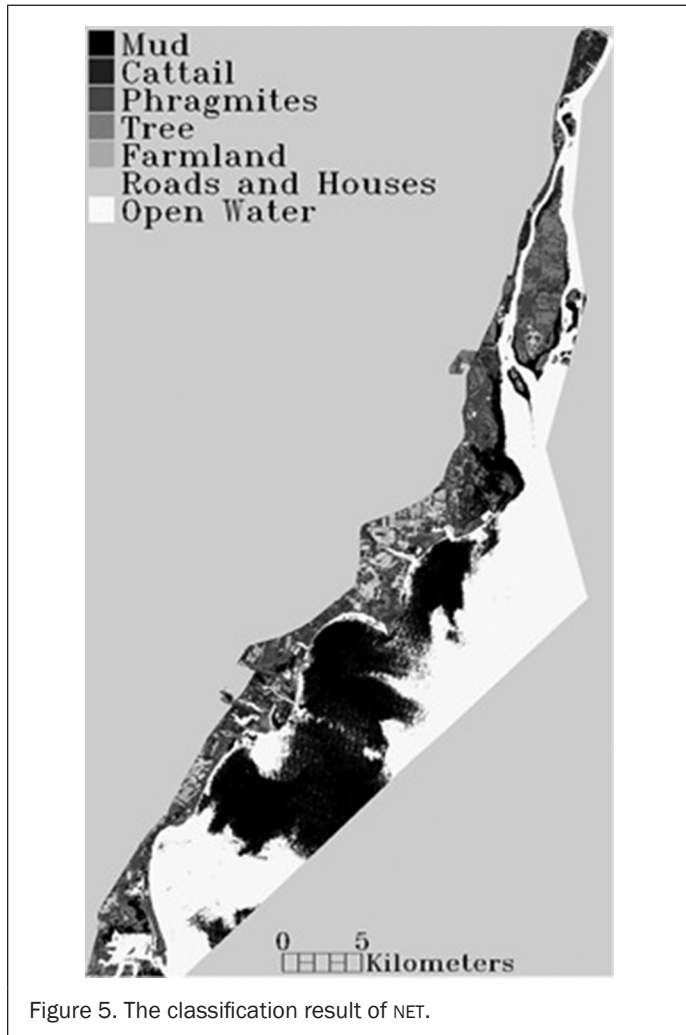


Figure 5. The classification result of NET.

TABLE 4. THE ACCURACY STATISTICS OF THE SVM CLASSIFIER FOR LANDSAT IMAGERY OVER THE ENTIRE STUDY AREA

Class	Produ. Acc. (Percent)	User Acc. (Percent)	Prod. Acc. (Pixels)	User Acc. (Pixels)
Phragmites	100.0	85.0	34/34	34/40
Cattails	66.7	85.7	6/9	6/7
Open water	100.0	100.0	25/25	25/25
Cropland	100.0	100.0	22/22	22/22
Aquatic plants	96.9	73.8	31/32	31/41
Urban land	76.9	100.0	10/13	10/10
Pond and lake	47.6	90.9	10/21	10/11
Forested wetlands	97.0	94.1	32/33	32/34
Shrub wetlands	66.7	85.7	6/9	6/7
Overall Accuracy = (52/61) 88.89%				
Kappa Coefficient = 0.87				

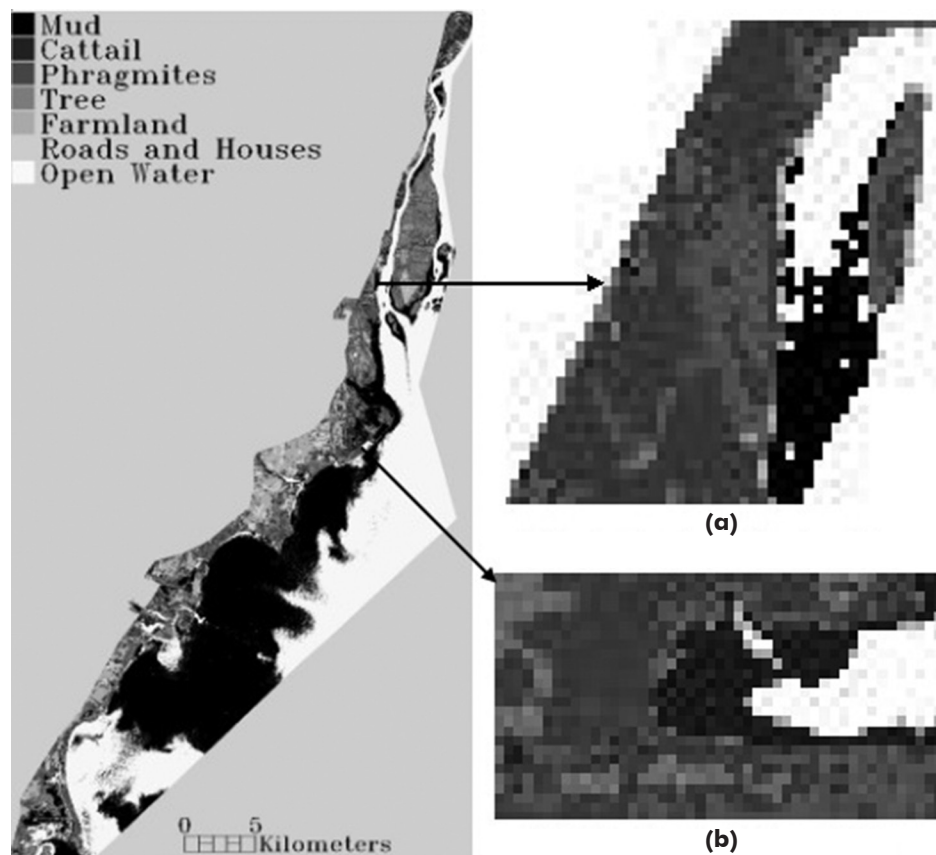


Figure 6. The classification result of svm: (a) svm classification of Humbug Unit, and (b) svm classification of Strong Unit.

classifiers, Maximum-likelihood (ML), Neural NET, and SVM in ENVI. We constructed the confusion matrices to compare the classification results with the ground reference points. For the ML method, the classification accuracy is 84.7 percent; kappa coefficient is 0.819; and *Phragmites* user accuracy is 83.63 percent (Story and Congalton, 1986). The classification accuracy of Neural NET is 78.1 percent; kappa coefficient is 0.734; and *Phragmites* user accuracy is 66.3 percent. The overall accuracy and Kappa coefficient are important statistics assessing whether general accuracy requirements are met. In particular, Kappa coefficient reflects the difference between the actual agreement and the agreement expected by chance. A Kappa value of 0.80 means there is 80 percent better agreement than by chance alone. The higher a Kappa value, the higher is the confidence concerning the accuracy assessment (Congalton, 1991). The Kappa values of the SVM classifications were higher than 0.92 (Table 2 for the Strong Unit and Table 3 for the Humbug Unit). By comparing the different results, it is clear that the SVM classifier obtained the best classification accuracy. Figure 3 shows the NAIP composite image, the interpreted map, and the SVM classified image of Strong Unit based on the NAIP image. Similarly, Figure 4 is Humbug Unit original and SVM classified images. Different gray-scale regions on these images represent different land cover types.

Landsat-5 TM Image

Landsat-5 TM image was processed for mapping invasive plant and wetlands over the entire study area, the Detroit River International Wildlife Refuge. The reflective bands (band 1, 2, 3, 4, 5, 7) of Landsat-5 TM were used for the classification experiments. Three classifiers, ML, NET (Figure 5) and SVM (Figure 6), were applied. For the ML, the classification accuracy is

82.8 percent, kappa coefficient is 0.8030, and *Phragmites* user accuracy is 91.67 percent. For NET, the classification accuracy is 86.36 percent, kappa coefficient is 0.8412, and *Phragmites* user accuracy is 91.89 percent. The results of SVM classification was reported in Table 4 and displayed in Figure 6. The SVM classifier attains the classification accuracy 88.89, the kappa coefficient 0.87 and the user accuracy of *Phragmites* 85.00 percent. By comparison, SVM obtains the best classification accuracy statistics.

Discussions and Conclusion

A reliable but low cost technique was developed to map coastal wetlands and invasive plant species, *Phragmites*, to support decision making in ecological restoration and environmental management projects. In terms of cost, two types of images that were easily accessible and had no or very low costs were tested. One was the airborne four-band NAIP image and the other was the satellite Landsat image. The NAIP image had higher spatial resolution but lower spectral resolution; it was a good image source for image interpretation to extract ground reference points and to validate other image classification outcomes. Moreover, the NAIP images covered smaller areas, i.e., the Strong unit and the Humbug unit in our case studies. The spatial and spectral information of NAIP were sufficiently good for site-specific mapping purposes. In addition, the experiments conducted in this paper also revealed that classification results based on NAIP images were usually better over a small area in comparison to Landsat images that covered a much larger area. It was also logical to assume that it would be labor-intensive to use the NAIP image, including four bands and covering small areas, for differentiating spectral

variations of land covers and uses over a large heterogeneous region, in comparison to Landsat TM.

In terms of reliability, it was recommended to achieve higher classification outcomes on publically available images by taking advantage of the “high (in relative sense)” spatial resolution of NAIP image to extract sufficient GRPs and then using them to classify the “high (in relative sense)” spectral resolution Landsat image with effective classifiers. The most important technique was to repetitively conduct data mining on the high spatial resolution of NAIP image to extract a sufficiently large size of GRPs or samples for classification training and validation. It was a critical step to extract GRPs of different classes as training and validation datasets when studying land cover and land use changes using remotely sensed data (Zhang and Xie, 2014). In the experiments, 546 pure pixels were obtained as GRPs from the extracted image areas of interest on both interpreted and processed NAIP images, in addition to 70 GRPs from the ground transects.

Three types of classifiers, ML, Neural Net, and SVM, were experimented in this case study. Over two small NAIP images, the ML, and SVM methods (especially the SVM classifier) performed much better than Neural Net. On the other hand, for the Landsat-5 image that covers the entire study area, the classification accuracy statistics of Neural NET and SVM methods were better than that of the ML method. Similarly to both NAIP and Landsat images, the SVM method had the highest overall accuracy statistics. Therefore, two conclusions could be drawn here: (a) the method for obtaining a large size of GRPs from NAIP images in combination with field observations, worked reasonably well; and (b) the SVM classifier performed better than ML and NET. Another note is that no ancillary information (except for a small number of GRPs from the ground transects) was taken into consideration in the current classifiers. The primary goal of this paper was to develop a low cost, easily reproducible technique to map wetland vegetation. The exclusion of ancillary information was to focus on the key techniques described in this paper. However, it is worth pointing out that many vegetation mapping projects strongly suggested to include ancillary datasets. When ancillary datasets, such as soil, landform, bedrock geology, terrain, hydrology, and climate data were added into classification processes, the classification accuracy was significantly improved in comparison with the sole consideration of Landsat derived variables (Wright *et al.*, 2007). When a large number of ancillary data layers were available, decision-tree-based image classification algorithms were able to produce accurate vegetation maps (Baker *et al.*, 2006; Davranche *et al.*, 2010).

Finally, although the classification outcomes were satisfactory based on the accuracy assessments, there were limitations that need to be addressed. For instance, we only selected seven types of land covers/uses based on what we found in the Strong Unit to classify habitats over the entire study area. In fact, some habitat types were neglected in our study, such as shrub, wet meadow, and others. In order to verify or validate the classification accuracy for various types of vegetation or invasive plant species, more experiments and tests should be repeated in other study areas or in other ecosystems. In addition, it might help if some systematic approaches of collecting ground reference samples and deriving surrogate reference data from aerial photos were designed or implemented. All of these suggested will be our efforts at near future.

Acknowledgments

This work was supported in part by US Department of Commerce Award # NA09OAR4170172, the National Science Foundation of China under Grant 41104005, and the Department of Education of Hebei Province of China under Grant YQ2013012.

Appreciation also goes to Dr. Eugene Jaworksi, Ms. Xiaoqin Ge, Ms. Lisa Denys, Mr. Greg Stevens, Mr. Jason Tallant, and Mr. Michael Dueweke at Eastern Michigan University for field data collection and aerial image interpretation.

References

- Andrew, M.E., and S.L. Ustin, 2008. The role of environmental context in mapping invasive plants with hyperspectral image data, *Remote Sensing of Environment*, 112:4301–4317.
- Asner, G.P., and R.E. Martin, 2008. Spectral and chemical analysis of tropical forests: Scaling from leaf to canopy levels, *Remote Sensing of Environment*, 112:3958–3970.
- Baker C., R. Lawrence, C. Montagne, and D. Patten, 2006. Mapping wetlands and riparian areas using Landsat ETM+ imagery and decision-tree-based models, *Wetlands*, 26:465–474.
- Baraldi, A., 2011. Fuzzification of a crisp near-real-time operational automatic spectral-rule-based decision-tree preliminary classifier of multisource multispectral remotely sensed images, *IEEE Transactions on Geoscience and Remote Sensing*, 49(6):2113–2134.
- Benz, U.C., P. Hofmann, G. Willhauck, I. Lingenfelder, and M. Heynen, 2004. Multiresolution object-oriented fuzzy analysis of remote sensing data for GIS-ready information, *ISPRS Journal of Photogrammetry and Remote Sensing*, 58(3-4):239–258.
- Bourgeau-Chavez, L.L., K. Riordan, M. Nowels, and N. Miller, 2004. *Remotely Monitoring Great Lakes Coastal Wetlands using a Hybrid Radar and Multi-spectral Sensor Approach*, Final Report to the Great Lakes Commission, Project No. WETLANDS2-WPA06, pp. 82, URL: <http://www.glc.org/wetlands/pdf/GD-landscapeReport.pdf> (last date accessed : 09 October 2013).
- Černá, L., and M. Chytrý, 2005. Supervised classification of plant communities with artificial neural networks, *Journal of Vegetation Science*, 16:407–414.
- Chavez, Jr., P.S., 1996. Image-based atmospheric corrections - Revisited and improved, *Photogrammetric Engineering & Remote Sensing*, 62:1025–1036.
- Chen, D.M., and D. Stow, 2002. The effect of training strategies on supervised classification at different spatial resolutions, *Photogrammetric Engineering & Remote Sensing*, 68(11):1155–1161.
- Chen, W.H., S.H. Hsu, and H.P. Shen, 2005. Application of SVM and ANN for intrusion detection, *Computers and Operations Research*, 32 (2005):2617–2634.
- Chi, M., and L. Bruzzone, 2005. A semilabeled-sample-driven bagging technique for ill-posed classification problems, *IEEE Geoscience and Remote Sensing Letters*, 2:69–73.
- Cingolani, A.M., D. Renison, M.R. Zak, and M.R. Cabido, 2004. Mapping vegetation in a heterogeneous mountain rangeland using Landsat data: An alternative method to define and classify land-cover units, *Remote Sensing of Environment*, 92:84–97.
- Congalton, R.G., 1991. A review of assessing the accuracy of classifications of remotely sensed data, *Remote Sensing of Environment*, 37:35–46.
- Corcoran, J.M., J.F. Knight, B. Brisco, S. Kaya, A. Cull, and K. Murnaghan, 2011. The integration of optical, topographic, and radar data for wetland mapping in northern Minnesota, *Canadian Journal of Remote Sensing*, 37:564–582.
- Dahl, T.E., 1990. *Wetlands-Losses in the United States, 1780 s to 1980 s*, Washington, D.C., US Fish and Wildlife Service Report to Congress, 13 p.
- Davranche, A., G. Lefebvre, and B. Poulin, 2010. Wetland monitoring using classification trees and SPOT-5 seasonal time series, *Remote Sensing of Environment*, 114:552–562.
- Du, C.J., and D.W. Sun, 2008. Multi-classification of pizza using computer vision and support vector machine, *Journal of Food Engineering*, 86:234–242.
- Du, P.J., K. Tan, and X.S. Xing, 2010. Wavelet SVM in reproducing kernel Hilbert space for hyperspectral remote sensing image classification, *Optics Communications*, 283:4978–4984.
- Everitt, J.H., C. Yang, and C.J. Deloach, 2005. Remote sensing of giant reed with QuickBird satellite imagery, *Journal of Aquatic Plant Management*, 43:81–85.

- Galatowitsch, S.M., N.O. Anderson, and P.D. Ascher, 1999. Invasiveness in wetland plants in temperate North America, *Wetlands*, 19:733–755.
- Guo, X.S., L.Y. Sun, G. Li, and S. Wang, 2008. A hybrid wavelet analysis and support vector machines in forecasting development of manufacturing, *Expert Systems with Applications*, 35(1-2):415–422.
- Henderson, F.M., and A.J. Lewis, 2008. Radar detection of wetland ecosystems: A review, *International Journal of Remote Sensing*, 29(20):5809–5835.
- Higdon, R., and D.W. Schafer, 2001. Maximum likelihood computations for regression with measurement error, *Computational Statistics and Data Analysis*, 35:283–299.
- Hsu, C.W., and C.J. Lin, 2002. A simple decomposition method for support vector machine, *Journal of Machine Learning*, 46(1-3):219–314.
- Huang, Y.M., and S.X. Du, 2005. Weighted support vector machine for classification with uneven training class sizes, *Proceedings of the Fourth International Conference on Machine Learning and Cybernetics*, 18-21 August, Guangzhou, China, Vol. 7, pp. 4365–4369.
- Kasischke, E.S., and L.L. Bourgeau-Chavez, 1997. Monitoring south Florida wetlands using ERS-1 SAR imagery, *Photogrammetric Engineering & Remote Sensing*, 63(3):281–291.
- Kozlov, A.I., L.P. Ligthart, and A.I. Logvin, 2001. *Mathematical and Physical Modeling of Microwave Scattering and Polarimetric Remote Sensing- Monitoring the Earth's Environment Using Polarimetric Radar: Formulation and Potential Applications*, Kluwer Academic Publishers, Boston, Massachusetts, 410 p.
- Krebel, U., 1999. Pairwise classification and support vector machines, *Advances in Kernel Methods: Support Vector Learning*, MIT Press, Cambridge, Massachusetts, pp. 255–268.
- Kwoun, O., and Z. Lu, 2009. Multi-temporal RADARSAT-1 and ERS backscattering signatures of coastal wetlands in southeastern Louisiana, *Photogrammetric Engineering & Remote Sensing*, 75(5):607–617.
- Lan, H., and Y. Xie, 2013. A semi-ellipsoid-model based fuzzy classifier to map grassland in inner Mongolia, China, *ISPRS Journal of Photogrammetry and Remote Sensing*, 85:21–31.
- Langley, S.K., H.M. Cheshire, and K.S. Humes, 2001. A comparison of single date and multi-temporal satellite image classifications in a semi-arid grassland, *Journal of Arid Environments*, 49:401–11.
- Lopez, R.D., D.T. Heggem, D.Sutton, T. Ehli, R.V. Remortel, E. Evanston, and L. Bice, 2006. *Using Landscape Metrics to Develop Indicators of Great Lakes Coastal Wetland Condition*, EPA/X-06/002. Las Vegas, Nevada, US Environmental Protection Agency, Environmental Sciences Division, 76p.
- Lu, D., and Q. Weng, 2007. A survey of image classification methods and techniques for improving classification performance, *International Journal of Remote Sensing*, 28(5):823–870.
- Lunetta, R.S., and M.E. Balogh, 1999. Application of multi-temporal Landsat 5 TM imagery for wetland identification, *Photogrammetric Engineering & Remote Sensing*, 65:1303–1310.
- Malon, C., S. Uchida, and M. Suzuki, 2008. Mathematical symbol recognition with support vector machines, *Pattern Recognition Letters*, 29(9):1326–1332.
- Maulik, U., and I. Saha, 2010. Automatic fuzzy clustering using modified differential evolution for image classification, *IEEE Transactions on Geoscience and Remote Sensing*, 48(9):3503–3510.
- Mills, E.L., J.H. Leach, J.T. Carlton, and C.L. Secor, 1993. Exotic species in the Great Lakes: A history of biotic crises and anthropogenic introductions, *Journal of Great Lakes Research*, 19:1–54.
- Mitrakis, N.E., C.A. Topaloglou, T.K. Alexandridis, J.B. Theocharis, and G.C. Zalidis, 2008. Decision fusion of GA self-organizing neuro-fuzzy multilayered classifiers for land cover classification using textural and spectral features, *IEEE Transactions on Geoscience and Remote Sensing*, 46(7):2137–2151.
- Mitra, P., B.U. Shankar, and S.K. Pal, 2004. Segmentation of multispectral remote sensing images using active support vector machines, *Pattern Recognition Letters*, 25:1067–1074.
- Mitsch, W.J., and J.G. Gosselink, 2007. *Wetlands*, Fourth edition, John Wiley & Sons, Hoboken, New Jersey.
- Nemmour, H., and Y. Chibani, 2006. Multiple support vector machines for land cover change detection: An application for mapping urban extensions, *ISPRS Journal of Photogrammetry & Remote Sensing*, 61:125–133.
- Nielsen, E.M., S.D. Prince, and G.T. Koeln, 2008. Wetland change mapping for the U.S. mid-Atlantic region using an outlier detection technique, *Remote Sensing of Environment*, 112:4061–4074.
- Nordberg, M.L., and J. Evertson, 2003. Vegetation index differencing and linear regression for change detection in a Swedish mountain range using Landsat TM and ETM+ imagery, *Land Degradation & Development*, 16:139–149.
- Pal, M., 2008. Support vector machines/relevance vector machine for remote sensing classification: A review, *Proceedings of the Brainstorming Workshop on Application of Advanced Soft Computing Techniques in Geospatial Data Analysis*, 22-23 September, Bombay, India, pp. 211–227.
- Pengra, B.W., C.A. Johnston, and T.R. Loveland, 2007. Mapping an invasive plant, *Phragmites australis*, in coastal wetlands using the EO-1 Hyperion hyperspectral sensor, *Remote Sensing of Environment*, 108:74–81.
- Pignatti, S., R.M., Cavalli, V. Cuomo, L. Fusilli, S. Pascucci, M. Poscolieri, and F. Santini, 2009. Evaluating Hyperion capability for land cover mapping in a fragmented ecosystem: Pollino National Park, Italy, *Remote Sensing of Environment*, 113(3):622–634.
- Rampi, L.P., J.F. Knight, and K.C. Pelletier, 2014. Wetland mapping in the upper Midwest United States: An object-based approach integrating lidar and imagery data, *Photogrammetric Engineering & Remote Sensing*, 80(5):553–562.
- Reyer, J., C. Wolf, and M. Murray, 2009. *Protecting and Restoring the Kidneys of the Great Lakes: An assessment of Wetlands Programs in Michigan, Minnesota, Ohio and Wisconsin*, Wetlands_Report_July_2009, National Wildlife Federation, 111 p.
- Sha, Z., Y. Bai, Y. Xie, M. Yu, and L. Zhang, 2008. Using a hybrid fuzzy classifier (HFC) to map typical grassland vegetation in Xilin River Basin, inner Mongolia, China, *International Journal of Remote Sensing*, 29(8):2317–2337.
- Skolnik, M.I., 2008. *Radar Handbook*, Third edition, McGraw-Hill, New York.
- Sohn, Y., and J. Qi, 2005. Mapping detailed biotic communities in the upper San Pedro Valley of southeastern Arizona using Landsat-7 ETM+ data and supervised spectral angle classifier, *Photogrammetric Engineering & Remote Sensing*, 71:709–718.
- Sohn, Y., and N.S. Rebelló, 2002. Supervised and unsupervised spectral angle classifiers, *Photogrammetric Engineering & Remote Sensing*, 68(12):1271–1280.
- Stavrakoudis, D.G., G.N. Galidaki, I.Z. Gitas, and J.B. Theocharis, 2012. A genetic fuzzy-rule-based classifier for land cover classification from hyperspectral Imagery, *IEEE Transactions on Geoscience and Remote Sensing*, 50(1):130–148.
- Story, M., and R.G. Congalton, 1986. Accuracy assessment: A user's perspective, *Photogrammetric Engineering & Remote Sensing*, 52(3):397–399.
- Stuart, N., T. Barratt, and C. Place, 2006. Classifying the neotropical savannas of Belize using remote sensing and ground survey, *Journal of Biogeography*, 33(3):476–490.
- Tan, K., and P.J. Du, 2009. Hyperspectral remote sensing image classification based on radical basis function neural network, *Spectroscopy and Spectral Analysis*, 28(9):2009–2013.
- Triepke, F.J., C.K. Brewer, D.M. Leavell, and S.J. Novak., 2008. Mapping forest alliances and associations using fuzzy systems and nearest neighbor classifiers, *Remote Sensing of Environment*, 112(3):1037–1050.
- Ustin, S.L., D. DiPietro, K. Olmstead, E. Underwood, and G.J. Scheer, 2002. Hyperspectral remote sensing for invasive species detection and mapping, *Proceedings of the Geoscience and Remote Sensing Symposium, 2002, IGARSS '02, IEEE International, 24-28 June, Toronto, Ontario, Canada*, 3:1658–1660.

- Vapnik, V.N., 1995. *The Nature of Statistical Learning Theory*, Springer-Verlag, New York, 188 p.
- Vapnik, V.N., 1998. *Statistical Learning Theory*, John Wiley & Sons, New York, 736 p.
- Varshney, P.K. and M.K. Arora, 2004. *Advanced Image Processing Techniques for Remotely Sensed Hyperspectral Data*, Spinger, Berlin, 323 p.
- Walsh, S.J., A.L. McCleary, C.F. Mena, Y. Shao, J.P. Tuttle, A. Gonzalez, and R. Atkinson, 2008. QuickBird and Hyperion data analysis of an invasive plant species in the Galapagos Islands of Ecuador: Implications for control and land use management, *Remote Sensing of Environment*, 112:1927–1941
- Wright, C., and A. Gallant, 2007. Improved wetland remote sensing in Yellowstone National Park using classification trees to combine TM imagery and ancillary environmental data, *Remote Sensing of Environment*, 107:582–605.
- Wilcox, K.L., S.A. Petrie, L.A. Maynard, and S.W. Meyer. 2003. Historical distribution and abundance of *Phragmites australis* at Long Point, Lake Erie, Ontario, *Journal of Great Lakes Research*, 29:664–680.
- Wu, Y.C., Y.S. Lee, and J.C. Yang, 2008. Robust and efficient multi-class SVM models for phrase pattern recognition, *Pattern Recognition*, 41:2874–2889.
- Xie, Y., Z. Sha, and M. Yu, 2008. Remote sensing imagery in vegetation mapping: A review, *Journal of Plant Ecology*, 1:9–23.
- Xie, Y., Z. Sha, and Y. Bai, 2010. Classifying historical remotely sensed imagery using a temporal feature evolution (T-SFE) model, *ISPRS Journal of Photogrammetry and Remote Sensing*, 65:182–190.
- Xu, M., P. Watanachaturaporn, P.K. Varshney, and M.K. Arora, 2005. Decision tree regression for soft classification of remote sensing data, *Remote Sensing of Environment*, 97:322–336.
- Zhang, A., and Y. Xie, 2014. A chaos-theory-based data-mining technique for image endmember extraction: Lyapunov Index and Correlation Dimension (L&D), *IEEE Transactions on Geoscience and Remote Sensing*, 52:1935–1947.
- Zhao, F.C., Y.H. Hu, and S.Q. Hao, 2008. Classification using wavelet packet decomposition and support vector machine for digital modulations, *Journal of Systems Engineering and Electronics*, 19(5):914–918.

(Received 23 October 2013; accepted 20 February 2014; final version 19 May 2014)

BOARD OF DIRECTORS

OFFICERS

President A. Stewart Walker*
BAE Systems
stewart.walker2@baesystems.com
President-Elect E. Lynn Usery*
U.S. Geological Survey
usery@usgs.gov
Vice President Charles Toth*
OSU Center for Mapping
toth@cfm.ohio-state.edu
Past President Stephen D. DeGloria*
Cornell University
sdd4@cornell.edu
Treasurer Donald T. Lauer*
U.S. Geological Survey (Emeritus)
lauerdc@gmail.com

BOARD MEMBERS

Alaska Region - 2016
Nicholas William Hazelton
Coolgardie LLC
nwjh@mac.com
www.asprs.org/All-Regions/Alaska.html
Central New York Region - 2017
Jason Smith
ITT Exelis - Geospatial Systems
jason.smith@exelisinc.com
www.asprs.org/All-Regions/Central-New-York.html
Columbia River Region - 2017
Marcus Glass
3Di
mglass@3dimapping.com
www.asprs.org/All-Regions/Columbia-River.html
Eastern Great Lakes Region - 2017
Srinivasan Dharmapuri
Michael Baker International
dssrini@gmail.com
www.asprs.org/All-Regions/Eastern-Great-Lakes.html
Florida Region - 2016
Thomas J. Young
Pickett & Associates
jyoung@pickett-inc.com
www.asprs.org/All-Regions/Florida.html
Geographic Information Systems Division - 2015
David Alvarez,* CMS, GISP
Woolpert
david.alvarez@woolpert.com
www.asprs.org/Divisions/GIS-Division.html
Heartland Region - 2015
David W. Kreighbaum*
NGA
David.W.Kreighbaum@nga.mil
www.asprs.org/All-Regions/Heartland.html
Intermountain Region - 2016
Lucinda A. Clark
Draper, UT 84020
cindyc1952@gmail.com
www.asprs.org/All-Regions/Intermountain.html
Lidar Division - 2016
Christopher Parrish
NOAA
chris.parrish@uwalumni.com
www.asprs.org/Divisions/Lidar-Division.html

Mid-South Region - 2016
Haluk Cetin
Murray State University
haluk.cetin@murraystate.edu
www.asprs.org/All-Regions/Mid-South.html
New England Region - TBA
www.asprs.org/All-Regions/New-England.html
North Atlantic Region - 2016
John Trunkwalter
BAE Systems
john.trunkwalter@baesystems.com
www.asprs.org/All-Regions/North-Atlantic.html
Northern California Region-2015
Lorraine Amenda
Towill, Inc.
Lorraine.Amenda@towill.com
www.asprs.org/All-Regions/Northern-California.html
Photogrammetric Applications Division - 2016
Robert Thomas
Integrity Applications, Inc.
rthomas@integrity-apps.com
www.asprs.org/Divisions/Photogrammetric-Applications-Division.html
Potomac Region - 2017
Barbara A. Eckstein
L-1 MCCLENDON
beckstein@surfbest.net
www.asprs.org/All-Regions/Potomac.html
Primary Data Acquisition Division - 2017
Pierre le Roux
Quantum Spatial
pleroux@quantumspatial.com
www.asprs.org/Divisions/Primary-Data-Aquisition-Division.html
Professional Practice Division - 2016
Michael Zoltek
Pictometry International Corp.
mike.zoltek@pictometry.com
www.asprs.org/Divisions/Professional-Practice-Division.html
Puget Sound Region - 2015
Terry A. Curtis
WA DNR, Resource Map Sect.
terry.curtis@wadnr.gov
www.asprs.org/All-Regions/Puget-Sound.html
Remote Sensing Applications Division - 2016
James Stuart Blundell
Exelis Visual Information Systems
Stuart.Blundell@exelisvis.com
www.asprs.org/Divisions/Remote-Sensing-Applications-Division.html
Rocky Mountain Region - 2015
Jeffrey M. Young*
Centennial, CO 80115
jeffreymyoung@msn.com
www.asprs.org/All-Regions/Rocky-Mountain.html
Southwest US Region - 2017
Steven Lambert, CP
Esri, Inc
slambert@esri.com
www.asprs.org/All-Regions/Southwest-US.html

Sustaining Members Council Chair - 2015
Brian E. Murphy
Northrop Grumman Information Systems
brian.murphy@ngc.com
www.asprs.org/About-Us/Sustaining-Members-Council.html
Western Great Lakes Region - 2016
Douglas Fuller*
Sheboygan, WI 53081
FullerDoug@charter.net
www.asprs.org/All-Regions/Western-Great-Lakes.html

DIVISION OFFICERS

Geographic Information Systems
Director: David Alvarez
Assistant Director: Matthew D. Dunbar
University of Washington
mddunbar@uw.edu
www.asprs.org/Divisions/GIS-Division.html
Lidar
Director: Christopher E. Parrish
Assistant Director: Jason Stoker
USGS
jstoker@usgs.gov
www.asprs.org/Divisions/Lidar-Division.html
Photogrammetric Applications
Director: Robert D. Thomas
Assistant Director: Scott Perkins
Surveying And Mapping (SAM) LLC
sperkins@sam.biz
www.asprs.org/Divisions/Photogrammetric-Applications-Division.html
Primary Data Acquisition
Director: Pierre le Roux
Assistant Director: TBD
www.asprs.org/Divisions/Primary-Data-Aquisition-Division.html
Professional Practice
Director: Michael J. Zoltek
Assistant Director: Frank Taylor
Midwest Aerial Photography
frank@midwestaerialphoto.com
www.asprs.org/Divisions/Professional-Practice-Division.html
Remote Sensing Applications
Director: James Stewart Blundell
Assistant Director: John McCombs
NOAA Coastal Services Center
john.mccombs@noaa.gov
www.asprs.org/Divisions/Remote-Sensing-Applications-Division.html

SUSTAINING MEMBERS COUNCIL

Chair: Brian Murphy
Vice Chair: Brenda S. Burroughs
Optech International
brendab@optechint.com
<http://www.asprs.org/About-Us/Sustaining-Members-Council.html>

STUDENT ADVISORY COUNCIL

Chair: Patrick Adda
University of New Brunswick
padda@unb.ca
Deputy Chair: Mingshu Wang
University of Georgia
mswang@uga.edu
<http://www.asprs.org/Students/Student-Advisory-Council.html>

*Executive Committee Member

SUSTAINING MEMBERS

3D Laser Mapping LTD

Bingham, Nottingham, United Kingdom
www.3dlasermapping.com
Member Since: 2/2010

Aerial Cartographics of America, Inc. (ACA)

Orland, Florida
www.aca-net.com
Member Since: 10/1994

Aerial Services, Inc.

Cedar Falls, Iowa
www.AerialServicesInc.com
Member Since: 5/2001

Aero-Graphics, Inc.

Salt Lake City, Utah
www.aero-graphics.com
Member Since: 4/2009

AeroTech Mapping Inc.

Las Vegas, Nevada
www.atmlv.com
Member Since: 8/2004

Aerovel Corporation

White Salmon, Washington
www.aerovelco.com
Member Since: 10/2014

Acute3D

Sophia Antipolis, Cedex, France
www.acute3d.com
Member Since: 4/2014

The Airborne Sensing Corporation

Toronto, Ontario, Canada
www.airsensing.com
Member Since: 1/2013

AGFA Materials Corporation

Goose Creek, South Carolina
www.agfa.com
Member Since: 1/1990

Air Photographics, Inc.

Martinsburg, West Virginia
www.airphotographics.com
Member Since: 1/1973

Altavian

Gainesville, Florida
www.altavian.com
Member Since: 2/2014

American Surveyor Magazine

Frederick, Maryland
www.TheAmericanSurveyor.com
Member Since: 12/2004

Applanix

A Trimble Company
Ontario, Canada
www.applanix.com
Member Since: 7/1997

Axis GeoSpatial, LLC

Easton, Maryland
www.axisgeospatial.com
Member Since: 1/2005

Ayres Associates, Inc.

Madison, Wisconsin
www.AyresAssociates.com
Member Since: 1/1953

BAE Systems

San Diego, California
www.baesystems.com/gxp
Member Since: 7/1995

BNP Media, Point of Beginning Magazine

(formally POB Magazine)
Troy, Michigan
www.bnpmedia.com
Member Since: 7/2006

Bohannon Huston, Inc.

Albuquerque, New Mexico
www.bhinc.com
Member Since: 11/1992

Cardinal Systems, LLC

Flagler Beach, Florida
www.cardinalsystems.net
Member Since: 1/2001

Certainty 3D LLC

Orlando, Florida
www.certainty3d.com
Member Since: 11/2012

COL-EAST, Inc.

North Adams, Massachusetts
www.coleast.com
Member Since: 1/1976

CompassData, Inc.

Centennial, Colorado
www.compassdatainc.com
Member Since: 3/2014

CRC Press - Taylor & Francis Group

Boca Raton, Florida
www.crcpress.com
Member Since: 9/2006

CRITIGEN

(formerly CH2M HILL)
Redding, California
www.critigen.com
Member Since: 1/1974

DAT/EM Systems International

Anchorage, Alaska
www.datem.com
Member Since: 1/1974

Dewberry

Fairfax, Virginia
www.dewberry.com
Member Since: 1/1985

DigitalGlobe

Longmont, Colorado
www.digitalglobe.com
Member Since: 7/1996

DMC International Imaging Ltd.

Guildford, Great Britain
www.dmcii.com
Member Since: 3/2008

Dynamic Aviation Group, Inc.

Bridgewater, Virginia
www.dynamicaviation.com
Member Since: 4/2003

Eagle Mapping, Ltd

British Columbia, Canada
www.eaglemapping.com
Member Since: 1/1999

Eastern Topographics

Wolfeboro, New Hampshire
www.e-topo.com
Member Since: 8/1978

Elecnor Deimos Imaging

Boecillo - Valladolid, Spain
www.deimos-imaging.com
Member Since: 1/2014

Environmental Research Incorporated

Linden, Virginia
www.eri.us.com
Member Since: 8/2008

Esri Research Institute, Inc.

Redlands, California
www.esri.com
Member Since: 1/1987

EXELIS

Boulder, Colorado
www.exelisvis.com
Member Since: 1/1997

Flatdog Media, Inc./Professional Surveyor Magazine

(formally Reed Business-Geo)
Frederick, Maryland
www.profsurv.com
Member Since: 1/1998

Fugro EarthData, Inc.

(formally EarthData, Inc.)
Frederick, Maryland
www.earthdata.com
Member Since: 1/1994

GeoBC

Victoria, British
www.geobc.gov.bc.ca
Member Since: 12/2008

GEOconnexion International

Cambridge, United Kingdom
www.geoconnexion.com
Member Since: 11/2011

GeoCue Corporation

(formerly NIIRS10, Inc.)
Madison, Alabama
info@geocue.com
Member Since: 10/2003

Geolas Consulting

Pöng, Germany
www.geolas.com
Member Since: 1/2002

Global Science & Technology, Inc.

Greenbelt, Maryland
www.gst.com
Member Since: 10/2010

GRW Aerial Surveys, Inc.

Lexington, Kentucky
www.grwinc.com
Member Since: 1/1985

HyVista Corporation

Castle Hill, Australia
www.hyvista.com
Member Since: 3/2010

ICAROS, Inc.

Fairfax, Virginia
www.lcaros.us
Member Since: 2/2013

Intergraph (ERDAS Inc.)

Norcross, Georgia
www.intergraph.com/geospatial
Member Since: 1/1985

Keystone Aerial Surveys, Inc.

Philadelphia, Pennsylvania
www.keystoneaerialsurveys.com
Member Since: 1/1985

KLT Associates, Inc.

Peabody, Massachusetts
www.kltassoc.com
Member Since: 11/1993

Kucera International

Willoughby, Ohio
www.kucerainternational.com
Member Since: 1/1992

Lead'Air, Inc.

(formerly Track'air BV)
 Kissimmee, Florida
www.trackair.com
Member Since: 6/2001

LizardTech

Seattle, Washington
www.lizardtech.com
Member Since: 10/1997

Magnolia River Geospatial

(formerly Aeroquest Optimal, Inc./Optimal Geomatics)
 Huntsville, Alabama
www.magnolia-river.com
Member since: 2/2006

MDA Information Systems LLC

(formerly MDA Federal Inc.)
 Gaithersburg, Maryland
www.mdaus.com
Member Since: 1/1993 (rejoined in 2011)

Merrick & Company

Greenwood Village, Colorado
www.merrick.com/gis
Member Since: 4/1995

Michael Baker Jr., Inc.

Beaver, Pennsylvania
www.mbakercorp.com
Member Since: 1/1950

Microsoft UltraCam Team (Vexcel Imaging, GmbH)

Graz, Austria
www.microsoft.com/ultracam
Member Since: 6/2001

NGA-National Geospatial-Intelligence Agency

Springfield, Virginia
<https://www.nga.mil>
Member Since: 11/2008

NASA Earth Science Division

Washington, DC
www.appliedsciences.nasa.gov
Member Since: 1/2001

NOAA National Geodetic Survey

Silver Spring, Maryland
www.ngs.noaa.gov
Member Since: 7/2009

NorPix, Inc.

Montreal, Quebec, Canada
www.norpix.com
Member Since: 1/2012

North West Group

Calgary, Canada
www.nwgeo.com
Member Since: 1/1998

NSTec, Remote Sensing Laboratory

Las Vegas, Nevada
www.nstec.com
Member Since: 7/2005

Observera, Inc.

Chantilly, Virginia
www.observera.com
Member Since: 7/1995

Optech Incorporated

Toronto, Canada
www.optech.ca
Member Since: 1/1999

PANalytical NIR

(formerly ASD)
 Boulder, Colorado
www.asdi.com
Member Since: 1/1998

PCI Geomatics

Richmond Hill, Ontario, Canada
www.pcigeomatics.com
Member Since: 1/1989

Pickett & Associates, Inc.

Bartow, Florida
www.pickett-inc.com
Member Since: 4/2007

Pictometry International Corp.

Rochester, New York
www.pictometry.com
Member Since: 5/2003

Quantum Spatial, Inc. (Quantum Spatial)

(formerly AeroMetric, Inc.)
 Sheboygan, Wisconsin
www.aerometric.com
Member Since: 1/1974

Riegl USA, Inc.

Orlando, Florida
www.rieglusa.com
Member Since: 11/2004

Robinson Aerial Survey, Inc. (RAS)

Hackettstown, New Jersey
www.robinsonaerial.com
Member Since: 1/1954

Sanborn

Colorado Springs, Colorado
www.sanborn.com
Member Since: 9/1984

Science Applications International Corporation

Mc Lean, Virginia
www.saic.com
Member Since: 1/1987

The Sidwell Company

St. Charles, Illinois
www.sidwellco.com
Member Since: 1/1973

SimActive, Inc.

Montreal, Quebec, Canada
www.simactive.com
Member Since: 1/2010

Spectral Evolution

North Andover, Massachusetts
www.spectralevolution.com
Member Since: 10/2010

Surveying and Mapping (SAM), Inc.

Austin, Texas
www.saminc.biz
Member Since: 12/2005

Trimble

Westminster, Colorado
www.trimble.com
Member Since: 4/1994

Towill, Inc.

San Francisco, California
www.towill.com
Member Since: 1/1952

U.S. Geological Survey

Reston, Virginia
www.usgs.gov
Member Since: 4/2002

University of Twente/Faculty ITC

[formerly International Institute for Geo-Information Science and Earth Observation (ITC)]
 Enschede, Netherlands
www.itc.nl
Member Since: 1/1992

USDA/National Agricultural Statistics Service

Fairfax, Virginia
www.nass.usda.gov
Member Since: 6/2004

Visual Intelligence Systems, LP

Houston, Texas
www.visualintelligenceinc.com
Member Since: 4/2014

Wilson & Company, Inc., Engineers & Architects

Albuquerque, New Mexico
www.wilsonco.com
Member Since: 3/2007

Wiser Company, LLC

Murfreesboro, Tennessee
www.wiserco.com
Member Since: 7/1997

Woolpert LLP

Dayton, Ohio
www.woolpert.com
Member Since: 1/1985

XEOS Imaging Inc.

Quebec, Canada
www.xeosimaging.com
Member Since: 11/2003

Photogrammetric Engineering and Remote Sensing (*PE&RS*)

Instructions for Authors Submitting a Manuscript for Peer Review

*Authors submitting a new manuscript for peer review should follow these instructions.
Failure to do so will result in the manuscript being returned to the author.*

INTRODUCTION: The American Society for Photogrammetry and Remote Sensing (ASPRS) seeks to publish in *Photogrammetric Engineering & Remote Sensing (PE&RS)* theoretical and applied papers that address topics in photogrammetry, remote sensing, geographic information systems (GIS), the Global Positioning System (GPS) and/or other geospatial information technologies. Contributions that deal with technical advancements in instrumentation, novel or improved modes of analysis, or innovative applications of these technologies in natural and cultural resources assessment, environmental modeling, or the Earth sciences (atmosphere, hydrosphere, lithosphere, biosphere, or geosphere) are especially encouraged. In addition, papers dealing with the practical or applied aspects for these disciplines will be published as “Applications” papers (see additional instructions below).

REVIEW PROCEDURES: Manuscripts are peer reviewed and refereed by a panel of experts selected by the Editor. A double-blind review procedure is used. The identities and affiliations of authors are not provided to reviewers, nor are reviewers’ names disclosed to authors. Our goal is to provide authors with completed reviews within 90 days of receipt of a manuscript by the Editor. Manuscripts accepted for publication will be returned to the author(s) for final editing before being placed in the queue for publication. Manuscripts not accepted will either be (1) rejected or (2) returned to the author(s) for revision and subsequent reconsideration by the review panel. Authors who do not revise and return a “to-be-reconsidered” manuscript within 90 days from receipt of reviews may have their manuscript withdrawn from the review process.

ENGLISH LANGUAGE: Authors whose first language is not English must have their manuscripts reviewed by an English-speaking colleague or editor to refine use of the English language (vocabulary, grammar, syntax). At the discretion of the Editor, manuscripts may be returned for English language issues before they are sent for review.

COVER LETTER: All submissions must also include a separate cover letter. Please modify the sample Cover Letter found at <http://www.asprs.org/pers/CoverLetter> and then convert it to a PDF file. It is important that we have the full names and titles (Dr. Russell G. Congalton not R. G. Congalton), complete mailing addresses, and email addresses of all the authors and any special instructions about the paper. Papers can not be submitted for review until this information is received by the editor. Also, the paper must be original work and not currently being considered for publication in any other journal. Finally, the authors must pay for any color figures in the manuscript and any page charges for articles longer than 7 journal pages. (Details on color costs can be found at <http://www.asprs.org/pers/ColorOrderForm>.)

“APPLICATIONS” PAPERS: A maximum of one “Applications” paper will be published each month as the last paper in the peer-reviewed section of *PE&RS*. The authors should follow all the instructions in this document. However, the “Applications” paper will be strictly limited to 7 journal pages. These papers will be peer-reviewed, but will emphasize the practical and applied aspects of our discipline. These papers must be identified by the author as an “Applications” paper in the cover letter and will be labeled as an “Applications” paper in the journal.

PREPARING A MANUSCRIPT FOR REVIEW: Authors must submit papers electronically in PDF format. Care must be taken to remove the author(s) name(s) from the electronic document. Please remove all author identification from the Properties of Microsoft Word before creating the PDF. Verify under Properties in Adobe Reader that your identity has been removed.

FORMAT REQUIREMENTS: Manuscripts submitted for peer review must be prepared as outlined below. Manuscripts that do not conform to the requirements described below will be returned for format revisions before they are sent for review.

- 1 TYPING:** All pages must be numbered at the bottom of the page. In addition, manuscripts must be single column and double-spaced. An 11 or 12-point font such as Times New Roman or Arial is preferred. Authors should use 8.5 by 11-inch or A4 International (210- by 297-mm) paper size, with 30-mm (1.25 inch) margins all around. For review purposes every part of the manuscript must be double-spaced, including title page/abstract, text, footnotes, references, appendices and figure captions. Manuscripts that are single-spaced or have no page numbers will be returned to authors.
- 2 PAPER LENGTH:** Authors are encouraged to be concise. Published papers are generally limited to 7–10 journal pages. A 27-page manuscript (including tables and figures), when typed as indicated above, equals about 7 journal pages. Authors of published papers will be charged \$125/page for each page exceeding 7 journal pages. These page charges must be paid before publication; without exception. (Details on page charges are included on the Offprint and Extra Page Order Form, available at <http://www.asprs.org/PE-RS-Submissions-Policy-and-Guidelines/Offprint-Order-Form.html>).
- 3 TITLE/ABSTRACT:** Authors should strive for titles no longer than eight to ten words. The first page of the paper should include the title, a one-sentence description of the paper’s content to accompany the title in the *PE&RS* Table of Contents, and the abstract. To facilitate the blind review process, authors’ names, affiliations, and addresses must be provided only in a separate cover letter, not on the title page. Authors should indicate both their current affiliation and, if different, their affiliation at the time the research was performed. Following the title and one-sentence and on the same page must be the abstract. All manuscripts submitted for peer review must include an abstract of 150 words or less. The abstract should include information on goals, methods and results of the research reported. The rest of the paper should begin on the second page.
- 4 FIGURES AND TABLES:** All figures and tables must be cited in the text. Authors should note that figures and tables will usually be reduced in size by the printer to optimize use of space, and should be designed accordingly. For purposes of peer review, figures and tables can be embedded in the manuscript. However, it should be noted that papers, once accepted, will require that all figures be included as separate files (see instructions for accepted papers) If the manuscript contains copyrighted imagery, a copyright statement must be included in the caption (e.g., ©SPOT Image, Copyright [year] CNES).

- 5 **COLOR ILLUSTRATIONS:** Authors should use black and white illustrations whenever possible. Authors who include color illustrations will be charged for the cost of color reproduction. These costs must be paid before an article is published. Details on color costs can be found at <http://www.asprs.org/pers/ColorOrderForm>. Authors should indicate in the cover letter that they have the funds to pay for any color figures in their paper.
- 6 **METRIC SYSTEM:** The metric system (SI Units) will be employed throughout a manuscript except in cases where the English System has special merit stemming from accepted conventional usage (e.g., 9- by 9-inch photograph, 6-inch focal length). Authors should refer to "Usage of the International System of Units," *Photogrammetric Engineering & Remote Sensing*, 1978, 44 (7): 923-938.
- 7 **EQUATIONS:** Authors should express equations as simply as possible. They should include only those equations required by an average reader to understand the technical arguments in the manuscript. Manuscripts that appear to have excessive mathematical notation may be returned to the author for revision. Whenever possible, authors are encouraged to use the Insert and Symbol capabilities of Microsoft Word to build simple equations. If that is not possible, the author must indicate in the cover letter which software was used to create the equations. *Microsoft Equation*, *Microsoft Equation Editor*, or *MathType* format should be used only if absolutely necessary. Equations must be numbered, but unlike tables, figures, color plates, and line drawings should be embedded in the text file.
- 8 **REFERENCES:** A complete and accurate reference list is essential. Only works cited in the text should be included. Cite references to published literature in the text in alphabetical order by authors' last names and date, as for example, Jones (1979), Jones and Smith (1979) or (Jones, 1979; Jones and Smith, 1979), depending on sentence construction. If there are more than two authors, they should be cited as Jones et al. (1979) or (Jones *et al.*, 1979). Personal communications and unpublished data or reports should not be included in the reference list but should be shown parenthetically in the text (Jones, unpublished data, 1979). Format for references will be as follows:

BOOKS:

Falkner, E., 1995. *Aerial Mapping: Methods and Applications*, Lewis Publishers, Boca Raton, Florida, 322 p.

ARTICLES (OR CHAPTERS) IN A BOOK:

Webb, H., 1991. Creation of digital terrain models using analytical photogrammetry and their use in civil engineering. *Terrain Modelling in Surveying and Civil Engineering* (G. Petrie and T.J.M. Kennie, editors), McGraw-Hill, Inc., New York, N.Y., pp. 73-84.

JOURNAL ARTICLES:

Meyer, M.P., 1982. Place of small-format aerial photography in resource surveys, *Journal of Forestry*, 80(1):15-17.

PROCEEDINGS (PRINTED):

Davidson, J.M., D.M. Rizzo, M. Garbelotto, S. Tjosvold, and G.W. Slaughter, 2002. Phytophthora ramorum and sudden oak death in California: II. Transmission and survival, *Proceedings of the Fifth Symposium on Oak Woodlands: Oaks in California's Changing Landscape*, 23-25 October

2001, San Diego, California (USDA Forest Service, General Technical Report PSW-GTR-184, Pacific Southwest Forest and Range Experiment Station, Berkeley, California), pp. 741-749.

PROCEEDINGS (CD-ROM):

Cook, J.D., and L.D. Ferdinand, 2001. Geometric fidelity of Ikonos imagery, *Proceedings of the ASPRS 2001 Annual Convention*, 23-27 April, St. Louis, Missouri (American Society for Photogrammetry and Remote Sensing, Bethesda, Maryland), unpaginated CD-ROM.

THESIS AND DISSERTATIONS:

Yang, W., 1997. *Effects of Spatial Resolution and Landscape Structure on Land Cover Characterization*, Ph.D. dissertation, University of Nebraska-Lincoln, Lincoln, Nebraska, 336 p.

WEBSITE REFERENCES:

Diaz, H.F., 1997. Precipitation trends and water consumption in the southwestern United States, USGS Web Conference, URL: <http://geochange.er.usgs.gov/sw/changes/natural/diaz/>, U.S. Geological Survey, Reston, Virginia (last date accessed: 15 May 2002).

- 9 **ACKNOWLEDGMENTS:** In keeping with the process of blind reviews, authors are asked not to include acknowledgments in manuscripts submitted for peer review. An acknowledgment may reveal a considerable amount of information for reviewers that is not necessary or desirable for their evaluation of the manuscript. After a manuscript is accepted for publication, the lead author will be encouraged to insert appropriate acknowledgments.

INFORMATION ON MANUSCRIPT REVIEW PROCEDURES: Corresponding authors of manuscripts submitted for review will receive an e-mail from the Editor acknowledging receipt of the manuscript. Details on *PE&RS* Manuscript Review Procedures can be found at <http://www.asprs.org/pers/ReviewProcedure>.

MANUSCRIPT SUBMISSION: All peer-reviewed manuscripts should be emailed to:

Dr. Russell G. Congalton, Editor-in-Chief
Photogrammetric Engineering & Remote Sensing
 4 Ryan Way
 Durham, NH 03824 USA
 E-mail: russ.congalton@unh.edu; Tel.: (603) 862-4644

SPECIAL ISSUE MANUSCRIPT SUBMISSION: These instructions also apply to manuscripts submitted for a Special Issue. However, Special Issue manuscripts and Cover Letters should be sent directly to the Guest Editor, not to Dr. Congalton. Please refer to the Special Issue Call for Papers for the Guest Editor contact information.

NOTE: Authors should NOT MAIL MANUSCRIPTS TO ASPRS HEADQUARTERS. This will cause the review to be delayed.

***Instructions last updated January 2013*

Everyone will benefit if YOU

Make a commitment to *Your Profession* and Join ASPRS Today.



Which membership is right for me?

ASPRS membership is for one year (12 months). Dues for Active and Associate members in the United States includes a printed copy of *PE&RS* in addition to access to the electronic version. Beginning with the January 2014 issue of *PE&RS*, all ASPRS members outside of the USA will only receive access to the full digital edition of the journal rather than the printed copy that has been routinely mailed. Dues for Non-US members will now be the same as the U.S. domestic (U.S. based) rate without the added postage surcharge. Dues for all Student members residing in the US, and outside of the U.S., including Mexico and Canada, receive a Full digital version of *PE&RS* only. **Please note:** Dues for all members in Canada include GST. Membership renewal is based on the anniversary date of the month you joined. Membership certificates are available for an additional charge (see below). Please allow 4–6 weeks for delivery of your membership materials.

Active

- Involved or interested in the practice of photogrammetry, remote sensing, and/or geographic information systems and related sciences.
- Full member benefits including; the right to vote and hold office, discounts on ASPRS conference registration fees, group insurance policy, eligibility for awards, discounts off ASPRS publications.

\$150.00 Domestic, 2nd Class \$158.00 Canada¹ \$150.00 Foreign

Associate

- An Associate Member shall NOT yet have reached the age of 35; shall pay dues that are approximately two-thirds of the full member dues.
- Eligible for this membership for a period of no more than five consecutive years; and may not revert to Student Member status. A person is not eligible for Associate Member status if he/she has previously held Member status.
- Associate Members shall be entitled to the same rights and privileges of the Society as an Active Member.

\$100.00 Domestic, 2nd Class \$105.00 Canada¹ \$100.00 Foreign

Student

- A Student Member shall be working towards a degree at a university or college. Certification of student status (examples may include copies of student identification or current registration, faculty or sponsor signature, etc.) is required for each year of student membership. **Attach a copy of your student ID or certifying faculty name and institution**
- A person is not eligible for student membership if he/she has previously held an Active or Associate Member status.
- Student members do not vote or hold office until they advance to Associate Membership.

\$50.00 Domestic \$53.00 Canada¹ \$60.00 Foreign

Membership Certificate

Hand-engrossed, framable certificate of membership is available for additional charge. \$20.00

Member Sponsorship (not mandatory)

Sponsor's Member ID: _____

Sponsor's Name: _____

Member Information

Technical Division Preferences: Number the following 6 ASPRS divisions in order of preference where your primary interests lie so you can be kept up to date on their activities (Order of Preference 1–6).

___ GIS Geographic Information Systems ___ PA Photogrammetric Applications
___ PDA Primary Data Acquisition ___ PP Professional Practice
___ Lidar Division (new) ___ RSA Remote Sensing Applications

New Member Renewal (ID number _____)

Mr. Ms. Dr. other: _____

Year of birth*: _____

Name (please print): _____

Check appropriate box for mailing address home business

Address: _____

Country: _____

Company's name/workplace: _____

Business Phone**: _____ Home Phone**: _____

fax**: _____ e-mail**: _____

*Required for Associate Members

**DO NOT PUBLISH: Business Phone Home Phone Fax E-mail

Method of Payment: Payment must be submitted with application.

Payment must be made in US Dollars drawn on a US Bank or appropriate credit card. Make checks payable to ASPRS.

Check (Print name on check.)
 Visa MasterCard American Express Discover

Credit Card Account Number Expires (MO/YR)

Signature Date

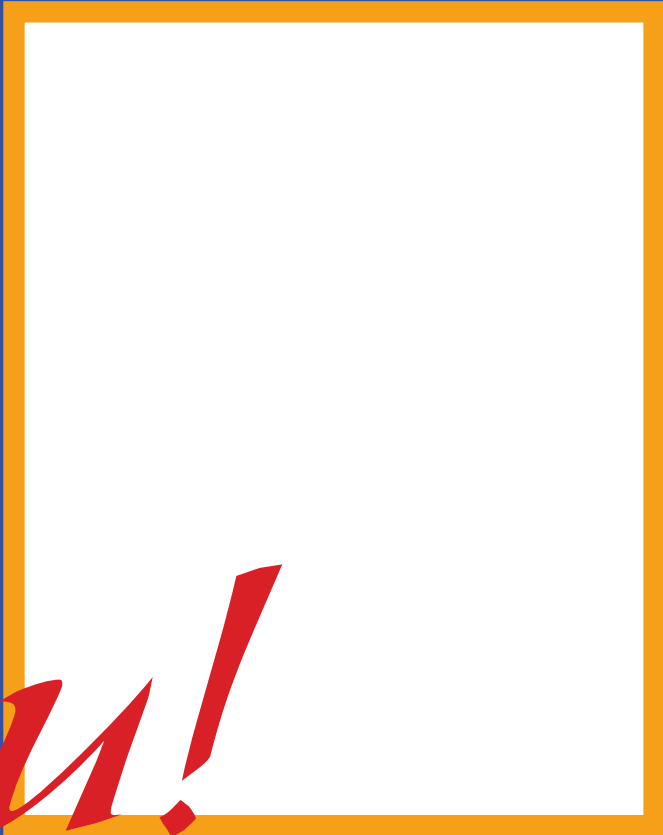
Total Amount Enclosed: \$ _____

Membership dues includes an annual subscription to *PE&RS*. Non-member subscription price is \$660.00 (libraries, universities, private companies etc.) Members may NOT deduct the subscription price from dues. ASPRS is an educational organization exempt from taxation under the 501(c) (3) code of the Internal Revenue Service. Dues payments are not deductible as a charitable contribution for federal tax purposes, but may be deductible as a business expense. Please check with your tax preparer.

Dues for Active and Associate domestic members includes Second Class Postage for *PE&RS*. Student members residing in the US, outside of the U.S., including Mexico and Canada, receive a Full digital version of *PE&RS* only.

¹DUES INCLUDES GST. (ASPRS is required by the Canada Customs and Revenue Agency to collect 5% of the total amount of dues for Canada's Goods and Services Tax — GST #135123065.)

What does an ASPRS Member look like?



You!

Join ASPRS (American Society for Photogrammetry and Remote Sensing), the premier international society of over 6,500 geospatial professionals from private industry, government, and academia. Together we advance imaging and geospatial information into the 21st century.

Geospatial professionals are critically needed to help rebuild our country's infrastructure. In this age of economic and environmental uncertainty, you are essential to building the tools for inventorying resources, monitoring change, and predicting the outcome of management and policy decisions across space and time. ASPRS provides you with a forum for networking, scientific exchange, consensus building, and outreach.



ASPRS Certification Program

A clear level of standard in an unclear environment

<http://www.asprs.org/Certification-Program/Introduction-to-ASPRS-Certification-Program.html>

